FACULTY
OF MATHEMATICS
AND PHYSICS
Charles University

DOCTORAL THESIS

Alexandr Prozorov

Neutral Meson Production in Ag+Ag Collisions at 1.58 A GeV with HADES Electromagnetic Calorimeter

Nuclear Physics Institute CAS, p.r.i

Supervisor of the doctoral thesis: RNDr. Andrej Kugler, CSc.
Study programme: Particle and Nuclear Physics
Study branch: Physics

Prague 2023

I declare that I carried out this doctoral thesis independently, and only with the cited sources, literature and other professional sources. It has not been used to obtain another or the same degree.

I understand that my work relates to the rights and obligations under the Act No. 121/2000 Sb., the Copyright Act, as amended, in particular the fact that the Charles University has the right to conclude a license agreement on the use of this work as a school work pursuant to Section 60 subsection 1 of the Copyright Act.

In .... date ....

Author's signature

Acknowledgement

In the first place, I would like to thank my family and my wife for supporting me throughout the study. I express my heartfelt gratitude to Pavel Tlustý for his help, patience, and fruitful discussions. Thank you for inspiring me to think critically, creatively. I owe a lot to my supervisor Andrej Kugler, who took the time to read and check this thesis and helped me in financial way during my doctoral studies. Your feedback and comments were incredibly helpful. I would like to thank my colleagues at Nuclear Physics Institute: Artem Isakov, Lukáš Chlad, Petr Chudoba, Filip Křižek, Daniil Koliadko, Ondřej Svoboda, Vladimír Wagner, Svetlana Kushpil and Jana Bielčíková. Last but not least, I thank a lot my colleagues from the HADES Collaboration: Malgorzata Gumberidze, Arseniy Shabanov, Adrian Rost, Tetyana Galatyuk and many others.

Title: Neutral Meson Production in Ag+Ag Collisions at 1.58 A GeV with HADES Electromagnetic Calorimeter

Author: Alexandr Prozorov

Department: Nuclear Physics Institute CAS, p.r.i

Supervisor: RNDr. Andrej Kugler, CSc., Nuclear Physics Institute of the CAS

Abstract: The Dielectron Spectrometer HADES operating at the SIS18 synchrotron, FAIR/GSI Darmstadt, recently provided new intriguing results on the production of electron pairs and strangeness from nucleus-nucleus collisions, as well as from elementary reactions, in the energy region of $1-2$ A GeV. In 2019 the spectrometer was complemented by an electromagnetic calorimeter based on lead-glass modules, which allows us to measure photons and thus study the production of π^0 and η mesons via their two-photon decay. Knowledge of the neutral-meson production is a mandatory prerequisite for the interpretation of dielectron data. In particular, the directed and elliptic flow of neutral mesons with respect to transverse momentum and rapidity will be shown for different centrality classes in Ag + Ag collisions at 1.58 A GeV. The results of the analysis corresponding to the 14×10^9 events will be confronted with the results of other experiments and with the current model calculations.

Keywords: baryonic medium, hadrons, relativistic heavy-ion collisions, neutral mesons, pion flow

Contents

Introduction

The main goal of this thesis is to study neutral pions produced in collisions of Ag + Ag with kinetic beam energy 1.58 A GeV with the HADES experiment.

This was possible due to the newly installed electromagnetic calorimeter which was used successfully in the experiment. The collected data allowed for multi-differential analysis on π^0 to study its multiplicity and directed as well as elliptic flow.

The measured pion yield is important for the normalization of the dielectron data obtained in the same experiment. The low-energy region of the invariant-mass spectra of dielectrons is dominated by the decay products of neutral pions.

The first chapter introduces the theoretical background, including the motivation for studying pion production in heavy ion collisions.

The next chapter describes the HADES experiment, briefly discussing each HADES subsystem. This chapter is base on corresponding TDR and description of the experimental setup published by HADES members elsewhere.

My main contribution to the Ag + Ag experiment is described in third, fourth and fifth chapters.

The third chapter covers the working principle and calibration of ECAL in detail.

The fourth chapter describes the analysis procedure used to extract π^0 multiplicity and the study of efficiency and acceptance correction.

The fifth chapter is devoted to the results of the π^0 yield and flow analysis and their discussion.

On my side, much work has been done not only in physics analysis but also in taking shifts during a beam time, preparation of ECAL modules, shielding PMTs, installing a small quantity of programming for read-out boards, and many other actions that are needed to make the calorimeter fully operational during an experiment.

1. Overview

1.1 Strongly interacting matter

There are four fundamental forces in our world, namely gravitational, electromagnetic, weak, and strong. Gravity can be described macroscopically via General Relativity. For electromagnetic interactions, there is a quantum field theory, quantum electrodynamics, which is the most precisely predicted and tested theory in physics today. The weak interaction is responsible for the β decay and the decay of pions, muons, and strange particles. Along with the electromagnetic force, the weak force is also part of a Standard model; both forces were unified as parts of an electroweak force. The strong force governs the structure of atomic nuclei and their ingredients, hadrons, which themselves consist of quarks[1]. It is described by a quantum field theory called Quantum Chromodynamics (QCD).

In the Standard Model, the propagation of charges associated with each of the fundamental forces is mediated by specific particles, namely gluons for strong interaction, photons for electromagnetic interaction, and W^+, W^-, and Z bosons for weak interaction. However, the Higgs boson differs from these gauge bosons as it plays a crucial role in generating particle mass; see Fig. 1.1

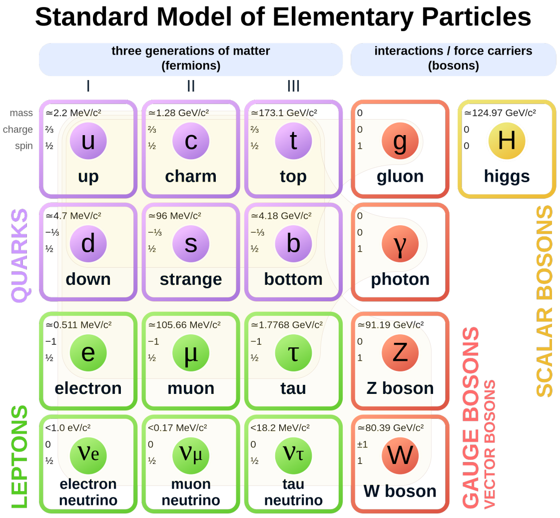

Figure 1.1: Elementary particles in Standard Model. Taken from [2].

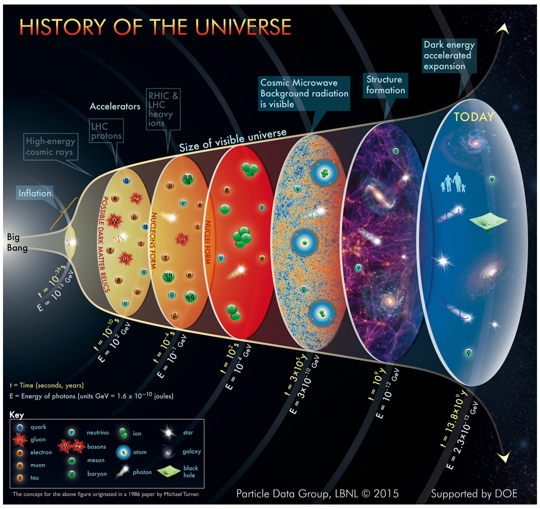

Figure 1.2: History of the universe. Taken from [3]

1.2 QCD Phase diagram

The QCD phase diagram is used to characterize nuclear matter schematically drawn in Fig. 1.3.

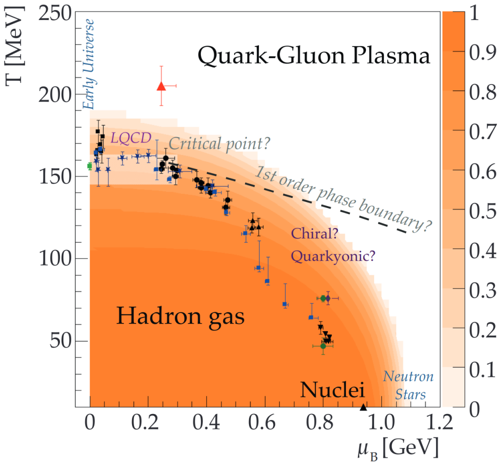

Figure 1.3: Sketch of the phase diagram of QCD matter including data points in T and μ_B describing the final chemical freeze-out from grand canonical statistical model [4].

The properties that characterize nuclear matter are the temperature T and baryochemical potential μ_B. The latter measures the difference between matter and antimatter produced during heavy-ion reactions. Matter can exist in different phases depending on the temperature and compression of the system, such as the hadronic phase, where quarks and gluons are confined to hadrons, the quark-gluon plasma phase, where they are deconfined, and there are also exotic phases of matter.

Whether a first-order phase transition or a critical point exists between the two phases of nuclear matter is presently unknown, as the critical point has yet to be identified. On top of this knowledge, the QCD phase diagram of matter is primarily based on the theory [5],[6].

The matter at extreme temperatures, in reality, existed for 10 microseconds after the Big Bang, see Fig. 1.2. On the other hand, there is a common belief, that matter in the interior of neutron stars have medium temperature and high baryon density. Moreover, in 2017 it was detected with gravitational waves that matter at high densities exists in neutron star merges[7]. This form of matter can also be accessed in laboratory settings through heavy-ion collisions at relativistic energies.

Following stages of heavy-ion collisions could be identified: nucleon-nucleon collision, fireball formation, adiabatic expansion, and the freeze-out phase, including chemical and later kinetic freeze-out.

The way to learn about the QCD phase-space diagram is by probing different regions with heavy-ion collisions in different energy ranges and using different geometry.

One of the extreme scenarios is a very high-energy collision; for example, at LHC, when $\sqrt{s_{NN}}$ reaches 2 TeV for heavy-ion collisions, the two colliding nuclei are very Lorentz contracted. When nuclei pass through each other within a certain fraction of the femtometer in time, a symmetric amount of particles and antiparticles is created, which leads to a very low or vanishing baryochemical potential. Another extreme scenario is the lower energy in the $\sqrt{s_{NN}}$ from 1 GeV to 5 GeV, which is accessible at the GSI facility. There nuclei have a much lower Lorentz contraction and are slowly moving toward each other. The system requires approximately seven fm/c for two nuclei to pass through each other. During nuclear stopping, a large amount of nuclear matter and a small fraction of antimatter can be produced in similar quantities. The high-density matter with a moderate temperature in the collision zone can be further connected to the matter produced in the neutron star merger.

From Lattice QCD, it has been calculated that a smooth crossover exists at the vanishing chemical potential [8]. If a first-order phase transition is found with high baryochemical potential, there should be a critical point.

1.3 Equation of state

The Equation-of-State (EOS) relates the total energy of the system to bulk observables, including pressure p, temperature T, density ρ, and the number of particles N.

Assuming an equilibrium state during the expansion of nuclear matter, the center-of-mass energy per nucleon of the reaction can be divided into three distinct components: the internal thermal energy E_{th}, the compression energy E_C, and the ground-state energy E_0.:

$$E = E_{th} + E_C + E_0. \tag{1.1}$$

The Bethe-Weizsacker formula provides a value of approximately -16 MeV for the binding energy of the ground state, with an average density of $\rho_0 \approx 0.16$ fm^{-3} [9]. At zero density ($\rho = 0$), the binding energy is zero because the nucleons are entirely separated. As a result, two points on the EOS are already established.

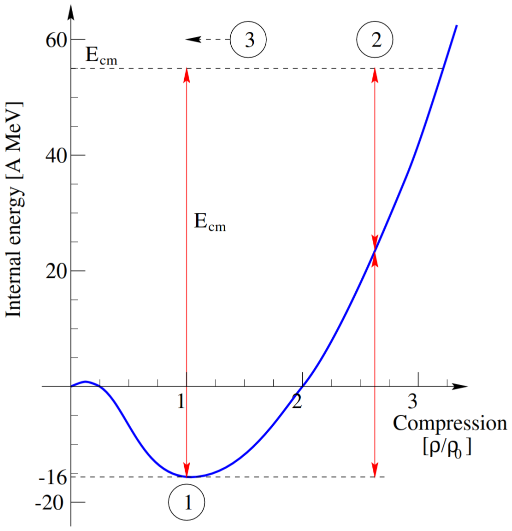

Figure 1.4: Energy per baryon of nuclear matter relating to the density given in units of,ρ_0= 0.15 nucleons/fm^3. The reaction cycle is denoted by 1 (before interaction), 2 (maximum compression), and 3 (expansion towards freeze-out). During stage 2, the internal energy is distributed between thermal energy (E_T) and compression energy (E_C). Taken from [10].

The question of nuclear compressibility has drawn much attention. The compressibility factor K quantifies how much energy per nucleon one needs to compress matter and is defined as the second derivative of the energy with respect to ρ:

$$K = -V\frac{dp}{dV} = 9\rho^2 \frac{\partial E_C}{\partial \rho^2}\bigg|_{\rho=\rho_0}. \tag{1.2}$$

EOS is generally called soft if $K < 290$MeV and stiff in the opposite case.

The equation of state also plays an essential role in our understanding of astrophysical processes such as supernova explosions or the composition and structure of neutron stars. One of the tests to see if EOS is soft or stiff is the upper limit of the neutron star mass, since these quantities are connected [11]. The other ways to test are connected to heavy-ion collision observables, such as meson production and collective flow.

There have been many studies in support of soft EOS [12], [13]. However, this assumption is challenged by recent studies of particle flow in HIC in favor of stiff EOS [14] [15], making the conclusion on EOS ambiguous.

This equation of state is used when comparing the results with model simulations.

1.4 Heavy-ion collisions

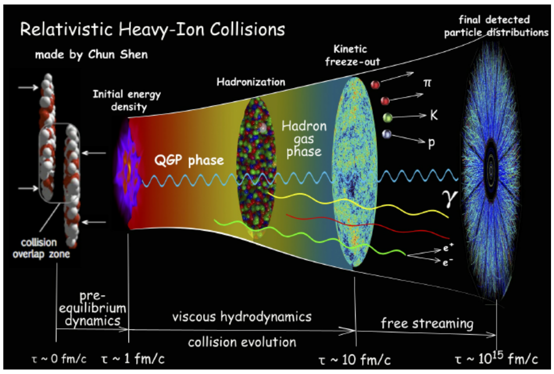

Figure 1.5

The baryochemical potential and temperature are collective thermodynamic properties that describe the macroscopic state of a medium. These quantities cannot be measured directly. Although the temperature at the kinetic freeze-out can be obtained from the kinetic distributions of the measured particles using the functions, the baryochemical potential can be obtained for the chemical freeze-out using a Statistical Hadronization Model[16].

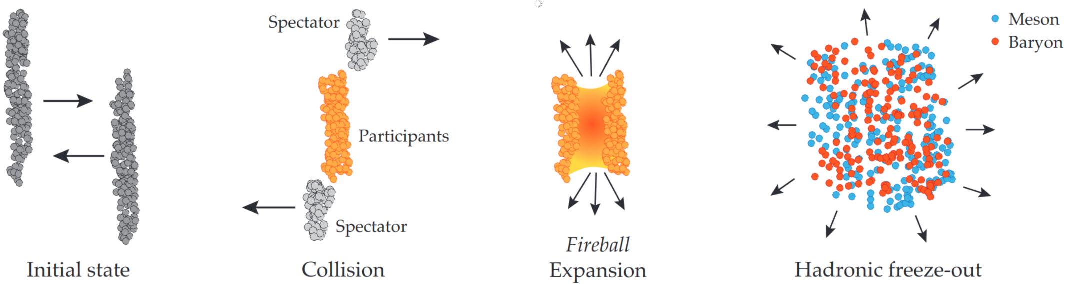

Figure 1.6: Schematic depiction of the time evolution of an Ag+Ag@1.58A GeV collision with an impact parameter of 3 fm simulated with UrQMD [17]. Nucleons that have not interacted(spectators) are depicted in light grey, and those that interacted (participants) are depicted in orange. Mesons and baryons are shown in blue and red, respectively. Credit to B.Kardan [4].

The time evolution of the collision can be schematically shown in Fig. 1.6 with the following stages:

- **Initial stage** The two nuclei in a ground state, where its configuration is approximated as frozen, approach each other, being Lorentz contracted.
- **High-Density stage** The kinetic energy of the colliding nuclei is transformed into compression energy, and the highest density is achieved in this phase.

- **Expansion stage** With the high pressure of the created medium in a collision place, the system expands rapidly with a decrease in temperature and density. Due to the pressure gradient, the system can experience hydrodynamic effects such as flow,
- **Freeze-out stage** At some point, expansion has progressed so that inelastic particle-particle interactions will cease due to an increase in mean nucleon distances. Except for resonance decay, the chemical composition of the particles remains unchanged regarding the strong interaction, except for short-lived resonances. Although it can still change through electromagnetic and weak decays, this time point is known as a chemical freeze-out. At some later stage, the elastic interaction between particles also ceases. After this point, termed kinetic freeze-out, the moment of the particles is unchanged again except for electromagnetic and weak decay. Both freeze-out points are essential for studying heavy-ion collisions because they represent particles' chemical and kinetic states when they are finally measured in detectors.

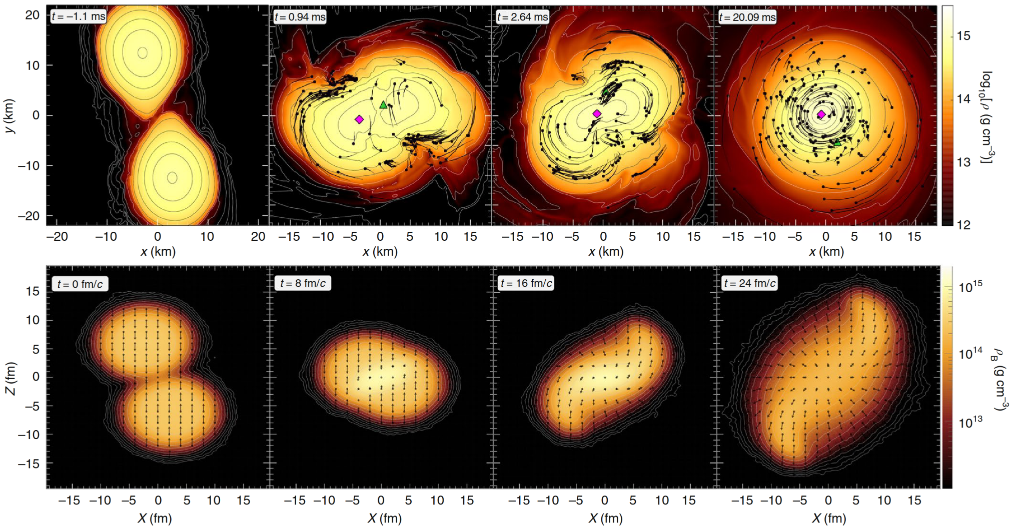

Figure 1.7: Simulations of nuclear matter in collisions yielding extreme conditions of density and temperature. Upper part: the neutron star merger, lower part - heavy ion collision.[18]

Until now, there has been only one observation of nuclear star merger, namely GW170817, which was a gravitational wave detected by the LIGO and VIRGO detectors.[7]. This event has opened a new era of gravitational wave measurements and provided invaluable information about processes occurring in neutron stars. Moreover, many model descriptions have been provided with post-merger neutron star properties. In addition, it has been proposed that temperatures around 50-80 MeV and densities twice as high as a typical nuclear density can be reached. In Fig. 1.7, the phases of the neutron star merger model are shown in the upper row, which are to be compared with stages of a non-central heavy-ion collision with a temperature of 71.8 ± 2.1 MeV. and a density up to three times the ordinary matter. [18].

Pions are the most abundantly produced mesons in the energy range around 1-2AGeV. Measurement of the multiplicity of π^0 in heavy-ion collisions provides information on the production of baryonic resonances in the medium.

1.5 Pion production rates in heavy ion collisions

Pions are the most abundant particles produced in heavy-ion collisions due to the smallest rest mass along all particles, hence, the threshold energy in nucleus-nucleus (NN) collisions for particle with masses $m_{\pi^\pm} = 139.57$ MeV and $m_{\pi^0} = 134.98$ MeV are $\approx$ 290 MeV and 280 MeV in laboratory energy, respectively.

Pions are created in a two-step process in the low-energy region: In a NN collision, a Δ resonance is created and decays later to produce a pion:$NN \rightarrow N\Delta \rightarrow NN\pi$.

A compilation of data on pion yields measured in symmetric nucleus-nucleus collisions and in proton-proton collisions is presented in Figure 1.8. The total pion multiplicities per participating nucleon are plotted as a function of the beam energy, which is expressed as the excess energy in the c.m. system $\sqrt{s} - 2m_N$.

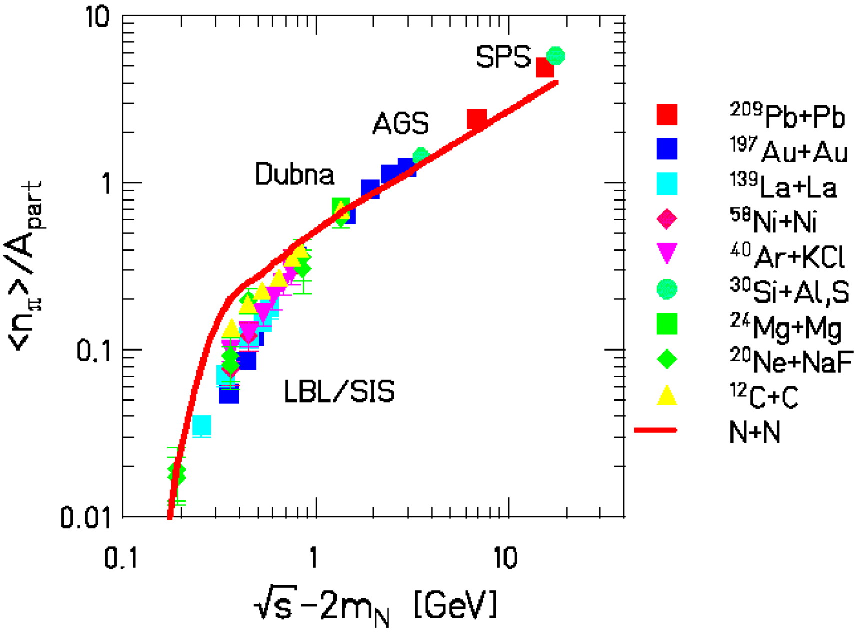

Figure 1.8: Pion multiplicity per number of participants in nucleus-nucleus collisions (symbols) and in nucleon-nucleon collisions(line) as function of available energy in the NN system [19].

Figure 1.8 indicates that the pion-to-nucleon ratio in the fireball is much lower for A+A collisions at SIS energies. At AGS energies, the number of pions produced in a fireball is about the same as of participating nucleons, whereas at top SPS energies, the pion production rate exceeds significantly the number of participating nucleons. At SIS energies, pions are produced mainly by excitation and decay of the Δ resonance. At higher beam energies, the decay of heavier baryonic resonances and vector mesons becomes increasingly important for pion production. The line in Fig. 1.8 is based on data on pion production in proton-proton collisions, which were corrected for isospin effects to obtain the pion yield from "nucleon-nucleon" (NN) collisions.

An interesting feature of the pion yields presented in Fig. 1.8 is the difference between the nucleus-nucleus data (symbols) and the nucleon-nucleon data (denoted as solid line). In the SIS energy range, the relative pion yield is smaller for A+A than for N+N collisions. This "pion suppression" in A+A collisions might be caused by true pion absorption, which is favored in systems where the number of pions is small as compared to the number of baryons and which live relatively long comparable with passing time . In the AGS energy range $\langle n_\pi \rangle / A_{part}$ reaches a value of approximately 1 for both N + N and A + A. At CERN-SPS energies, the pion yield per participating nucleon is larger for A+A than for N+N collisions. At these very high beam energies, additional pions can be created in subsequent collisions of projectile and target participant nucleons, an effect that occurs only in A + A collisions.

The pions are constantly produced during the collision and thus contain information on the various phases of the reaction. The information can be obtained by measuring the collective movement of the pions. In a non-central nucleus-nucleus collision, the spectator fragments shadow the pions which are emitted from the fireball in the reaction plane. This effect destroys the azimuthal isotropy of the pion emission pattern and introduces a "collective flow" of the pions. More overview information on the pion production can be found in [20],[21],[22],[19].

1.6 Experimental Data

The Two Arm Photon Spectrometer (TAPS) was an experiment that specifically looked for neutral-meson production via their two-photon decay [23].

TAPS has measured π^0 and η multiplicities in different energy regimes that cover incident energies from 0.2A GeV to 2.0A GeV, and for different types of colliding nuclei, such as light (C + C), intermediate mass (Ar, Ca + Ca) and heavy symmetric systems (Ni + Ni, Kr + Zr, Au +Au)[24, 25, 26, 27, 28]. They have shown that observed meson yields are consistent with the formation of a hadronic fireball in chemical equilibrium. In contrast to particle yields, which convey the state at chemical freeze-out, the shapes of the related transverse-mass spectra reflect thermal freeze-out. The observed thermal freeze–out temperatures are equal to or slightly lower than the chemical freeze-out temperature, indicating an almost simultaneous chemical and thermal freeze–out[29]. However, the TAPS acceptance area has only covered the midrapidity region, whereas HADES can perform multidifferential analysis in the forward rapidity region for heavy-ion collisions.

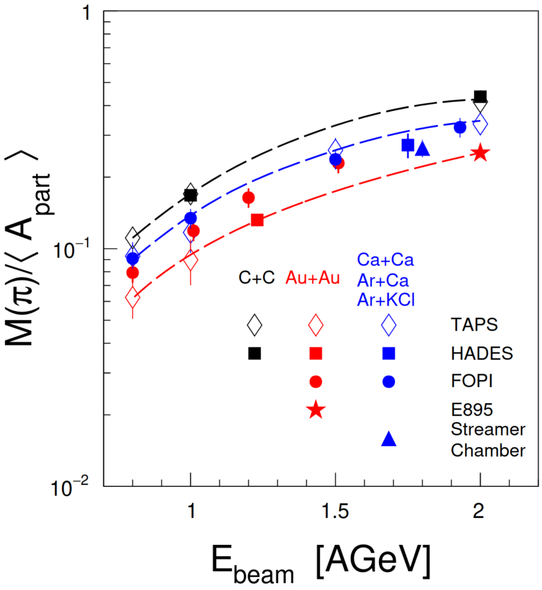

Figure 1.9: Production cross section for different systems and energies measured with the HADES, TAPS, FOPI, E895 and Streamer Chamber : C+C (black) Ar+KCl (blue) and Au+Au (red). The curves are polynomial fits to these data used to interpolate the multiplicities as a function of bombarding energy for corresponding systems. Taken from [20].

HADES has also performed measurements of the neutral pion yield using conversion e^+e^- pairs in Dalitz decays of the corresponding particles[30]. The measurements are compared with world data and calculations of theoretical models — Fig.1.9.

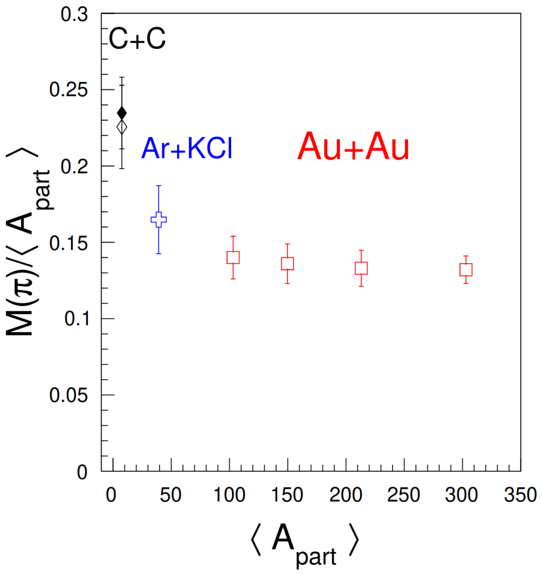

Figure 1.10: Pion multiplicity per participating nucleon as a function of centrality given by $\langle A_{part} \rangle$ measured by HADES. The data points for Ar+KCl (open cross) measured at 1.76 A GeV as well as the C+C at 1 A GeV (closed diamond) and at 2 A GeV (open diamond) were scaled to be at a beam energy of 1.23 A GeV. Taken from [20].

The available experimental data on pion production in HI collisions at an incident energy of 1 AGeV are collected in Fig.1.10. The measured pion yields are shown in terms of the mean number of pions per mean number of participants, $\langle n_\pi \rangle / A_{part}$. That the pion production is reduced to a single number was already shown with the Streamer Chamber [31],[32]. In experiments with Ar + KCl and La + La it was shown that the number of pions per participant rises linearly with energy. Moreover, at all measured energies no difference was observed for these two reactions. The conclusion was drawn that the pion production per participant is independent of the system size and increases with increasing incident energy. This result is commonly referred to as the Harris systematic.

It should be mentioned that all the data shown in Fig. 1.9 are extrapolated in somewhat different ways. Taps measures only π^0 at midrapidity and adds unmeasured charged-pion yields, while FOPI measures charged-pions only. The Streamer Chamber measured only π^-. In all cases, the correction due to the unmeasured pion species is calculated using the isobar model (see [33]).

1.7 Theoretical models

In order to fully understand and interpret a complicated structure of the physics processes, a comparison with models is needed. There are mainly two types of transport models, namely dynamic and static [34]. A static model is time-invariant and describes an equilibrium system state in which the most famous representatives are statistical models based on stochastic probability distributions. It is assumed that particle production occurs at chemical freeze-out, and all possible final states of a heavy-ion collision are used here as statistical ensembles. The beauty of this model lies in its simplicity, since the description depends only on a few parameters. However, during the collision, many mechanisms take place. The created system can be seen as a mixture of fluid cells (hydrodynamic model) or particles (kinetic transport model). Compared to the statistical description of heavy-ion collisions, dynamic models represent a somewhat contrary description in many aspects. Such models offer a microscopic (as opposed to macroscopic) and dynamic (as opposed to static) representation of the system without requiring thermal equilibrium, where particles are propagated through phase space, and the heavy-ion collision is described as a superposition of the individual NN collisions, the so-called kinetic transport models.

1.7.1 Statistical models

Statistical models successfully predict particle yields even without complete thermal equilibrium for various systems and energies. They need only a few numbers to describe the particle yields at chemical freeze-out. On the contrary, the fitting parameters such as temperature T, baryochemical potential μ_B, and volume V of the model provide information on the data and can reveal the properties of particle creation. In the Grand-Canonical Ensemble, the number of particles is no longer fixed but is conserved on average only by introducing a chemical potential μ. The probability p_i that a particle of species i occupies a given state with a quantum number q in a system depends as follows:

$$p_i \propto \exp\Big(\frac{-E_i + \mu_q}{kT}\Big) \tag{1.3}$$

This approach is further extended to describe the conservation of quantum numbers such as charge Q, baryon number B, and strangeness via chemical potentials μ_Q,μ_B, and μ_S, respectively. With particle density $\rho_{i,q}$ for particle i and quantum numbers $\vec{q} = (Q_i, B_i, S_i)$ and chemical potentials $\vec{\mu} = (\mu_Q, \mu_B, \mu_S)$ being :

$$\rho_{i,q} \propto \int_0^\infty p^2 dp \exp\Big(\frac{-E_i + \vec{\mu}\vec{q_i}}{kT}\Big) \tag{1.4}$$

From an experimental point of view, the parameters of these models can be deduced from the experiment, allowing the prediction of general trends in particle production.

1.7.2 Dynamical models

The first set of dynamical models is kinetic transport models in which particles are propagated in time through space and interact with each other. The degrees of freedom are particles themselves and strongly depend on the chosen system. These models are susceptible to input parameters such as vacuum lifetime, all elementary cross sections, and particle pole mass. However, it is difficult to fix them precisely; therefore, parametrization with resonance production can be used[35]. The production of particles below a threshold is made using multi-step processes, in which resonance is excited in the first step, and this is propagated through the medium without affecting the encased properties—previously interacting with its higher energy level, resulting in the production of rare particles.

Cascade models are transport models with point-like particles propagating in space-time, obeying the Boltzmann equation.

$$\Bigg(\frac{\partial}{\partial t} + \frac{\vec{p}}{m}\nabla_{\vec{x}} + \vec{F}\cdot\nabla_{\vec{p}}\Bigg) f(\vec{x}, \vec{p}, t) = I_{coll} \tag{1.5}$$

with the single particle distribution function $f(\vec{x}, \vec{p}, t)$, a collision term I_{coll} , a diffusion term $\nabla_{\vec{x}}$ and an external force term $\vec{F}\cdot\nabla_{\vec{p}}$. The right-hand side includes decay and scattering cross sections and important input from microscopic theories.

As an exact Boltzmann equation solution is complicated, various simplified descriptions can be used under certain assumptions. Examples are Boltzmann-Ueling-Uhlenbeck [36], Giessen BUU (Boltzmann-Ueling-Uhlenbeck)[37] or HSD (Hadron String Dynamics)[38].

The molecular dynamics approach can be used for many-body systems, mainly based on the Quantum Molecular Dynamics model[39]. In contrast to the cascade models, particles are represented by a Gaussian density distribution in phase space. The most popular models are IQMD (Isospin QMD) [40], RQMD [41], and UrQMD [42] (Relativistic respective Ultra-relativistic QMD). Today, most advanced models combine an effective solution of the relativistic Boltzmann equation with binary interactions: JAM [43], and SMASH [44].

1.7.3 Relativistic hydrodynamics for heavy-ion collisions

The large elliptic flow measured at the Relativistic Heavy-Ion Collider (RHIC) at Brookhaven National Laboratory is one of the most striking observations in heavy-ion collision experiments. The asymmetry of particle production in the transverse plane of the collision is interpreted as a sign of the system's hydrodynamic response to the initial conditions.

The evolution of heavy-ion collisions in terms of hydrodynamic formalism is characterized by five conservation laws: the conservation of energy-momentum and the net baryon number:

$$\partial_\mu T^{\mu\nu} = 0, \quad \partial_\mu J^\mu_B = 0, \tag{1.6}$$

with $T^{\mu\nu}$ being the energy-momentum tensor and J^μ_B being the net baryon current. It can be further re-expressed as time-like four-vector $u^{\mu\nu}$

$$T^{\mu\nu} = (\epsilon + \mathcal{P})u^\mu u^\nu - \mathcal{P}g^{\mu\nu}, \quad J^\mu_B = \rho_B u^\mu, \tag{1.7}$$

where ϵ is the energy density, $\mathcal{P}$ is the pressure, ρ_B is the baryon density, and $g^{\mu\nu} = diag(1, -1, -1, -1)$ is the metric tensor. The equilibrium equation of state is the final equation required to complete the description of the system.

$$\mathcal{P} = \mathcal{P}(\epsilon, \rho_B) \tag{1.8}$$

The system's behavior in both simulation and experiment was successfully described for the first time using ideal hydrodynamics, without considering any viscous effects. By comparing experimental data with hydrodynamic simulations, it is possible to obtain properties of the created matter and other relevant measures, for example shear viscosity η over the entropy density ratio s [45],[46], [34].

2. The HADES detector system

The High Acceptance Di-Electron Spectrometer (HADES) operating on the SIS18 accelerator is located at the International Facility for Antiproton and Ion Research (FAIR) in Darmstadt, Germany. FAIR is currently under construction at the GSI Helmholtzzentrum für Schwerionenforschung. The accelerator infrastructure to be build is shown by red color in Fig. 2.1.

The low kinetic energy ions begin their way in the Universal Linear accelerator and are accelerated up to 11.4 MeV/nucleon. Furthermore, in the Heavy-Ion Synchrotron 18 Tm, they reach even higher energies up to 2 GeV/nucleon. In addition, there is a possibility to produce secondary beams of rare radioactive nuclei in the Fragment Separator and store, and cool accelerated ions in the Experimental Storage Ring [47].

At the time of writing, the current FAIR infrastructure is being constructed, which will allow in future particle acceleration at even higher energies, namely up to 10 GeV per nucleon for heavy ions and 14.5 GeV per nucleon in the case of protons. The current SIS18 accelerator ring will serve as an injector for the new Heavy-Ion Synchrotron, 100 Tm rigidity ring accelerator (SIS100), along with a new, improved fragment separator and a unique antiproton storage ring. The HADES detector system measured Ag+Ag collisions at 1.58A GeV in March 2019 as part of the so-called FAIR Phase-0 program, within which the FAIR equipment shall be used for physics experiments at other facilities before the actual start of FAIR.

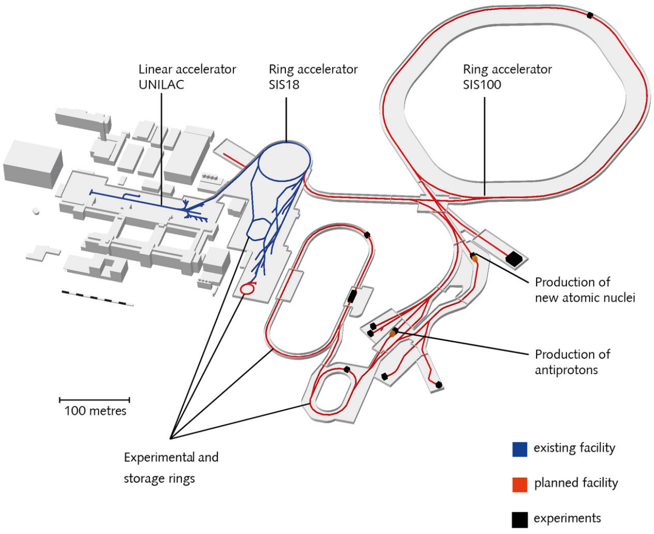

Figure 2.1: A schematic view of FAIR accelerator facility[48].

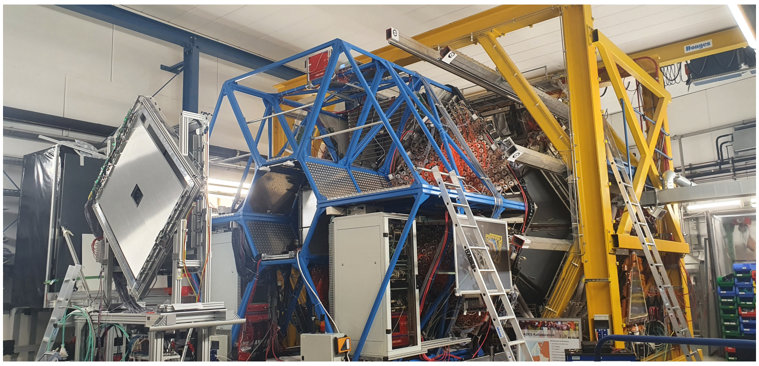

Figure 2.2: A photo of the HADES detector system. Taken in October 2020.

2.1 The HADES

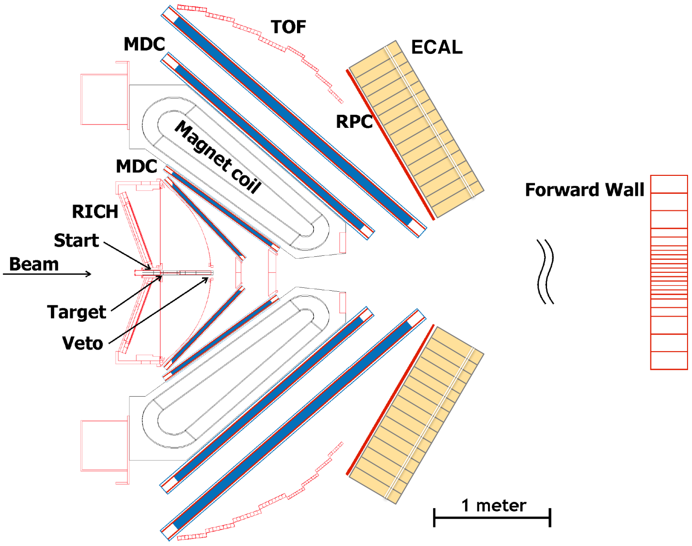

Figure 2.3: A schematic view of a cross-section through two opposite sectors of HADES.

The HADES experiment focuses on a kinetic energy range of 1 to 2 A GeV for heavy ions. However, it was also used for pion beam and proton beam experiments. The photo of HADES detector is shown in Fig.2.2. From the beginning, the detector has been designed as a multipurpose fixed target detector along with an optimized detection of electron-positron pairs for studying light vector mesons ρ, ω, ϕ as they are excellent probes of the high-density phase of heavy-ion collisions. They decay electromagnetically to e^+e^- pairs, which do not interact strongly with matter and therefore contain essential information on the evolution of fireballs. Because the branching ratios to dielectron pairs are tiny compared to other channels, a lot of heavy-ion collision statistical data are needed for research, which in turn implies a demand for high acquisition rates in time and high-speed subdetector performance. The lower the dead time, the higher the number of

Year	Collision system	$\sqrt{s_{NN}}$[GeV]	Events[$\times 10^9$]
2002	C + C	2.70	0.25
2004	$p + p$	2.77	0.44
2004	C + C	2.32	0.50
2005	Ar + KCl	2.61	0.93
2006	$d + p$	2.37	0.85
2007	$p + p$	2.42	1.70
2007	$p + p$	3.18	1.18
2008	p + Nb	1.93	4.21
2012	Au + Au	2.42	7.31
2014	π^- + C	1.98	0.40
2014	π^- + p	1.47-1.56	1.23
2019	Ag + Ag	2.55	13.61
2019	Ag + Ag	2.42	1.3
2022	$p + p$	3.42	14

Table 2.1: Overview of HADES experiments carried up to 2022 with important information about individual beam times.

events collected for the same period. Moreover, low-material-budget subdetectors are used to reduce background electron-positron pairs from photon conversion. The HADES setup consists of an ironless six-coil toroidal magnet centered on the beam axis and six identical detector sectors between the coils with nearly complete azimuthal coverage and polar angles spanning between $18° \leq \theta \leq 85°$. Fig. 2.3 shows a schematic view of the setup.

To summarize, the key features of HADES are as follows:

- **High geometric acceptance**
- **High event rate** - on average 10 kHz for the March 2019 Ag + Ag experiment
- **High reconstruction efficiency**
- **Excellent separation between hadrons and electrons**
- **Light material setup** - allowing one to reduce the background of conversion pairs e^+e^-

The list of production runs is shown in table 2.1.

For further reference and detector capabilities, see [49].

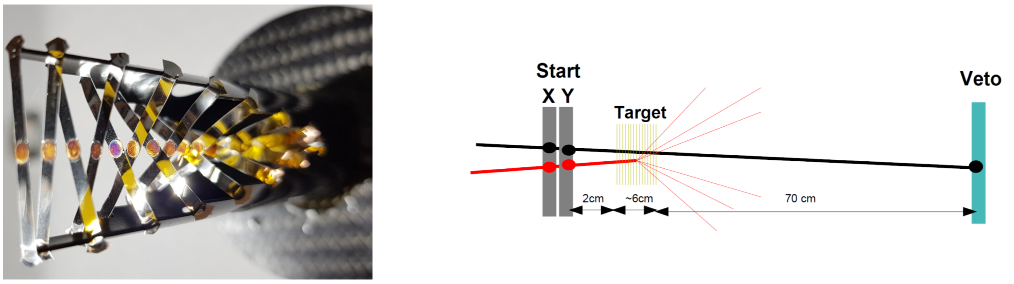

Figure 2.4: **Left**: Photo of the segmented silver target used during beam time. Each target segment is fixed with a thin kapton strip to the carbon tube. **Right**: Schematic of the Start-Target-Veto system

2.2 Target

During the beam time in March 2019, a 15-segmented silver target was used; see Fig. 2.4. Each silver disc was glued to a kapton foil fixed to the carbon support. Segmentation was done to decrease the probability of interaction of the particles produced in collision with the target material itself. By maximizing the distance, the contribution of conversion in the following segments can be neglected, as radiation γ typically leaves the target material with a large opening angle.

Consequently, a total nuclear interaction of 1.5% is achieved while maintaining a photon conversion probability below 1% [50].

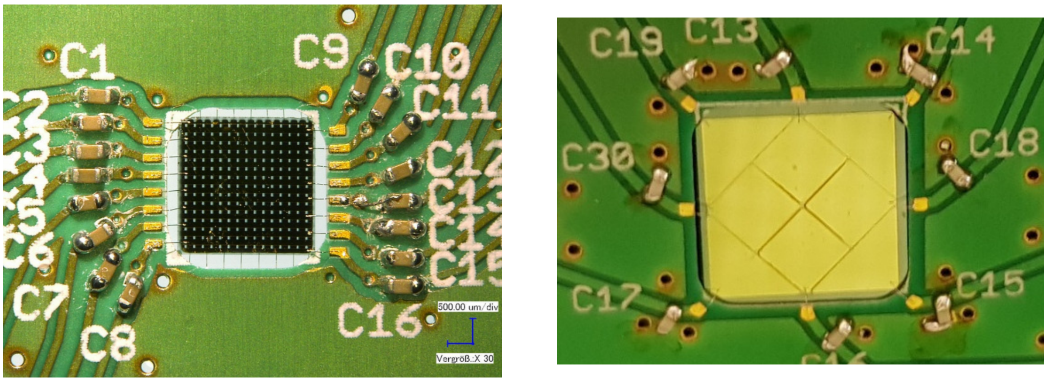

Figure 2.5: **Left**:Start detector. **Right**:Veto detector

2.3 START and VETO detectors

The Start-Veto system allows one to determine a starting time within 50 ps and monitor the beam focusing. The multi-strip detector consists of monocrystalline diamond-based semiconductors and has a side length of $4.7mm$ and a thickness of $50\mu m$. Each module contains 16 stripes (in the x- and y-directions). See Fig. 2.5.

The first double-sided Start detector is located about 2 cm in front of the target; the second Veto detector is placed 70 cm behind the target. Together, they provide information about the reaction: if a beam particle hits the target, there should not be any signal in the veto detector due to particle scattering.

The anti-coincidence system is shown in Fig. 2.4, right. The efficiency of the T0 detector was determined to be $> 95\%$ [51].

2.4 Tracking system

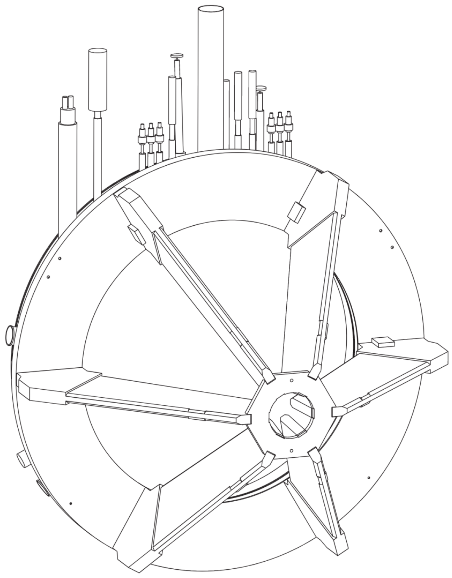

Figure 2.6: Scheme of ILSE (Iron-Less Superconducting Electromagnet)[52].

The HADES tracking system consists of Mini Drift Chambers(MDCs)[53] and a superconducting toroidal magnet[54]. It provides a particle track and momentum reconstruction for charged particles with momentum acceptance $p \in (0.1 - 2)$ GeV/c. A combination of the magnetic field with MDC tracking measurements allows for momentum resolution $\sigma_p/p < 2\%$.

The magnet has six superconducting Nb Ti coils and has a gradient field starting from 3.6 T at the coils; the sketch is depicted in Fig.2.6. The main purpose is to generate a magnetic field between the inner MDCs and outer MDCs.

The cooling system cools the coils by a liquid nitrogen/helium system down to the superconductive state at 4.7K, allowing currents up to 3464 A and a strong magnetic field of 3.6T despite the compact coil setup. The coil geometry was specially designed to account for the RICH detector performance, as it is most sensitive to a residual magnetic field. [54].

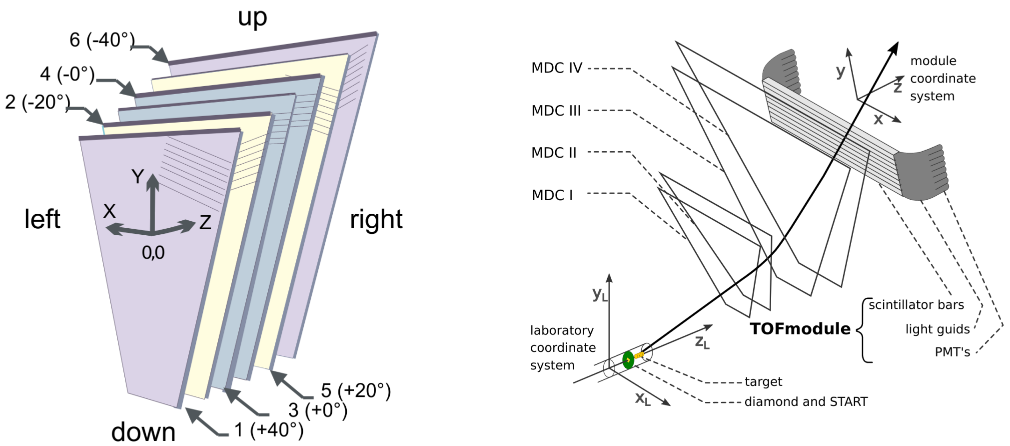

Figure 2.7: **Left**:Six layers orientation of a single MDC.**Right**: Track reconstruction using MDCs and TOF

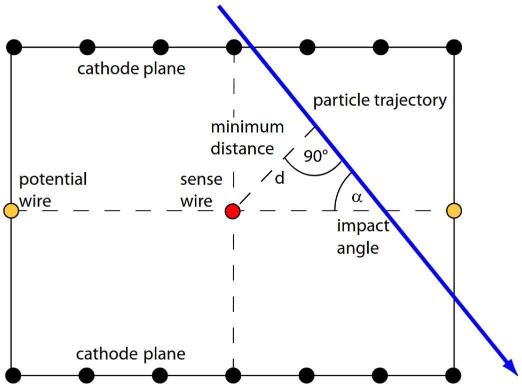

Figure 2.8: Wires disposition with an example of particle track, taken from [52]

The MDC configuration contains 24 trapezoidal gas-filled mini-drift chambers, which are filled with a mixture of argon and $CO_2 (70\% : 30\%)$. Argon serves as a counting gas, whereas carbon dioxide is a quencher, absorbing secondary particles that do not provide valuable information about the traversing particle.

Two inner MDC planes are situated in front of the magnet and two behind it. A traversing charged particle ionizes the counting gas, thus accelerating electrons toward the wires and creating an avalanche close to the wires as a result of a high electric field gradient.

Each MDC plane consists of six wire layers; each layer has different inclination angles, which allows for reconstructing the traversing point of a charged particle by projecting the fired wire onto a common plane. The time resolution of the MDCs is below four ns, and the spatial resolution is around 100 μm.

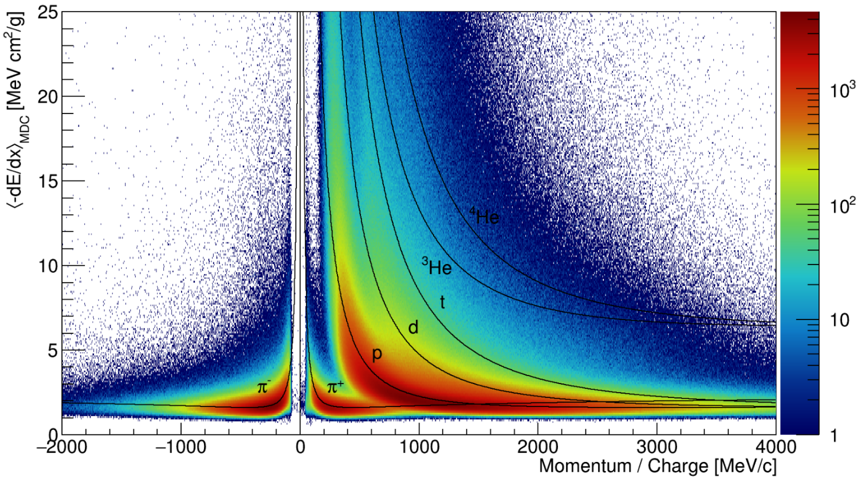

Figure 2.9: Momentum over charge versus specific energy loss measured by the MDCs distribution of reconstructed charged particles. The solid lines correspond to the theoretical energy losses of various particle species.

Furthermore, it is possible to identify the energy loss per unit path length dE/dx of the traversing particle, increasing the reconstruction efficiency. The chambers operate at very high voltages in a proportional mode; the deposited energy of the particle can be deduced from the integrated signal.

A charged particle traversing through matter may interact with atom electrons and deposit some energy. Energy losses can be described using the Bethe-Bloch formula 2.1 [55].

$$-\frac{dE}{dx} = Kz^2 \frac{Z}{A} \frac{1}{\beta^2} \left[\frac{1}{2} \ln \left(\frac{2m_e c^2 \beta^2 \gamma^2 W_{max}}{I^2} \right) - \beta^2 - \frac{\delta}{2} \right], \tag{2.1}$$

$$W_{max} = \frac{2m_e c^2 \beta^2 \gamma^2}{1 + 2\gamma m_e/M + (m_e/M^2)}, \tag{2.2}$$

where K is a constant equal to 0.307075 MeV cm^2 / mol, z is the charge of the particle that traverses it, β is its velocity, $\gamma = 1/\sqrt{1-\beta^2}$ and M is the mass, Z is the charge of matter, A is its mass number, and I is the excitation energy. δ is a function accounting for density effects for relativistic particles. W_{max} is the maximum energy that can be transferred to the electron in a collision.

2.5 META detectors

Detectors for triggering and time-of-flight information create a Multiplicity Electron Trigger Array (META). It consists of Resistive Plate Chambers (RPCs) and Time-of-Flight (TOF) detectors. TOF detector covers the range of polar angles above $\theta > 44°$ up to 88° while the RPC covers the range below $\theta < 45°$ and down to 18°.

2.5.1 Time Of Flight detector

The TOF detector consists of 48 modules arranged in 6 sectors, the same as for MDC plates. Each of these modules, in turn, consists of eight plastic scintillator rods, that is, in total, 384 rods. Both ends of the rod are connected to their photomultiplier tubes (PMT). A charged particle passing through the scintillator rod creates an excitation of atoms, which leads to photon emission, which both PMTs can further detect. The position of the incident particle can be calculated using the timing information for each of the PMT t_{PMT}

$$x = \frac{1}{2}(t_{right} - t_{left}) \cdot v_g,$$

where v_g is the group velocity of light in the scintillator. The time and space coordinates are available with a resolution of 150 ps and 2.5 cm, respectively.

Furthermore, it is possible to determine the energy loss dE/dx of a charged particle based on the signal amplitude of both PMTs:

$$\Delta E = k\sqrt{a_{right} \cdot a_{left} \cdot e^{-\frac{L}{\lambda_{att}}}},$$

where $a_{left/right}$ are the amplitudes of the PMT signals, L is the length of the rod, λ_{att} is the length of attenuation of light and k is the calibration constant.

Moreover, the density of the scintillation plastic is higher than that of the gas in the MDCs, and the particles deposit a more significant part of their energy, consequently improving the energy loss measurement of the TOF detector compared with that of the MDC system.

2.5.2 Resistive plate chambers detector

The RPC is the second detector for time determination, which covers an area of 8 m^2 for polar angles $12° < \theta < 45°$ and an almost complete azimuth angle. The detector is divided into 1116 cells for high multiplicities and interaction rates. One sector consists of 187 channels; each of them, in turn, consists of three stacked aluminum electrodes with two glass plates in between. The typical gas mixture is 85 % of $C_2H_2F_4$, 10% of SF_6, and 5 % of iso C_4H_{10}. Each gas has some purpose: in $C_2H_2F_4$ the electron avalanche is well propagated, SF_6 extends the so-called streamer-free zone, and iso C_4H_{10} is UV quencher. A multi-gap method is applied to increase the time resolution σ_N and the detection efficiency, as the number of gaps N improves the total efficiency ϵ_N.

$$\epsilon_N = 1 - (1 - \epsilon_1)^N,$$
$$\sigma_N = \frac{\sigma_1}{\sqrt{N}},$$

where ϵ_1 and σ_1 are the single layer efficiency and resolution, respectively.

The schematic layout and cell distribution are shown in Fig.2.10. A traversing charged particle ionizes the gas between the gaps of the plates, producing an electron avalanche that leads to a discharge. The time precision is below 73 ps.

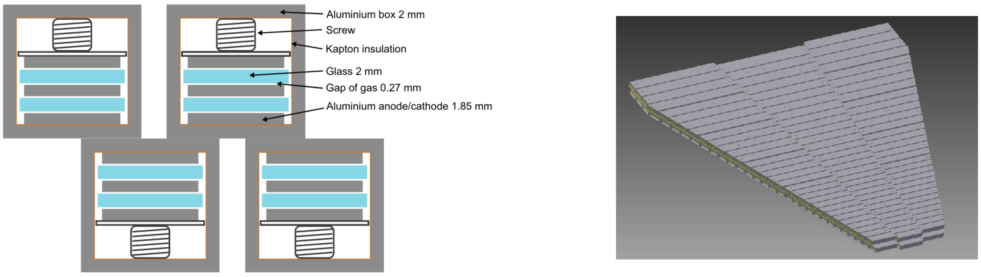

Figure 2.10: **Left**: Schematic layout of the RPC cell **Right**: Cell distribution of an RPC sector [56]

2.6 RICH detector

The Ring Imaging Cherenkov (RICH) detector aims to identify and separate relativistic electrons and positrons from light hadrons[57]. It is filled by the radiator gas C_4F_{10} in which high-velocity particles produce Cherenkov radiation as a conical wavefront. A charged particle that passes through a dielectric medium at speed greater than the phase velocity (the speed of propagation of a wave in a medium) of light emits Cherenkov radiation along its trajectory. In the RICH system, it is further reflected by the spherical ultraviolet mirror and projected as a ring onto the photon detection plane. Recently, it was upgraded with new H12700 multianode photomultiplier tubes, as well as new front-end electronics[58]. Fig. 2.11 shows the principal components of the RICH detector.

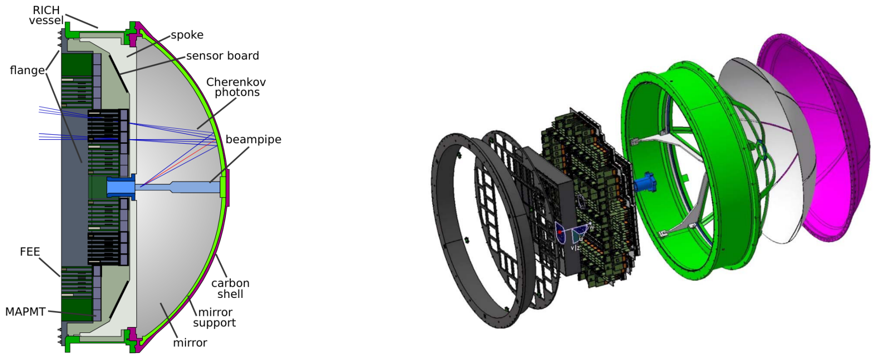

Figure 2.11: **Left**:Cross section of the HADES RICH detector. **Right**:Sketch of the upgraded HADES RICH detector, taken from [58]

2.7 ECAL detector

The Electromagnetic CALorimeter (ECAL) replaced the previously used Pre-Shower detector. It is used to identify photons and provide a separation between relativistic pions and leptons. A detailed description of the HADES ECAL detector is given in the next chapter.

2.8 Forward Wall detector

The Forward Wall measures the reaction plane by registering the reaction spectators and fragments. It is located 7 m from the target and has a polar angle coverage of $\theta = 0.33°$ to $7.17°$, which is not covered by any other detector component. It consists of 288 scintillator blocks varying in 3 sizes to achieve a sufficient spatial resolution to deal with different track densities. Each of the cells is read out by PMT. The cell dimensions range from 4 x 4 cm^2 for the innermost cells to 16 x 16 cm^2 for the outermost cells, and the sizes were chosen to achieve better detector granularity. HADES is a fixed target experiment. Therefore, because of the forward boost, the particle density decreases with increasing polar angle; in other words, the module size decreases at lower polar angles. The experimental time resolution $\sigma_t \approx 500$ ps, and the angular resolution of the deduced reaction plane is $\sigma_\phi \approx 50°$and depends strongly on the centrality. The Forward wall detector scheme is shown in Fig.2.12.

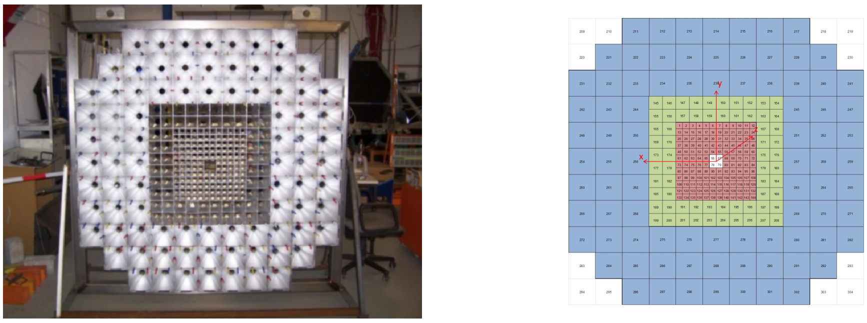

Figure 2.12: Front layout of forward hodoscope indicating the scintillator blocks [59]

2.9 Data acquisition

HADES Data Acquisition (DAQ) reads and writes information in real-time from all detector subsystems. The DAQ system consists of two main components: the custom field-programmable gate array (FPGA) network and the TrbNet network. The FPGA network employs optical connections and is responsible for triggering, data collection, and slow control. The second part of the DAQ is used for data transport from storage to the server farm and is based on a gigabit Ethernet structure. The DAQ system can have an event rate of up to 50 kHz; for more details, see [60].

In the March 2019 experiment, 360 TB of data were written to the server, the average event rate was 10 kHz, and the data rate was 150 MB/s.

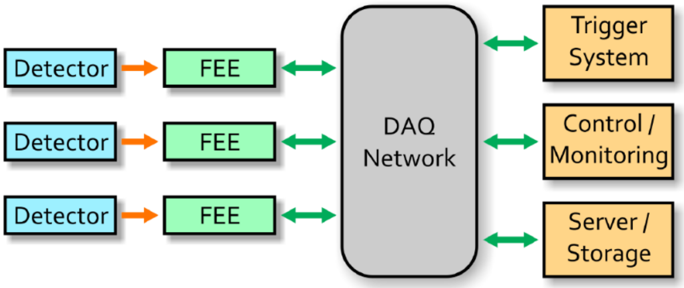

Figure 2.13: Simplified DAQ system. Taken from [60]

3. Electromagnetic Calorimeter

3.1 Motivation for the calorimeter

The newly installed Electromagnetic Calorimeter offers a unique possibility for the HADES spectrometer to measure neutral particles through their direct two-photon decays [61]. As Dalitz decay of $\pi^0 \rightarrow \gamma e^+ e^-$ contribute significantly to the low invariant mass of dilepton yields, channels such as $\pi^0 \rightarrow \gamma\gamma$ and $\eta \rightarrow \gamma\gamma$ are essential for experimental determination of this contributions. There is also a method for reconstruction of π^0 based on photon conversion; see [62]. However, because of the small probability of photon conversion and lower branching ratio for Dalitz decays, ECAL allows us to increase the precision of the measurements and provide information in more differential analysis.

Moreover, with the help of ECAL, the hyperon structure can be studied; there is a particular interest in the Σ baryon decays through the radiative decay $\Sigma^0 \rightarrow \Lambda^0\gamma$ and Dalitz decay $\Sigma^0 \rightarrow \Lambda^0\gamma* \rightarrow \Lambda^0 e^+ e^-$ channels. The hyperon structure can be probed via measurement of the electromagnetic transition form factors. Its evolution from a space-like to a time-like region can be studied via Dalitz decays for the mass region $-4M^2 \leq -Q^2 \leq 0$.

Finally, ECAL provides an essential separation between electrons and pion at high momenta $p > 400$ MeV/c. Pions deposit a constant energy independent of their momentum, whereas electrons produce a linear energy response.

3.2 Working principle of a calorimeter

A photon passing through the lead glass block with an energy greater than 1 MeV has a high probability of interacting with the material via pair production in the presence of an atomic nucleus. The produced particles will interact further via the Bremsstrahlung process, creating high-energy photons. Radiation length X_0 is a mean distance for traversing electrons where it loses all but $1/e$ of its energy by Bremsstrahlung, and it is equal to 7/9 of the mean free path of a photon for pair production.

For measuring shower development, it is useful to describe the distance in units normalized by the radiation length, $t = x/X_0$. Let E_0 be the energy of an incident photon. At one radiation length, the photon produces one electron-positron pair; they, in turn, emit after another radiation length one Bremsstrahlung photon each, which are transformed into e^+e^- pairs. Under the assumption of symmetrically equal energy after each step of multiplication, the number of particles at depth t is

$$N(t) = 2^t \tag{3.1}$$

Then, the energy of a particle at each step t is given by

$$E(t) = E_0 \cdot 2^{-t} \tag{3.2}$$

The process of shower development is repeated until the particles reach their critical energies $E_0/N > E_c$. When the energy of a particle is below the critical energy E_c, different processes dominate, namely the ionization of electrons and Compton and the photoelectric effect for photons.

$$E_c = E_0 \cdot 2^{-t_{max}} \tag{3.3}$$

This equation implies that

$$t_{max} = \frac{\ln(E_0/E_c)}{\ln 2} \propto \ln(E_0/E_c) \tag{3.4}$$

An example of the development of the shower in lead glass from a 1 GeV photon - using the value $E_c \approx 10$ MeV, the number of particles in the maximum shower $N_max = E_0/E_c = 100$ and the depth of the shower $\approx 6.6X_0$ could be obtained.

It is crucial to consider the length of the radiator to keep the full shower inside to measure the total energy of the electromagnetic particle. When a particle hits a radiator near the edge, the shower can extend to neighboring modules, thus forming a cluster.

The angular distribution of the particles produced by Bremsstrahlung and pair production is very narrow. The characteristic angles are of the order of $m_e c^2/E_\gamma$. Therefore, the lateral width of an electromagnetic cascade is mainly determined by multiple scattering and can be best characterized by the Molière radius.

$$R_M = \frac{21MeV}{E_c} X_0\{g/cm^2\}. \tag{3.5}$$

Figure 3.2 shows the development of the shower of a 6 GeV electron cascade in the lead calorimeter. About 95% of the shower energy is contained in a cylinder around the shower axis whose radius is $R = 2R_M$ almost independently of the particle energy.

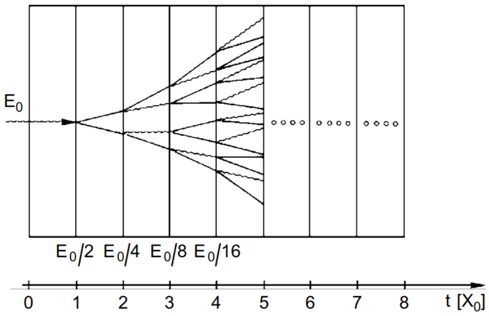

Figure 3.1: Sketch of a simple model for shower parametrization

This straightforward model already correctly describes the most important qualitative characteristics of electromagnetic cascades [55] .

- To absorb most of the incident photon's energy, the total calorimeter thickness should be greater than 10-15 X_0.
- The position of the shower maximum increases slowly with energy. Therefore, the calorimeter thickness should increase as the logarithm of energy.

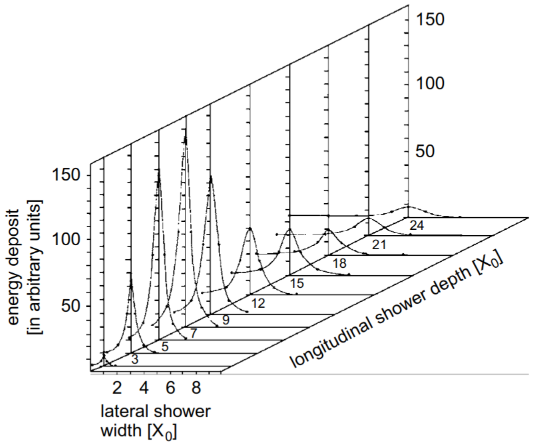

Figure 3.2: Longitudinal and lateral development of an electron shower in the lead.

- Energy leakage is caused mainly by soft photons that escape the calorimeter at the sides (lateral leakage) or the back (rear leakage).

For shower detection, one can use the Cherenkov effect: When charged particles created in a shower process travel at a faster speed than the phase velocity of light in the matter, they will emit the so-called Cherenkov photons. The frequency of Cherenkov photons in lead glass has its maximum near-ultraviolet and visible blue light. The threshold energy for Cherenkov photons in lead glass is $T_c \approx 120$ keV, indicating that the total number of Cherenkov photons is proportional to the total track length of all charged particles in the shower process, which in turn is proportional to the energy of the incident particle.

Photomultipliers (PMTs) are also used to detect these Cherenkov photons. They provide a large sensing area, a fast response, and good resolution in exchange for a high price. The PMT detects visible and ultraviolet light and converts it into an electrical signal. The basic principle is depicted in Fig. 3.3.[63].

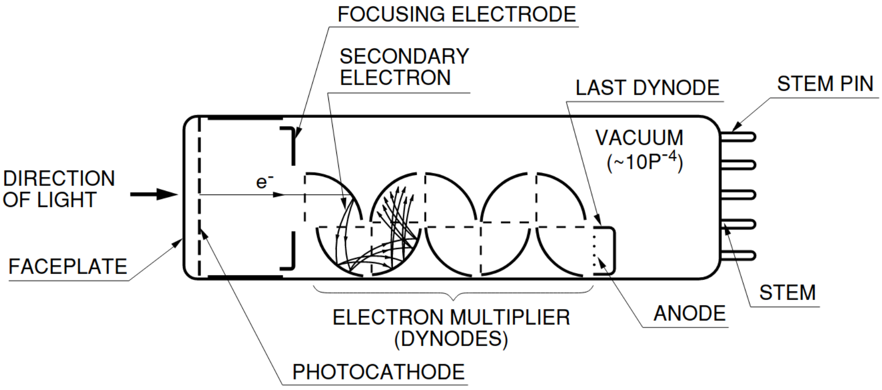

Figure 3.3: Construction of a photomultiplier tube

The main parameters of an electromagnetic calorimeter are its energy and position resolution for photons and electrons. The energy resolution can be derived from the response of a module irradiated by gamma photons with known energy. The width of the distribution gives the energy resolution. The energy resolution is given by the following:

$$\frac{\sigma_E}{E} = \frac{a}{\sqrt{E}} \oplus \frac{b}{E} \oplus c, \tag{3.6}$$

where a stands for photoelectron statistics (sometimes called a stochastic term), b for electronics noise, and c appears due to the calibration uncertainty and crystal non-uniformity (the symbol $\oplus$ means summation in quadrature). The HADES calorimeter uses lead glass, which the OPAL end-cap calorimeter has granted at Large Electron-Positron collider (LEP) CERN. The OPAL collaboration reported an energy resolution of:

$$\frac{\sigma_E}{E} = \frac{6\%}{\sqrt{E}}, \tag{3.7}$$

dominated by the stochastic term. The ECAL uses only the brass cover and lead glass, which was taken out of the old modules, polished and assembled with new PMTs. To determine that resolution, we have tested ECAL modules with different photon beams. The measurement [64] was carried out at the Mainzer Mikrotron (MAMI) facility in Mainz. In Fig.3.4 the energy resolution of a HADES ECAL module is shown for different photon energies. Among others, the PaDiWa ECAL read-out electronics have been compared with a CAEN flash ADC reference measurement (GSI MA8000 shaper and CAEN ADC) for an ECAL module containing a 3-inch PMT.

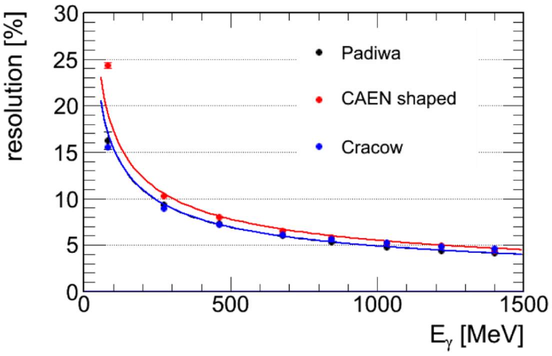

Figure 3.4: Energy resolution of a HADES ECAL module with a 3-inch PMT irradiated with different photon energies. Among others, PaDiWa ECAL read-out electronics were compared with CAEN flash ADC reference measurements (GSI MA8000 shaper and CAEN ADC)[64].

3.3 The electromagnetic calorimeter

The detector is made up of 978 modules arranged in 6 sectors. Each sector includes 15 rows of modules. The dimensions of ECAL are approximately 4.7 m in height and width, as shown in Fig. 3.5. The total area of the calorimeter is approximately 8, m^2 and covers the polar angles between 12° and 45° with almost complete azimuthal coverage. The photon and electron energy resolution

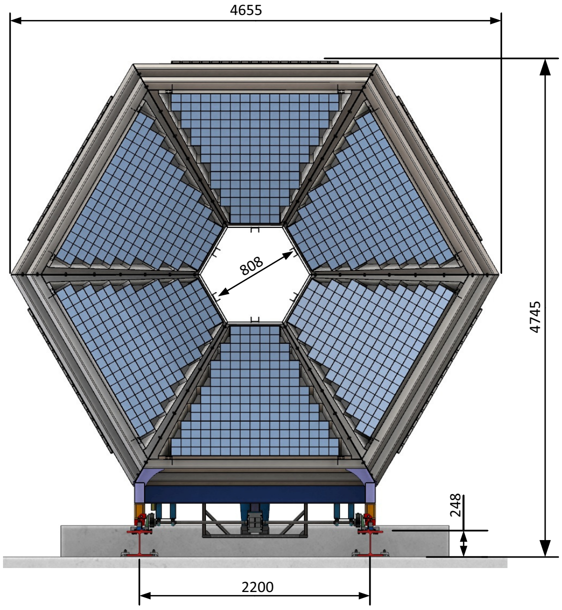

Figure 3.5: Electromagnetic calorimeter, front view.

achieved in the test experiments amounts to $\approx 6\%/\sqrt{E}$ which is sufficient for the reconstruction of η mesons.

The main element of the HADES ECAL is the modified module of the OPAL end-cap electromagnetic calorimeter with CEREN 25 lead glass inside that is used as a Cherenkov radiator [65]. The 420mm long (16.7 radiation lengths) glass is contained within a 0.45mm thick brass case. Each lead glass block has transverse dimensions of $92x92$, mm^2 that are comparable to the transverse size of electromagnetic showers. The glass blocks are mirror polished and wrapped in white paper (TYVEK 1060B) to reduce the lateral escape of photons. Special housing is used for each PMT, including a plastic quadratic spacer and an optical fiber with a standard Lampert Connector (LC) on one side, which allows external light from a LED or LASER system to be sent into the module. The laser system can be used for precalibration, an initial set of high-voltage values, and monitoring purposes.

Furthermore, optical grease (Rhodorsil Paste No. 7) with a refraction index of $n = 1.5$ is used to connect the optical fiber of the lead glass radiator to the PMT.

Two similar types of PMT are used in the 1.5-inch EMI 9903KB from the WA80 experiment at CERN [66] and the new 3-inch Hamamatsu R6091[63]. An example of the PMT response signal is given in Fig.3.7.

The CAEN SY1527LC HV system is used as the HV power supply. It is based on the 24-channel A1535 modules that provide a voltage up to 3.5 kV and a current up to 3 mA.

The properties of lead glass are summarized in Table 3.1, and a schematic view of the module is shown in Fig.3.6.

Density	4.06 g/cm^3
Refractive index	1.708 (at 410 nm)
Radiation length X_0	2.51 cm
Molière radius	3.6 cm
Light transmission coefficient	0.96 (at 400 nm)
Length of module	420 mm (16.7 of X_0)
Transverse dimensions	92 × 92 mm^2

Table 3.1: Properties of the lead-glass CEREN 25 module.

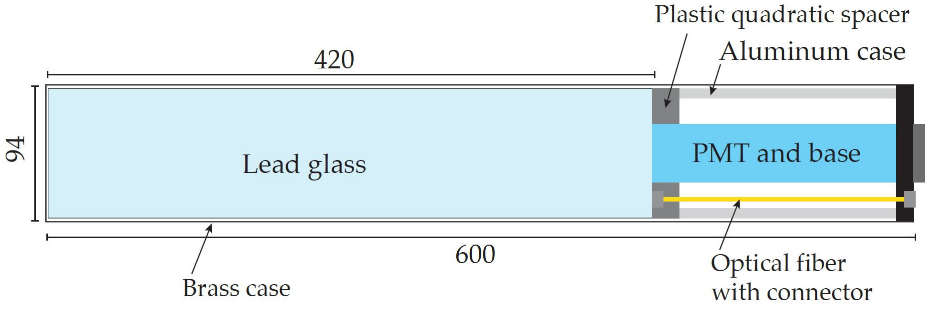

Figure 3.6: Schematic view of the calorimeter module.

3.3.1 Electronics and Read-Out

The simplified read-out scheme of the HADES ECAL detector is shown in Fig. 3.1. The signals from the photomultiplier tubes are processed on the PaDiWa-AMPS [67] front-end board for the TRB3 [68] platform. Charge and time measurements are based on commercially available data Field-Programmable Gate Arrays (FPGAs), which allows digitizing many channels using low-cost tools. On the front-end board, the arrival time and pulse charge, which are proportional to the deposited energy in the ECAL module, are measured via a modified time-over-threshold method. The TRB3 platform carries out the needed high-precision time-to-digital conversion. It concentrates the data sent to the HADES data acquisition system when a read-out is requested by the HADES physics trigger. The HADES data acquisition system is based on the TRBNet custom network structure, which contains three trigger, data, and slow control channels.

After attenuation/amplification, the input signal is split into a FAST component that contains the arrival time and a SLOW component that contains charge information. The FAST signal is discriminated with the help of an FPGA. Subsequently, a TDC implemented in a second FPGA is used to measure its leading edge, which contains arrival-time information. The SLOW signal is integrated by a capacitor and discharged by a discriminator-driven current source. The SLOW signal is also discriminated in an FPGA and measured as a time-over-threshold, representing the charge. The scheme of the process is shown in Fig.3.9.

In summary, the energy deposited inside an ECAL module is proportional to the charge measurement of a PMT pulse. The charge measurement is converted into a width measurement encoded in the SLOW signal's width. The width can be calculated from the leading edge (LE) and trailing edge (TE) measurements

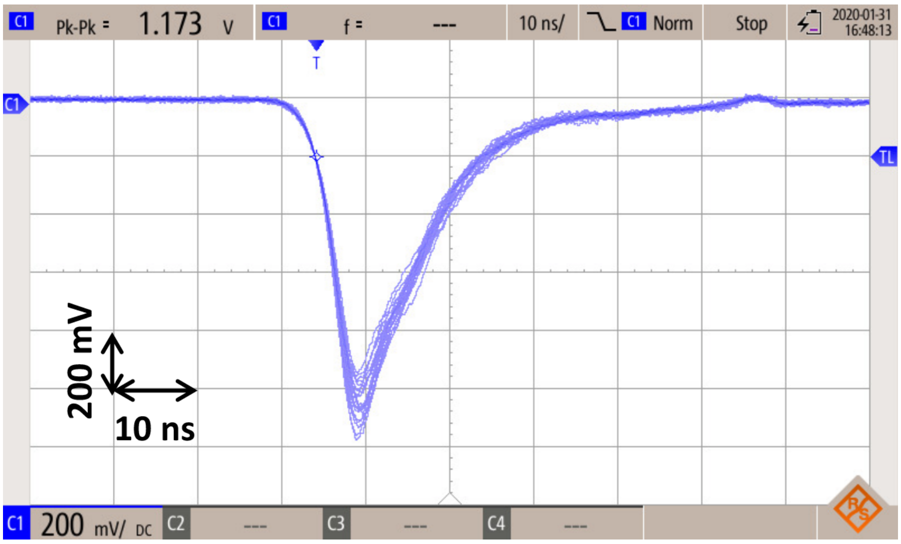

Figure 3.7: Raw signals of an ECAL module containing a 3-inch Hamamatsu R6091 PMT. The signals are generated by LASER light, which is coupled to lead glass

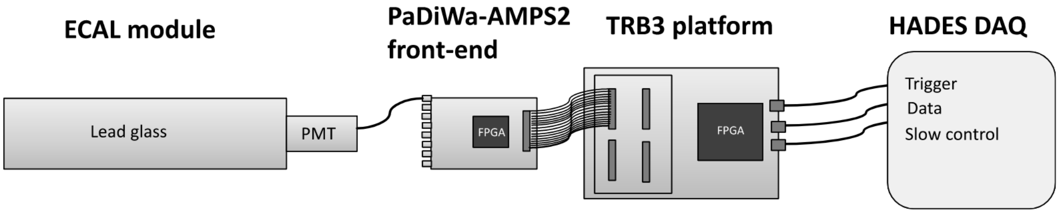

Figure 3.8: Simplified read-out scheme of the HADES ECAL detector.

of the SLOW signal. During the experiment in March 2019, it was found that the best stable response with high multiplicity events is achieved when using the difference between the trailing edge of the SLOW signal and the leading edge of the FAST signal.

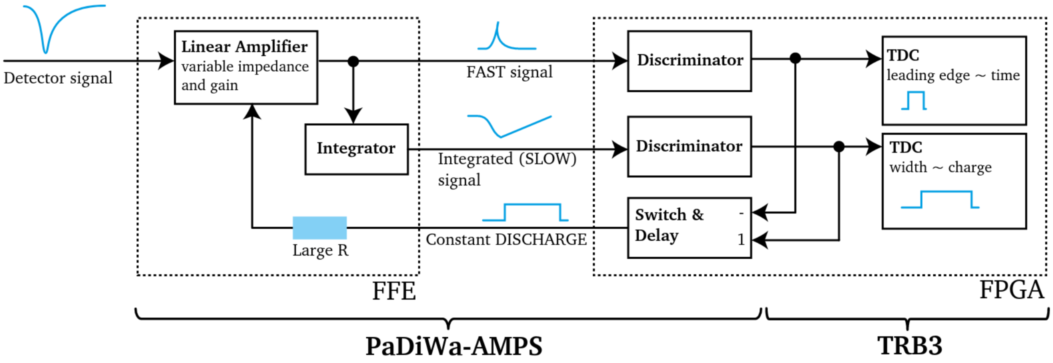

Figure 3.9: Operation of FEE, Taken from [67]

$$Energy \propto Charge = f(TE_{SLOW} - LE_{FAST}) \tag{3.8}$$

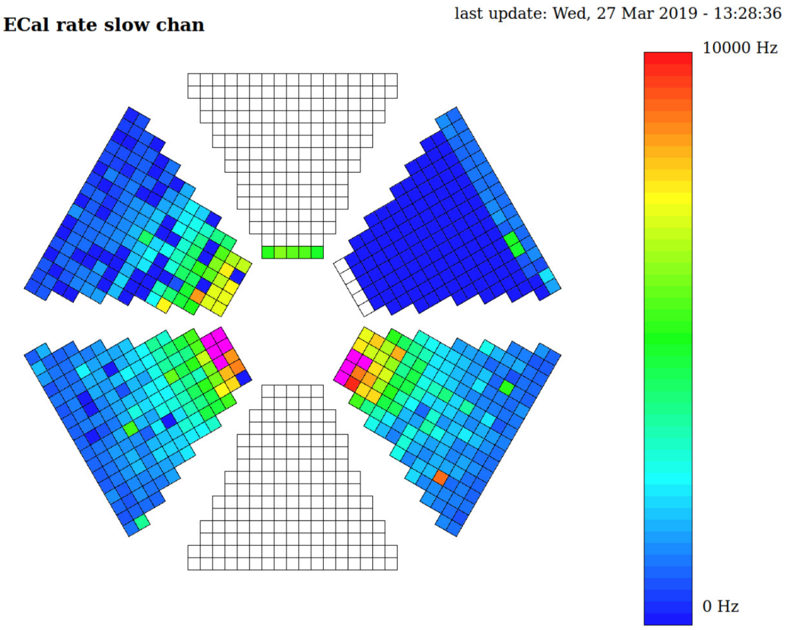

Figure 3.10: The number of hits per second in each operational ECAL module during the Ag+Ag beam time in March 2019. The white areas indicate where the modules were not installed, and the dark blue modules were switched off. Plot was taken during onlinde operation. Sector numbering is done clock-wise starting from upper sector Nr.0.

During the beam time of the March 2019 experiment, only some of the ECAL modules were in operation, as shown in Fig. 3.10. The white area indicates modules that were not installed. By now, all sectors are completed.

3.4 ECAL calibration

Calorimeters measure the energy, which a particle deposits as it passes through the detector. It is usually designed to stop entire particles or 'absorb' most of them coming from a collision, forcing them to deposit all their energy within the detector. Electrons and positrons, as well as photons, create an electromagnetic shower of the same origin; therefore, leptons can be used for the precalibration of the electromagnetic calorimeter.

3.4.1 Lepton selection

Since leptons are highly relativistic at small energies starting from 10 MeV, their momentum approximately equals energy. ECAL calibration can be performed using leptons that have been identified in HADES. They are reconstructed using tracking, time-of-flight systems, and a RICH detector. The identification of leptons is made by demanding rather loose conditions on particle candidates:

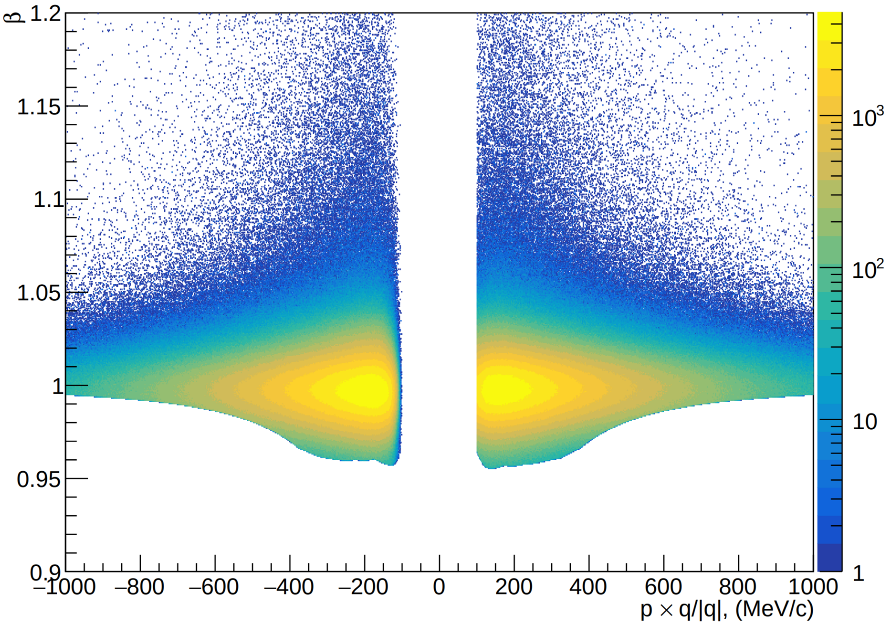

Figure 3.11: Population of identified leptons in the velocity (β) vs. laboratory momentum over charge (p/q) plane for leptons seen in the RPC detector.

- hits in inner and outer MDCs, RICH, and RPC detectors.
- tracks reconstructed by Runge-Kutta fit with $\chi^2_{RK} < 500$
- RICH ring radius bigger than 17 mm
- RICH matching quality with a fitted track below 1.5 sigma
- $\beta > 0.9$
- momentum dependent cut on effective mass $m^2_{eff} = p^2(1-\beta^2)/\beta^2$

The distribution in the velocity-momentum space for leptons selected under the above conditions is shown in Fig. 3.11.

A lepton interacting with lead glass produces an electromagnetic shower, determined by the Moliere radius, larger than a module's size. The best energy response can be achieved by summing the information from several adjacent modules grouped in the so-called *clusters*. For calibration purposes, only cluster size one leptons (all energy deposited in only one module) have been used for calibration. Track matching to the center of the ECAL module within approximately 1.5° has been used.

3.4.2 Energy calibration

The energy of the incident particle deposited in the lead glass is proportional to the amplitude and charge of the PMT signal. Here, the method of *charge-to-time-over-threshold* is used for better signal discrimination. The calibration curve that links the measured Time over Threshold (TOT) with a signal amplitude is shown in Fig.3.12. This curve was generated using LASER signals, varying their amplitude, and measuring the TOT. As expected, the dependence of TOT on the amplitude is non-linear. For further details, see [69].

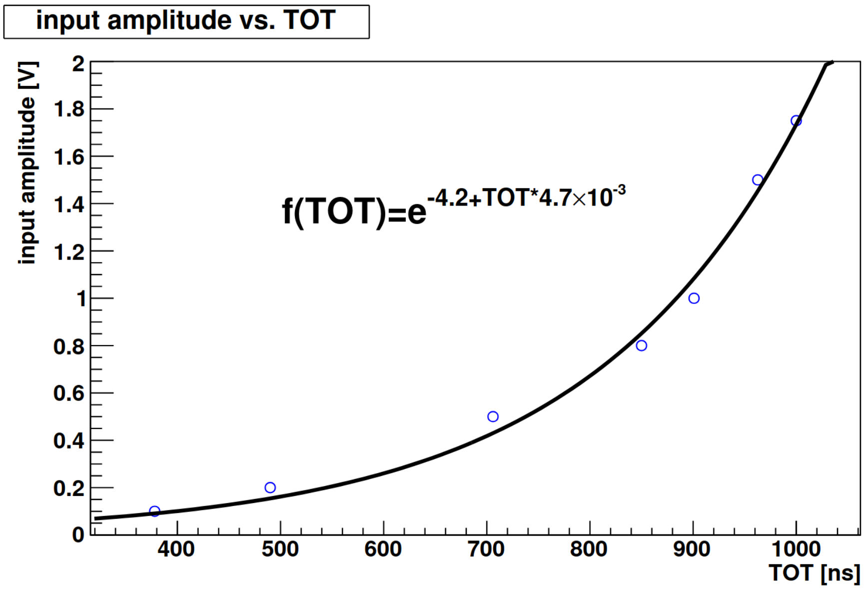

Figure 3.12: Connection of measured TOT and signal amplitude, where the LASER system generated the signals.

The response of the signal with the TOT method has an exponential shape.

$$E = a_0 + \exp\left(a_1 + a_2 TOT\right), \tag{3.9}$$

where a_0, a_1 and a_2 are fit parameters. An example of a fitting procedure for a single selected ECAL module is shown in Fig. 3.13 (left) with the resulting fit parameters: $a_0 = -281.2 \pm 2.5$, $a_1 = 5.27 \pm 0.09$, and $a_2 = (1.63 \pm 0.07) \cdot 10^{-3}$.

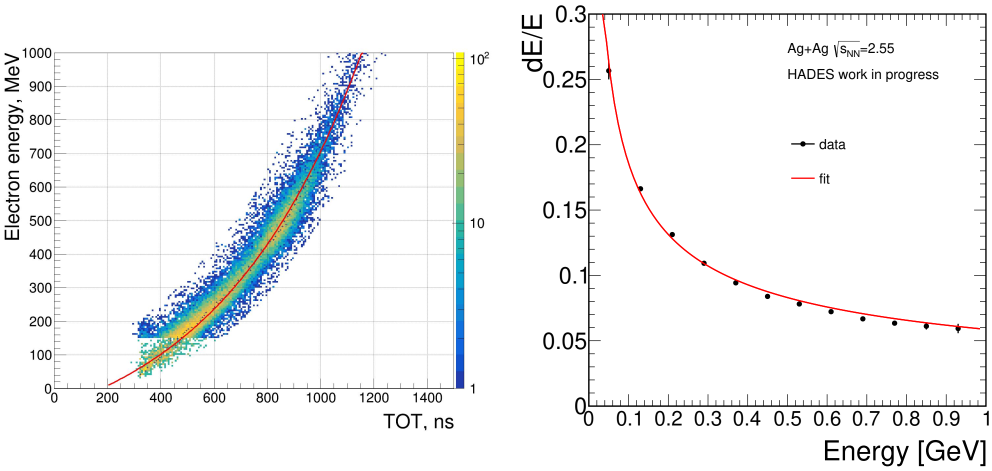

Figure 3.13: **Left**: Calibration of the energy using the measured TOT of leptons for a single module. **Right**: An energy resolution for the sum of all modules.

In contrast to magnetic spectrometers, where the momentum resolution deteriorates linearly with the momentum of the particles, the relative energy resolution of the calorimeter improves with energy as $\sim 1/\sqrt{E}$(see [70]). The resulting sum of all ECAL modules is shown in Fig. 3.13 (right), and the fit value corresponds to the relative resolution at 1 GeV of 5.9% on the leptons:

$$\frac{dE}{E} = \frac{5.9\%}{\sqrt{E}}$$

The lepton energy in ECAL is however lower than energy deduced from reconstructed momentum as leptons have to pass RPC detector before entering ECAL, therefore losing some part of energy.

3.4.3 Energy loss in RPC

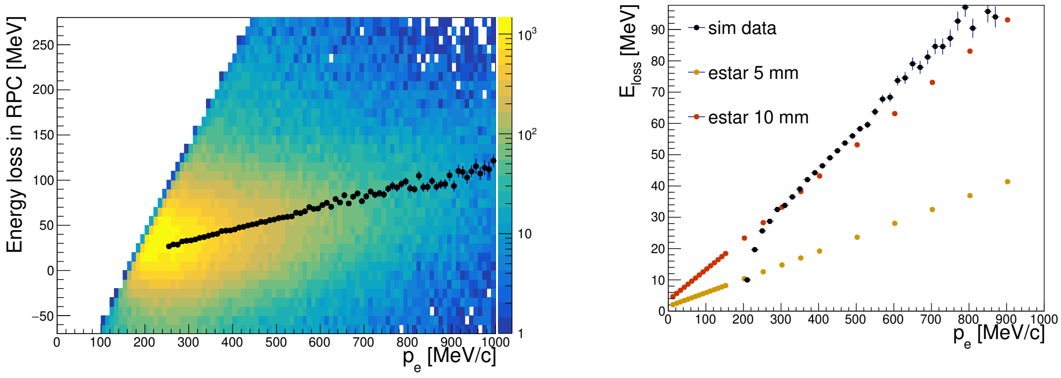

Figure 3.14: **Left**: Energy loss in RPC vs lepton momentum 2D histogram **Right**: Comparison of mean energy loss with ESTAR data[71].

RPC is estimated to contain approximately 1 cm of aluminum in width; therefore, leptons lose part of their energy before reaching ECAL. Geant simulations allow one to calculate the difference between the actual energy of the particle and the registered energy in ECAL. The energy loss, or, moreover, $E_{GEANT} - E_{ECAL}$ versus lepton momentum p_e, is plotted in Fig. 3.14, as well as a comparison with the ESTAR data[71], for the aluminum layer with various thicknesses, showing approximately 1 cm of aluminum.

However, after energy loss corrections the π^0 peak mean value was still not at the correct position due to the fact that GEANT does not store all secondary particles, which may fly to the calorimeter after lepton scattering in the RPC and add the energy to the calorimeter. Therefore, a more precise method, dependent on the known mass of π^0 is used further; the procedure is described in the next section.

3.4.4 The π^0 peak calibration

It can be easily proven that due to energy-momentum conservation, the invariant mass of two photons obeys the following relation:

$$m_{\pi^0} = \sqrt{2E_{\gamma_1}E_{\gamma_2}(1 - \cos\Theta_{12})}, \tag{3.10}$$

where E_{γ_i} is the energy of a reconstructed photon i and Θ_{12} is the opening angle between two photons.

The final calibration of the ECAL involves an iterative process on all modules. An invariant mass distribution is reconstructed for a specific module and for a very clean photon sample within one sigma of beta distribution and centrality 20-30 % where the combinatorial background is lower. One of two photons is reconstructed in the particular module, whereas the second can be anywhere in ECAL. The analysis uses the event-mixing method for the background estimation due to the low Signal-to-Background S/B ratio. In the same way, a mixed event combinatorial background is used for each cell to have a good extraction of the π^0 peak. More information is given in the next section 4.7. The corrected energy E_{corr} is equal to $E_{corr} = c_i \cdot E_{prev}$, where c_i is the calibration coefficient for each ECAL module i. The first approximation for each module $c_i^0 = 1$. At each iteration step k, c_i is adjusted.

$$c_i^k = c_i^{k-1} \cdot \left(\frac{m_{\pi^0}}{m_i} \right)^n , \tag{3.11}$$

where m_{π^0} is the true mass of π^0, equal to ≈ 134.977 MeV [72], m_i is the value of the π^0 mean for a given module i and $n > 0$ is the convergence parameter that can be optimized. The iterative procedure is repeated until the absolute difference between the reconstructed mass and the PDG π^0 mass is less than some value chosen for each cell i and a given energy range.

One could assume that n should be equal to $n = 2$ from the relation 3.10 since the reconstructed mass and the actual π^0 mass are related.

$$\frac{m_{\pi^0 PDG}}{m_i} = \frac{\sqrt{2E_{corr,i,\gamma_1} E_{corr,\gamma_2}(1 - \cos\Theta_{12})}}{\sqrt{2E_{i,\gamma_1} E_{\gamma_2}(1 - \cos\Theta_{12})}} = \sqrt{\frac{E_{corr,i,\gamma_1} E_{corr,\gamma_2}}{E_{i,\gamma_1} E_{\gamma_2}}} , \tag{3.12}$$

$$c_i = \frac{E_{corr,i}}{E_i} = \left(\frac{m_{\pi^0 PDG}}{m_i} \right)^2 . \tag{3.13}$$

However, this assumption must be corrected because the calibration of other modules changes simultaneously; thus, at each iteration step, all other calibration coefficients affect the final reconstructed π^0 mass for a given cell. For the convergence of parameters n, the values of parameters 0.8 to 2.0 were studied with 14 iterations. The calibration of each module is very processor time-consuming; hence, the value of $n = 1.0$ was chosen for the best convergence. The results of the difference between the mean value and PDG value π^0 mass versus iterations are presented in Fig. 3.15, see also [73].

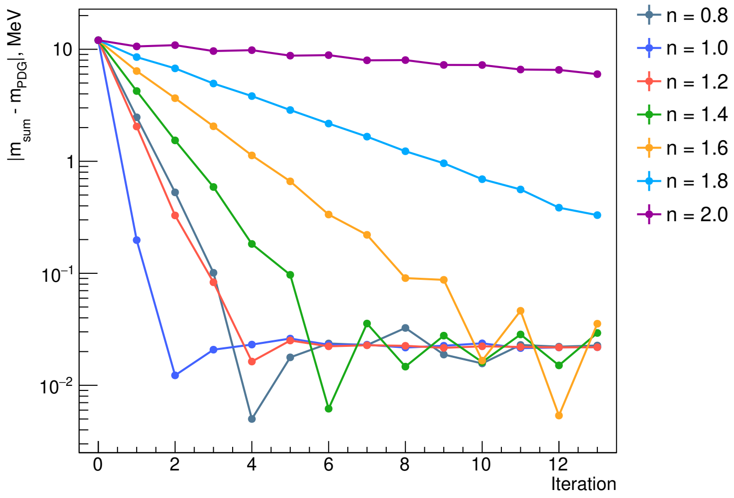

Figure 3.15: Residual de-calibration versus iteration number for several values of power n.

Calibration was performed using approximately $4 \cdot 10^9$ events for each of the 478 operating modules. The mixed-event combinatorial background had event selection criteria in which only photons with the same topology were combined into pairs. An example of such calibration is presented in Fig.3.16 and Fig.3.17.

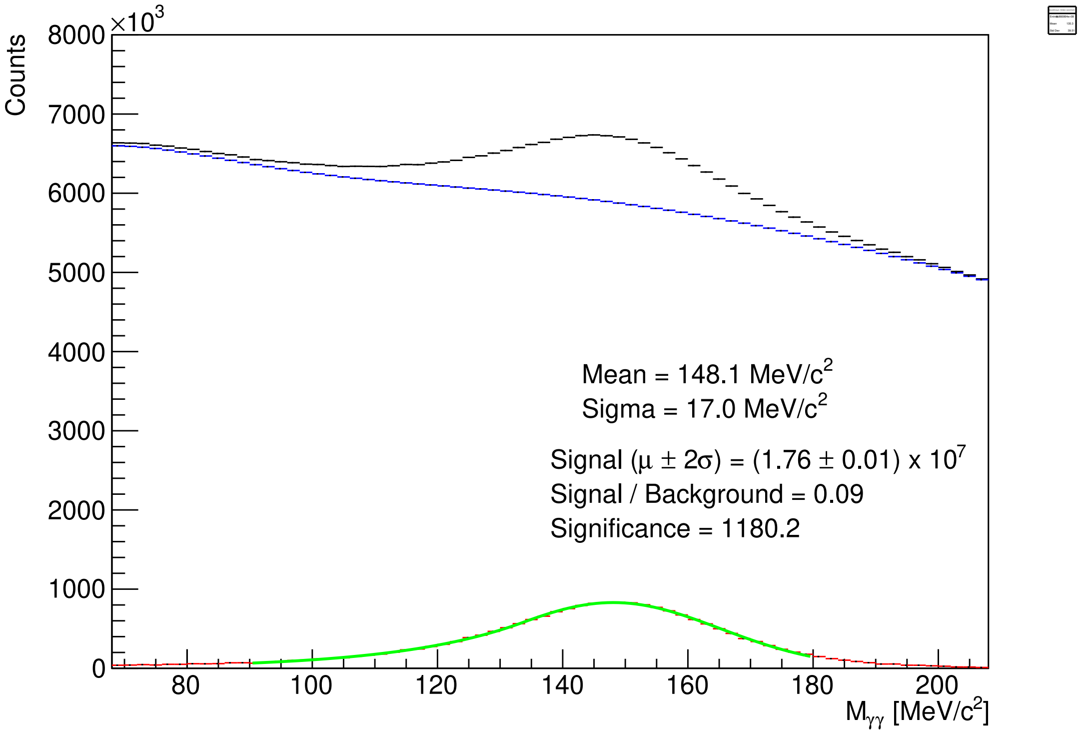

Figure 3.16: A very clean photon sample before calibration

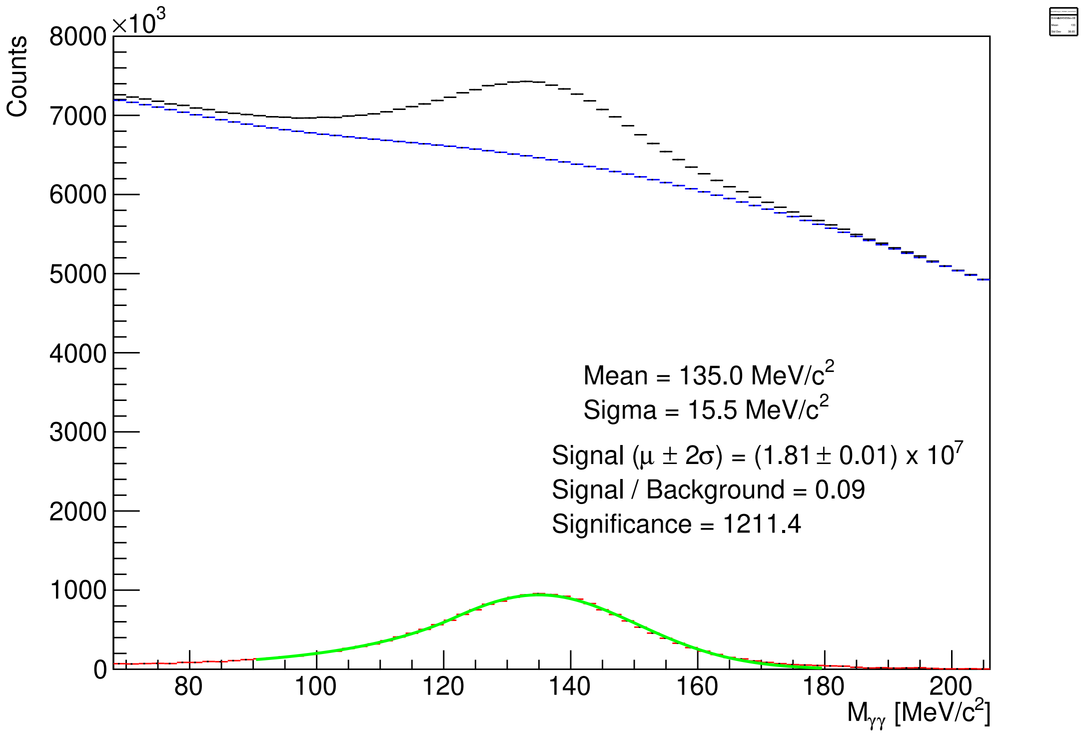

Figure 3.17: A very clean photon sample after calibration

Several factors can affect the linearity of energy measurements. For lower energies, threshold settings, as well as digitization, affect the response of the detector. In contrast, for high-energy photons, shower leakage takes place. Therefore, a calibration based on single-photon energy was needed to improve the resolution.

The nonlinearity is corrected by recalculating the cluster energy E using the following parameterization:

$$E_{corr} = aE + b\sqrt{E} + c + d/\sqrt{E} + e/E. \tag{3.14}$$

Figure 3.18 shows the PDG π^0 mass ratio to the measured π^0 peak position as a function of the mean photon energy E_γ. Data were restricted to symmetric π^0 decays with $|E_{\gamma,1} - E_{\gamma,2}| < 0.05(E_{\gamma,1} + E_{\gamma,2})$. The fit with the function $E_{corr}(E)/E$ (Eq. 3.14) is shown by the red curve.

Finally, the calibration dependence on the time of the data taking was estimated for the sum of all modules. Unfortunately, due to the small *Signal-to-Background* ratio, it was impossible to calibrate the modules for separate time slices; therefore, the stability of calibration during the experiment was checked by comparing charged pions response, as they produce a rather constant energy response in the lead glass. It was found that 1.5” PMTs (sector Nr. 2 and 4) were not as stable during the experiment as 3” PMTs (sector Nr. 5). As can be seen in Fig.3.19, the average charged pion response in ECAL in sector Nr. 2 and sector Nr.4 tends to decrease from the straight line. The total instability is within few percents and does not influence the final result for the signal extraction of neutral pions.

After all these corrections were taken into account, a peak can be extracted, as seen in Fig.3.20 with a mean value comparable to the PDG value.

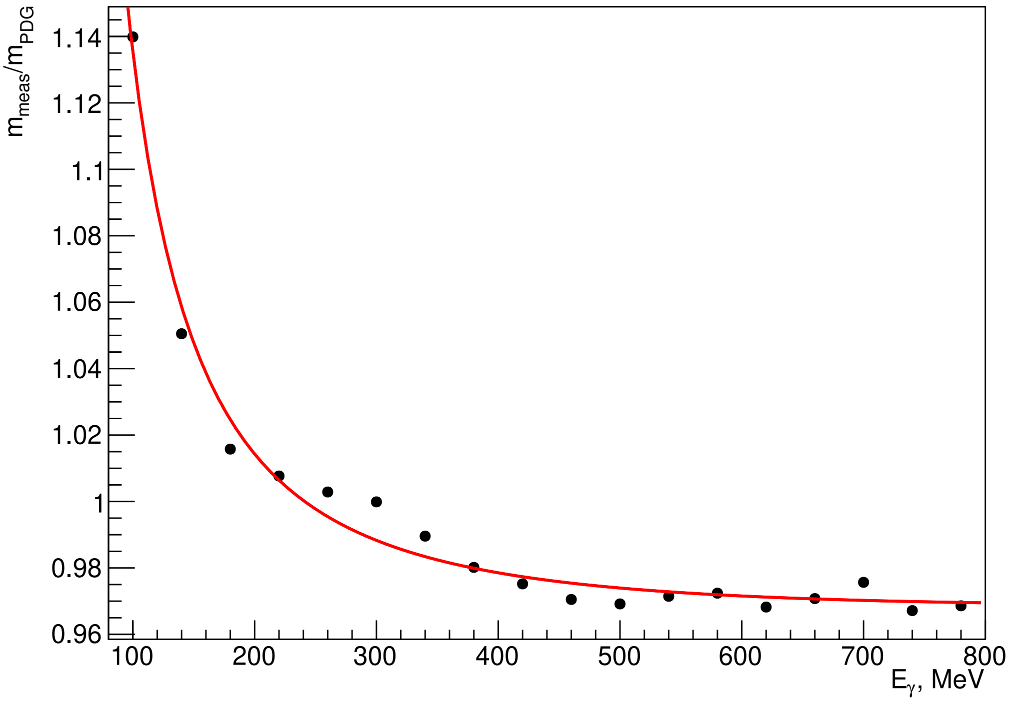

Figure 3.18: Estimation of nonlinearity using symmetric π^0 decays , with both photons having approximately the same energy, see text. Data fit with function 3.14.

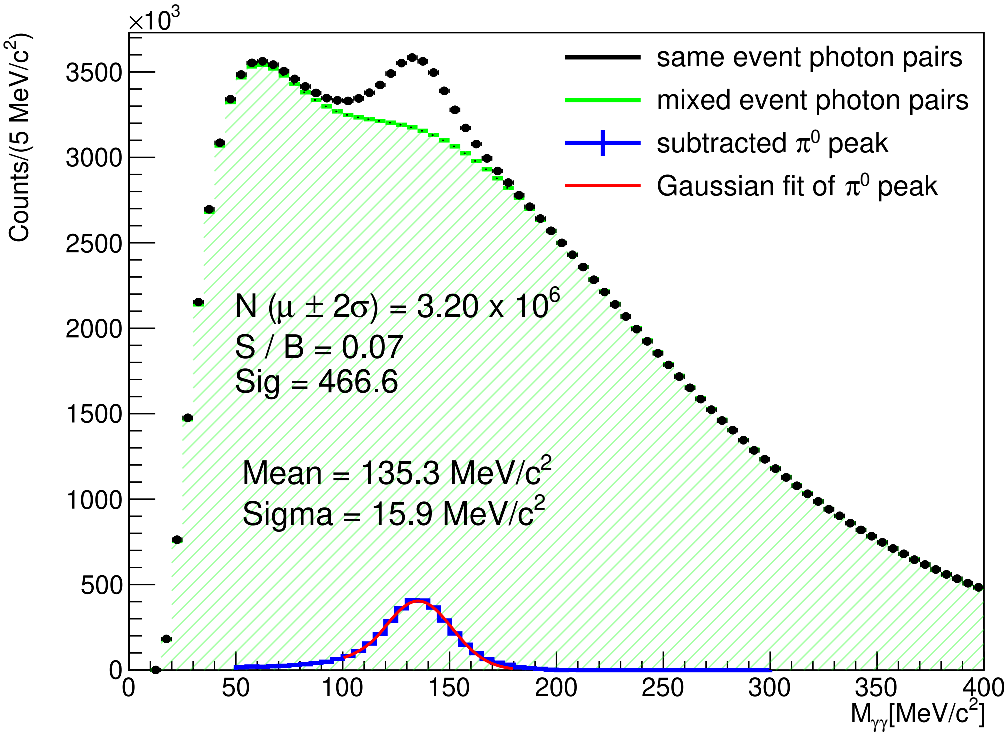

Figure 3.20: Invariant mass distribution of $\gamma\gamma-$ pairs from the 20-30 % centrality events after calibration with per-channel π^0 peak equalization.

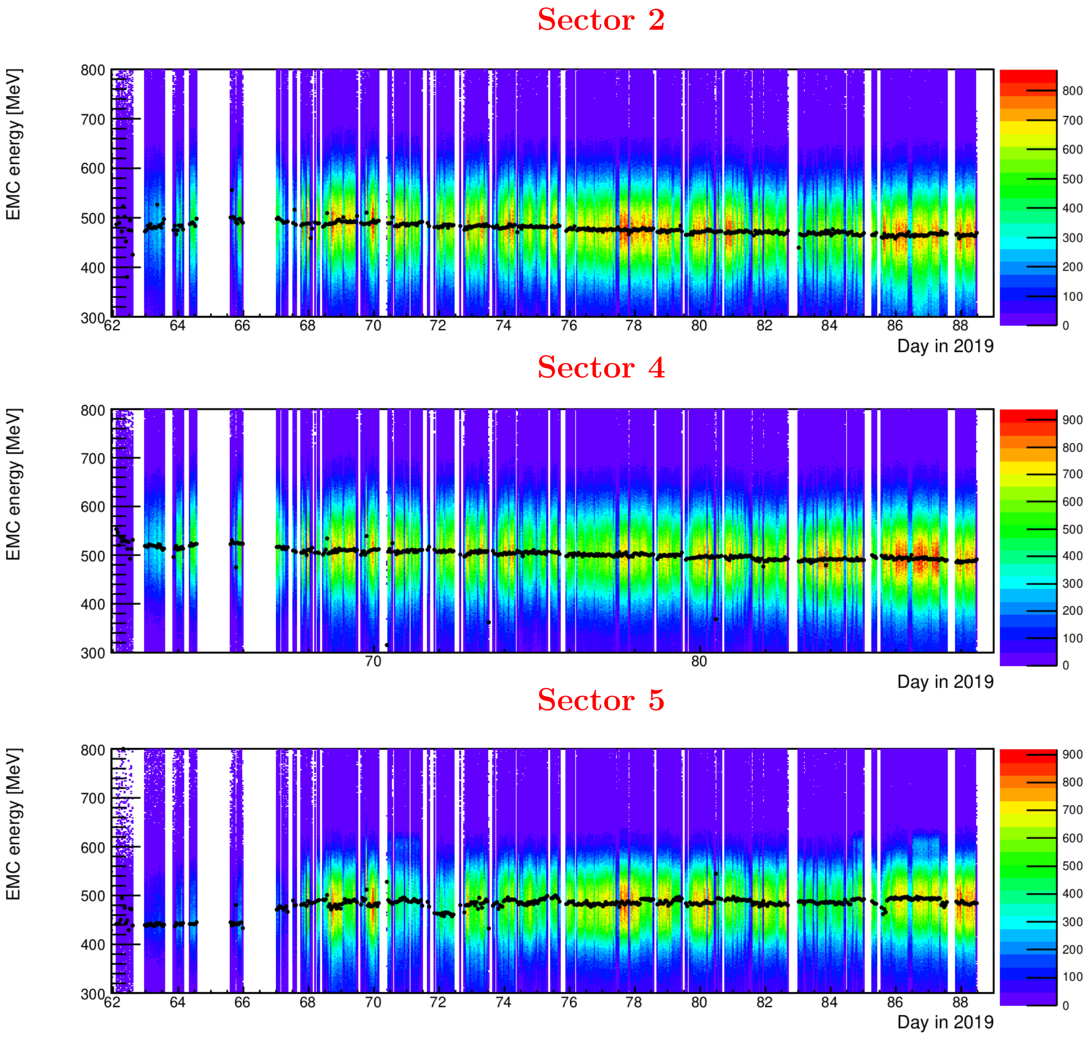

Figure 3.19: Response of the identified charged pions to ECAL during the experiment.

3.4.5 Time calibration

A threshold-based method is affected by the so-called *time-walk effect*. An illustration of this fact is shown in Fig. 3.21. Input signals with different amplitudes reach the threshold at different times, and the effect is more visible for low-amplitude signals. This effect influences determination of particle's time of flight when they arrive to ECAL; and is taken into account and corrected for. This correction can be performed with the help of the RPC detector located right in front of the ECAL. Charged particles in RPC can be matched to ECAL hits and used for the time calibration of every ECAL module. This procedure for a particular ECAL channel is shown in Fig. 3.22. The time calibration function is chosen as follows:

$$t_{ECAL} = t_{RPC} + \Delta_{dist} + a_0 + \frac{a_1}{\sqrt{E - a_2}}, \tag{3.15}$$

where the coefficients a_0, a_1 and a_2 are taken from the fit values, Δ_{dist} is the time correction to account for the time of flight between the ECAL and RPC detectors, and E is the energy. At first, the fit function was chosen to have TOT instead of E in the denominator, however that fit had a poor performance when compared to the usage of energy E which is linear to the signal amplitude.

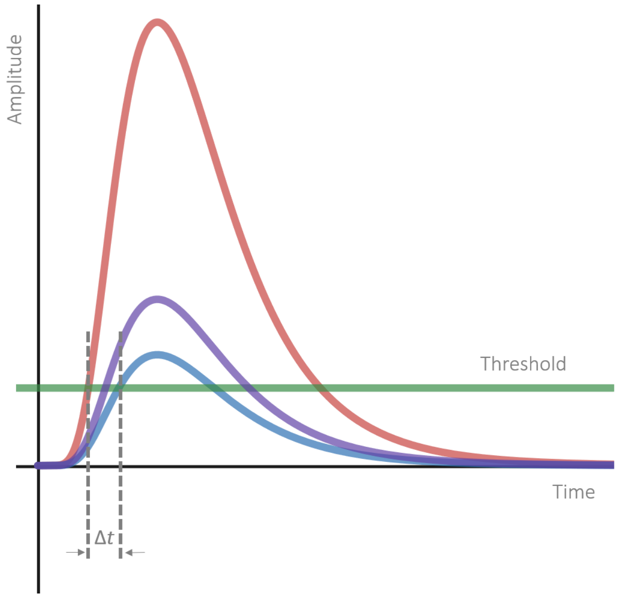

Figure 3.21: Schematic illustration of the *time-walk effect* (Δt)

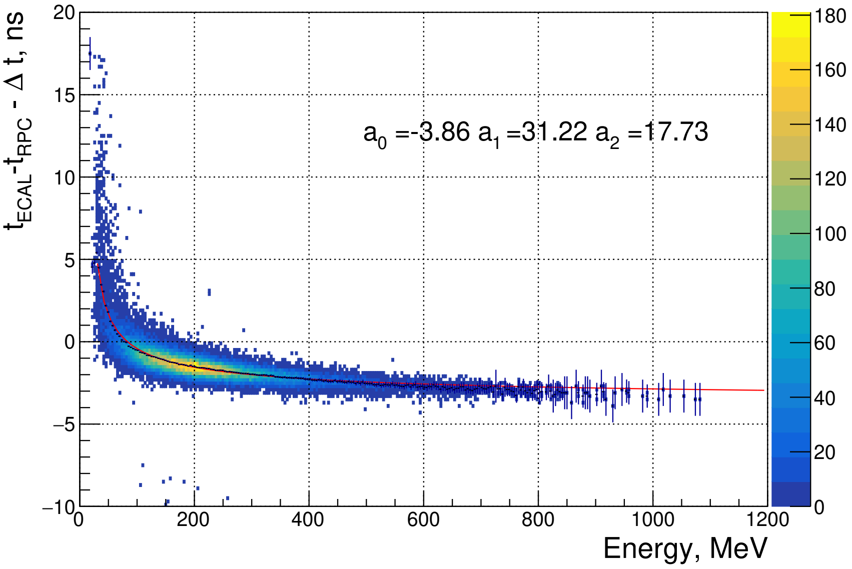

Figure 3.22: Illustration of *time-walk effect* for a single ECAL module. Fit is performed with a function of 3.15.

4. Data analysis

4.1 March 2019 Beam Time overview

In March 2019, the High Acceptance DiElectron Spectrometer (HADES) collaboration performed an experiment in which the heavy-ion collisions were studied. We used ^{107}Ag beam and target, made of natural Silver, consisting of 51.8 % ^{107}Ag and 48.2 % ^{109}Ag isotopes. For more info, see section 2.2. The beam time was divided into three phases of data collection. The properties of different phases are summarized in the following table.

	Phase 1	**Phase 2**	**Phase 3**
Kinetic beam energy	1.58A GeV	1.23A GeV	
Magnet current	3200 A	2500 A	200 A
Duration	430.9 h	39.1 h	6.3 h
Number of events	13.64×10^9	1.32×10^9	0.24×10^9
Mean event rate	8.8 kHz	9.4 kHz	10.7 kHz
Data on disk	333.6 TB	29.3 TB	5.5 TB
Mean data rate	215.1 MB/s	208.2 MB/s	239.9 MB/s
Beam intensity	1.5 – 3.5 MHz		

Table 4.1: Specifications and characteristics of the three phases of the March 2019 measurement campaign.

With a total of 15.28 billion recorded collisions and 368.1 TB raw data, including commissioning and calibration data, the March 2019 beam time was the largest amount of data collected by the HADES collaboration in a single beam time. Only data from phase 1 of the beam time was analyzed in this thesis, see Fig.4.1.

The experimental data are recorded in blocks of events called runs. For the March 2019 beam time, 32966 runs were recorded, each containing, on average, 450,000 events, corresponding to $\approx$ 50 seconds of data taking.

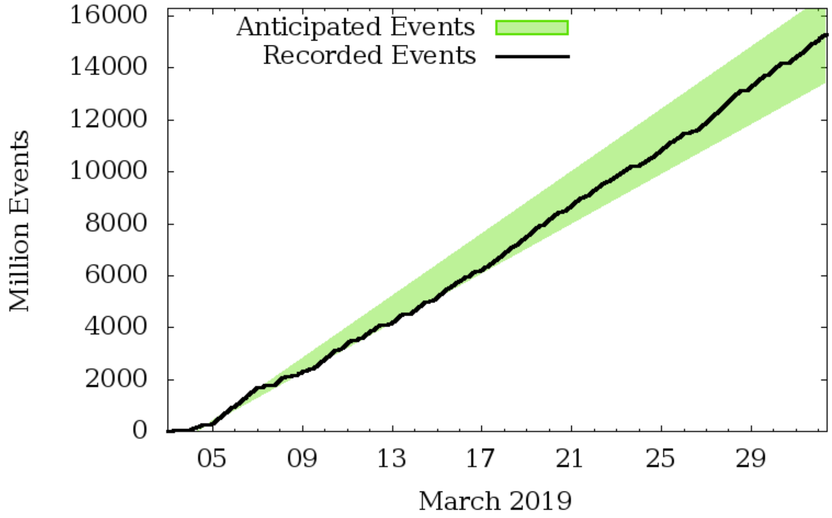

Figure 4.1: The HADES run statistic for the March 2019 Ag+Ag 1.58A GeV production beam time.

The HLD file format was used to write events, which are uniquely identified by a number that indicates the data type (DT), the last two digits of the year (YY), the day of the year (DAY), the time of day in the format HHMMSS, and the event builder number (EB) ranging from 01 to 08. For instance, an event file might be named be1908216020506.hld (DTYYDAYHHMMSSEB.hld). To ensure the stability of detector performance, a successful calibration of each subsystem was needed; several sets of parameters could be used for specific intervals of beam time using the ORACLE system database. After each calibration step, a set of preprocessed data was produced in a type of Data Summary Tapes (DSTs) using the HADES sYstem for Data Reduction and Analysis (HYDRA) framework.

4.2 Event selection

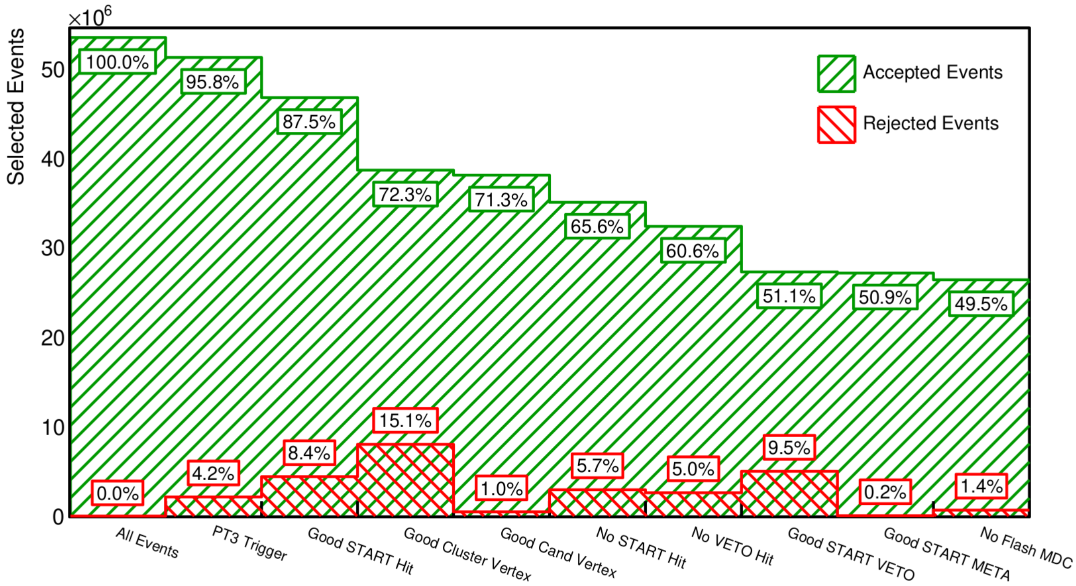

Figure 4.2: Event reduction by the various criteria to discard problematic events. The green bars show the number of events accepted after the corresponding selection criteria have been applied sequentially, and the red bars show how many events are removed. Credit to S.Spies.

Several sources can influence and harm the analysis, such as pile-up events and interactions outside of the silver target. The following list describes the criteria used in the event selection procedure. They are listed in the same order as in Figure 4.2, which shows the proportions of events that remain accepted after applying the criteria sequentially and the proportion of events rejected by each criterion. Most recorded events have a Physics Trigger 3 (PT3), which requires at least 20 hits in the RPC and TOF detectors, which is fulfilled by the most central Ag + Ag events $\approx 55\%$.

- **Good START Hit**: At least one hit in a START detector within a window of 2 ns with a calculated time-of-flight measurement from META.

  This criterion aims to reject events in which the flight times of charged particles cannot be determined by the time difference between their META hit and the selected START hit.

- **Good Cluster Vertex**: This criterion is based on the MDC Cluster-Vertex. It requires a successfully estimated event vertex with a position corresponding to one of the 15 target segments. Therefore, the events in which an Ag+C or Ag+Au reaction occurred in the START detector are almost completely removed.

- **Good Candidate Vertex**: This criterion is connected with the previous one, since it also rejects events outside the target region by the estimated primary vertex. However, it uses the more precise Track-Candidate-Vertex.

The criterion requires a successfully estimated vertex with a z-coordinate larger than -70 mm, which roughly corresponds to the region of the target.

- **No additional START Hit**: This criterion is used to reject events in which multiple beam ions interacted in the target less than 15 ns after each other. In such events, it is difficult to disentangle the particles from the different collisions, and thus assigning appropriate flight times to the particles is difficult. Rejection is achieved by requiring that in a time window of ±15 ns around the START detector hit, no additional START detector hits were recorded. Since a single beam ion traversing the START detector can induce multiple hits due to cross-talk between adjacent channels and the two sides of the START detector, which are treated independently, hits within a time window of ±0.5 ns around the selected hit are accepted.

- **No VETO Hit**: If there is a particle registered in the VETO detector 15 ns around the START time, the event is refused based on the No VETO Hit criterion because it is very probable that the beam particle did not interact with the target.

- **Good START VETO**: The event is excluded if a second START hit without a correlated VETO hit is detected after the triggered START time between times 15 and 350 ns.

- **Good START META**: Exclusion of events, where a later START hit was found within the range of 80-350 ns, was correlated with more than four META hits within the time window of 7 ± 5 ns to remove pile-up in MDCs. The offset of 7 ns corresponds to the fastest particles.

- **No Flash MDC**: During the analysis of the Ag + Ag data, it turned out that almost all sense wires from one or more MDC chambers recorded hits in some events. Large amounts of active cells are non-physical and make it impossible to accurately reconstruct MDC track clusters, which is why these events need to be identified and removed.

4.3 Simulations

The comparison with the Monte Carlo (MC) simulation is necessary to ensure a reliable result. The analysis scheme is shown in Fig. 4.3. It is essential to understand all detector effects, as they can influence the experimental results. Acceptance and efficiency estimation can be easily accessed in simulations, and all analysis steps can be checked for systematic error evaluation. The HADES experiment is precisely aligned in every collision program, utilizing photogrammetry, cosmic-ray test data, and measurement without a magnetic field, i.e. situation when charged pions and protons are flying in straight lines. Complete knowledge of the inside detector material is implemented, and exact detector resolution is achieved after parameter tuning in simulations.

The first input to simulations is taken from the Event generator; in case of HADES, it is mainly PLUTO and UrQMD models, which are introduced further:

- **PLUTO** A very fast and easy MC generator, particles are generated within the thermal source model with arbitrary momentum and angular distributions; however, it is limited to lower collision energies [74].
- **UrQMD** Ultra relativistic Quantum Molecular Dynamics (UrQMD) is a kinetic transport model with complete information on spacetime evolution. Version 3.3p2 was used for the current experiment [75].

The interactions of the particles in the detector material and theirs bending in the magnetic field are simulated as a second step. Therefore, the HGeant package is used, based on the GEometry And TRacking (GEANT) 3.21 software package [76], which comprises the complete three-dimensional geometry of the HADES detector system, as well as all materials used and their properties. The GEANT propagates particles from the event generator, allowing them to interact with the rest of the environment. The final step of simulations is to mimic each detector response and convert the particle signal into measured properties as in an actual experiment. The digitization procedure is well explained in [77].

Afterward, the simulated events are treated in the same manner as experimental ones; e.g., the same cuts are applied for track selections, event parameters, etc. The acceptance and efficiency corrections can be extracted from the simulation; the details are further written in section 4.6.

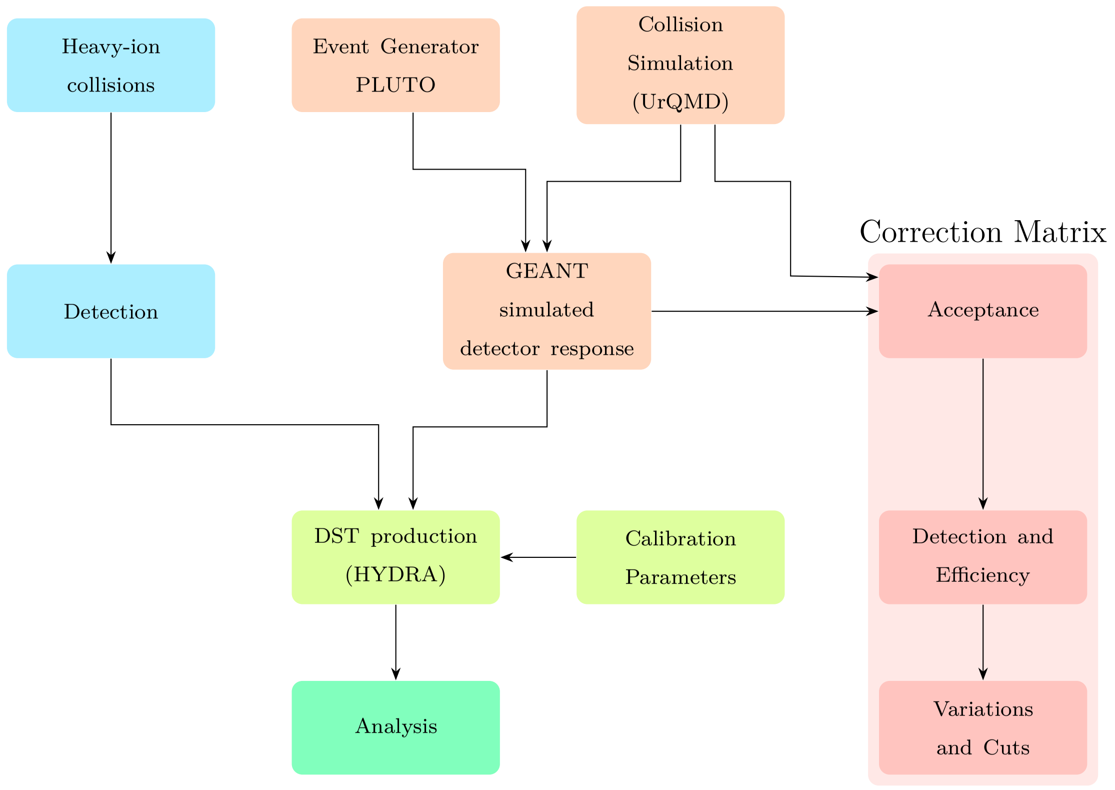

Figure 4.3: Flow chart of the analysis scheme showing the individual steps and the required tools. At each step, separate parts of the correction matrix are displayed.

4.4 Centrality determination

The main property of the collision is the centrality at which it occurs. Centrality describes the number of participating nucleons and is characterized by the impact parameter b, defined as the minimum distance between the centers of the colliding nuclei. Nucleons that go through the reaction zone are called participants, while those that only pass around are called spectators. Centrality estimation can be deduced from the Glauber model and Monte Carlo simulations[78], which connect a measurable quantity of particle multiplicity with the centrality of the collision. A detailed overview of the procedure steps and how it was performed for the previous heavy-ion experiment Au + Au at $\sqrt{s_{NN}} = 2.42A$ GeV can be found in [79].

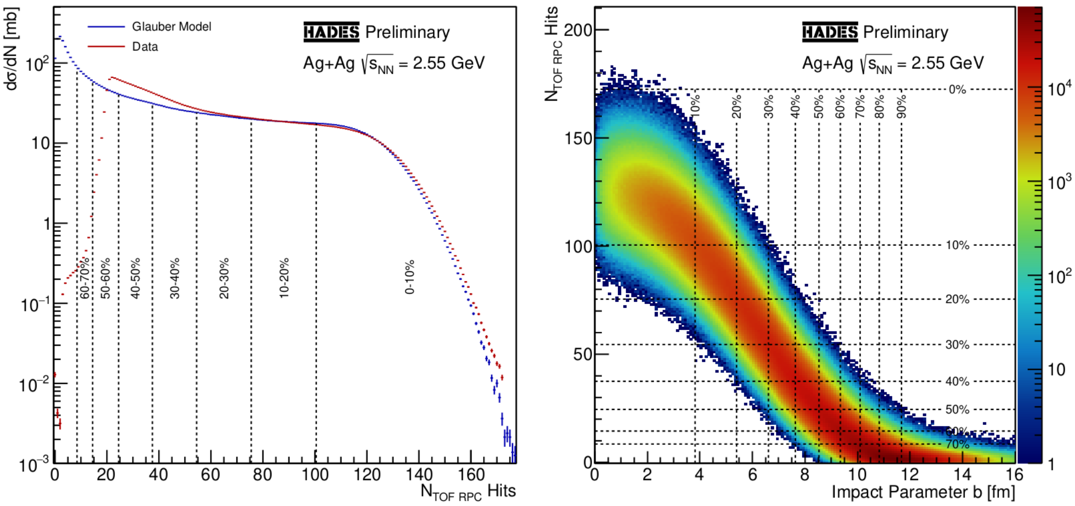

Figure 4.4: Differential cross-sections in dependence of the amount of the sum of RPC and TOF detector hits (left) for the Glauber model simulations (blue) and experimental data (red). The right plot shows the correlation between the impact parameter and the amount of RPC and TOF detector hits for the applied Glauber model. The dotted lines divide the total cross-section into centrality classes comprising 10 % each according to the corresponding quantity. Credit to [80].

Summary of the centrality in the table:

Class	A_{part}	b	$N_{RPC} + N_{TOF}$
00 - 10 %	160.9 ± 6.9	0.00 - 3.82 fm	101 - 172
10 - 20 %	114.5 ± 6.2	3.82 - 5.40 fm	76 - 100
20 - 30 %	81.1 ± 5.1	5.40 - 6.62 fm	55 - 78

Table 4.2: Centrality class selection ranges used in the analyses. The classes can be related to the mean number of participants A_{part} as well as the impact parameter b of a collision and the hit multiplicities in the time-of-flight detectors.

The average number of charged tracks N_{ch} is sampled by the Negative Binomial Distribution (NBD) to take into account event-by-event fluctuations, described as :

$$P_{\mu,k}(n) = \frac{\Gamma(n+k)}{\Gamma(n+1)\Gamma(k)} \frac{(\mu/k)^n}{(\mu/k+1)^{n+k}}, \tag{4.1}$$

where μ is the mean of the distribution, the dispersion parameter k is calculated from the mean μ and the standard deviation σ as:

$$k = \frac{\mu^2}{\sigma^2 - \mu}. \tag{4.2}$$

Thus, one can get $N_{ch} = \mu N_{part}$. The simulated spectra are then compared with the experimental one and can be used for centrality separation; see the left Figure 4.4.

Due to the contamination of peripheral Ag + Ag events by Ag + C events, the focus is placed on the most central 0-30 % events, where good agreement is observed between the experimental data and the Glauber model simulation.

4.5 Photon identification

A photon candidate can be identified by the HADES detector selecting signals in ECAL that require anticoincidence with the RPC detector, which is located just in front of ECAL, and by demanding antimatching conditions with any reconstructed track in the direction of the corresponding ECAL module. The lowest ECAL energy, when it is possible to extract a π^0 signal with respect to the combinatorial background in most of the phase-space bins, was determined to be 100 MeV. This energy cut is varied to study the systematic effects further. This cut removes noise, most of the neutrons, which could also interact hadronically with ECAL, and consequently removes a large part of combinatorics. In addition to these cuts, a cut is applied to the velocity of the particles $\beta_{ECAL}(E_\gamma) < \pm 1\sigma$ is applied. This beta cut also serves to remove neutrons even further and to have a good-quality photon sample. This cut is included in systematic error estimation.

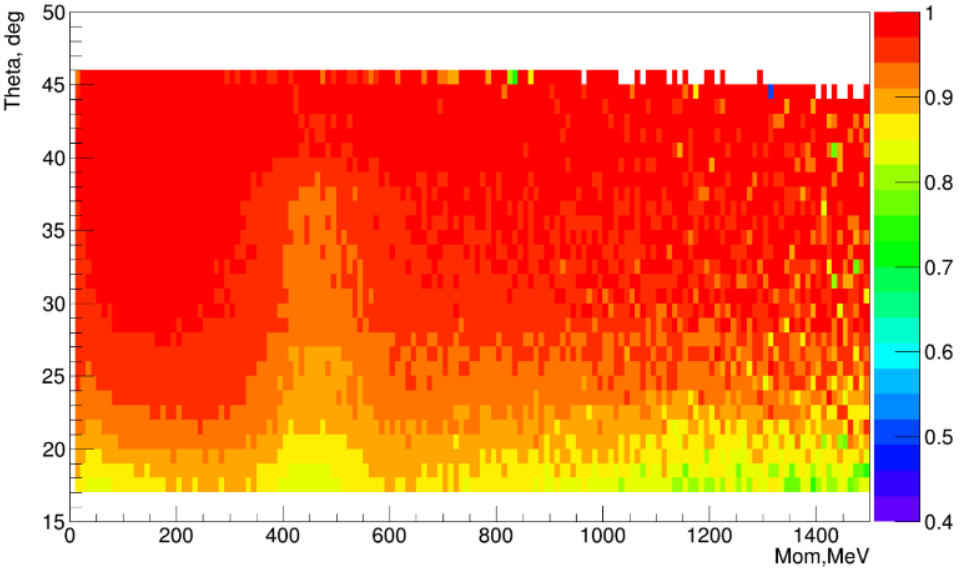

Figure 4.5: Simulation of the purity of the photon candidate versus the photon momenta on the x-axis and theta on the y-axis. The lowest theta modules are excluded from the analysis.

4.5.1 Photon purity

The purity of the reconstruction of the photon candidate was checked using HADES Monte-Carlo simulations. This quality parameter is calculated as the ratio of the number of real photons divided by the number of photon candidates. Here, a photon candidate refers to a hit in ECAL, that fulfills the criteria for photon identification, see section 4.5. The purity plot can be seen in Fig. 4.5. Purity was found to be at the mean level of 95% with some visible structure around 480 MeV, which corresponds to the constant energy deposit of charged pions that can interact hadronically with ECAL.

The lowest theta angles below 15° are excluded from the selection of photon candidates due to the very high probability of photon interaction with the material of the RICH detector, as can be seen in the HADES tomography plot in Fig. 4.6 and in Fig.4.7.

The enlarged picture of photon interaction with aluminum is shown in Fig. 4.7

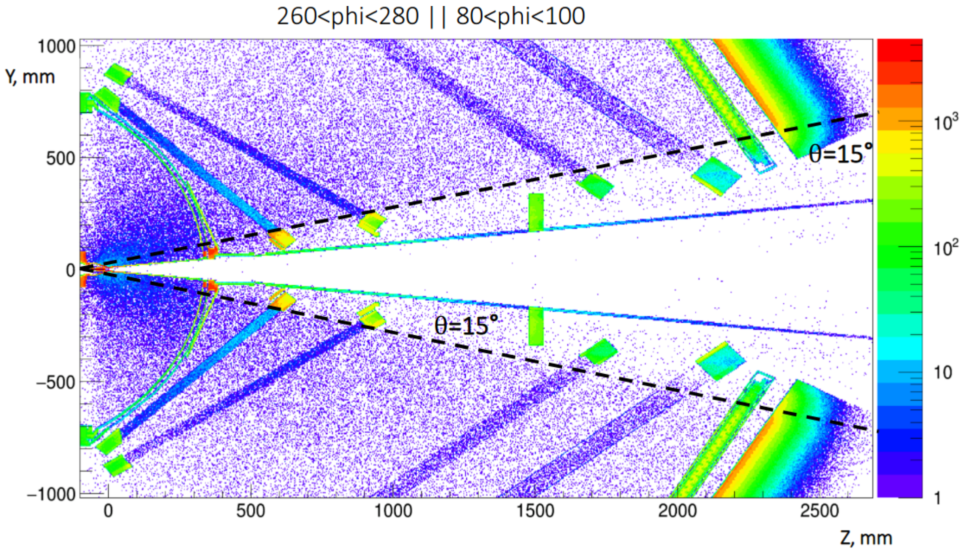

Figure 4.6: Geant simulation of photon interaction points in the material of HADES. The last detector in the scheme is the ECAL.

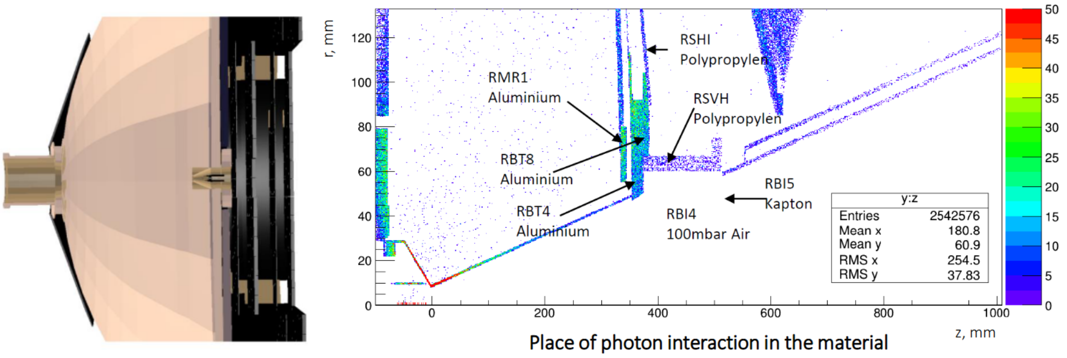

Figure 4.7: **Left**:RICH detector GEANT image. **Right**: Point of photon interaction with material in simulation

4.5.2 Single photon acceptance and efficiency

The acceptance of single photons in the $\theta - \phi$ coordinates was calculated using the simulation information of the primary π^0 photons that interact with the ECAL material and can be seen in Fig.4.8. The operating ECAL setup consisted only of 4 sectors for the March 2019 experiment and it is shown in Fig. 4.9. One can see that some modules have been excluded from the analysis due to module instability, bad PADIWA behavior; or modules have been disconnected during the experiment due to DAQ-related problems. The same setup is used in the simulations to obtain acceptance and efficiency information further.

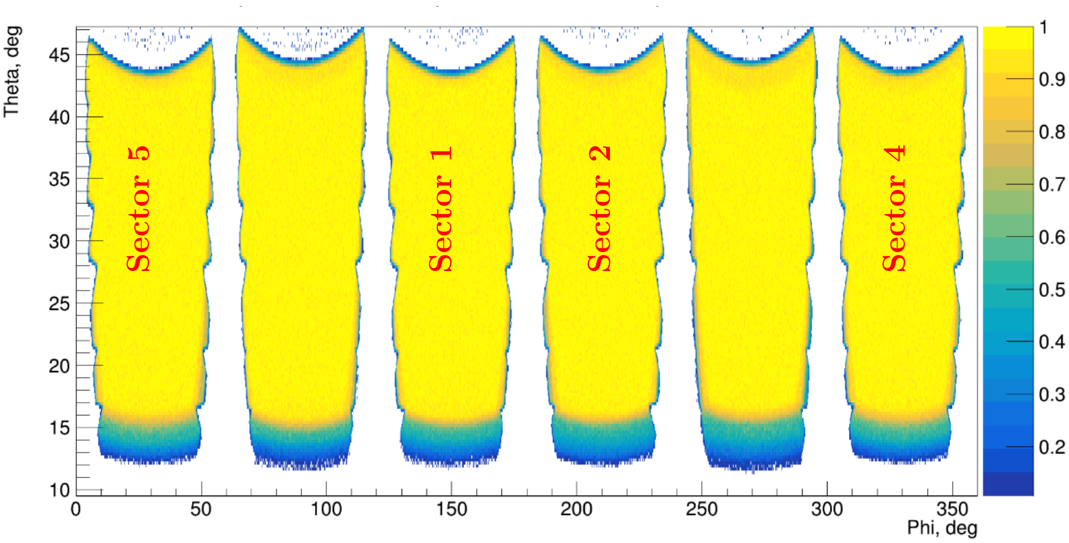

Figure 4.8: Full ECAL setup in simulations.

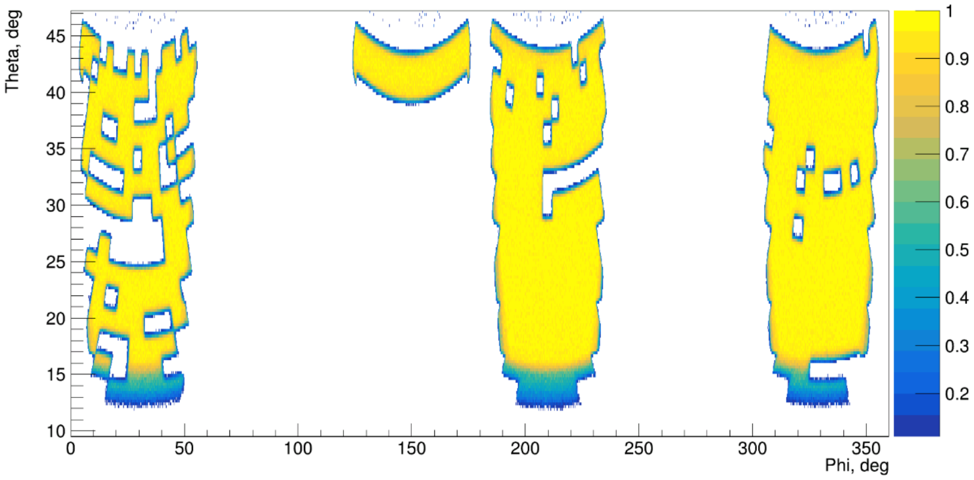

Figure 4.9: March 19 experiment setup with good operating modules.

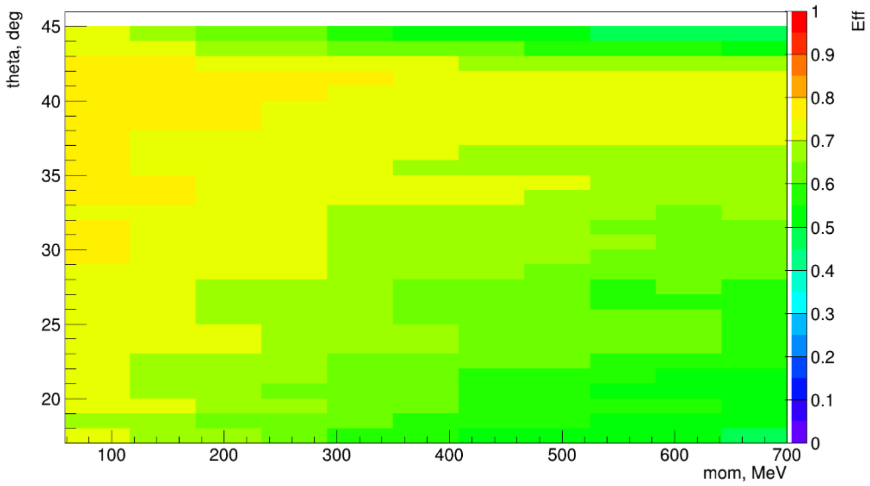

Figure 4.10: Efficiency of a single photon based on simulation.

The simulated efficiency of the accepted photons is shown in Fig.4.10, which shows the ratio of the number of reconstructed photons N_{reco} with a correctly reconstructed energy within a three-sigma energy resolution divided by the number of all accepted photons N_{acc}. See Equation 4.3. The value fluctuates near the mean value of 0.7.

$$\epsilon(E,\theta) = \frac{N_{reco} \quad (\forall \quad |E_{ECAL} - E_{real}| < 3\sigma_E)}{N_{acc}} \tag{4.3}$$

4.5.3 Data-driven efficiency correction

HADES detector was built in the first place with excellent identification for the e^- e^+ pair. Since leptons interact electromagnetically with ECAL in the same way as photons, they can be used for independent efficiency estimation. Therefore, in both experiment and simulation, one can study the efficiency of the detection of leptons identified by the rest of the HADES detectors (RICH, MDC and RPC) in the ECAL. This efficiency is estimated in the region of ECAL geometric acceptance, for that purpose the lepton position in RPC is used, see equation 4.4.

$$\epsilon(E) = \frac{N_{reco} \quad (\forall \quad |E_{ECAL} - p_e| < 3\sigma_E)}{N_{acc}} \tag{4.4}$$

For the efficiency numerator, the number of leptons N_{reco} with a time and position match to ECAL is used. At the same time, the difference between the reconstructed momentum and energy in ECAL should be within 3 sigma of the ECAL energy resolution.

Here, N_{reco} fulfill the following conditions:

- 3-sigma reconstructed energy cut
- matching quality with a reconstructed track in HADES
- matching quality with an RPC: time and position

In the denominator, N_{acc} the number of leptons that should have hit the ECAL module determined by the corresponding RPC hit position. In addition to the above mentioned conditions, both N_{acc} and N_{reco} leptons satisfy the standard lepton selection conditions which are written in Section 3.4.1.

The same lepton identification method is applied for reconstruction in the simulation and in the experiment. Then, the real ECAL efficiency for leptons is compared with the one in the simulation.

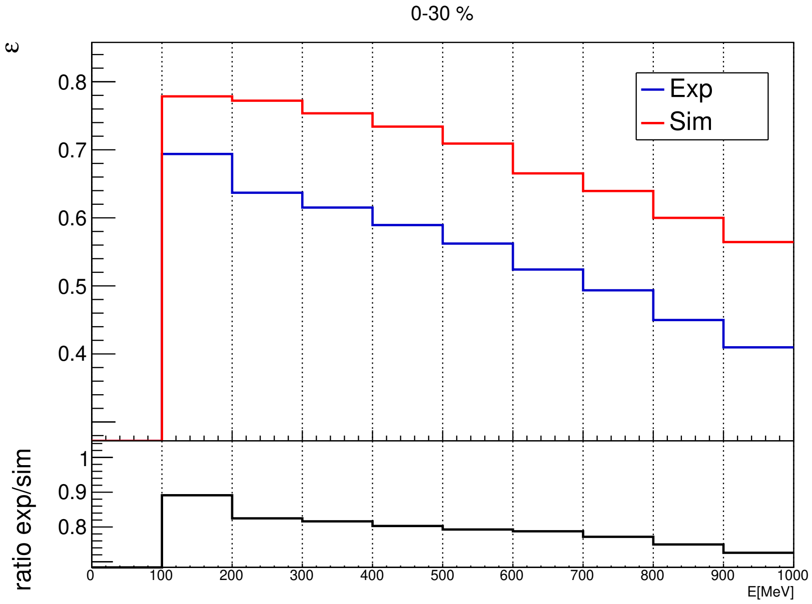

Figure 4.11: Comparison of ECAL efficiency between reconstructed experimental leptons (blue line) and reconstructed simulated leptons (red line) and their ratio (black line) for 0-30 % centrality.

During calibration, some modules were found to change their behavior during operation, causing the inefficiency of the ECAL detector. Such problems can be resolved using information from, for example, lepton energy reconstruction by comparing the HADES tracking momentum with the ECAL detected energy. In Fig.4.11, this effect can be seen as a disagreement between the efficiency of the identified leptons in the experiment and in the simulation data in blue and red, respectively, the ratio of efficiencies is shown in black line.

4.6 Embedding of $\pi^0 \rightarrow \gamma\gamma$ into data

Another way to obtain efficiency is by embedding simulated photons from the decay of π^0 into real data. This allows us to calculate the direct photon efficiency instead of using lepton efficiency as shown in section 4.5.3. Using a PLUTO generator, a phase-space distribution of π^0 can be produced with the main properties defined, such as the fireball temperature in AgAg collisions. One gets a more realistic response for hadrons and therefore the better multi-hit description of the detector.

In Fig. 4.12, the distribution of π^0 is shown in the phase space p_t - y before and after reconstruction to present the acceptance coverage of the ECAL setup used during the experiment. The rapidity y_{cm} is defined as $y_{lab} - 0.822$, see Appendix A.

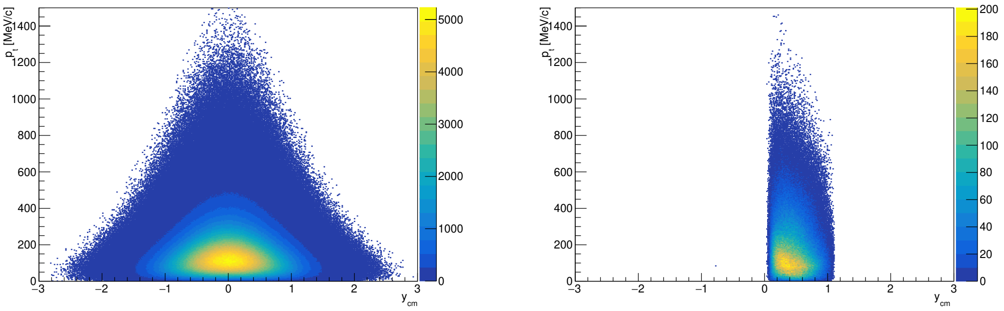

Figure 4.12: **Left**: PLUTO π^0 distribution in full phase space. **Right**: Reconstructed PLUTO π^0 in HADES

Furthermore, the π^0 decay to two photons per event from PLUTO is first processed in Geant, the response is digitized, then embedded in the defined event, and passed to Hydra DST processing. Comparing the original number of embedded photons from pions with the accepted and reconstructed photons gives acceptance and efficiency, respectively. This embedding analysis can be done in the same manner as for simulations to have an estimation of real-photon efficiency. This is shown in Fig.4.13, where the red line shows the perfect efficiency ϵ in simulation and the blue line shows the real efficiency in the experiment based on the same π^0 embedded data. The black line shows the ratio between two efficiencies, which remains almost constant regardless of the photon energy. This ratio can be compared with the exp/sim ratio for lepton efficiency (see Section 4.5.3). The lower efficiencies for photons as compared to leptons can be associated with multi-hit effects, i.e. pions and/or protons hitting same ECAL modules as a photon. This effect is automatically excluded in previous simulation of lepton detection, as leptons with close charged tracks are excluded in the HADES standard data analysis. The difference between the efficiencies of embedded photons in simulation and in the experiment can be explained by detector effects in real data, such as instability of operation, different behavior of specific modules, and imperfect calibration, whereas this is not the case in simulation. The experimental data used for embedding was varied using several days as subsets, the check did not show significant differences between days, and the sum of all embedded data was used for the final calculations. The above described combined efficiency-acceptance correction is later used as a track weight when filling invariant mass histograms for the corresponding centrality, transverse momentum, and rapidity.

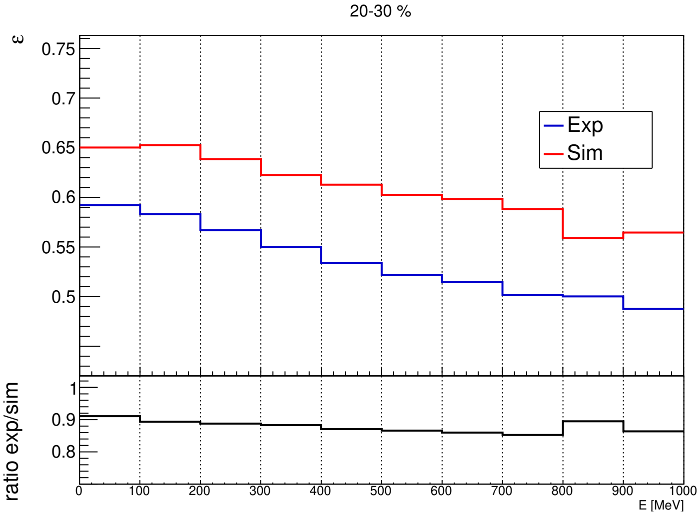

Figure 4.13: Efficiency of single photons based on the embedding of one π^0 per event from PLUTO model both in experimental and simulation data for 20-30% centrality.

Here, in efficiency numerator, photons fulfill the following conditions:

- 3-sigma reconstructed energy cut
- no match with RPC
- no match with a track
- 3-sigma ECAL beta cut

In denominator, there are all photons that have hit ECAL.

Finally, the overall efficiency and acceptance corrected yields $N_{corrected}$ are given by the following formula 4.5:

$$N_{corrected} = \frac{N_{raw}}{(eff * acc \cdot corr_{exp/sim})}, \tag{4.5}$$

where N_{raw} is the raw extracted number of π^0 , $eff * acc$ is a ratio obtained from the same analysis in simulations divided by the original number of particles from the generator used in simulations, and $corr_{exp/sim}$ is the correction factor from embedding, which is suited for accounting of differences between real data and simulations.

The efficiency-acceptance correction matrix for $p_t - y$ phase-space for centrality 20-30% is shown in Fig.4.14.

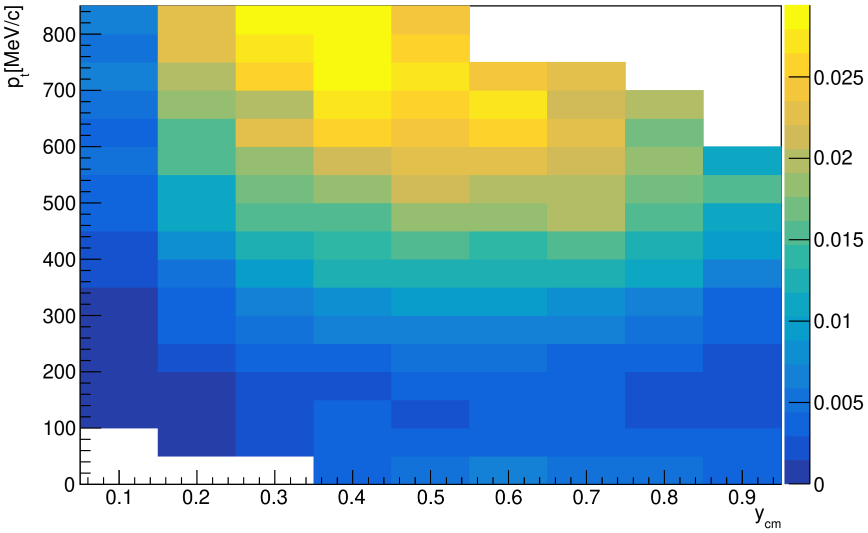

Figure 4.14: Correction matrix for efficiency-acceptance of π^0 in the simulation for 20-30% centrality.

4.7 Invariant mass reconstruction

After all calibration steps, the photon hit information can be used to reconstruct the π^0 and η mesons.

Meson	Mass[MeV/c^2]	Life time[fm/c]	Decay channel	Branching ratio
π^0	134.977	$7.7 \cdot 10^5$	$\gamma\gamma$ $\gamma e^+ e^-$	$98.82 \pm 0.03\%$ $1.17 \pm 0.04\%$

Table 4.3: Quantities of π^0 mesons

The fact that different p_t regions are covered by different sector topologies is shown in Fig.4.15. One can see that the high p_t regions ($\approx p_t > 300$ MeV/c) are detected mostly as the same sector photon combination with small opening angles, whereas the low p_t regions detected as combinations of photons from the different sectors with high opening angles. For that reason, all available stable ECAL modules were used for the experiment, e.g., even including only two upper rows from Sector Nr. 1 and Sector Nr. 5 with many switched off cells as one can see in Fig.4.9. However, there were some problems with the low p_t extracted yield of π^0 due to the limited acceptance of the used ECAL setup, as will be shown in the next chapter. For the η particle, as seen in Fig. 4.16, photon pairs belong to different sectors with very high opening angles above 40 degrees.

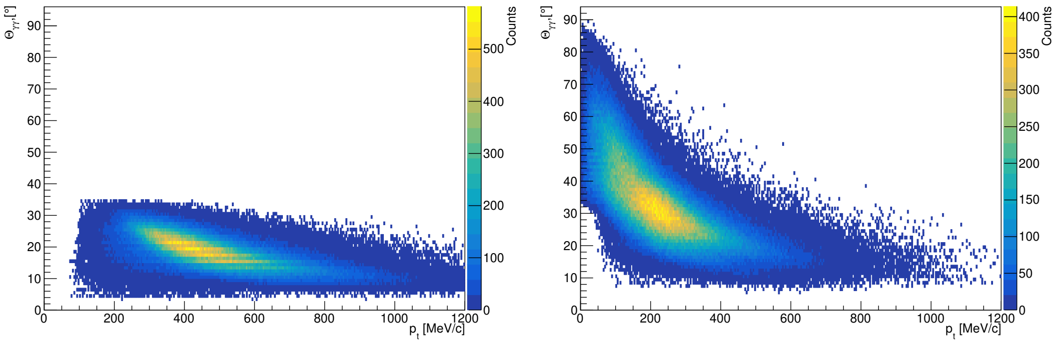

Figure 4.15: Opening angle of reconstructed true π^0 photon pairs versus p_t in simulations. **Left**: both photons are in the same sector. **Right**: both photons belong to different sectors.

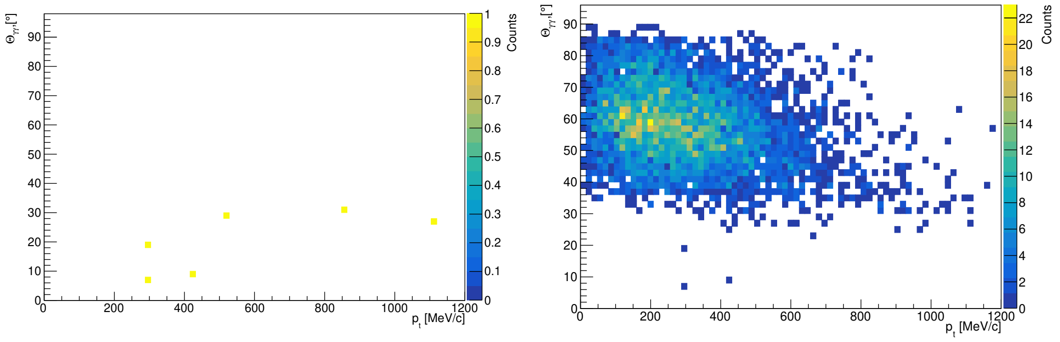

Figure 4.16: Opening angle of reconstructed true η photon pairs versus p_t in simulations. **Left**: both photons are in the same sector. **Right**: both photons belong to different sectors.

In Fig.4.17 there is a distribution of the opening angle of true π^0 photons pairs. Furthermore, the cut on 8 degrees minimum opening angle is applied to avoid problems with the mixed-event background estimation; the event-mixing technique can combine very close photon pairs - that is not possible in reality because two tracks would not be reconstructed as two photons but one due to the clustering procedure. In Fig.4.21 it is seen that the minimum angle cut removes most of the low-invariant mass pairs that could cause a problem in the mixed-event spectrum shape.

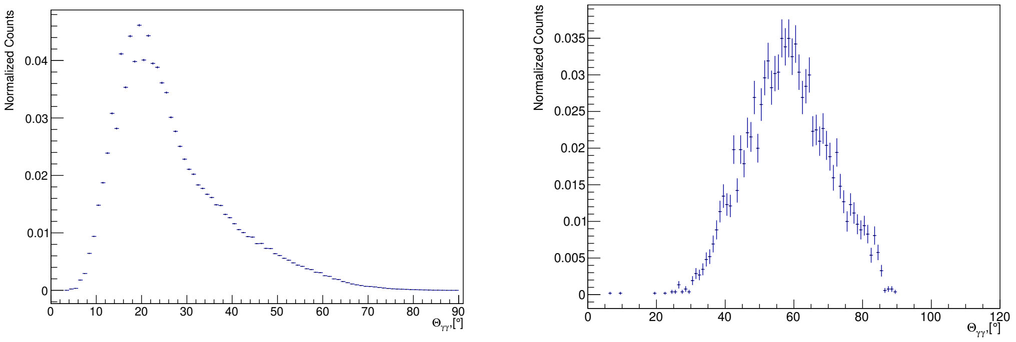

Figure 4.17: **Left**: Opening angle of reconstructed true π^0 photon pairs in simulations. **Right**: Opening angle of reconstructed true η photon pairs in simulations.

It is impossible to identify which photons originated from the same meson decay; therefore, all possible combinations of photons are considered within one event. The invariant mass of 2 photons is given by the formula 4.6

$$m_{\pi^0} = \sqrt{2E_{\gamma_1}E_{\gamma_2}(1-\cos\Theta_{12})}, \tag{4.6}$$

The diphoton invariant mass spectrum includes:

- **Signal** pairs of photons originating from the same decayed π^0 .
- **Uncorrelated combinatorial background** the photons that originate from different mother particles.
- **Correlated background** tracks from the same mother particle, but not from π^0 .
- **Misidentified tracks**.

Most of the combinations contribute to the combinatorial background. The number of produced π^0 can be obtained after subtracting that background.

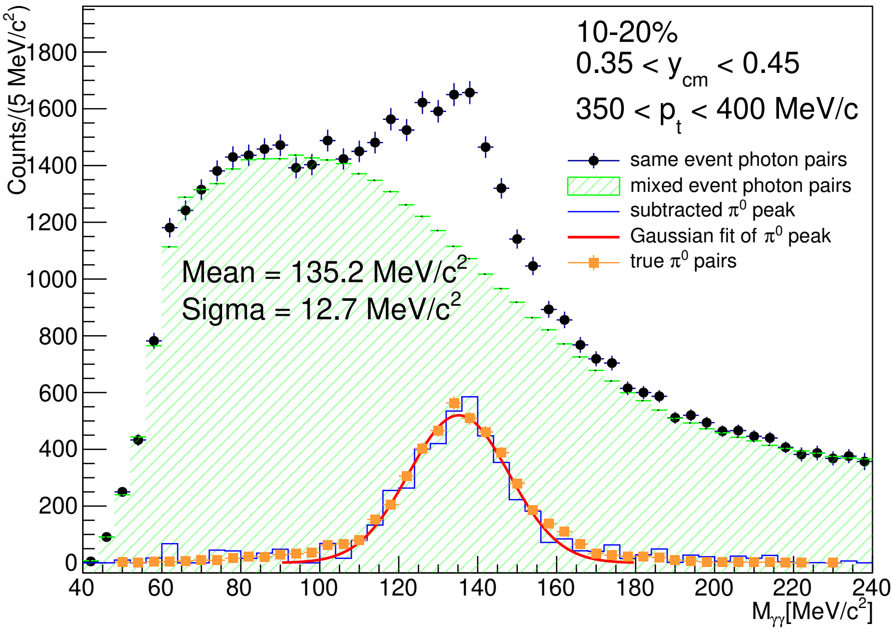

Figure 4.18: π^0 simulations closure test for an example phase space bin in 10-20% centrality.

To estimate the combinatorial background, one can perform a polynomial fit outside the peak region or use the very powerful **Mixed-Event** method. This method combines two photons from different events, thus destroying any correlation between them. Due to the complex shape of the background for different phase-space regions, this method was used further in the analysis. Another advantage of the event-mixing technique is that it provides very large statistics, which does not introduce any statistical uncertainty to the results. This method combines photons originating from different events because those particles are not correlated; hence, the correlated signal is absent and can be used to subtract the same-event photon combinations. The events from which photons are combined must also have the same event topology, including centrality, photon multiplicity, and vertex position.

The following event selection classes were used to mix events with the same:

- centrality class
- target bin (the reconstructed silver target layer)
- photon multiplicity
- event plane angle bin (for flow study).

For mixing, the pool of 50 events was used. The events are mixed within a close-time pool to avoid problems with stability over the beam time. All available data were used to estimate the combinatorial background.

The first step is to test the validity of the mixed-event background using simulations. In Fig. 4.18 the black point shows the distribution of same-event pairs, the green area represents a mixed-event combinatorial background, and the blue line shows a signal calculated by subtracting the combinatorial background from the same-event combinations, the red line is the Gaussian fit of the peak π^0, and the orange markers show the true π^0 diphoton combinations, obtained with additional Geant information. One can see that the mixed-event technique is capable of reconstructing the real π^0 signal. This method is also applied to real data as can be seen in Fig.4.19.

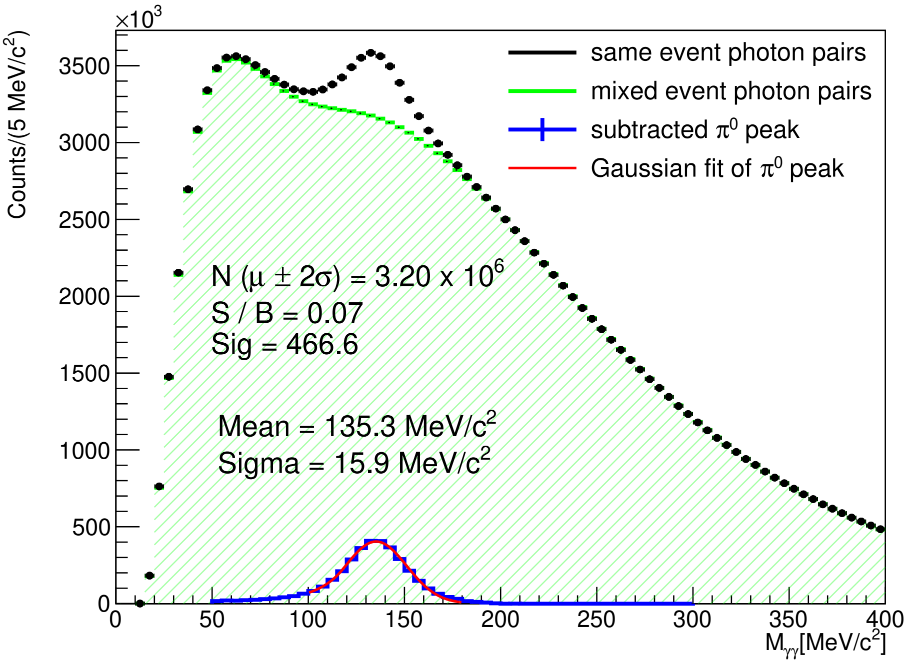

Figure 4.19: Integrated π^0 yield for 20-30 % centrality.

In Fig. 4.20, the same-event diphoton mass is shown versus p_t for two cases of sector combinations, whether 2 reconstructed photons belong to the same sector or to different sectors. The π^0 peak at nominal mass is visible for a higher transverse momentum.

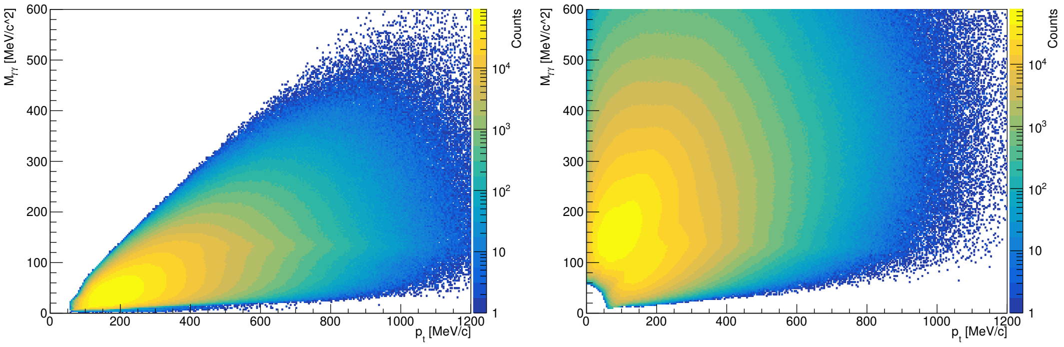

Figure 4.20: Invariant diphoton mass versus transverse momentum in experiment. **Left**: both photons are in the same sector. **Right**: both photons belong to different sectors.

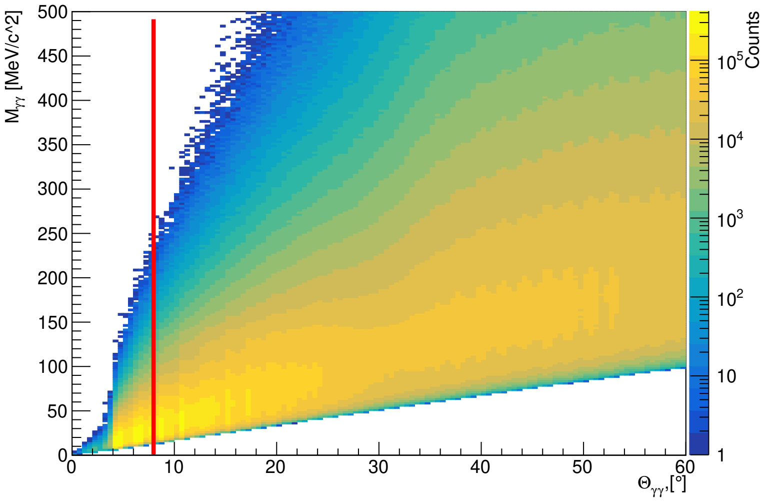

Figure 4.21: Opening angle of same-event photon pairs versus the invariant mass of these photons in experiment.

An interesting fact that was found was that the normalization for each $p_t - y$ phase space bin was the same as for the given centrality bin. This means that the photons are mixed evenly for the whole phase space. This normalization coefficient was estimated from the integrated yield of the given centrality. This is shown in Fig.4.22. Arbitrarily chosen units for the x-axis represent different phase-space regions with the best signal reconstruction. They are defined as $y_i \cdot nPtBins + pt_i$ with $nPtBins = 24$. Deviations from the straight lines were caused by incorrect normalization in problematic phase-space bins. This one coefficient per centrality class has significantly reduced deviations in the results. The normalization coefficient was calculated by the ratio of the integrals in same-event pairs and mixed-event pairs outside the π^0 peak and varied to check for systematic error sources. The integral region was chosen to be 220 MeV up to 250 MeV.

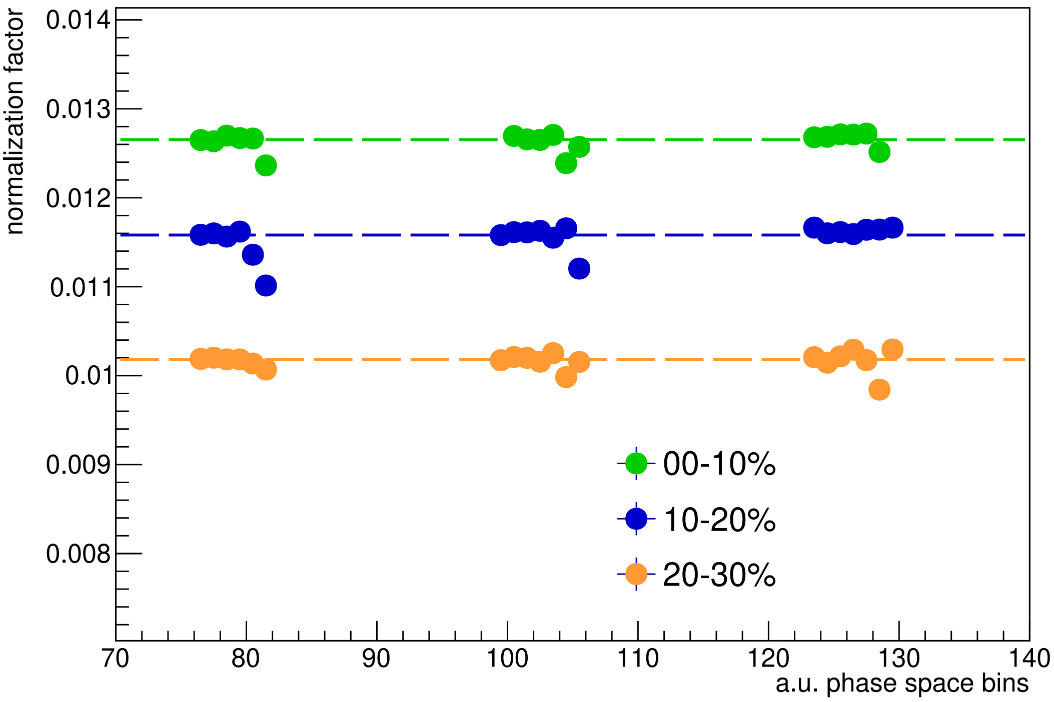

Figure 4.22: Normalization factor for mixed-event technique vs different $p_t - y$ bins within one centrality class.

4.7.1 η extraction

Unfortunately, the η particle with the same 2-photon decay could not be reconstructed due to lack of coverage of high opening angles, holes in the detector (which influence proper energy reconstruction since photons from η carry higher energy and are reconstructed on average as ECAL cluster with 2 and more active modules), see Fig.4.9 and Fig.4.16, and it is not visible in the invariant mass spectrum - because of the huge background contamination. Therefore, the η analysis was not possible for the current experiment. However, recently, in February 2022, there was a $p+p$ experiment with $\sqrt{s} = 3.46$ GeV where the η peak is quite visible with a 8% Signal-to-Background ratio. Fig.4.23 shows the online η yield extracted with the same analysis procedure as for π^0 with no cut on velocity β for the initial energy calibration, which will be improved.

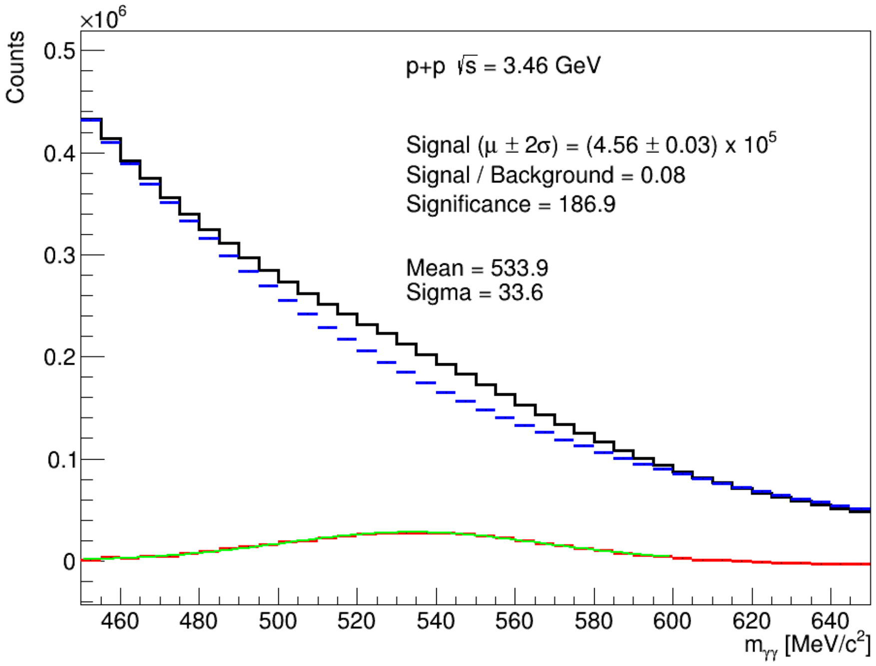

Figure 4.23: η yield extraction in the $p+p$ experiment with $\sqrt{s} = 3.46$ GeV. The black line shows same-event pairs, the blue histogram is a mixed-event combinatorial background, the red histogram is the signal, and the green line shows Gaussian fit.

4.8 Flow

One of the properties of nuclear matter is its incompressibility, which is caused by the resistance of the matter to external pressure and is closely related to the flow emitted of the particles.

The available energy of the nuclear collision is converted into thermal and compression energy; the latter is carried away by the collective flow of reaction products, and the non-participating nucleons are pushed out by the high pressure in the nuclear interaction region, hence taking away some available energy. This phenomenon was predicted according to the hydrodynamics model applied to nuclear fluid matter, and the importance of transverse expansion was first shown, see [81].

There are many methods to study the collective motion of particles[82].

The particle emission at the azimuthal angle with respect to the reaction plane could be well expanded into the Fourier series :

$$E\frac{d^3N}{d^3p} = \frac{1}{2\pi}\frac{d^2N}{p_t dp_t dy}\left(1 + \sum_{n=1}^{\infty} 2v_n \cos[n(\phi - \Psi_{RP})]\right), \tag{4.7}$$

where Ψ_{RP} denotes the angle of the reaction plane, ϕ is the angle of the particle, and $v_n = v_n(p_t, y)$ are the Fourier coefficients. These coefficients are calculated by averaging all particles in all events, that is, $v_n = \langle\cos[n(\phi - \Psi_{RP})]\rangle$. The real value of the reaction plane is not accessible within the experiment; instead, the angle of the event plane Ψ_{EP} is used with some finite resolution. Due to the finite number of particles and the limited resolution of the event plane, the

Fourier coefficients should be corrected up to what they would be with respect to the reaction plane; this can be done by dividing the observed coefficients by the event plane resolution correction factor R_n.

For the estimation of the reaction plane of the event plane Ψ_n, the event flow vector Q_n is introduced.

$$Q_n \cos(n\Psi_n) = X_n = \sum_i w_i \cos(n\phi_i),$$
$$Q_n \sin(n\Psi_n) = Y_n = \sum_i w_i \sin(n\phi_i),$$

where some particles i with weight w_i are selected. An example of the determination of the reaction plane is shown in Fig. 4.24.

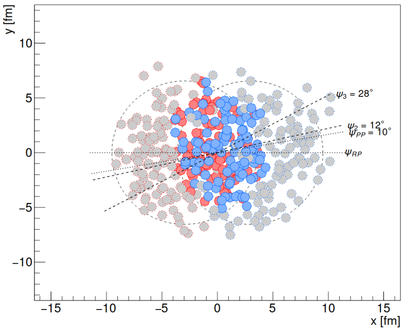

Figure 4.24: An example event shows the participating nucleons (full-colored dots) and the spectators (light-colored dots). The reaction plane Ψ_{RP}, the participant plane Ψ_{PP}, and its harmonic decompositions into higher-order phase angles are shown. Taken from [83]

In our case, a dedicated detector Forward wall allows one to measure the emission angles and the charge states of projectile spectators and is used to determine the reaction plane. It covers a different phase space region than ECAL and the rest of HADES; therefore, auto-correlation is excluded by the definition. Projectile spectators are measured in the polar angle interval $0.34° < \theta < 7.4°$ and hits with charges of $Z \geq 1$ are used. The charge is used as weightw_i and the hit position determines the azimuthal angle $\phi_{FW,i}$:

$$Q_n \cos(n\Psi_n) = \frac{1}{N_{FW}} \sum_{FW,i} |Z_i| \cos(n\phi_{FW,i}),$$
$$Q_n \sin(n\Psi_n) = \frac{1}{N_{FW}} \sum_{FW,i} |Z_i| \sin(n\phi_{FW,i}).$$

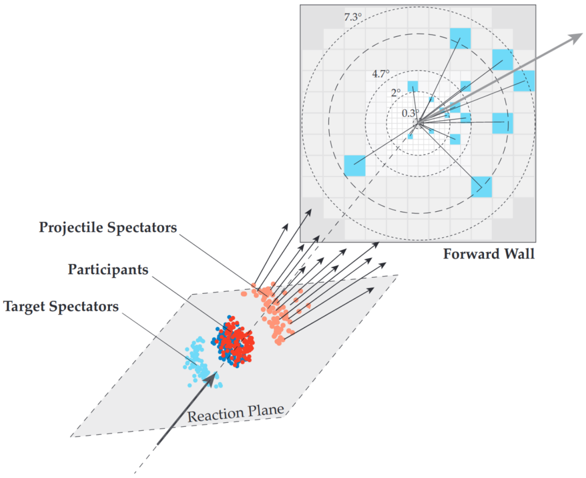

Figure 4.25: Sketch illustrating the event plane reconstruction using the projectile spectator hits recorded in the Forward Wall [52]

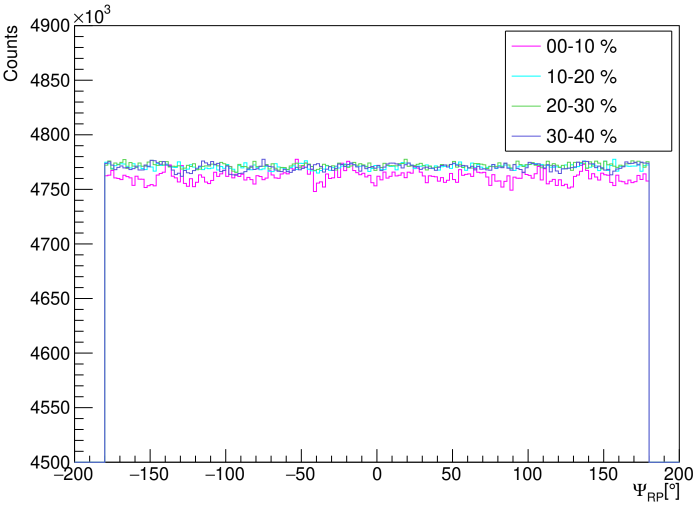

Figure 4.26: Distribution of the reconstructed event plane angle for the considered centrality classes up to 40 %. The event plane angle is reconstructed by determining a Q vector parallel to the impact vector. For the extraction, the Hydra class HParticleEvetChara is used. It includes a re-centering procedure for non-uniformities and a by-day dependent flattering procedure.

To account for the finite acceptance of the Forward wall detector, which causes anisotropy in the particle distribution, HADES uses the standard method of re-centering the positions X_{FW} and Y_{FW} by shifting first moments $(\langle X_{FW}\rangle, \langle Y_{FW}\rangle)$ and dividing them by the second moments $(\sigma_{X_{FW}}, \sigma_{Y_{FW}})$. An additional flattening procedure is used to remove residual non-uniformities [84].

A new angle is introduced.

$$\Psi_1' = \Psi_1 + \Delta\Psi_1, \tag{4.8}$$

where $\Delta\Psi_1$ equals:

$$\Delta\Psi_1 = \sum_n (A_n \cos(n\Psi_1) + B_n \sin(n\Psi_1)) \tag{4.9}$$

When asking for the vanishing of the n-th Fourier moment of the new distribution, the coefficients are expressed as:

$$\begin{aligned} A_n &= -\frac{2}{n}\langle\sin(n\Psi_1)\rangle, \\ B_n &= \frac{2}{n}\langle\cos(n\Psi_1)\rangle. \end{aligned}$$

In practice, the flattening procedure is of a few percent and does not affect the reaction plane resolution; instead, it improves the detector performance by accounting for imperfect calibration, dead channels, beam tuning, or any other asymmetry.

The event plane$\Psi_{EP,n}$ is defined as:

$$\Psi_{EP,n} = \arctan\frac{Q_{n,y}}{Q_{n,x}}. \tag{4.10}$$

As the orientation of the reaction plane is connected to the deflection of projectile spectators, the angle of the first-order event plane $\Psi_{EP,1}$ gives the highest possible resolution. It is used in all flow coefficients extracted v_n.

$$v_n^{obs} = \langle\cos[n(\phi - \Psi_{EP,1})]\rangle \tag{4.11}$$

The observed flow coefficients are always smaller than the real ones, since the calculated event plane will fluctuate around the reaction plane, thus decreasing the correlation between the particles. This fact can be considered by correcting the event plane with a resolution correction factor for each harmonic n.

$$v_n = \frac{v_n^{obs}}{\Re_n} \tag{4.12}$$

The resolution correction factor can be expressed as

$$\Re_n = \langle\cos[n(\Psi_{EP,1} - \Psi_{RP})]\rangle = \frac{\sqrt{\pi}}{2}\chi e^{-\chi^2/2}\left[I_{\frac{n-1}{2}}(\frac{\chi^2}{2}) + I_{\frac{n+1}{2}}(\frac{\chi^2}{2})\right], \tag{4.13}$$

where I_ν are the modified Bessel functions of order ν and χ is the resolution parameter [85]. The modified Bessel function of order n is given by

$$I_x(\chi) = \sum_{m=0}^{\infty}\frac{1}{m!\Gamma(m+x+1)}\Big(\frac{\chi}{2}\Big)^{2m+x} \tag{4.14}$$

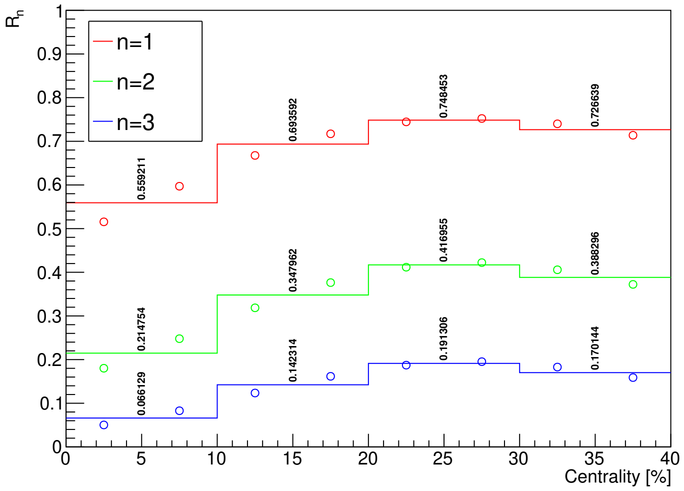

Figure 4.27: Event plane resolution $\Re_n$ for different harmonics of Fourier decomposition as a function of centrality. Open circles are for 5% bins and histogram lines for 10% centrality classes

The so-called sub-event method is used to calculate the values of $\Re_n$. The hits in the forward wall are divided with the same multiplicity into two sub-events, A and B, separated in phase space. From the correlation of the two resolutions for the sub-events:

$$\Re_n^{sub} = \langle \cos[n(\Psi_{EP,A(B)} - \Psi_{RP})] \rangle = \sqrt{\langle \cos[n(\Psi_A - \Psi_B)] \rangle} \tag{4.15}$$

By inverting Eq.4.13, the value of χ^{sub} can be extracted. Furthermore, the value of the resolution parameter for the whole Forward wall is calculated as $\chi = \sqrt{2}\chi^{sub}$, which is inserted again in Eq.4.13, which provides the full resolution $\Re_n$. The square root of 2 comes from the fact that the multiplicity of particles is $M/2$ and χ is proportional to $\sqrt{M}$. More details can be found in [86].

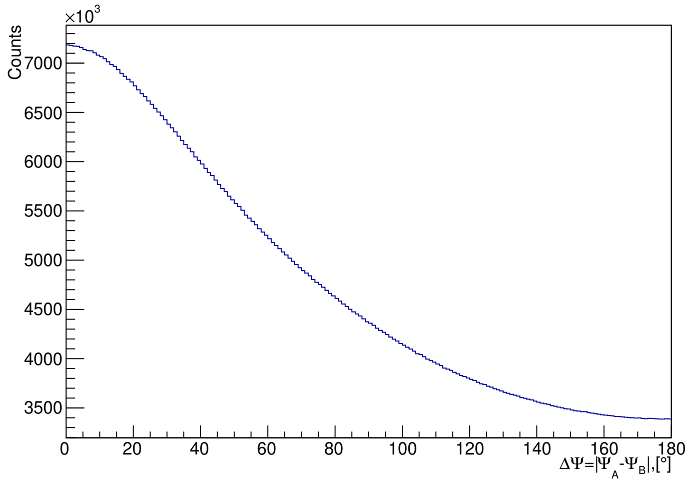

Figure 4.28: Distribution of $\Delta\Psi = |\Psi_{EP,A} - \Psi_{EP,B}|$ for the 0-10 % most central events.

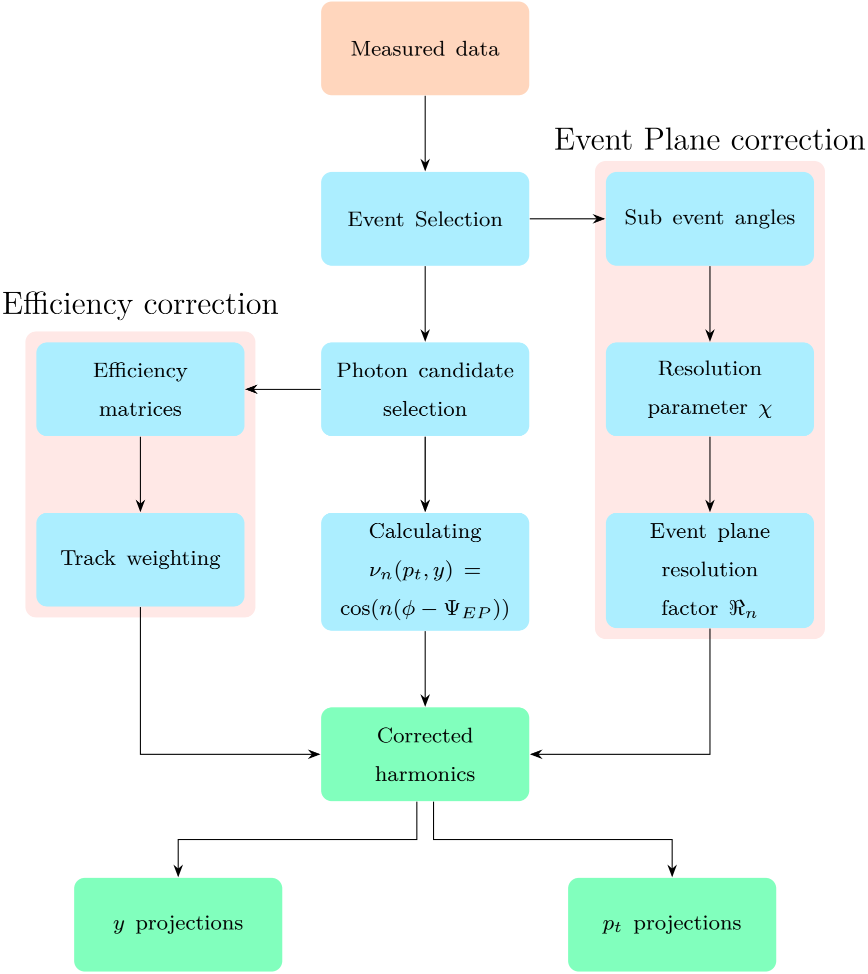

Figure 4.29: Flow chart of the analysis scheme of flow

The values obtained from 4.13 are shown in Fig.4.27 and summarized in Table 4.4.

Centrality	$0-10\%$	$10-20\%$	$20-30\%$	$30-40\%$
$\Re_1$	0.559	0.694	0.748	0.727
$\Re_2$	0.215	0.348	0.417	0.388
$\Re_3$	0.066	0.142	0.191	0.170

Table 4.4: Resolution correction factors.

4.8.1 Multidifferential neutral pion analysis

Reconstructed diphoton pair distribution $dN(p_t, y, \mathcal{C})/\Delta\phi$ are examined in different phase space regions in p_t and y as well as centrality class $\mathcal{C}$. The number of extracted π^0 is different $\Delta\phi = \phi - \Psi_{EP}$ bins. This distribution is further fitted with a Fourier decomposition:

$$\frac{dN(p_t, y, \mathcal{C})}{\Delta\phi} = \frac{N}{2\pi}(1 + 2v_1^{obs}\cos\Delta\phi + 2v_2^{obs}\cos 2\Delta\phi). \tag{4.16}$$

The extracted coefficients should also be normalized by the resolution of the event plane, summarized in Table 4.4.

The flow extraction procedure was first tested with a simulation model. The closure test is shown in Fig.4.30. The UrQMD flow is shown with a dark blue line. The tracks were further analyzed with Geant and HYDRA algorithms. The experimental extraction method of π^0 , described above, was applied to obtain the data points shown with black dots. Additional information from the simulation was used to plot the true data with light blue dots. Finally, the black points were fitted to extract the flow coefficient.

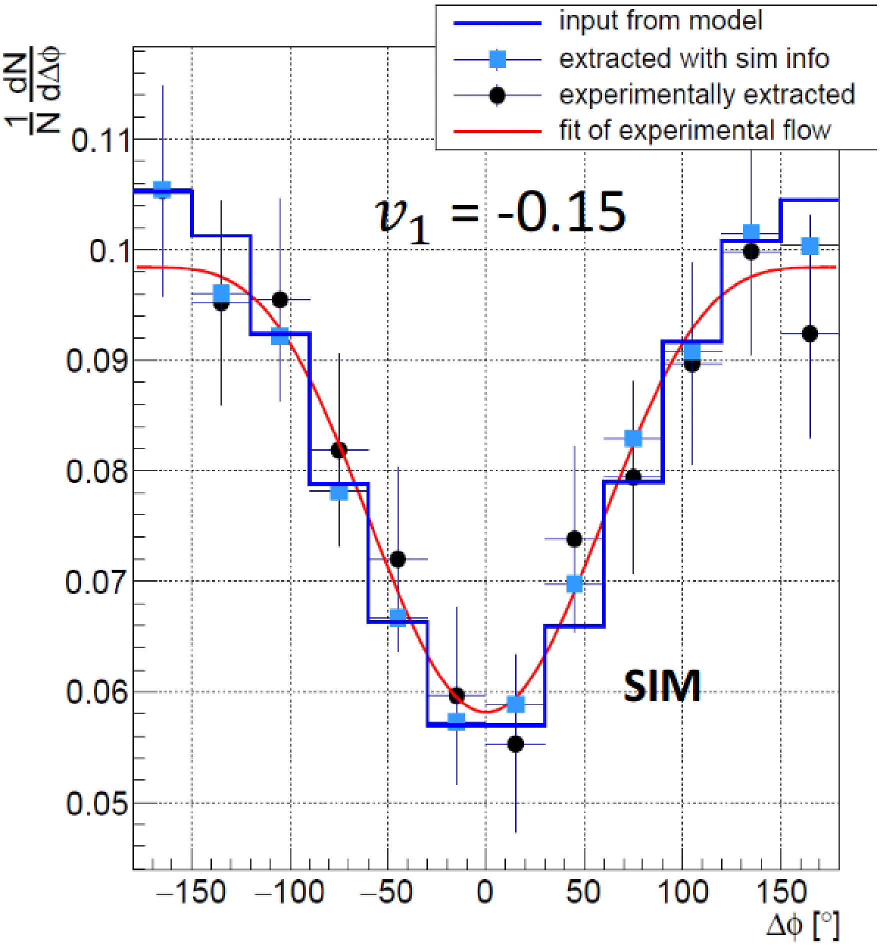

Figure 4.30: An example of reconstructed flow in $p_t \in (300-500)$ MeV, $y_{cm} \in (0.5-0.7)$, centrality $20-30\%$. The dark blue solid line histogram shows the original UrQMD model distribution, light blue squares show the best-case extraction yield using real photons, black dots represent the extraction method used in the experiment using the event-mixing technique, and the red line represents the fit of the black dots.

The angle of the reaction plane is determined with finite resolution; therefore, the extracted flow coefficient is smeared by that resolution. However, the flow method testing was performed using an exact angle of the reaction plane to avoid any correlation. The generator reaction plane is always zero with infinite precision.

The standard extraction procedure for different phase-space bins is shown in Fig.4.31.

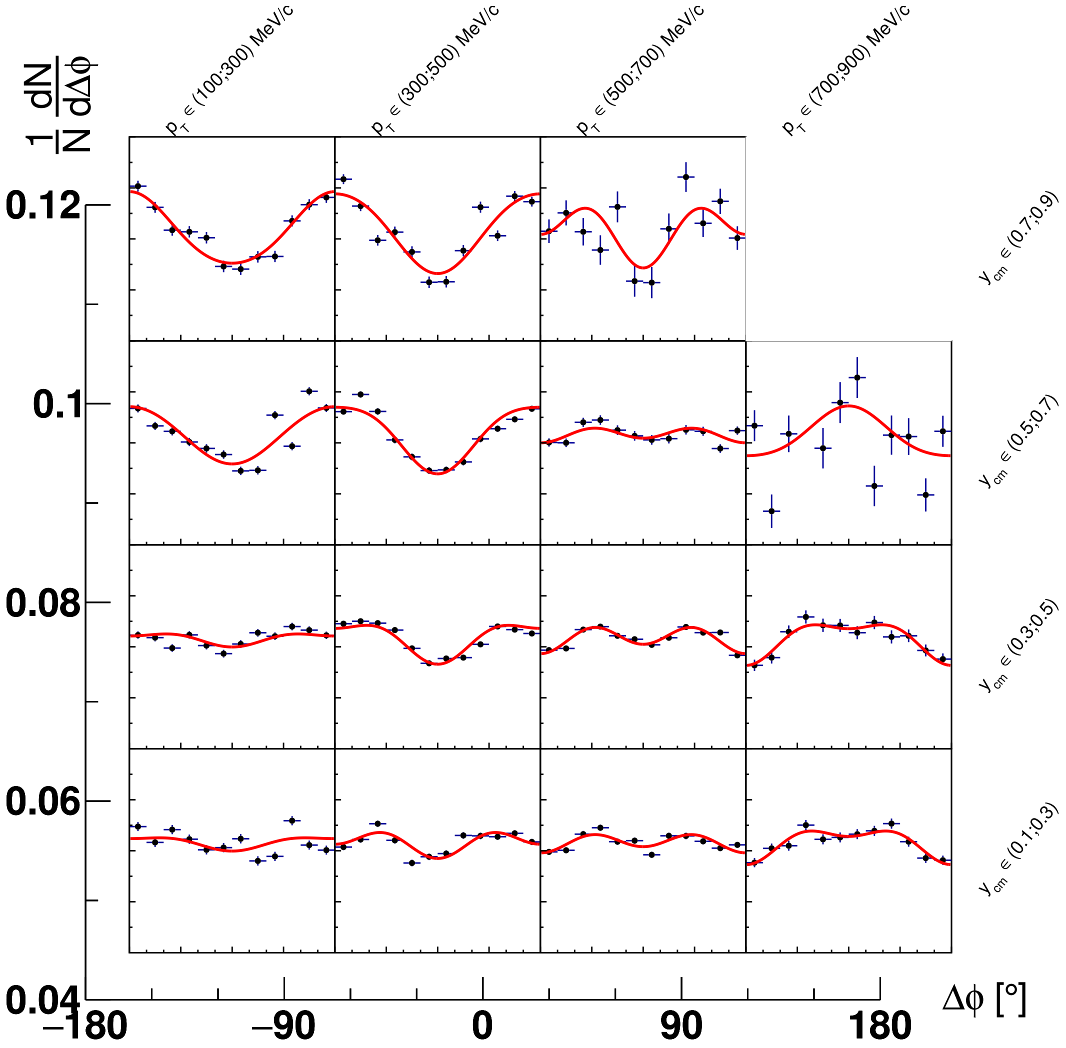

Figure 4.31: π^0 normalized azimuthal angle distributions w.r.t. event plane for centrality class 20 - 30 %, fit is done with a function 4.16.

4.8.2 Systematics errors of π^0 yield

Systematic error evaluation can be notorious and difficult. "Systematic effects" is a general category that includes effects such as background, selection bias, scanning efficiency, energy resolution, angle resolution, variation of counter-efficiency with beam position and energy, dead time, etc. [87]. This is the definition used in this thesis to estimate systematic errors. There is a good article that covers the principles of systematic errors and how not to overestimate them [88].

Several variations were made for the systematic uncertainty assessment to compare the final results and calculate the deviations.

The total systematic error is equal to the sum of errors for each phase-space bin:

$$\sigma_{total\ sys} = \sqrt{\sum_{groups} (N - \overline{N}_{var})^2}, \tag{4.17}$$

where N is the reconstructed number of π^0 , $\overline{N}_{var}$ is the average over variations in a group.

Many checks have been performed using the following sources of systematic errors, each of which includes at least two variations within a systematic group.

- Photon velocity cut β_{ECAL}
- Minimum energy of the cluster
- Maximum cluster size
- Diphoton mass histogram binning
- Minimum opening angle
- Number of p_t bins
- Number of y_{cm} bins
- Background normalization
- Different π^0 window integration
- Sector combination
- Matching the ECAL and RPC times
- Quality of matching in space between ECAL and track hit positions
- Data subset
- Transverse momenta extrapolation
- Rapidity extrapolation

All checks show consistent results within each phase-space bin whenever comparing is possible. For example, a higher energy cut or sector exclusion can reduce acceptance; thus, some low $p_t - y$ bins are not considered for comparison.

The efficiency of photons had the most significant effect on systematic uncertainty. It can be estimated by varying the RPC time window for charge tracks, track positioning and matching with ECAL, and timing information. The systematic errors are shown in Fig.5.8 and Table 5.1.

	% of N_{π^0}
min. opening angle	3
velocity cut	13.8
RPC time match	0.7
track match	1
max. cluster size	0.5
number of mass bins	0.5
minimum photon energy	0.6
background subtraction	5.6

Table 4.5: An example of summary table of the influence of individual systematic groups on π^0 yield for one phase-space bin.

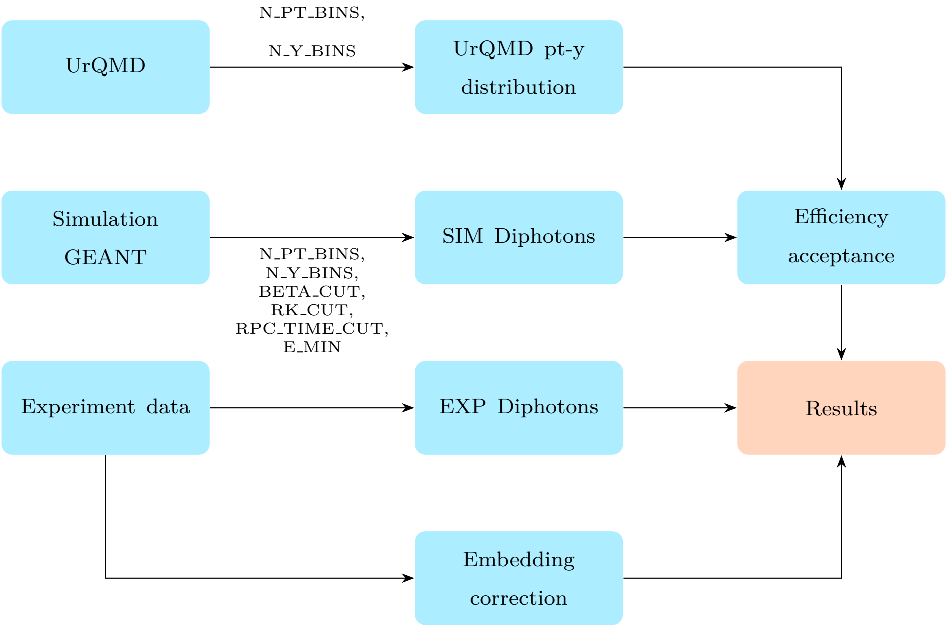

Figure 4.32: Flow chart of the systematic error scheme.

4.8.3 Systematic uncertainties of π^0 flow

For the systematic uncertainty of the flow coefficients, two additional methods were used in addition to the usual standard fitting method. The second method uses the invariant mass method proposed in [89]. The invariant mass distribution consists of the background (uncorrelated and other particle species)and the signal(peak in the spectrum). $N_{cand}(m_{inv}) = N_S(m_{inv}) + N_B(m_{inv})$. Furthermore, the decomposition of the flow harmonic n can be done for the observed mean value over all candidates in events.

$$v^{obs}_{n,S+B}(m_{\gamma\gamma}) = \langle \cos[n(\phi - \Psi_1)] \rangle (m_{inv}) \tag{4.18}$$

$$v^{obs}_{n,S+B}(m_{\gamma\gamma}) = v^{obs}_{n,S}(m_{\gamma\gamma}) + v^{obs}_{n,B}(m_{\gamma\gamma}), \tag{4.19}$$

with the assumption that $v^{obs}_{n,B}(m_{\gamma\gamma})$ is a polynomial function $\sum_i p_i m^i_{inv}$.

The TProfile histogram is filled with $\langle \cos[n(\phi - \Psi_1)] \rangle (m_{inv})$ for each diphoton track. The histogram for the invariant mass of two photons is filled in parallel, using both same-event and mixed-event techniques. Then the signal-to-background ratio is calculated based on these usual histograms and then used to fit TProfile to $v^{obs}_{n,S}(m_{\gamma\gamma})$. For the second term, the third-order polynomial is used for the fitting $v^{obs}_{n,B}(m_{\gamma\gamma})$.

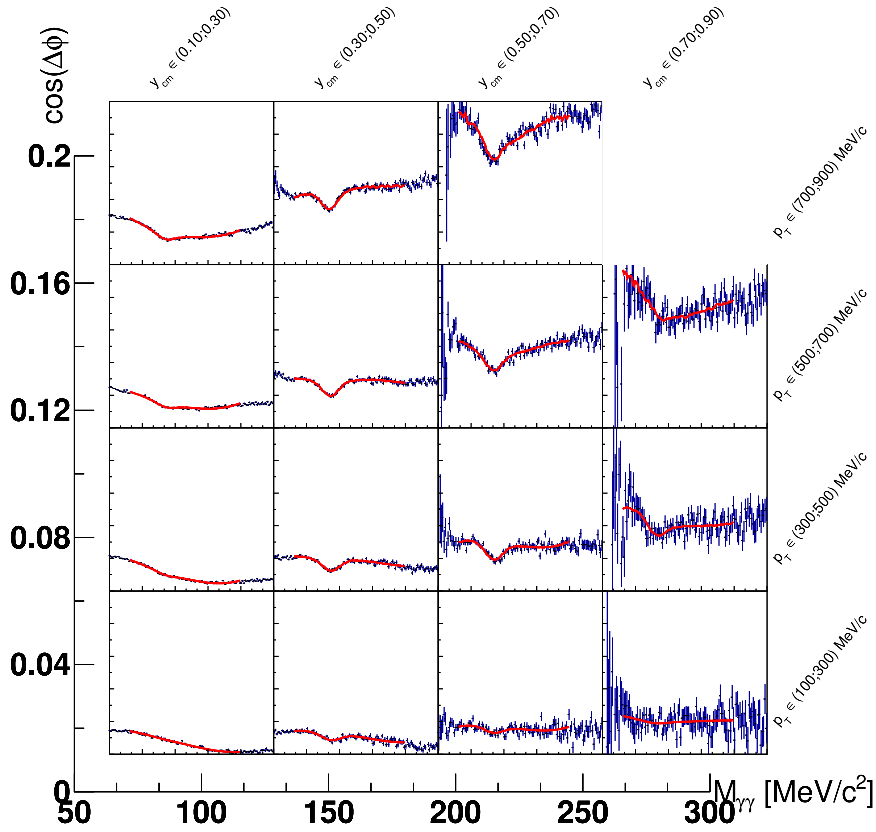

Figure 4.33: Mean values of $\cos(\phi - \Psi_1)$, fit is done with a function 4.19 .

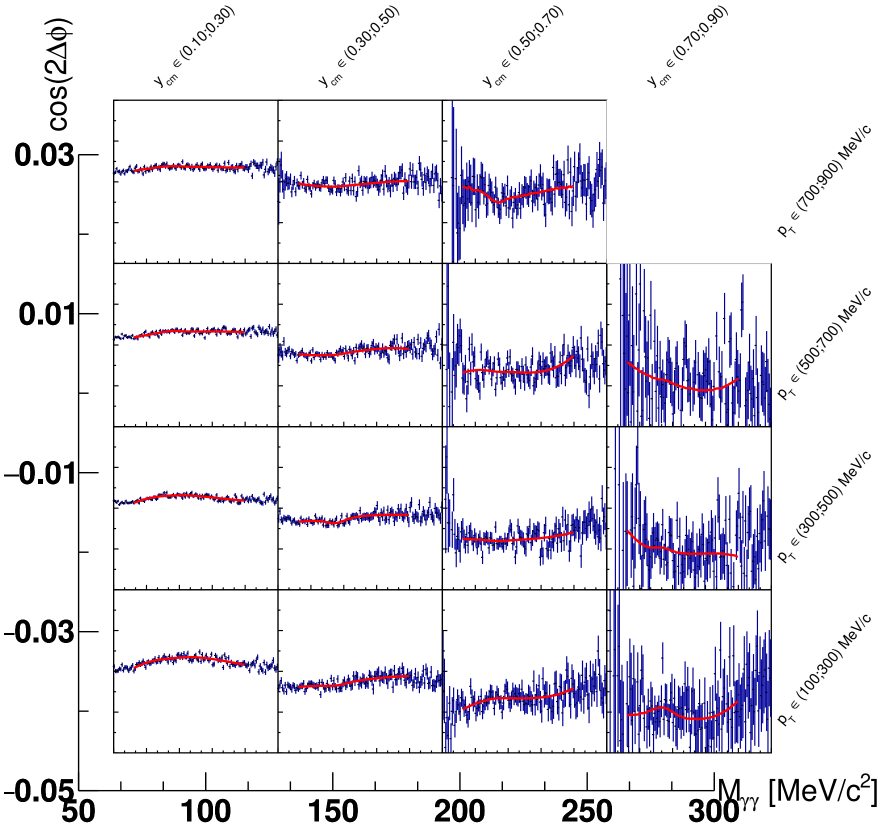

Figure 4.34: Mean values of $\cos(2(\phi - \Psi_1))$, fit is done with a function 4.19 .

The third method involves the distribution of the azimuthal angle in quarters with respect to the event plane[90].

$$
\begin{aligned}
R_{in-plane} &= \frac{N_0}{N_{180}}, \\
R_{squeeze} &= \frac{N_{90} + N_{270}}{N_0 + N_{180}},
\end{aligned}
$$

where N_m is the number of reconstructed π^0 in the 90° bin around its middle value m. Using these quantities, one could construct v_n^{obs}

$$
\begin{aligned}
v_2^{obs} &= \frac{1}{2}\frac{1 - R_{squeeze}}{1 + R_{squeeze}}, \\
v_1^{obs} &= \frac{1}{2}\frac{(1 + 2v_2^{obs})(R_{in-plane} - 1)}{1 + R_{in-plane}},
\end{aligned}
$$

The consistency test for all three methods is shown in Fig.4.35 and is the largest part of the systematic error.

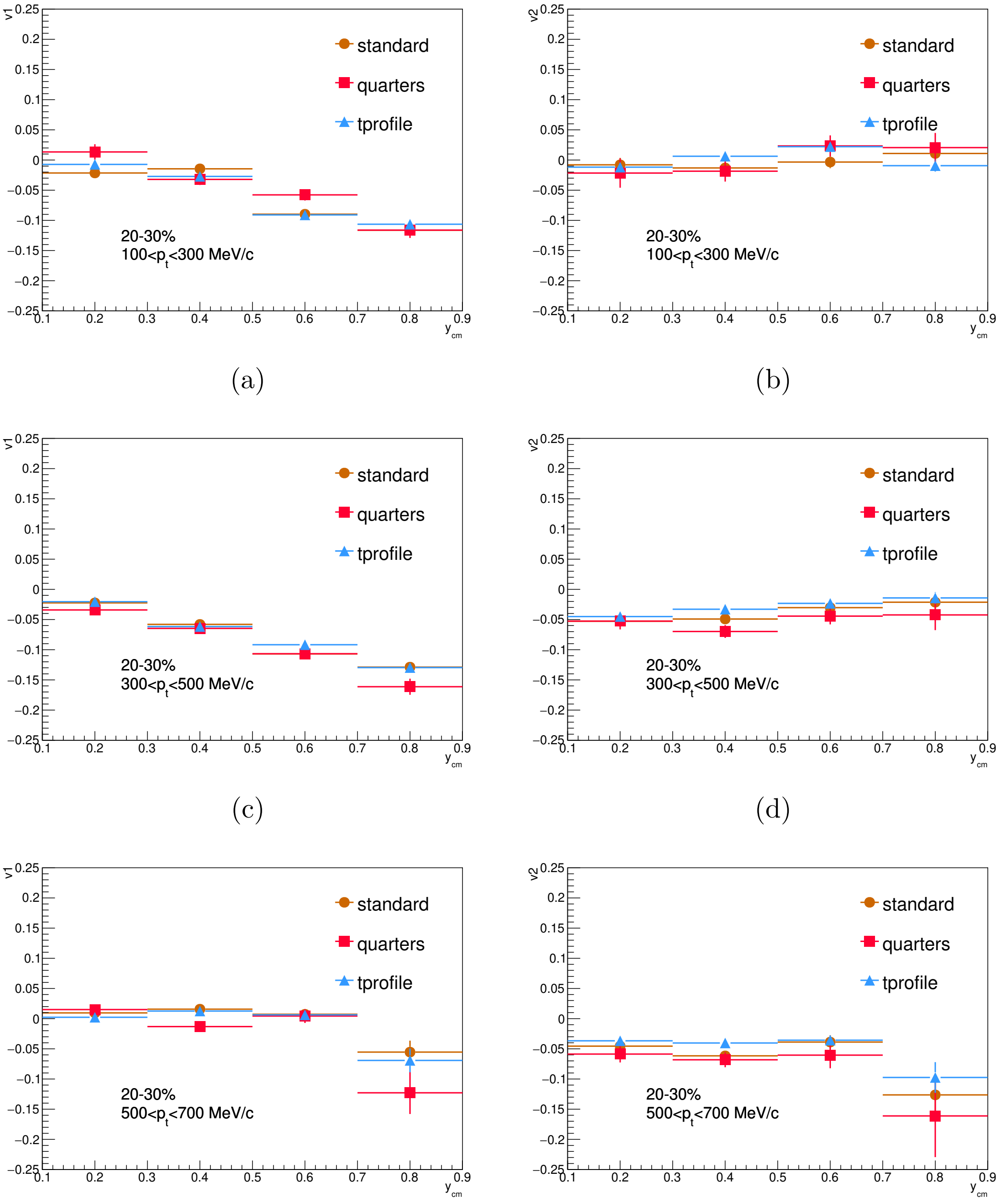

(a) (b)

(c) (d)

(e) (f)

Figure 4.35: Comparison of different flow methods for π^0 for centrality $20-30\%$. Dots represent the standard method, squares for the invariant mass method, and triangles for the quarter method.

4.8.4 Background flow effect

It was also found that there was a non-zero flow of background. This effect was checked in simulations using Geant information for true π^0 tracks (shown in Fig.4.36) and for the background when there is only a combinatorial background (shown in Fig. 4.37. This effect of combinatorial background flow was also present in the experimental data in Fig.4.38. It seems that one of the two photons is carrying the information from the π^0 about its flow to some degree.

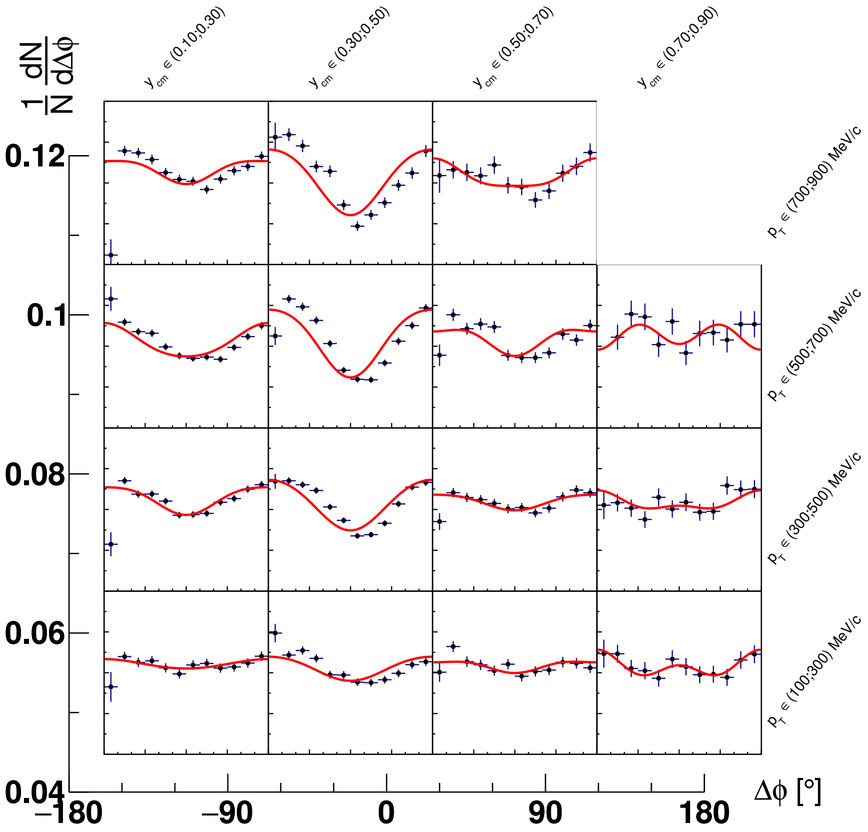

Figure 4.36: Simulation check flow of true π^0 tracks for 20-30% centrality

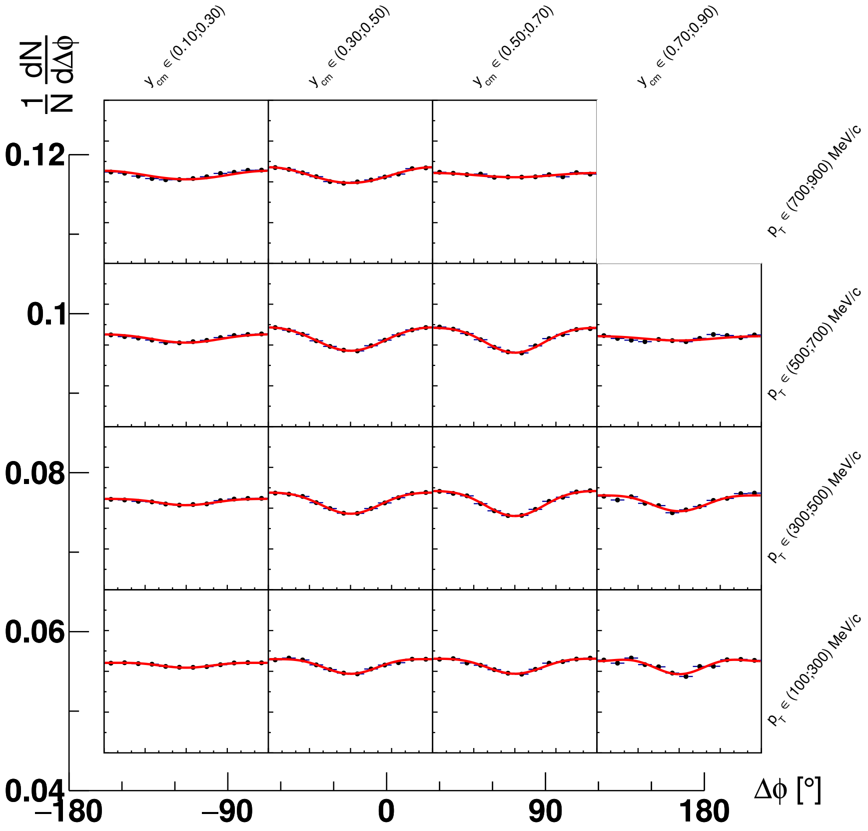

Figure 4.37: Simulation check flow of background tracks for 20-30% centrality

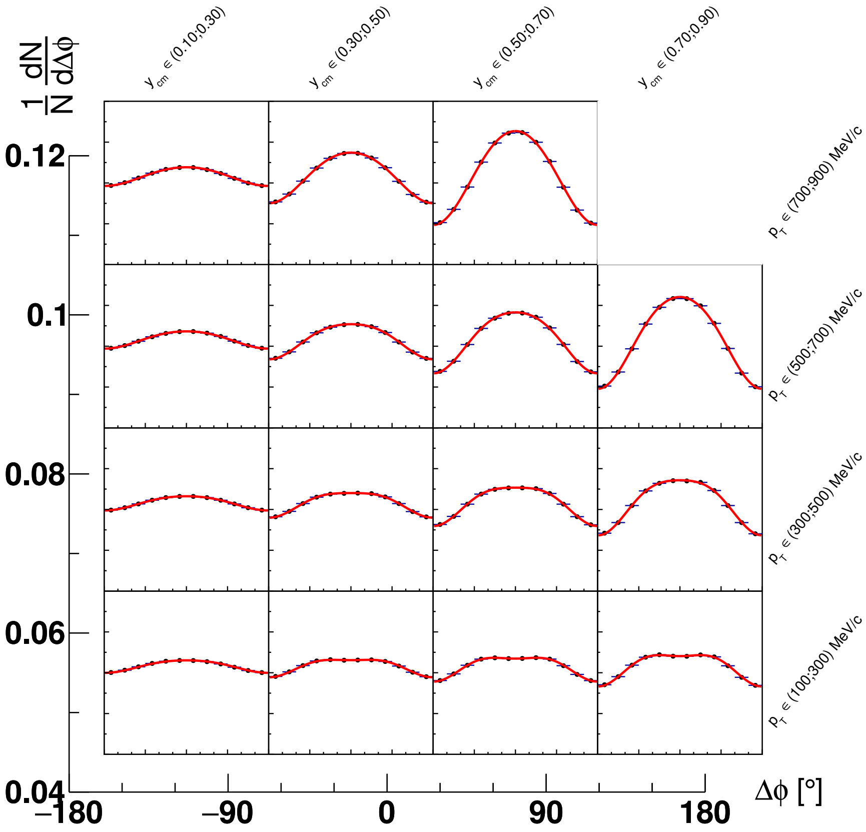

Figure 4.38: Flow of background tracks for 20-30% centrality in experiment.

5. Results

In this chapter, π^0 yields fully corrected for the acceptance and efficiency of the spectrometer, as a function of the transverse momentum and rapidity, are presented, and they are compared to the yields of charged pions determined in the same experiment. The total pion multiplicity is also compared with the world data from different experiments, and various systematic effects are discussed. The last section contains a flow study of neutral pions along with its natural comparison to the flow of charged pions and to model predictions.

5.1 Production yields and inverse-slope parameter

The resulting fully corrected for efficiency and acceptance (see Section 4.6) neutral pion p_t spectra with systematic errors are shown in Figs.5.1, 5.2 and 5.3.

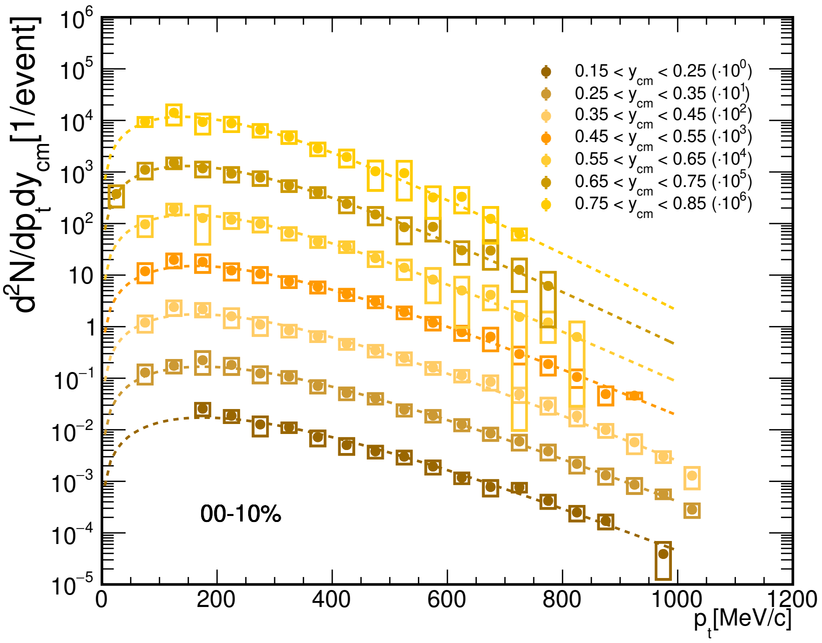

Figure 5.1: Yields for 0-10% centrality. Transverse momentum distributions of the neutral pion in the rapidity bin of width $dy = 0.1$ between 0.15 and 1.05 corrected for efficiency and acceptance. The most backward rapidity bin is shown unscaled, whereas the following rapidity slices are scaled by a successive factor of 10.

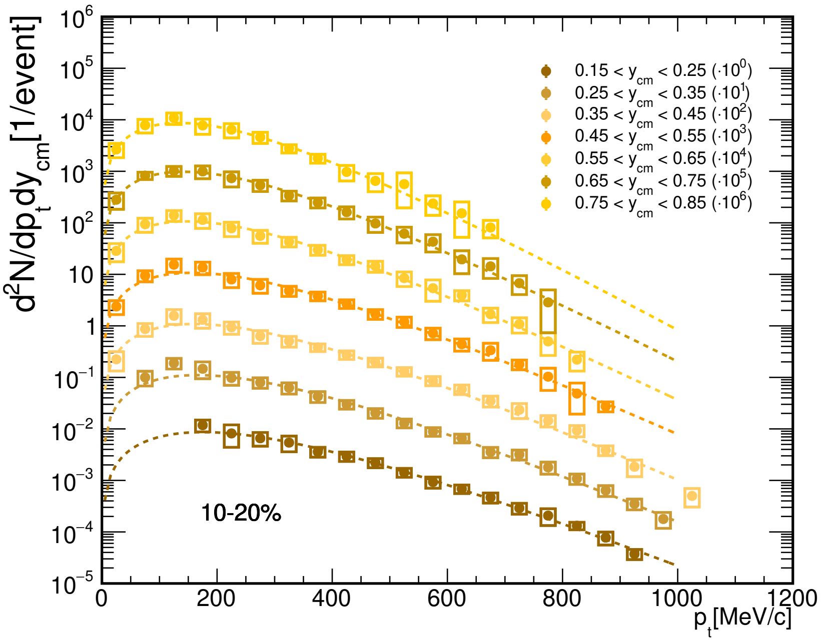

Figure 5.2: Yields for 10-20% centrality.

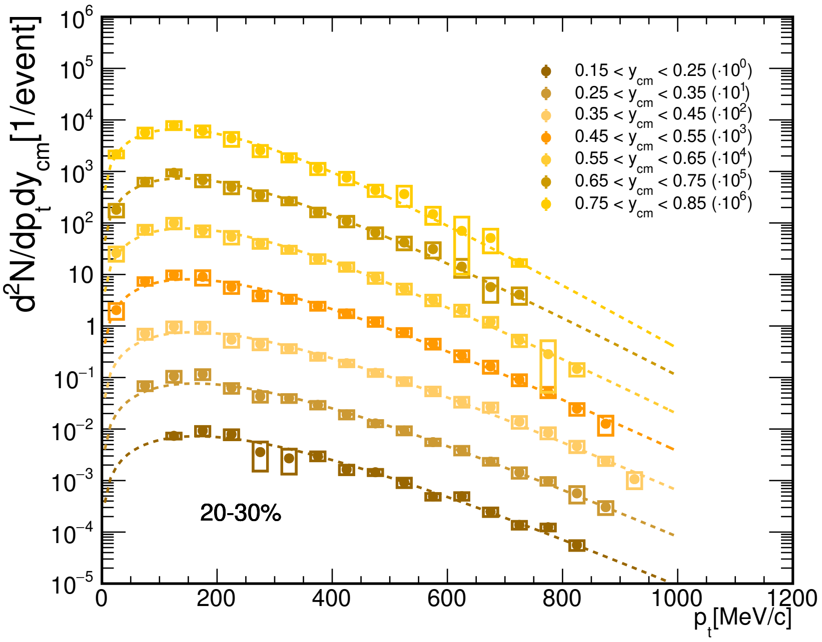

Figure 5.3: Yields for 20-30% centrality.

For the extraction of the inverse slope parameter, the p_t spectra are fitted with a single-slope Boltzmann distribution function(see Appendix B):

$$\frac{d^2N}{dp_t dy} = C p_t m_t \cosh y \exp\Big(-\frac{m_t \cosh y}{T_{kin}}\Big), \tag{5.1}$$

where N is a number of particles in a given phase space, p_t is transverse momenta, y is rapidity, $m_t = \sqrt{p_t^2 + m^2}$ is a transverse mass, and T_{kin} is an inverse slope parameter.

The measured value at mid-rapidity is defined as the effective temperature T_{eff} of an isotropically emitting thermal source. The distribution can be described by an inverse cosh dependence as a function of rapidity, relating T_{eff} to the kinetic freeze-out temperature T_{kin} in a thermalized system as follows:

$$T_{kin}(y) = \frac{T_{eff}}{\cosh{(y)}} \tag{5.2}$$

where $T_{kin}(y)$ is the inverse slope parameter in each differential spectrum p_t. In Fig.5.4 closed circles represent the measured data, and the open circles are reflected around the midrapidity. The histograms with the inverse slope parameter are fitted with a function $C/\cosh(y)$, and the resulting T_{eff} for each centrality is shown under the fit.

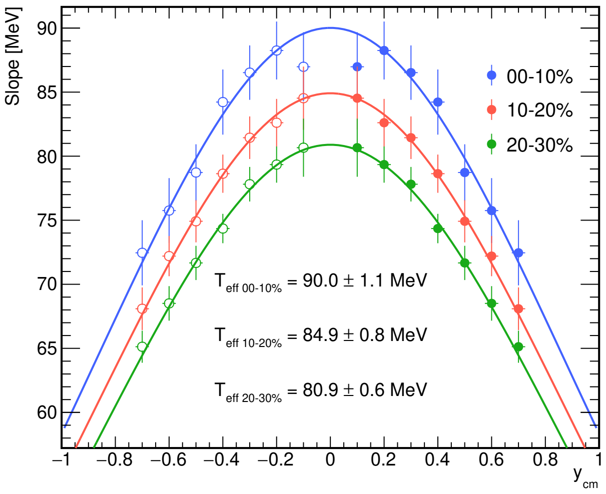

Figure 5.4: Inverse slope parameter as a function of rapidity. Solid curves represent the fits.

5.1.1 Neutral pion yields and comparison with charged pions

To validate the reconstructed π^0 multiplicity, one can compare it with the multiplicity of charged pions. Charged pions were identified in HADES using their velocity information in the 30% most central events in the same experiment. The details are described in [91] and the corresponding analysis is not part of this thesis. The main results of their study together with my π^0 data are shown below for three regions of centrality. Extrapolation to unmeasured phase-space regions using a Gaussian fit and integration over this spectrum gives $M(\pi^{\pm})$ per centrality class. It is worth mentioning, that due to isospin conservation, the ratio of charged to neutral pions in a symmetric system has to be [92]:

$$M(\pi^0) = \frac{M(\pi^+) + M(\pi^-)}{2} \tag{5.3}$$

As an example, in Figs.5.5, 5.6 and 5.7 the π^0 p_t spectrum is compared to charged pions. The low p_t bins are fluctuating due to the problems with a background subtraction and detector setup as discussed in section 4.7. Nevertheless, one can conclude that the p_t spectrum of charged pions is in agreement with that of neutral pions for p_t above 250 MeV/c.

Charged pions have much greater acceptance, whereas ECAL covers only the forward rapidity region for the given colliding system. The extrapolation of the neutral pion yield in transverse momentum was performed using a single-slope Boltzmann distribution according to equation 5.1.

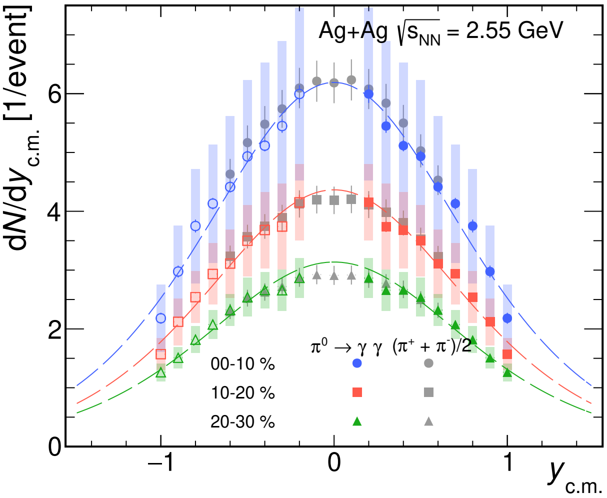

Figure 5.8: Transverse momentum integrated distributions of the neutral and charged pions. The colored points represent neutral pion yields, while the gray points represent the average of charged pions. Systematic errors are shown as colored boxes, and statistical errors are shown in vertical lines.

Since ECAL covers only the forward rapidity region, the integrated p_t yields for the given rapidity range are further reflected around the midrapidity, since there should be no difference between the backward and forward rapidity regions due to the symmetry of the yield. The resulting histograms of dN/dy_{cm} are shown in Fig.5.8. The fit function is the following (for details, see Appendix B):

$$\frac{dN}{dy} = CT\exp\Big(-\frac{m_{\pi^0}\cosh y}{T}\Big)\left({m^2}_{\pi^0} + 2m_{\pi^0}\frac{T}{\cosh y} + 2\frac{T^2}{\cosh^2 y}\right) \tag{5.4}$$

To extract the total number of π^0 per event, it is necessary to extrapolate the data to the full phase space. The data in a given rapidity range is extrapolated with equation 5.1 to cover the full transverse momentum. This fit is mostly used to obtain the values for the lowest p_t bins whenever data is missing, as well as missing points in the end p_t spectrum, see Fig. 5.1, 5.2 and 5.3.

The results obtained for π^0 yield, as seen in Fig.5.8 and Table 5.1, are in good agreement with the charged pions within the systematic errors. This direct measurement of π^0 allows one to reduce the common systematic error of the average of two results: obtained via two-photon decay and via the average of

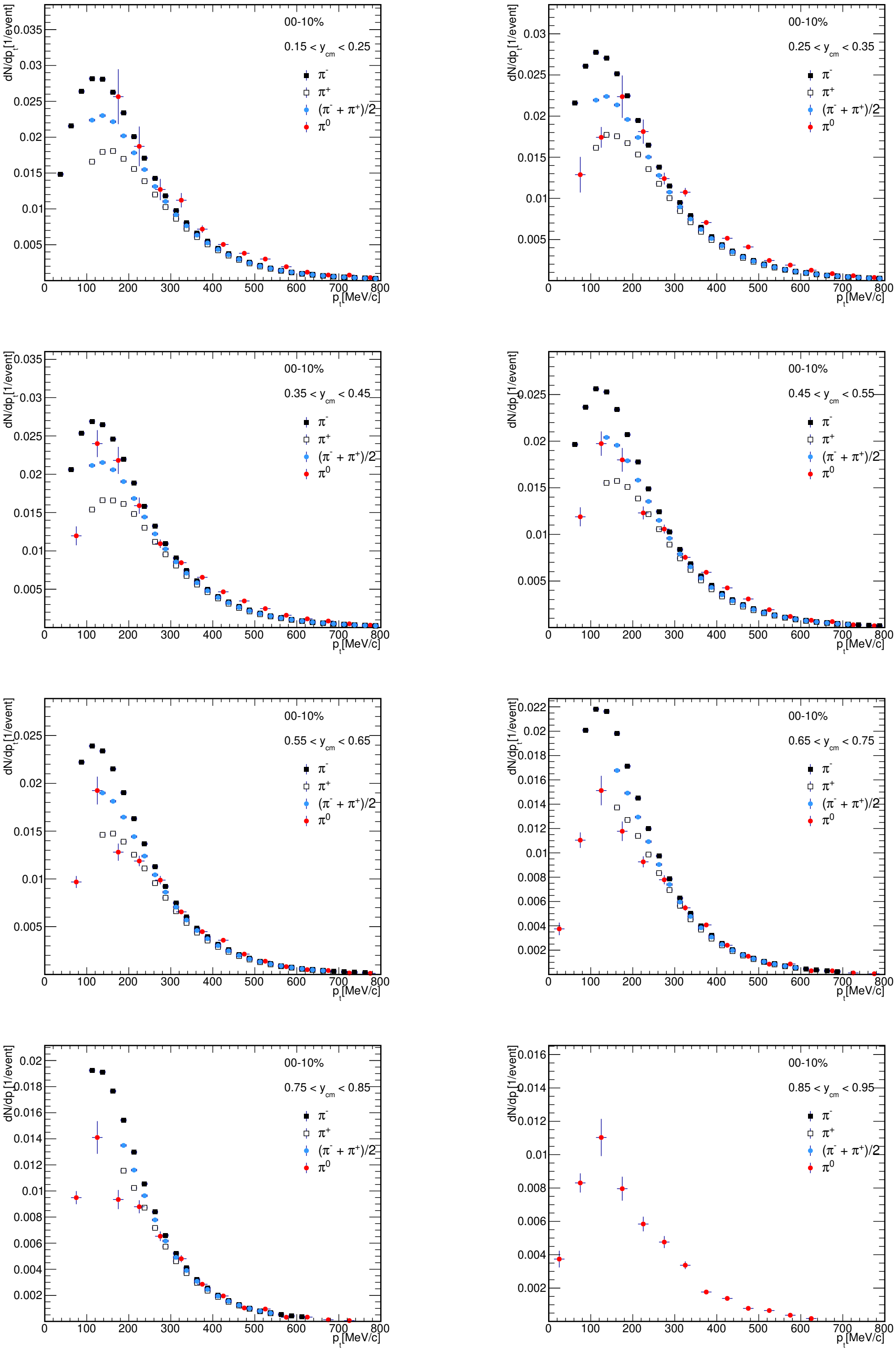

Figure 5.5: Comparison of π^0 yield to charged pions in linear scale for 0-10% centrality.

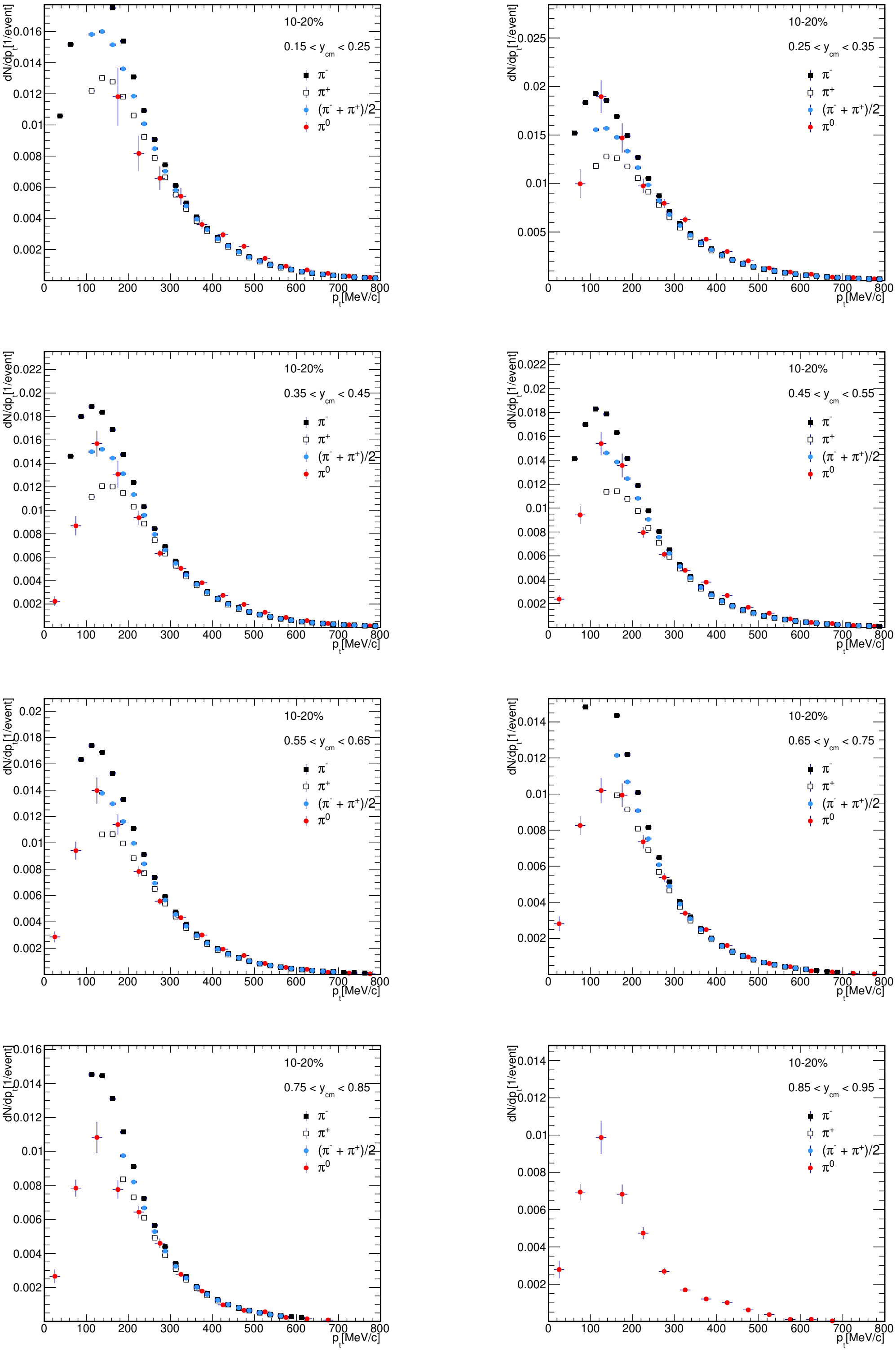

Figure 5.6: Comparison of π^0 yield to charged pions in linear scale for 10-20% centrality.

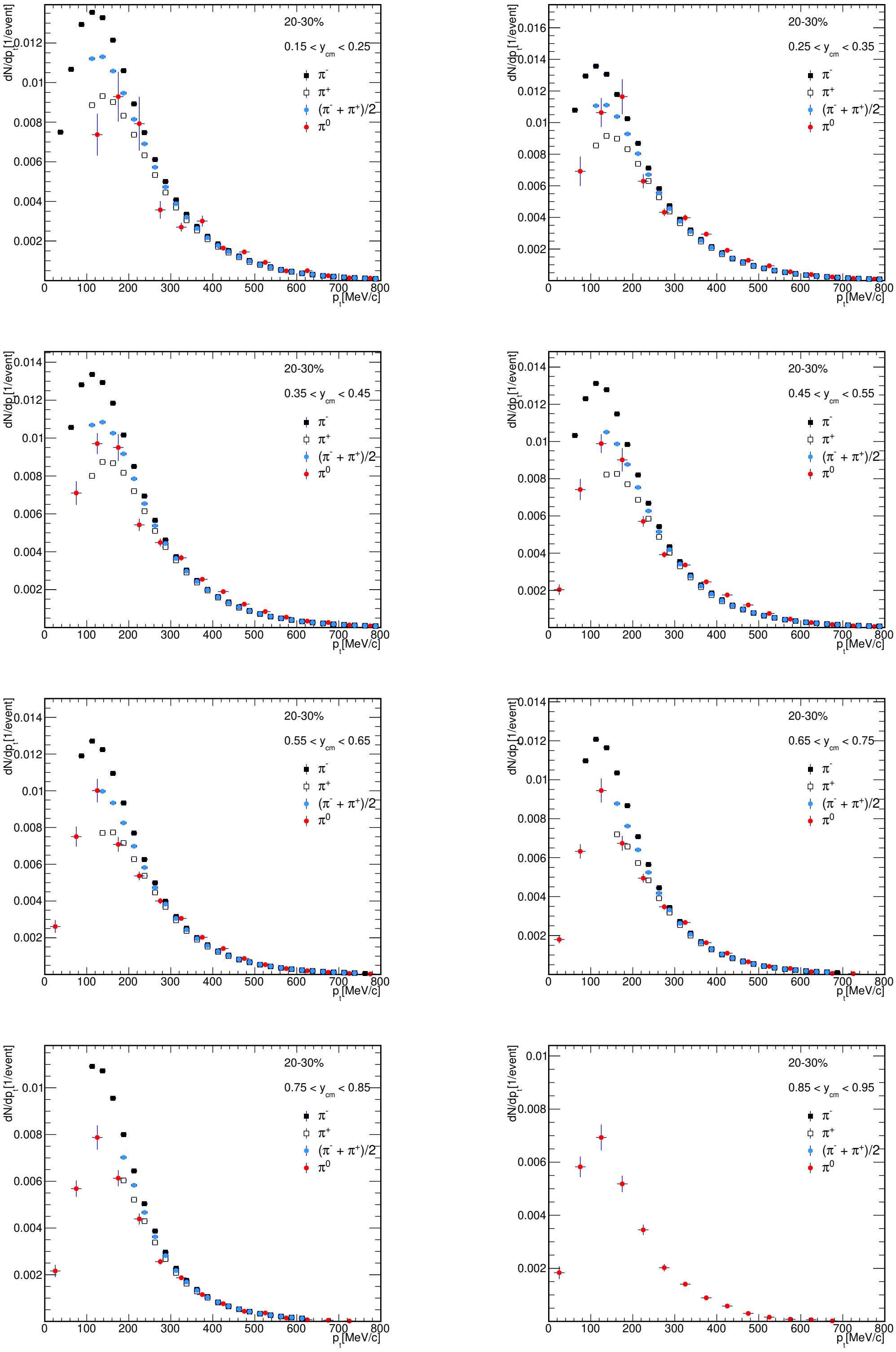

Figure 5.7: Comparison of π^0 yield to charged pions in linear scale for 20-30% centrality.

charged pions. The total π^0 yield is used in HADES collaboration for the realistic description of cocktail and normalization of dileptons in the Ag+Ag experiment.

Centrality	$M(\pi^0)$	$1/2(M(\pi^+) + M(\pi^-))$	$M(\pi)/A_{part}$
00-10 %	11.9 ± 3.2	11.8 ± 1.3	$35.2/160.9 = 0.219$
10-20 %	8.3 ± 1.5	8.2 ± 0.9	$24.7/114.5 = 0.216$
20-30 %	6.1 ± 0.75	5.9 ± 0.7	$17.9/81.1 = 0.220$

Table 5.1: Pions production yields for the three centrality classes in 0-30 %.

Our resulting pion multiplicity per participant, see Table 5.1, is compared with those obtained for different collision energies and systems in Fig.5.9 The fitted curves of a second-order polynomial show the excitation function; they are taken from [20].

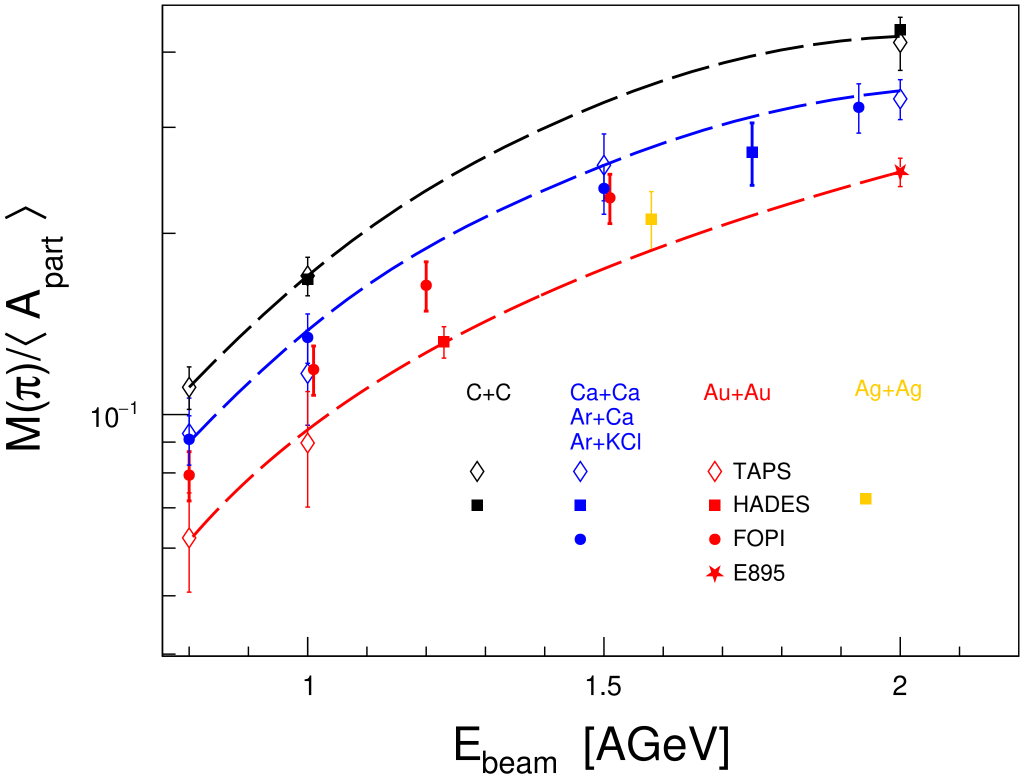

Figure 5.9: Pion multiplicity per participant as a function of beam energy for four different systems: C + C (black) [93], Ar + KCl (blue) [94], and Au + Au (red) [20]. The obtained results for Ag+Ag collisions are plotted in orange. The curves are polynomial fits to these data used to interpolate the multiplicities as a function of bombarding energy for corresponding systems

5.2 Flow

As the centrality of the collision decreases, the flow must increase. Therefore, the most peripheral bin that was studied, i.e. the 20-30% centrality range, will be further focused upon. In addition, it has the highest event plane resolution, which in turn affects the error bars, see Fig.4.27. Results for other two bins 0-10 % and 10-20% are shown in Appendix D and E. The results of the multidifferential flow with systematic errors versus rapidity in different transverse momentum bins are shown in Fig.5.10. The directed flow changes its slope versus rapidity with increasing transverse momentum in Fig.5.10(a). The detailed comparison of directed flow for different p_t bins is given in Fig 5.10(c). At low p_t, the directed flow has a negative slope, at mid p_t the $v_1 \approx 0$, and at high transverse momentum, the slope of the directed flow is slightly positive. It is seen that there is almost no dependence of the elliptic flow on rapidity in Fig.5.10(b) and that it saturates at a constant level with increasing transverse momentum in Fig.5.10(d). However, this raw information is not very useful without a proper comparison with other particles, such as charged pions and simulation models, which is described in the next section.

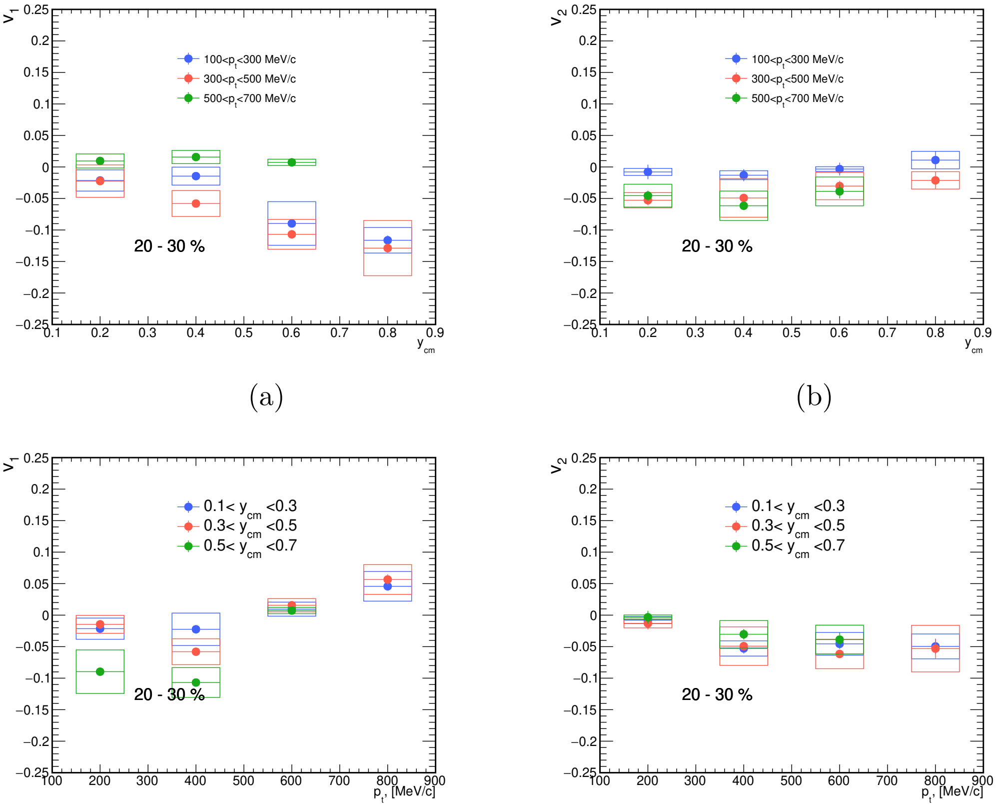

(a) (b)

(c) (d)

Figure 5.10: Results for flow 20-30%

5.2.1 Comparison with Models

Next, the obtained experimental π^0 results are compared with the models. For comparison of the experimental results, several model simulations were performed using dynamical models, see Section 1.7.2, namely:

UrQMD with EoS for UrQMD v3.4 with a hard Skyrme equation of state. The hard Skyrme equation of state assumes a high compressibility of nuclear matter, which leads to a stiff equation of state. This, in turn, leads to a rapid increase in the pressure of the system as the density increases, resulting in a faster expansion of the system and a shorter duration of the high-density phase of the collision. Moreover, it has been shown that the use of this equation of state can reproduce some of the experimental observables, such as the transverse momentum spectra and the elliptic flow of particles produced in heavy-ion collisions.

UrQMD cascade for UrQMD v3.4 running in cascade mode, with no additional potentials such as Coulomb, Symmetry, or Skyrme.

GiBUU for GiBUU version 2022 with non-relativistic Skyrme-type potentials, which is based on a semi-phenomenological model that includes density-dependent terms to simulate the compression and expansion of the system. The configuration parameters adopted were based on the 2014 Shanghai meeting, where a soft momentum-independent equation of state with a value of $K = 240$ MeV and Coulomb potential switched on were utilized.

As shown in Fig.5.11, all models predict trends similar to the experimental data. The directed flow v_1 from the UrQMD cascade is not consistent with data at high transverse momentum. On the contrary, the directed flow v_1 from UrQMD with EoS and GiBUU models follow the experimental trend very well. For v_2, the UrQMD with EoS model agrees well with the data, while the GiBUU and UrQMD cascade shows an almost negligible zero elliptic flow. A similar picture is reproduced for different centralities shown in the Appendix E.

Therefore, the best model to describe the experimental data was chosen **UrQMD with EoS**. It is worth mentioning that this model was tuned for the flow of different experimental data and contains phenomenological parameters.

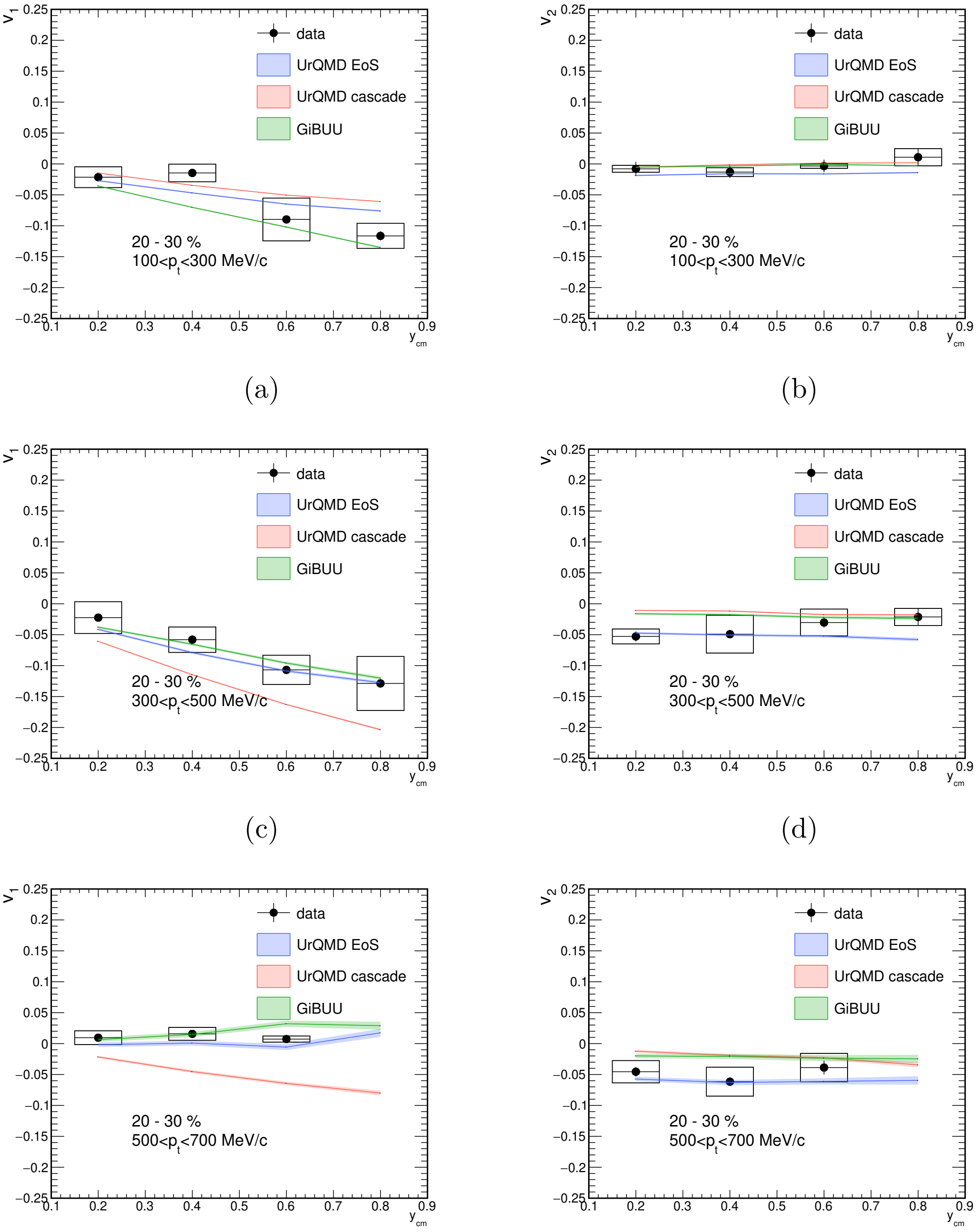

(a) (b)

(c) (d)

(e) (f)

Figure 5.11: comparison of the π^0 results from data and the predictions of the flow for three models - **UrQMD cascade**, **UrQMD with EoS**, and **GiBUU**. Left plots show directed flow; right plots show elliptic flow

5.2.2 Charged pion flow comparison

The charged pion analysis was carried out mainly by M. Nabroth [91]. The results for charged pions together with my data for neutral pions for directed and elliptic flow are presented in Fig.5.12 and Fig.5.13 versus rapidity and transverse momentum, respectively. The π^+ and π^- have a similar flow, while they differ from π^0 for some phase-space bins. For example, v_1 of neutral pions is stronger in the p_t bin up to 300-500 MeV/c, see Fig.5.12(c). The elliptic flow of π^0 has a similar dependence to p_t in Fig.5.12 for all rapidity ranges, with no significant differences from charged pions.

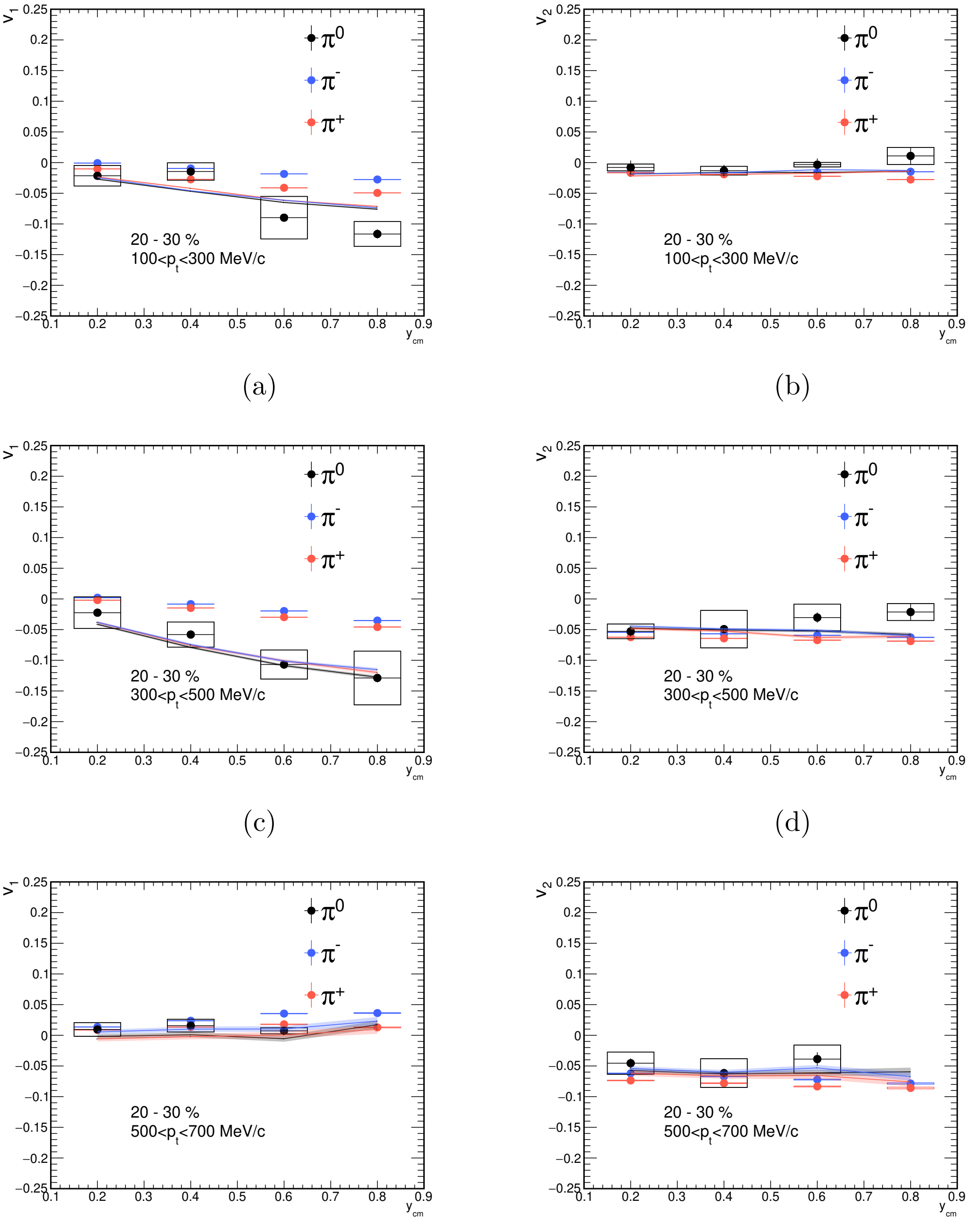

(a) (b)

(c) (d)

(e) (f)

Figure 5.12: Neutral pion flow comparison with charged pions versus rapidity. Transparent colors represent model UrQMD EOS **Left**: directed flow, **Right**: elliptic flow.

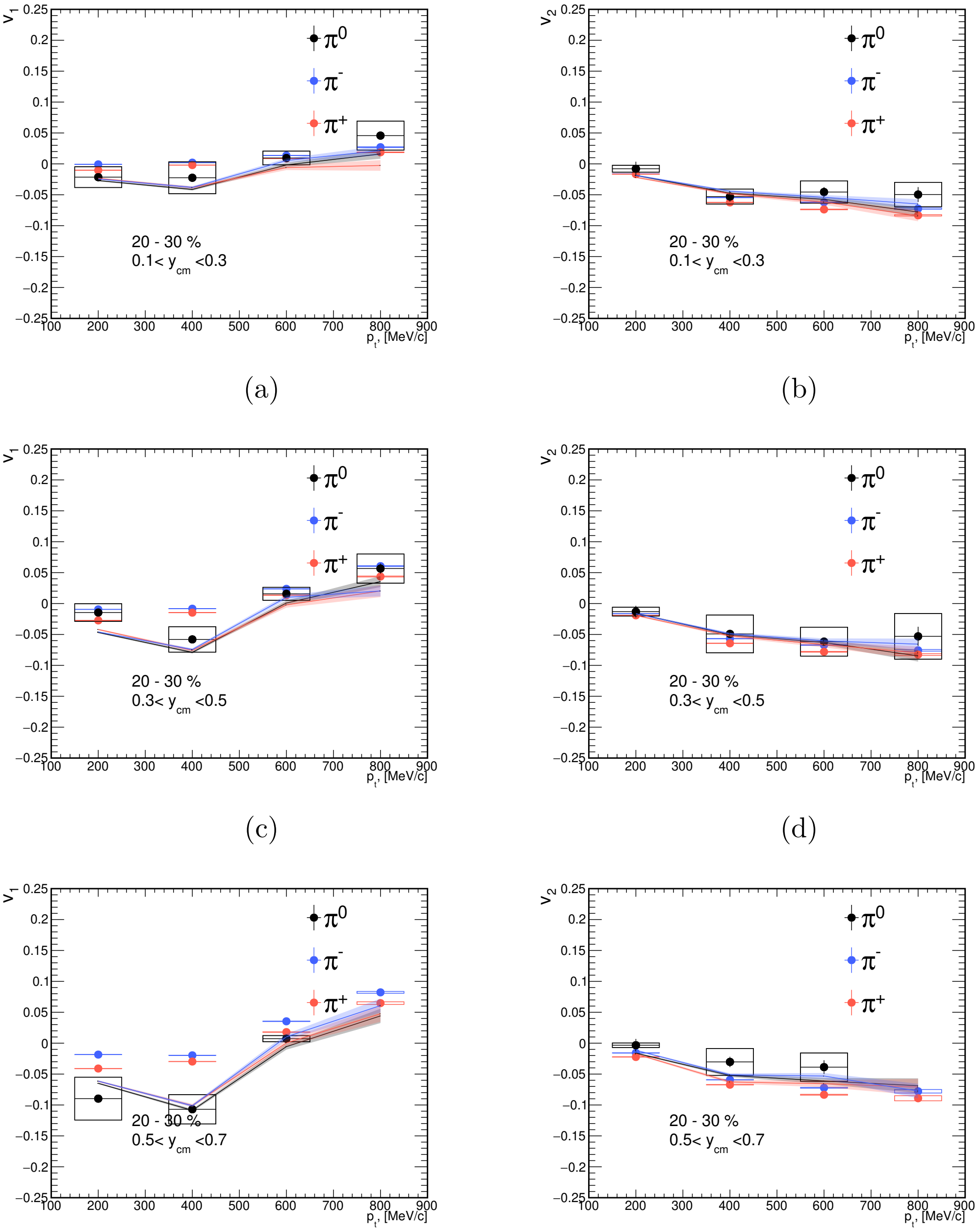

(a) (b)

(c) (d)

(e) (f)

Figure 5.13: Neutral pion flow comparison with charged pions versus p_t. Transparent colors represent model UrQMD EOS. **Left**: directed flow, **Right**: elliptic flow.

It is seen that v_1 changes the slope from negative to positive with increasing transverse momenta, while v_2 remains constant through different rapidities. It is also seen that the elliptic flow has the same saturation character with increasing transverse momentum (Fig .5.13 (b,d,f)) and is independent of the rapidity (Fig .5.12 (b,d,f)). The results for other centralities are shown in Appendix D. To conclude, while in the model all three species of pions have a similar flow, it is not the case for the experiment; see also Appendix E for the other two models and different centrality classes.

Conclusion

In this thesis, I focussed on the analysis of pion yield and pion flow in Ag + Ag collisions at a kinetic beam energy of 1.58 A GeV during the experiment in March 2019 with HADES. During the experiment, HADES acquired more than 14 billion events, of which one-third were selected for the current analysis.

These are the first results of a pioneering experiment using an ECAL detector in HADES. All calibration and analysis techniques were developed from scratch; they will also be used to calibrate future experiments.

The results obtained for π^0 are the first of their kind for a given energy range and the size of the colliding nuclei. The measured π^0 yield agrees very well with that obtained from the average of charged pions for the same experiment.

Until now, there has been little to no information on π^0 flow outside the midrapidity for heavy systems and low energies.

The comparison with selected kinetic models has been made: UrQMD cascade, UrQMD EoS, and GiBUU. The best description of the neutral pion flow is given by UrQMD EoS. It also suggests that the ”hard” equation of state is favored. However, any conclusive statement should take into account data on all produced particles, not only flow of pions, but also flow of other particles, particularly flow of subthreshold (strange) particles.

From the results on the directed and elliptic flow of neutral pions, the following observations can be made:

- directed flow is dependent on a transverse momentum,
- elliptic flow is approximately constant as a function of rapidity and decreases towards higher transverse momentum,
- neutral pion species show similar behavior as in UrQMD with EoS,
- neutral pion directed flow is stronger in some p_t bins than that of charged pions, which is not the case for UrQMD with EoS.
- elliptic flow of all three pion species is the same.

The final goal is to extract information on the restoration of Chiral symmetry in dense baryonic matter. The highest baryon densities will be produced and explored with the Compressed Baryonic Matter (CBM) experiment at the future accelerator facility FAIR.

Bibliography

[1] M Gell-Mann. The eightfold way: A theory of strong interaction symmetry. 3 1961. doi: 10.2172/4008239. URL `https://www.osti.gov/biblio/4008239`.

[2] Standard model. `https://en.wikipedia.org/wiki/Standard_Model`. [Accessed on 22.06.2022].

[3] Particle Data Group. History of the universe. 2015. URL `https://particleadventure.org/images/history-of-the-universe-2015.pdf`. [Accessed on 18.04.2022].

[4] B.Kardan. *Centrality Determination at 1.23 AGeV Gold-Gold collision and readout-electronics for the HADES electromagnetic calorimeter*. PhD thesis, 2015.

[5] Zoltan Fodor and Sandor D Katz. Lattice determination of the critical point of qcd at finite t and μ. *Journal of High Energy Physics*, 2002(03):014, 2002.

[6] Mikhail Stephanov. Qcd phase diagram and the critical point. *arXiv preprint hep-ph/0402115*, 11:13, 2004.

[7] LIGO and Virgo collaborations. GW170817: Observation of gravitational waves from a binary neutron star inspiral. *Physical Review Letters*, 119(16), oct 2017. doi: 10.1103/physrevlett.119.161101. URL `https://doi.org/10.1103%2Fphysrevlett.119.161101`.

[8] Yasumichi Aoki, G Endrődi, Zoltán Fodor, Sándor D Katz, and Kálmán K Szabó. The order of the quantum chromodynamics transition predicted by the standard model of particle physics. *Nature*, 443(7112):675–678, 2006.

[9] H A Bethe. Theory of nuclear matter. *Annual Review of Nuclear Science*, 21 (1):93–244, 1971. doi: 10.1146/annurev.ns.21.120171.000521. URL `https://doi.org/10.1146/annurev.ns.21.120171.000521`.

[10] R. Stock. Particle production in high energy nucleus-nucleus collisions. *Physics Reports*, 135(5):259–315, 1986. ISSN 0370-1573. doi: https://doi.org/10.1016/0370-1573(86)90134-1. URL `https://www.sciencedirect.com/science/article/pii/0370157386901341`.

[11] J. R. Oppenheimer and G. M. Volkoff. On massive neutron cores. *Phys. Rev.*, 55:374–381, Feb 1939. doi: 10.1103/PhysRev.55.374. URL `https://link.aps.org/doi/10.1103/PhysRev.55.374`.

[12] Ch. Hartnack, H. Oeschler, and Jörg Aichelin. Hadronic matter is soft. *Phys. Rev. Lett.*, 96:012302, Jan 2006. doi: 10.1103/PhysRevLett.96.012302. URL `https://link.aps.org/doi/10.1103/PhysRevLett.96.012302`.

[13] Zhigang Xiao, Bao-An Li, Lie-Wen Chen, Gao-Chan Yong, and Ming Zhang. Circumstantial evidence for a soft nuclear symmetry energy at

suprasaturation densities. *Phys. Rev. Lett.*, 102:062502, Feb 2009. doi: 10.1103/PhysRevLett.102.062502. URL `https://link.aps.org/doi/10.1103/PhysRevLett.102.062502`.

[14] A. et.al Andronic. Directed flow in au+au, xe+csi, and ni+ni collisions and the nuclear equation of state. *Phys. Rev. C*, 67:034907, Mar 2003. doi: 10.1103/PhysRevC.67.034907. URL `https://link.aps.org/doi/10.1103/PhysRevC.67.034907`.

[15] A. et.al Andronic. Excitation function of elliptic flow in Au+Au collisions and the nuclear matter equation of state. *Phys. Lett. B*, 612:173–180, 2005. doi: 10.1016/j.physletb.2005.02.060.

[16] A Andronic, P Braun-Munzinger, and J Stachel. Hadron production in central nucleus–nucleus collisions at chemical freeze-out. *Nuclear Physics A*, 772(3-4):167–199, 2006.

[17] Hannah Petersen, Jan Steinheimer, Gerhard Burau, Marcus Bleicher, and Horst Stöcker. Fully integrated transport approach to heavy ion reactions with an intermediate hydrodynamic stage. *Physical Review C*, 78(4):044901, 2008.

[18] J Adamczewski-Musch, O Arnold, C Behnke, A Belounnas, A Belyaev, JC Berger-Chen, Jacek Biernat, A Blanco, C Blume, M Böhmer, et al. Probing dense baryon-rich matter with virtual photons. *Nature Physics*, 15(10): 1040–1045, 2019.

[19] Peter Senger. Particle production in heavy-ion collisions. *Progress in Particle and Nuclear Physics*, 53(1):1–23, 2004.

[20] J Adamczewski-Musch, O Arnold, C Behnke, A Belounnas, A Belyaev, JC Berger-Chen, A Blanco, C Blume, M Böhmer, P Bordalo, et al. Charged-pion production in au+ au collisions at $\sqrt{s_{NN}} = 2.4$ gev. *The European Physical Journal. A, Hadrons and Nuclei*, 56(10), 2020.

[21] Marc R Stockmeier. *Pion Production in Relativistic Heavy Ion Collisions*. PhD thesis, 2002.

[22] W Reisdorf, M Stockmeier, A Andronic, ML Benabderrahmane, ON Hartmann, N Herrmann, KD Hildenbrand, YJ Kim, M Kiš, P Koczoń, et al. Systematics of pion emission in heavy ion collisions in the 1agev regime. *Nuclear Physics A*, 781(3-4):459–508, 2007.

[23] Rainer Novotny. The baf/sub 2/photon spectrometer taps. *IEEE transactions on nuclear science*, 38(2):379–385, 1991.

[24] A. R. Wolf, M. Appenheimer, R. Averbeck, Y. Charbonnier, J. Díaz, A. Döppenschmidt, V. Hejny, S. Hlaváč, R. Holzmann, A. Kugler, H. Löhner, A. Marín, V. Metag, R. Novotny, R. W. Ostendorf, R. Pleskač, A. Schubert, Y. Schutz, R. S. Simon, R. Stratmann, H. Ströher, P. Tlustý, P. H. Vogt, V. Wagner, J. Weiß, H. W. Wilschut, F. Wissmann, and M. Wolf. Multistep production of η and hard π^0 mesons in subthreshold au-au collisions. *Phys.*

Rev. Lett., 80:5281–5284, Jun 1998. doi: 10.1103/PhysRevLett.80.5281. URL `https://link.aps.org/doi/10.1103/PhysRevLett.80.5281`.

[25] F.-D. Berg, M. Pfeiffer, O. Schwalb, M. Franke, W. Kühn, H. Löhner, V. Metag, M. Notheisen, R. Novotny, A. E. Raschke, J. Ritman, M. Röbig-Landau, R. S. Simon, M. Sumbera, L. Venema, and H. Wilschut. Transverse momentum distributions of eta mesons in near-threshold relativistic heavy ion reactions. *Phys. Rev. Lett.*, 72:977–980, Feb 1994. doi: 10.1103/PhysRevLett.72.977. URL `https://link.aps.org/doi/10.1103/PhysRevLett.72.977`.

[26] O. Schwalb, M. Pfeiffer, F.-D. Berg, M. Franke, W. Kühn, V. Metag, M. Notheisen, R. Novotny, J. Ritman, M.E. Röbig-Landau, J.P. Alard, N. Bastid, N. Brummund, P. Dupieux, A. Gobbi, N. Herrmann, K.D. Hildenbrand, S. Hlaváč, S.C. Jeong, H. Löhner, G. Montarou, W. Neubert, A.E. Raschke, R.S. Simon, U. Sodan, M. Šumbera, K. Teh, L.B. Venema, H.W. Wilschut, J.P. Wessels, T. Wienold, and D. Wohlfahrt. Mass dependence of π^0-production in heavy ion collisions at 1 a gev. *Physics Letters B*, 321(1): 20–25, 1994. ISSN 0370-2693. doi: https://doi.org/10.1016/0370-2693(94)90322-0. URL `https://www.sciencedirect.com/science/article/pii/0370269394903220`.

[27] TAPS Collaboration. Production of π 0 and η mesons in carbon-induced relativistic heavy-ion collisions. *Zeitschrift für Physik A Hadrons and Nuclei*, 359:65–73, 1997.

[28] A Marin, J Diaz, R Averbeck, S Hlaváč, R Holzmann, F Lefèvre, A Schubert, RS Simon, Y Charbonnier, G Martínez, et al. Exclusive πo-and η-meson production in 40ar+ natca at 800a mev. *Physics Letters B*, 409(1-4):77–82, 1997.

[29] R. Averbeck, R. Holzmann, V. Metag, and R. S. Simon. Neutral pions and η mesons as probes of the hadronic fireball in nucleus-nucleus collisions around 1a gev. *Phys. Rev. C*, 67:024903, Feb 2003. doi: 10.1103/PhysRevC.67.024903. URL `https://link.aps.org/doi/10.1103/PhysRevC.67.024903`.

[30] Claudia Behnke. *Reconstruction of π^0 and η mesons via conversion in Au+Au at 1.23 GeV with the HADES Spectrometer*. doctoralthesis, Universitätsbibliothek Johann Christian Senckenberg, 2017.

[31] JW Harris, R Bock, R Brockmann, A Sandoval, R Stock, H Stroebele, G Odyniec, HG Pugh, LS Schroeder, RE Renfordt, et al. Pion production as a probe of the nuclear matter equation of state. *Physics Letters B*, 153(6):377–381, 1985.

[32] John W Harris, G Odyniec, Howel G Pugh, LS Schroeder, ML Tincknell, W Rauch, R Stock, R Bock, R Brockmann, A Sandoval, et al. Pion production in high-energy nucleus-nucleus collisions. *Physical Review Letters*, 58 (5):463, 1987.

[33] Reinhard Stock. Particle production in high energy nucleus-nucleus collisions. *Physics Reports*, 135(5):259–315, 1986.

[34] Lukáš Chlad. *Study of transverse flow of kaons in Au+ Au collisions at 1.23 A GeV*. PhD thesis, 2021.

[35] Steffen A Bass, Mohamed Belkacem, Marcus Bleicher, Mathias Brandstetter, L Bravina, Christoph Ernst, Lars Gerland, Max Hofmann, Sigurd Hofmann, Jens Konopka, et al. Microscopic models for ultrarelativistic heavy ion collisions. *Progress in Particle and Nuclear Physics*, 41:255–369, 1998.

[36] George F Bertsch and S Das Gupta. A guide to microscopic models for intermediate energy heavy ion collisions. *Physics Reports*, 160(4):189–233, 1988.

[37] O Buss, T Gaitanos, K Gallmeister, H Van Hees, M Kaskulov, O Lalakulich, AB Larionov, T Leitner, J Weil, and U Mosel. Transport-theoretical description of nuclear reactions. *Physics Reports*, 512(1-2):1–124, 2012.

[38] Wolfgang Ehehalt and Wolfgang Cassing. Relativistic transport approach for nucleus-nucleus collisions from sis to sps energies. *Nuclear Physics A*, 602(3-4):449–486, 1996.

[39] Jörg Aichelin. “quantum” molecular dynamics—a dynamical microscopic n-body approach to investigate fragment formation and the nuclear equation of state in heavy ion collisions. *Physics Reports*, 202(5-6):233–360, 1991.

[40] Christoph Hartnack, Rajeev K Puri, Jörg Aichelin, J Konopka, SA Bass, Horst Stoecker, and W Greiner. Modelling the many-body dynamics of heavy ion collisions: Present status and future perspective. *The European Physical Journal A-Hadrons and Nuclei*, 1(2):151–169, 1998.

[41] Heinz Sorge, Horst Stöcker, and Walter Greiner. Poincaré invariant hamiltonian dynamics: Modelling multi-hadronic interactions in a phase space approach. *Annals of Physics*, 192(2):266–306, 1989.

[42] Steffen A Bass, Mohamed Belkacem, Marcus Bleicher, Mathias Brandstetter, L Bravina, Christoph Ernst, Lars Gerland, Max Hofmann, Sigurd Hofmann, Jens Konopka, et al. Microscopic models for ultrarelativistic heavy ion collisions. *Progress in Particle and Nuclear Physics*, 41:255–369, 1998.

[43] Y Nara, N Otuka, A Ohnishi, K Niita, and S Chiba. Relativistic nuclear collisions at 1 0 a gev energies from p+ be to au+ au with the hadronic cascade model. *Physical Review C*, 61(2):024901, 1999.

[44] Janus Weil, V Steinberg, J Staudenmaier, LG Pang, D Oliinychenko, J Mohs, M Kretz, T Kehrenberg, A Goldschmidt, B Bäuchle, et al. Particle production and equilibrium properties within a new hadron transport approach for heavy-ion collisions. *Physical Review C*, 94(5):054905, 2016.

[45] Jean-Yves Ollitrault. Relativistic hydrodynamics for heavy-ion collisions. *European Journal of Physics*, 29(2):275, 2008.

[46] Charles Gale, Sangyong Jeon, and Bjoern Schenke. Hydrodynamic modeling of heavy-ion collisions. *International Journal of Modern Physics A*, 28(11): 1340011, 2013.

[47] 218642. GSI-FAIR Scientific Report 2018. Technical Report GSI Report 2019-1, GSI, Darmstadt, 2019. URL `https://repository.gsi.de/record/218642`.

[48] Gsi facility. `https://fair-center.eu/overview/accelerator`. [Accessed on 22.06.2022].

[49] G. Agakishiev et al. The High-Acceptance Dielectron Spectrometer HADES. *Eur. Phys. J. A*, 41:243–277, 2009. doi: 10.1140/epja/i2009-10807-5.

[50] HADES Collaboration. Proposals for experiments at SIS18 during FAIR Phase-0. Technical Report HADES, GSI, Darmstadt, 2017. URL `https://repository.gsi.de/record/220071`.

[51] J. Pietraszko, L. Fabbietti, W. Koenig, and M. Weber. Diamonds as timing detectors for minimum-ionizing particles: The HADES proton-beam monitor and START signal detectors for time of flight measurements. *Nuclear Instruments and Methods in Physics Research Section A: Accelerators, Spectrometers, Detectors and Associated Equipment*, 618(1-3):121–123, jun 2010. doi: 10.1016/j.nima.2010.02.113. URL `https://doi.org/10.1016%2Fj.nima.2010.02.113`.

[52] Hades collaboration. internal materials.

[53] C. Muntz et al. The hades tracking system. *Nucl. Instrum. Meth. A*, 535: 242–246, 2004. doi: 10.1016/j.nima.2004.07.232.

[54] P. Salabura. HADES: A High Acceptance DiElectron Spectrometer. *Acta Phys. Polon. B*, 27:421–440, 1996.

[55] C. Grupen and B. Shwartz. *Particle Detectors*. Cambridge Monographs on Particle Physics, Nuclear Physics and Cosmology. Cambridge University Press, 2008. ISBN 9781139469531. URL `https://books.google.cz/books?id=XCPlJTu3GQkC`.

[56] Georgy Kornakov. *New advances and developments on the RPC tof wall of the HADES experiment at GSI*. PhD thesis, 2013.

[57] K. Zeitelhack et al. The HADES RICH detector. *Nucl. Instrum. Meth. A*, 433:201–206, 1999. doi: 10.1016/S0168-9002(99)00371-X.

[58] C. Pauly, J. Eschke, M. Faul, J. Friese, C. Höhne, K.-H. Kampert, T. Kunz, S. Lebedev, J. Michel, W. Niebur, V. Patel, D. Pfeifer, P. Skott, M. Traxler, C. Ugur, A. Weber, and P. Zumbruch. Upgrade of the hades rich photon detector with h12700 mapmts. *Nuclear Instruments and Methods in Physics Research Section A: Accelerators, Spectrometers, Detectors and Associated Equipment*, 876:164–167, 2017. ISSN 0168-9002. doi: https://doi.org/10.1016/j.nima.2017.02.067. URL `https://www.sciencedirect.com/science/article/pii/S0168900217302632`. The 9th international workshop on Ring Imaging Cherenkov Detectors (RICH2016).

[59] O. V. Andreeva et al. Forward scintillation hodoscope for nuclear fragment detection at the high acceptance dielectron spectrometer (hades) setup. *Instruments and Experimental Techniques*, 57(02):103–119, mar 2014. doi: 10.1134/S0020441214020146. URL `https://doi.org/10.1134/S0020441214020146`.

[60] J. Michel. *Development and Implementation of a New Trigger and Data Acquisition System for the HADES Detector.* PhD thesis, 2012.

[61] W. Czyzycki et al. Electromagnetic calorimeter for hades, 2011.

[62] J. Adamczewski-Musch et al. A facility for pion-induced nuclear reaction studies with HADES. *Eur. Phys. J. A*, 53(9):188, 2017. doi: 10.1140/epja/i2017-12365-7.

[63] Hamamatsu Photonics K.K. *"PHOTOMULTIPLIER TUBES - Basics and Applications (THIRD EDI- TION (Edition 3a))*, 2007. URL `https://www.hamamatsu.com/content/dam/hamamatsu-photonics/sites/documents/99_SALES_LIBRARY/etd/PMT_handbook_v3aE.pdf`. [Accessed on 20.04.2022].

[64] O Svoboda et al. Verification of electromagnetic calorimeter concept for the HADES spectrometer. *Journal of Physics: Conference Series*, 599:012026, apr 2015. doi: 10.1088/1742-6596/599/1/012026. URL `https://doi.org/10.1088/1742-6596/599/1/012026`.

[65] M. Akrawy et al. Development studies for the opal end cap electromagnetic calorimeter using vacuum photo triode instrumented leadglass. *Nuclear Instruments and Methods in Physics Research Section A: Accelerators, Spectrometers, Detectors and Associated Equipment*, 290(1):76 – 94, 1990. ISSN 0168-9002. doi: https://doi.org/10.1016/0168-9002(90)90346-8.

[66] T.C. Awes et al. The mid-rapidity calorimeter for the relativistic heavy-ion experiment wa80 at cern. *Nuclear Instruments and Methods in Physics Research Section A: Accelerators, Spectrometers, Detectors and Associated Equipment*, 279(3):479–502, 1989. ISSN 0168-9002. doi: https://doi.org/10.1016/0168-9002(89)91295-3. URL `https://www.sciencedirect.com/science/article/pii/0168900289912953`.

[67] A. Rost, T. Galatyuk, W. Koenig, J. Michel, J. Pietraszko, P. Skott, and M. Traxler. A flexible FPGA based QDC and TDC for the HADES and the CBM calorimeters. *Journal of Instrumentation*, 12(02):C02047–C02047, feb 2017. doi: 10.1088/1748-0221/12/02/c02047. URL `https://doi.org/10.1088/1748-0221/12/02/c02047`.

[68] Neiser et al. Trb3: a 264 channel high precision tdc platform and its applications. *Journal of Instrumentation*, 8(12):C12043, 2013.

[69] Adrian Rost. *Design, installation and commissioning of new read-out electronics for HADES ECAL and diamond detectors for T0-reconstruction and beam diagnostics.* PhD thesis, Technische Universität Darmstadt, Darmstadt, 2020. URL `http://tuprints.ulb.tu-darmstadt.de/12235/`.

[70] Christian W. Fabjan and Fabiola Gianotti. Calorimetry for particle physics. *Rev. Mod. Phys.*, 75:1243–1286, 10 2003. URL `https://link.aps.org/doi/10.1103/RevModPhys.75.1243`.

[71] Estar data. `https://physics.nist.gov/PhysRefData/Star/Text/ESTAR.html`. [Accessed on 27.09.2022].

[72] Particle Data Group. Review of Particle Physics. *Progress of Theoretical and Experimental Physics*, 2022(8), 08 2022. ISSN 2050-3911. doi: 10.1093/ptep/ptac097. URL `https://doi.org/10.1093/ptep/ptac097`. 083C01.

[73] Alice Collaboration. Calibration of the photon spectrometer phos of the alice experiment. *Journal of instrumentation*, 14(05):P05025, 2019. doi: 10.1088/1748-0221/14/05/p05025. URL `https://doi.org/10.1088/1748-0221/14/05/p05025`.

[74] Ingo Froehlich, L Cazon Boado, T Galatyuk, V Hejny, R Holzmann, M Kagarlis, W Kühn, JG Messchendorp, V Metag, M-A Pleier, et al. Pluto: A monte carlo simulation tool for hadronic physics. *arXiv preprint arXiv:0708.2382*, 2007.

[75] Marcus Bleicher, E Zabrodin, Christian Spieles, Steffen A Bass, Christoph Ernst, Sven Soff, L Bravina, Mohamed Belkacem, Henning Weber, Horst Stöcker, et al. Relativistic hadron-hadron collisions in the ultra-relativistic quantum molecular dynamics model. *Journal of Physics G: Nuclear and Particle Physics*, 25(9):1859, 1999.

[76] R Brun, F Bruyant, M Maire, AC McPherson, and P Zanarini. Geant3 user guide cern data handling division dd. *EE/841*, 1985.

[77] Jaroslav Bielcık. *Dilepton spectroscopy with HADES*. PhD thesis, Dissertation, Technische Universität Darmstadt, 2004.

[78] M. Alvioli, H.J. Drescher, and M. Strikman. A monte carlo generator of nucleon configurations in complex nuclei including nucleon–nucleon correlations. *Physics Letters B*, 680(3):225–230, 2009. ISSN 0370-2693. doi: https://doi.org/10.1016/j.physletb.2009.08.067. URL `https://www.sciencedirect.com/science/article/pii/S0370269309010442`.

[79] HADES collaboration. Centrality determination of au au collisions at 1.23a GeV with HADES. *The European Physical Journal A*, 54(5), may 2018. doi: 10.1140/epja/i2018-12513-7. URL `https://doi.org/10.1140%2Fepja%2Fi2018-12513-7`.

[80] Simon Spies. *Strange hadron production in Ag+Ag collisions at 1.58A GeV*. doctoralthesis, Universitätsbibliothek Johann Christian Senckenberg, 2022.

[81] Werner Scheid, Hans Müller, and Walter Greiner. Nuclear shock waves in heavy-ion collisions. *Phys. Rev. Lett.*, 32:741–745, Apr 1974. doi: 10.1103/PhysRevLett.32.741. URL `https://link.aps.org/doi/10.1103/PhysRevLett.32.741`.

[82] A. M. Poskanzer and S. A. Voloshin. Methods for analyzing anisotropic flow in relativistic nuclear collisions. *Phys. Rev. C*, 58:1671–1678, Sep 1998. doi: 10.1103/PhysRevC.58.1671. URL `https://link.aps.org/doi/10.1103/PhysRevC.58.1671`.

[83] Behruz Kardan. Flow harmonics of au+au collisions at 1.23 AGeV with HADES. *Journal of Physics: Conference Series*, 742:012008, aug 2016. doi: 10.1088/1742-6596/742/1/012008. URL `https://doi.org/10.1088/1742-6596/742/1/012008`.

[84] J. Barrette et al(E877). Proton and pion production relative to the reaction plane in au + au collisions at. *Physical Review C*, 56(6):3254–3264, dec 1997. doi: 10.1103/physrevc.56.3254. URL `https://doi.org/10.1103%2Fphysrevc.56.3254`.

[85] Jean-Yves Ollitrault. Determination of the reaction plane in ultrarelativistic nuclear collisions. *Phys. Rev. D*, 48:1132–1139, Aug 1993. doi: 10.1103/PhysRevD.48.1132. URL `https://link.aps.org/doi/10.1103/PhysRevD.48.1132`.

[86] J Adamczewski-Musch, O Arnold, C Behnke, A Belounnas, JC Berger-Chen, A Blanco, C Blume, M Böhmer, P Bordalo, L Chlad, et al. Proton, deuteron and triton flow measurements in au+au collisions at $\sqrt{s_{NN}} = 2.4$ gev. *arXiv preprint arXiv:2208.02740*, 2022.

[87] Jay Orear. *Notes on statistics for physicists*. University of California, Lawrence Radiation Laboratory; printed for the US . . . , 1958.

[88] Roger Barlow. Systematic errors: facts and fictions. *arXiv preprint hep-ex/0207026*, 2002.

[89] N. Borghini and J.-Y. Ollitrault. Azimuthally sensitive correlations in nucleus-nucleus collisions. *Phys. Rev. C*, 70:064905, Dec 2004. doi: 10.1103/PhysRevC.70.064905. URL `https://link.aps.org/doi/10.1103/PhysRevC.70.064905`.

[90] Jean-Yves Ollitrault. Reconstructing azimuthal distributions in nucleus-nucleus collisions, 1997. URL `https://arxiv.org/abs/nucl-ex/9711003`.

[91] Marvin Nabroth. *Emission patterns of charged pions from Ag+Ag collisions at 1.58A GeV*. PhD thesis, Master thesis, Goethe-Universität in Frankfurt am Main, 2022.

[92] HADES Collaboration. Charged-pion production in au-au collisions at $\sqrt{s_{NN}}$= 2. 4 gev. *Eur. Phys. J. A*, 56:259, 2020.

[93] G Agakishiev, C Agodi, A Balanda, G Bellia, D Belver, A Belyaev, J Bielcik, A Blanco, A Bortolotti, JL Boyard, et al. Measurement of charged pions in 12c+ 12c collisions at 1 a gev and 2 a gev with hades. *The European Physical Journal A*, 40(1):45–59, 2009.

[94] G Agakishiev, A Balanda, D Belver, A Belyaev, A Blanco, M Böhmer, JL Boyard, P Cabanelas, E Castro, S Chernenko, et al. Dielectron production in ar+ kcl collisions at 1.76 a gev. *Physical Review C*, 84(1):014902, 2011.

List of Figures

List of Tables

List of Abbreviations

ADC	Analog to Digital Converter
ATLAS	A Toroidal LHC ApparatuS
BNL	Brookhaven National Laboratory
BR	Branching Ratio
BT	BackTracking
CAEN	Computer Aided Design
CAD	Computer Aided Design
CBM	Compressed Baryonic Matter experiment
CERN	*Conseil Européen pour la Recherche Nucléaire* (European Organization for Nuclear Research)
CL	Confidence Level
CM	Center of Mass
CMOS	Complementary Metal-Oxide-Semiconductor
COSY	COoler SYnchrotron
CPT	Chiral Perturbation Theory
CTS	Central Trigger System
DAC	Digital to Anlaog Converter
DAQ	Data AcQuisition
DST	Data Summary Tape
EB	Event Builder
ECAL	Electromagnetic CALorimeter
EoS	Equation of State
ESR	Experimental Storage Ring
eV	electron Volt
FAIR	Facility for Antiproton and Ion Research
FEE	Front-End Electronic
FOPI	FOur PI experiment
FPGA	Field-Programmable Gate Array
fRPC	forward RPC
FRS	FRagment Separator
FW	Forward Wall
FWHM	Full Width at Half Maximum
GEANT	GEometry And TRacking
GeV	Giga electron Volt
GSI	*Gesellschaft für SchwerIonenforschung* Helmholtz Center for Heavy-Ion Research
HADES	High Acceptance DiElectron Spectrometer
HIC	Heavy-Ion Collision
HLD	HADES List mode Data
HSD	Hadron String Dynamics model
HV	High Voltage
HYDRA	HADES sYstem for Data Reduction and Analysis
IQMD	Isospin-dependent Quantum Molecular Dynamics model
IS	Isotropic-Statistical model
JINR	Joint Institute for Nuclear Research
KaoS	Kaon Spectrometer
keV	kilo electron Volt
LAN	Local Area Network
LBNL	Lawrence Berkeley National Laboratory
LD	Linear Discriminant analysis
LEP	Large Electron-Positron collider
LHC	Large Hadron Collider
LO	Leading Order
LV	Low Voltage
MAP	MAximum ionizing Particle
MAPMT	Multi-Anode PhotoMultiplier Tube
MAMI	*MAinzer MIkrotron*
MB	Minimum Bias
MC	Monte-Carlo
MDC	Mini Drift Chamber
ME	Mixed-Event
MEP	MEdium ionizing Particle
META	Multiplicity Electron Trigger Array
MeV	Mega electron Volt
MIP	Minimum Ionizing Particle
MMQ	META Match Quality
MVD	Micro Vertex Detector
NBD	Negative Binomial Distribution
NDF	Number of Degrees of Freedom
NLO	Next to Leading Order
NN	Nucleon-Nucleon
NNLO	Next to Next to Leading Order
OPAL	Omni-Purpose Apparatus at Large Electron-Positron collider
OVD	Off-Vertex-Decay
PAC	Program Advisory Committee
PCB	Printed Circuit Board
PDG	Particle Data Group
PDF	Probability Density Function
PID	Particle IDentification
PMF	Probability Mass Function
PMT	PhotoMultiplier Tube
PT	Physics Trigger
QCD	Quantum Chromo Dynamics
QED	Quantum Electro Dynamics
QGP	Quark Gluon Plasma

RICH	Ring Imaging CHerenkov detetctor
RMS	Root Mean Square
RPC	Resistive Plate Chamber
SE	Same-Event
SHINE	SPS Heavy Ion and Neutrino Experiment
SHM	Statistical Hadronization Model
SIS18	*SchwerIonenSynchrotron 18 Tm* (Heavy-Ion Synchrotron 18 Tm)
SIS100	*SchwerIonenSynchrotron 100 Tm* (Heavy-Ion Synchrotron 100 Tm)
SMASH	Simulating Many Accelerated Strongly-interacting Hadrons
SPPS	Super Proton antiProton Synchrotron
SPS	Super Proton Synchrotron
STS	Strawtube Tracking Station
TAPS	Two-Three-Arm Photon Spectrometer
TDC	Time to Digital Converter
TDR	Technical Design Report
TeV	Tera electron Volt
TPC	Time Projection Chamber
TRB	Trigger and Readout Board
TRD	Transition Radiation Detector
ToF	Time of Flight
TOF	Time Of Flight detetor
TOT	Time over Threshold
UNILAC	UNIveral Linear ACcelerator
UrQMD	Ultra relativistic Quantum Molecular Dynamics model
UV	UltraViolet
VD	Vertex Distance
VDM	Vector Dominance Model

List of publications

Author

- Prozorov, Alexandr. ”Simulation study of effects induced by final granularity of detector in particle flow.” *Journal of Physics: Conference Series.* Vol. 1667. No. 1. IOP Publishing, 2020.
- Prozorov, A., and Hades Collaboration. ”Neutral mesons flow and yields in AgAg@1.58 A Gev at HADES” *Journal of Physics: Conference Series.* in publishing
- Prozorov, A., and Hades Collaboration. ”Diphotons in Ag+Ag 1.58 A GeV at the HADES experiment” Report - GET_INvolved Program (2019)
- Shabanov, A.,Prozorov, A and Hades Collaboration. ”π^0 production in Ag+ Ag collisions at 1.23 A GeV beam energy measured with HADES.” *Particles and Nuclei International Conference 2021.*, p.217, 2022
- Shabanov, A.,Prozorov, A. et al. ”Calibration of the electromagnetic calorimeter ECal of the HADES experiment.” *Journal of Physics: Conference Series.* Vol. 1667. No. 1. IOP Publishing, 2020.
- Chudoba, P.,Prozorov, A et al. ”Commissioning of the electromagnetic calorimeter ECAL of the HADES experiment.” *Journal of Physics: Conference Series.* Vol. 1667. No. 1. IOP Publishing, 2020.

Co-author

- Abgaryan, V., R. Acevedo Kado, S. V. Afanasyev, G. N. Agakishiev, E. Alpatov, G. Altsybeev, M. Alvarado Hernández et al. ”Status and initial physics performance studies of the MPD experiment at NICA.” *The European Physical Journal A 58*, no. 7 (2022): 1-50.
- Adamczewski-Musch, J., A. Belyaev, A. Blanco, C. Blume, C. Charlotte, D. S. Borisenko, L. Chlad et al. ”Production and electromagnetic decay of hyperons: a feasibility study with HADES as a phase-0 experiment at FAIR.” *The European Physical Journal A 57*, no. 4 (2021): 1-21.
- Salabura, Piotr, J. Adamczewski-Musch, B. Arnoldi-Meadows, A. Belounnas, A. Belyaev, A. Blanco, C. Blume et al. ”Exploring time like tranistions in pp, πp and AA reactions with HADES.” In *EPJ Web of Conferences*, vol. 241, p. 01013. EDP Sciences, 2020.
- Adamczewski-Musch, J., Arnold, O., Atomssa, E.T., Behnke, C., Belounnas, A., Belyaev, A., Berger-Chen, J.C., Biernat, J., Blanco, A., Blume, C. and Böhmer, M., 2020. Two-pion production in the second resonance region in $\pi - p$ collisions with the High-Acceptance Di-Electron Spectrometer (HADES). *Physical Review C*, 102(2), p.024001.

- Adamczewski-Musch, J., O. Arnold, E. T. Atomssa, C. Behnke, A. Belounnas, A. Belyaev, J. C. Berger-Chen et al. ”Strong absorption of hadrons with hidden and open strangeness in nuclear matter.” *Physical Review Letters 123*, no. 2 (2019): 022002.

- Kornakov, G., and Hades Collaboration. ”Sub-threshold strangeness production measured with HADES.” *Nuclear Physics A 982* (2019): 803-806.

- Kardan, Behruz, and Hades Collaboration. ”Collective flow and correlations measurements with HADES in Au+ Au collisions at 1.23 AGeV.” *Nuclear Physics A 982* (2019): 431-434.

- Harabasz, Szymon, and Hades Collaboration. ”Multi-differential pattern of low-mass e^+e^- excess from $\sqrt{s_{NN}}$ =2.4 GeV Au+ Au collisions with HADES.” *Nuclear Physics A 982* (2019): 771-774.

A. Relativistic kinematics

The collision coordinate system is defined by the z-axis, which coincides with a beam direction, and the $x-y$ plane is perpendicular to it. At first, the particle's momentum p has a direction along the beam and is naturally decomposed into longitudinal momentum p_l and transverse momentum p_t.

$$\begin{aligned} p_t &= p \cdot \sin\theta \\ p_l &= p \cdot \cos\theta \end{aligned} \tag{A.1}$$

where θ is the polar angle.

The alternative for the transverse momentum for the particle with mass m is a transverse mass m_t,

$$m_t = \sqrt{m^2 + {p^2}_t}, \tag{A.2}$$

The transverse component is Lorentz invariant under transformations along the z axis, which is not the case for longitudinal momentum. Thus, a more appropriate variable, called rapidity y, is chosen to describe the particles. It is Lorentz-invariant under additions.

$$y = \frac{1}{2}\log\Big(\frac{E + p_l}{E - p_l}\Big), \tag{A.3}$$

with E being the total energy of the particle:

$$E = \sqrt{p^2 + m^2}. \tag{A.4}$$

It is easy to show from the relations of A.2, A.3, and A.4 the following:

$$E = m_t \cdot \cosh y \tag{A.5}$$

It is easy to transform frames from the laboratory system to the center-of-mass (c.m.) system by adding or subtracting the c.m. system's rapidity in the laboratory frame. It is called midrapidity, and for fixed-target experiments defined for a projectile nucleon with energy E_p and momentum p_p as:

$$y_{cm} = \frac{1}{4}\log\Big(\frac{E_p + p_p}{E_p - p_p}\Big), \tag{A.6}$$

The c.m. rapidity for symmetric collision for a nucleon mass of 940 MeV and incident kinetic energy of 1.58 GeV $y_{cm} = 0.822$.

B. Particle distribution transformations

The Boltzmann distribution for particles is given by:

$$\frac{d^3N}{dp^3} = \frac{d^3N}{p_t dp_t d\phi dp_z} \propto \exp\Big(-\frac{E}{T}\Big), \tag{B.1}$$

with energy $E = \sqrt{p^2 + m^2}$ and temperature T.

A Boltzmann distribution is justified by the high-level density for particles in heavy-ion collisions, whether Bose-Einstein or Fermi-Dirac distributions are for the low-density level.

Using $dp_z = Edy$ and integrating with ϕ gives the following:

$$\frac{d^2N}{dp_t dy} \propto 2\pi p_t E \exp\Big(-\frac{E}{T}\Big).$$

Substituting $E = m_t \cosh y$ yields in :

$$\frac{d^2N}{dp_t dy} \propto p_t m_t \cosh y \exp\Big(-\frac{m_t \cosh y}{T}\Big). \tag{B.2}$$

Or, using the transverse mass relation $m_t = \sqrt{{p_t}^2 + m^2}$ and $p_t dp_t = m_t dm_t$

$$\frac{d^2N}{dm_t dy} \propto m_t^2 \cosh y \exp\Big(-\frac{m_t \cosh y}{T}\Big). \tag{B.3}$$

Furthermore, finally, the integration over m_t gives:

$$\begin{aligned}\frac{dN}{dy} &\propto \cosh y \int_{m_0}^{\infty} dm_t {m_t}^2 \exp\Big(-m_t \frac{\cosh y}{T}\Big) \\ &= T \exp\Big(-\frac{m_0 \cosh y}{T}\Big)\bigg({m^2}_0 + 2m_0 \frac{T}{\cosh y} + 2\frac{T^2}{\cosh^2 y}\bigg)\end{aligned} \tag{B.4}$$

This equation can be approximated by the Gaussian function using the second-order Taylor expansion of the $\cosh y$ function around the point $y = 0$ and assuming the term in brackets to be a constant. The second moment of the rapidity distribution is determined as the thermal width of the spectrum and is defined as $\sigma = \sqrt{T/m_0}$ in B.5

$$\frac{dN}{dy} \propto \exp\Big(-\frac{y^2}{2\sigma^2}\Big). \tag{B.5}$$

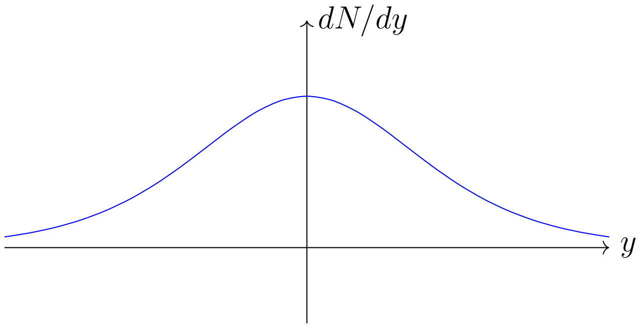

Figure B.1: An example of distribution dN/dy.

C. Invariant mass in Phase Space

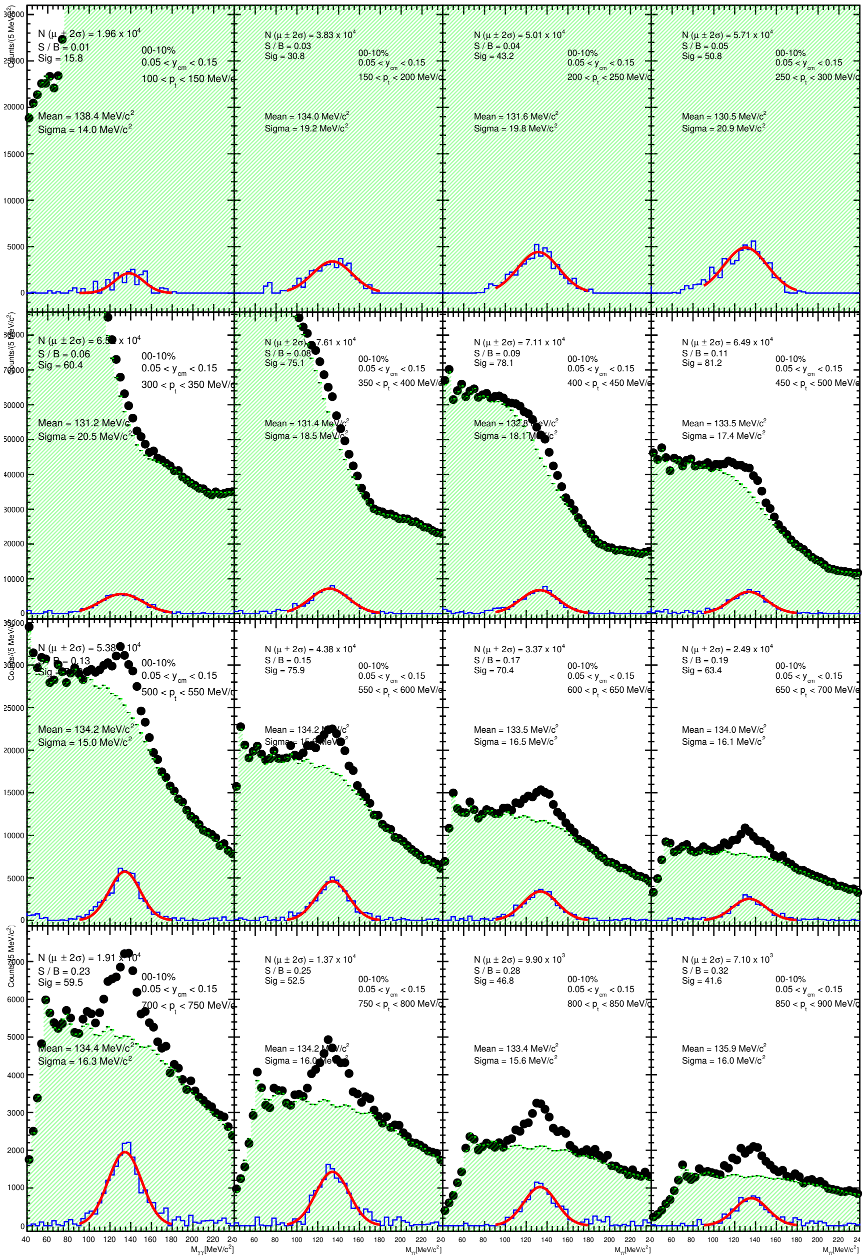

Figure C.1: Phase space dependent diphoton invariant mass spectrum with mixed event background (green)

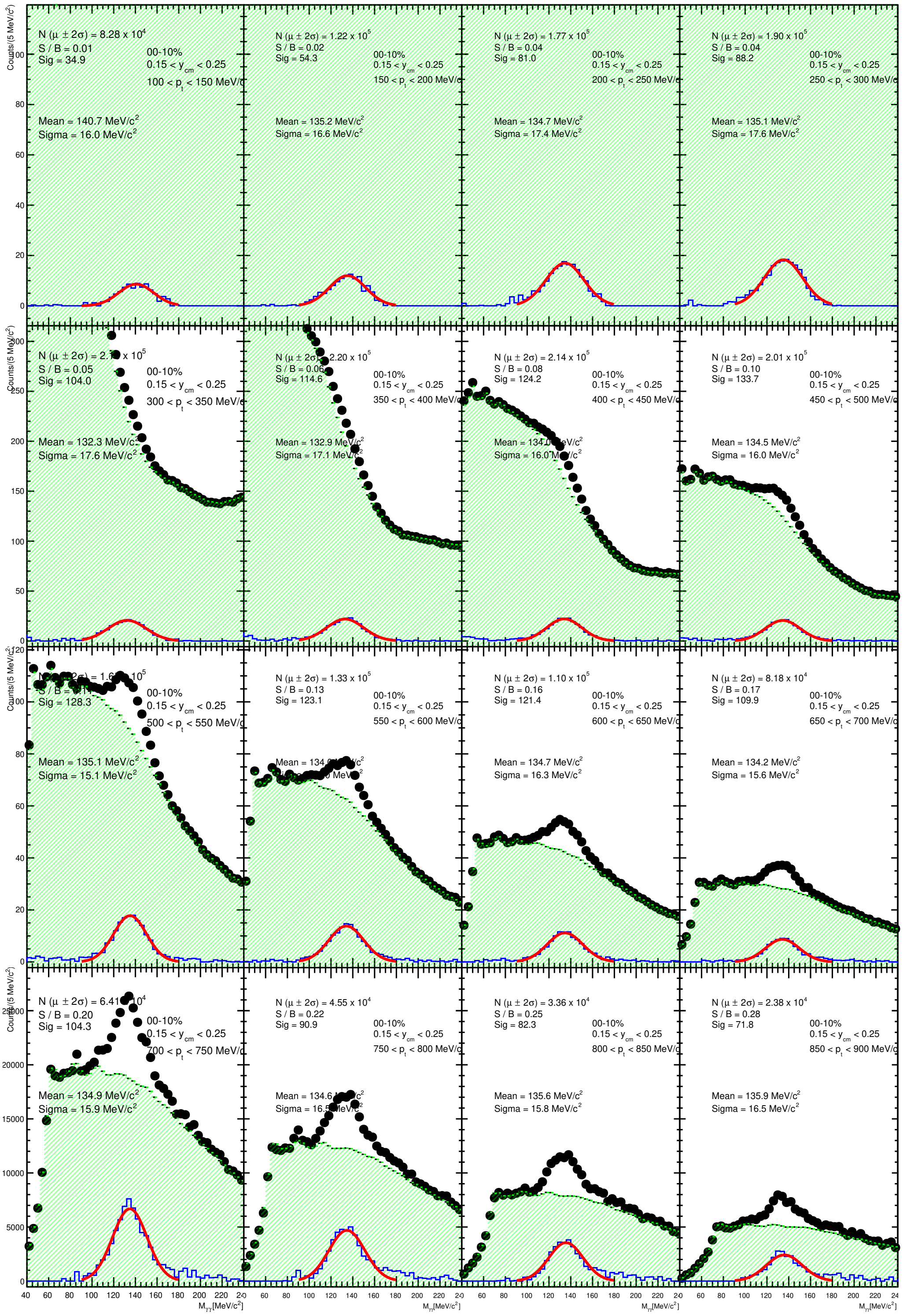

Figure C.2: Phase space dependent diphoton invariant mass spectrum with mixed event background (green)

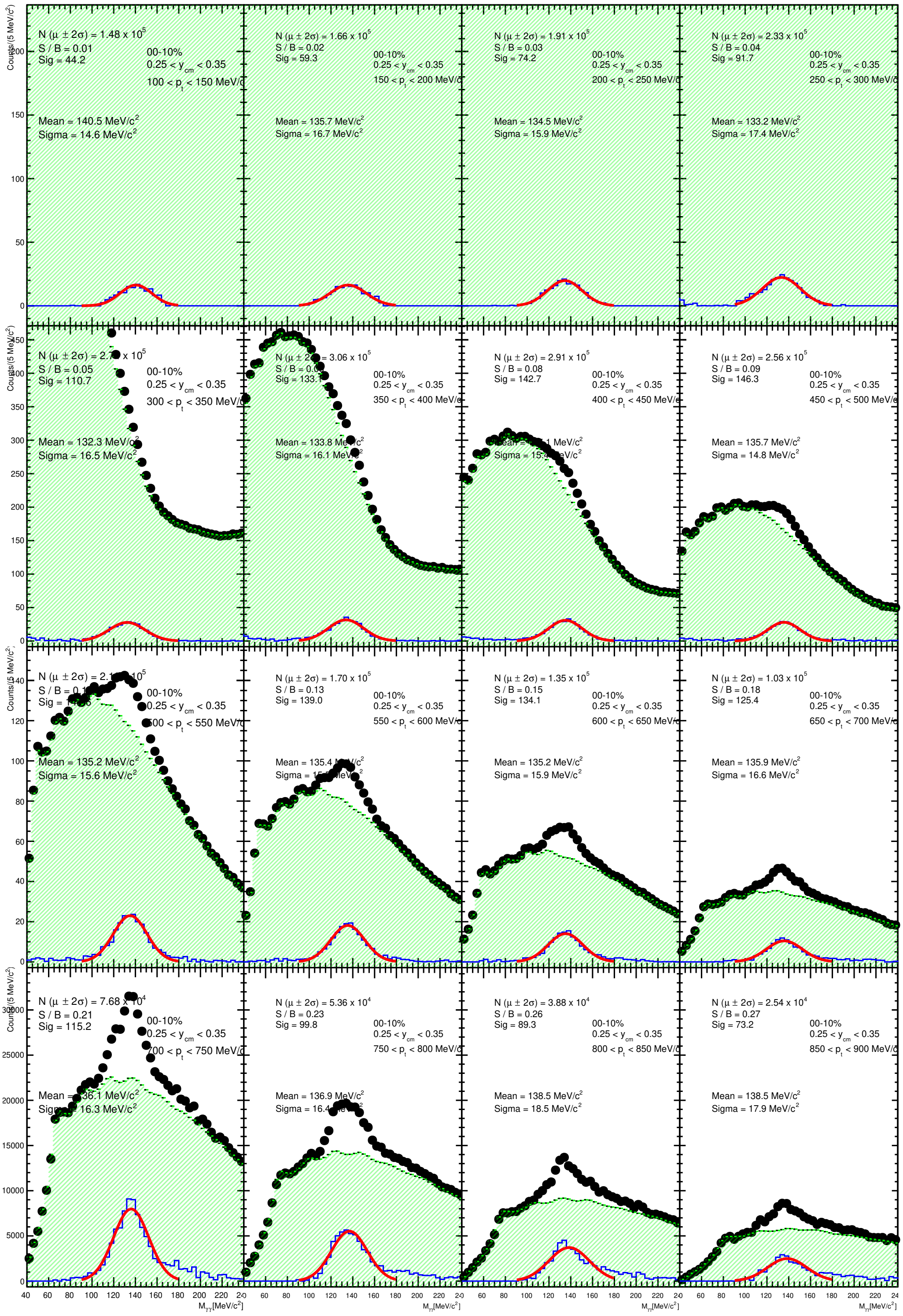

Figure C.3: Phase space dependent diphoton invariant mass spectrum with mixed event background (green)

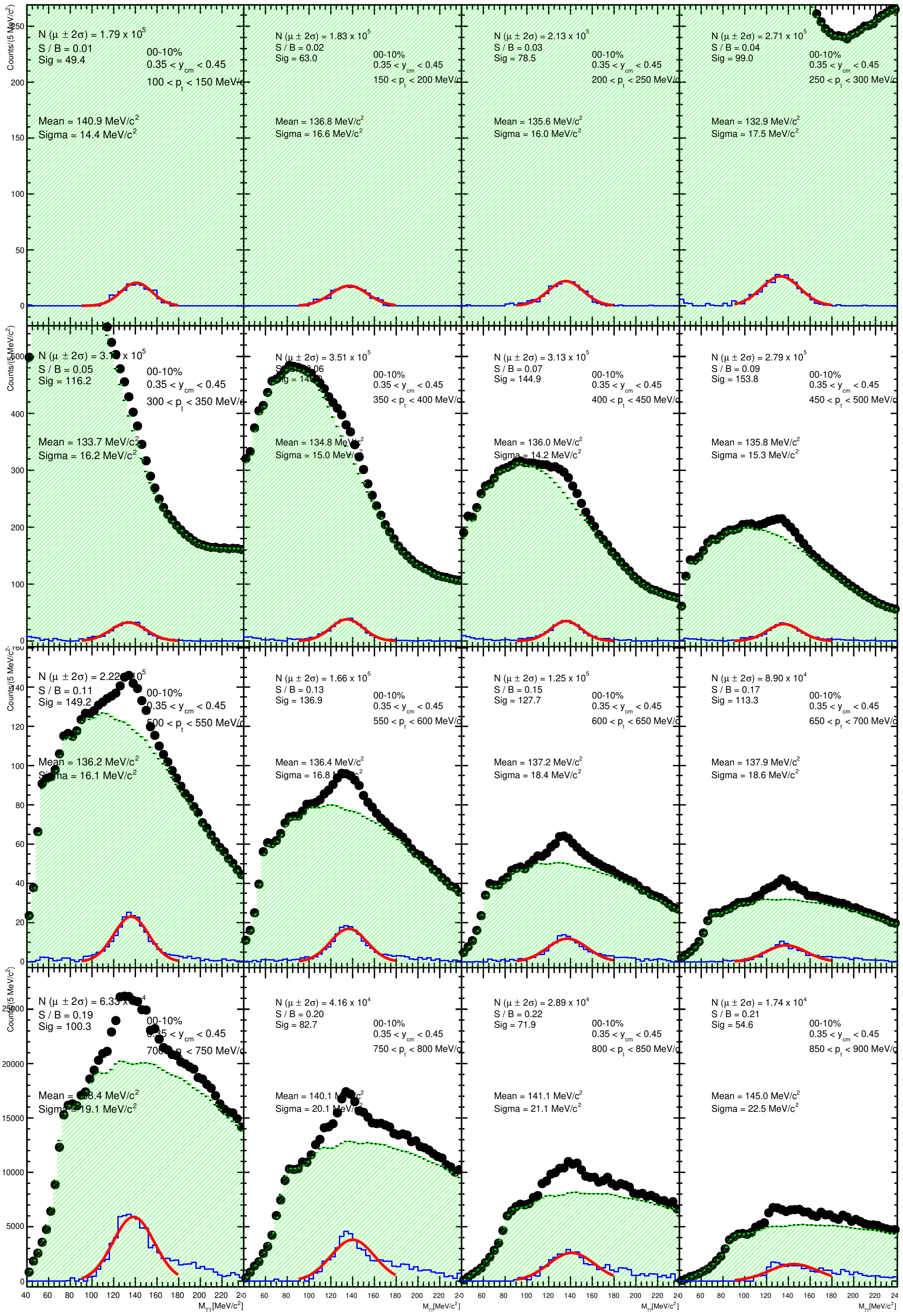

Figure C.4: Phase space dependent diphoton invariant mass spectrum with mixed event background (green)

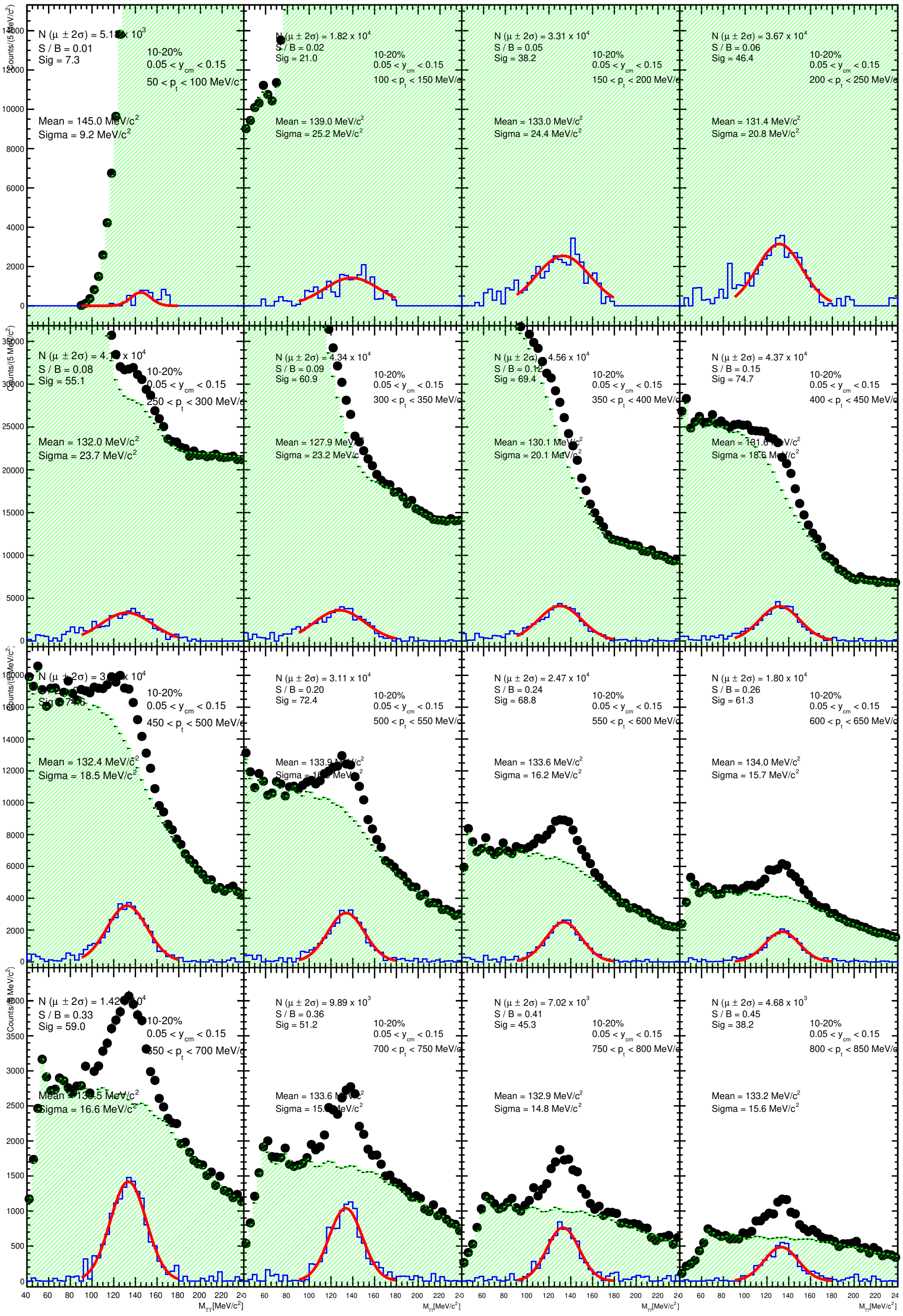

Figure C.5: Phase space dependent diphoton invariant mass spectrum with mixed event background (green)

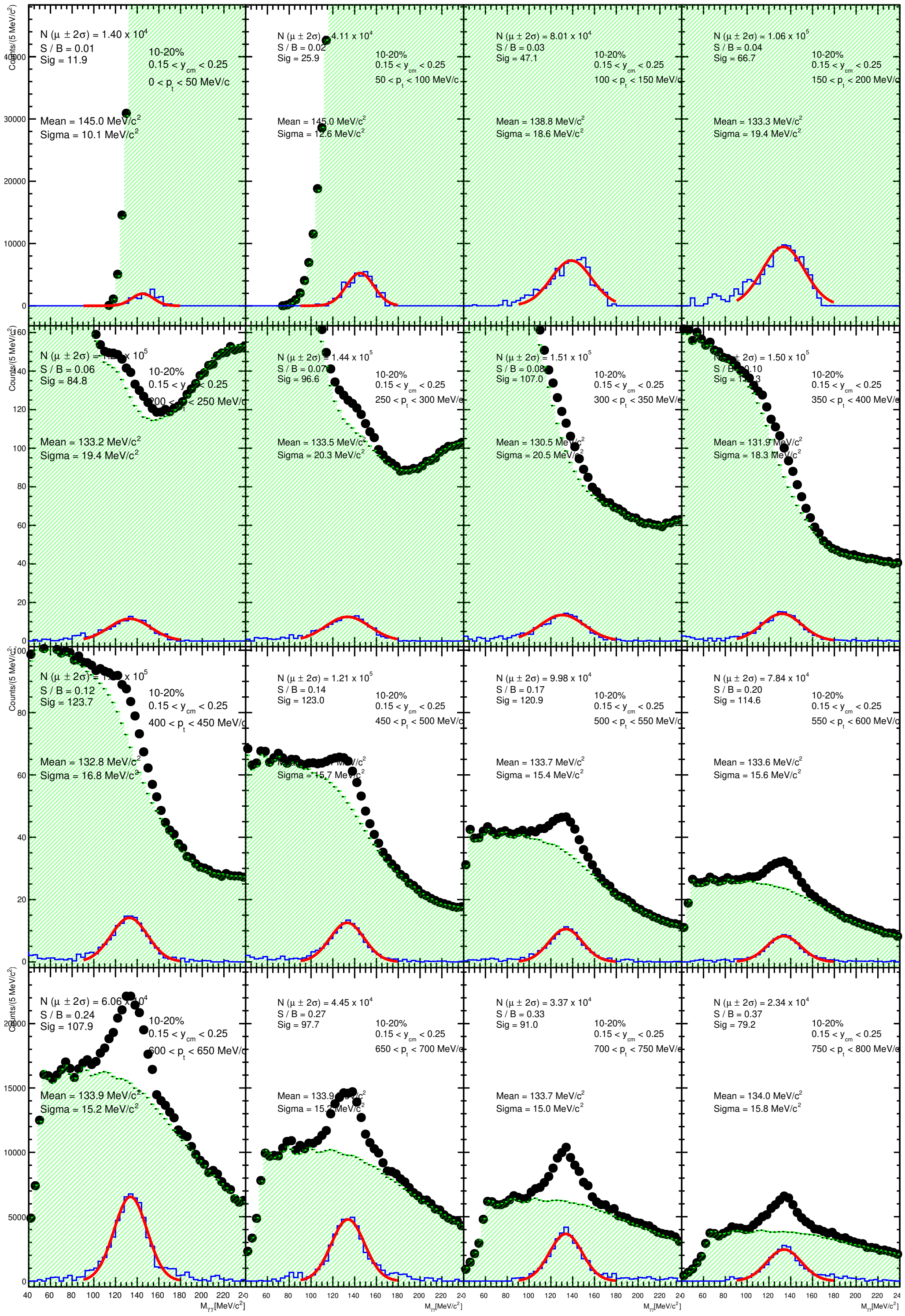

Figure C.6: Phase space dependent diphoton invariant mass spectrum with mixed event background (green)

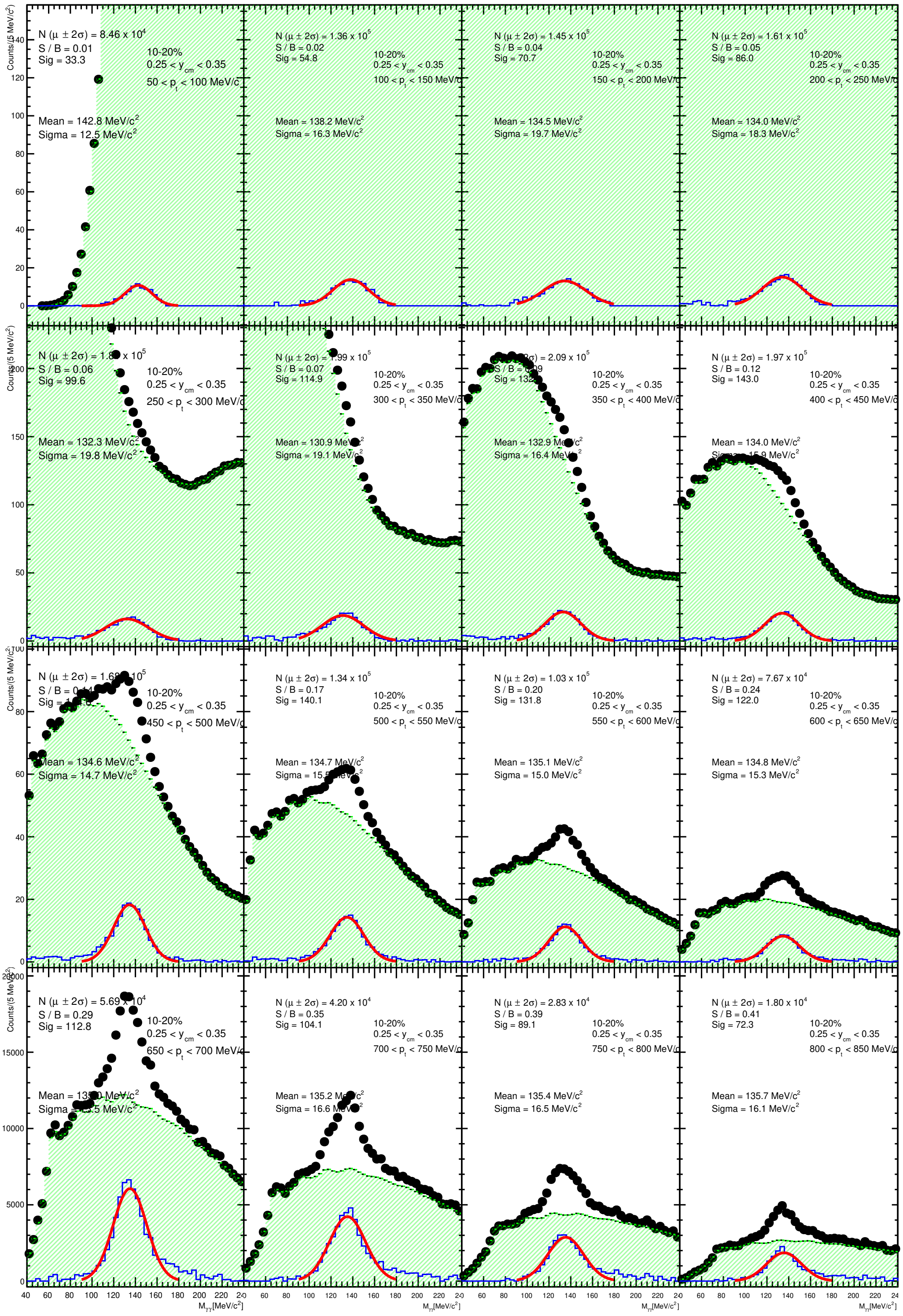

Figure C.7: Phase space dependent diphoton invariant mass spectrum with mixed event background (green)

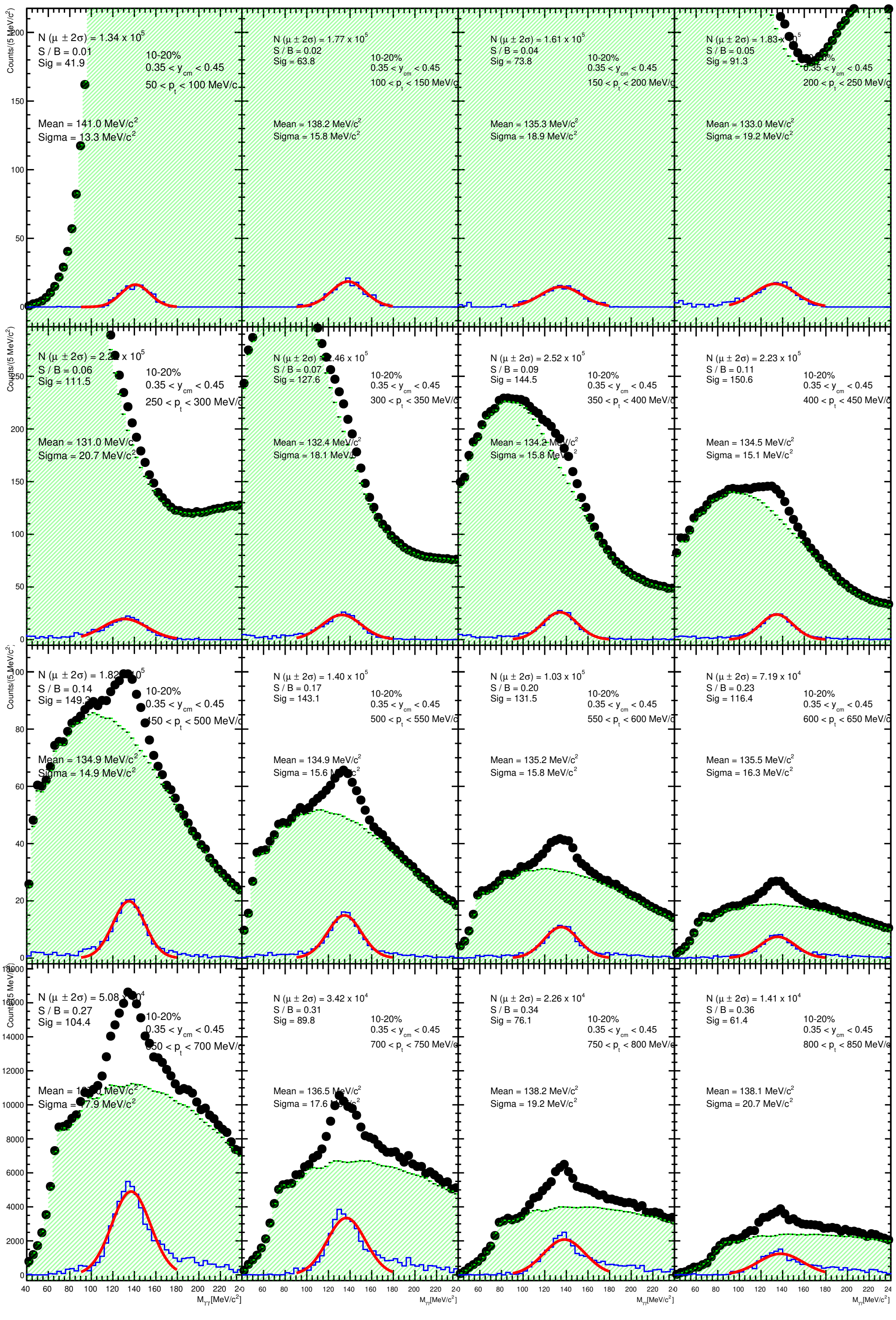

Figure C.8: Phase space dependent diphoton invariant mass spectrum with mixed event background (green)

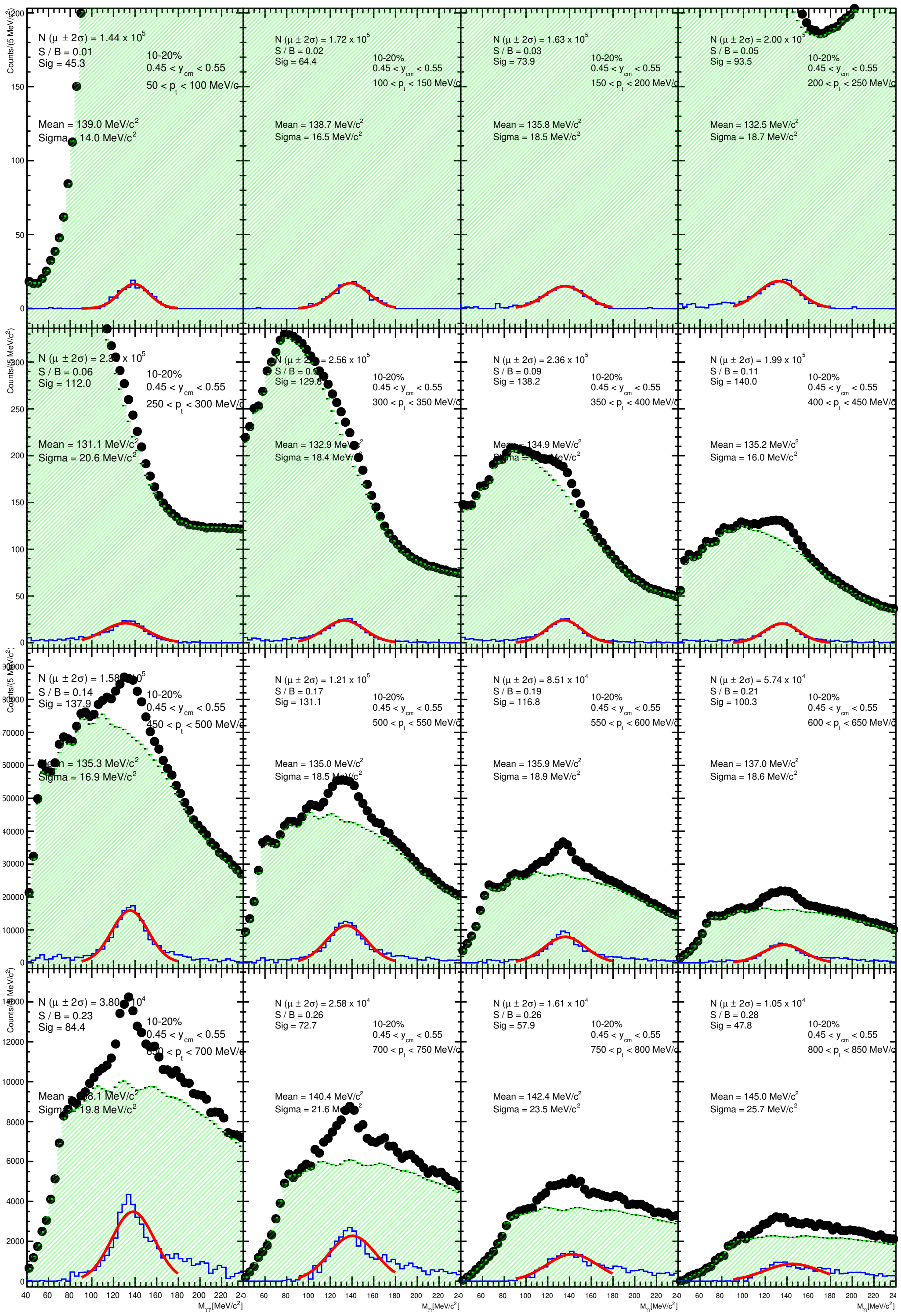

Figure C.9: Phase space dependent diphoton invariant mass spectrum with mixed event background (green)

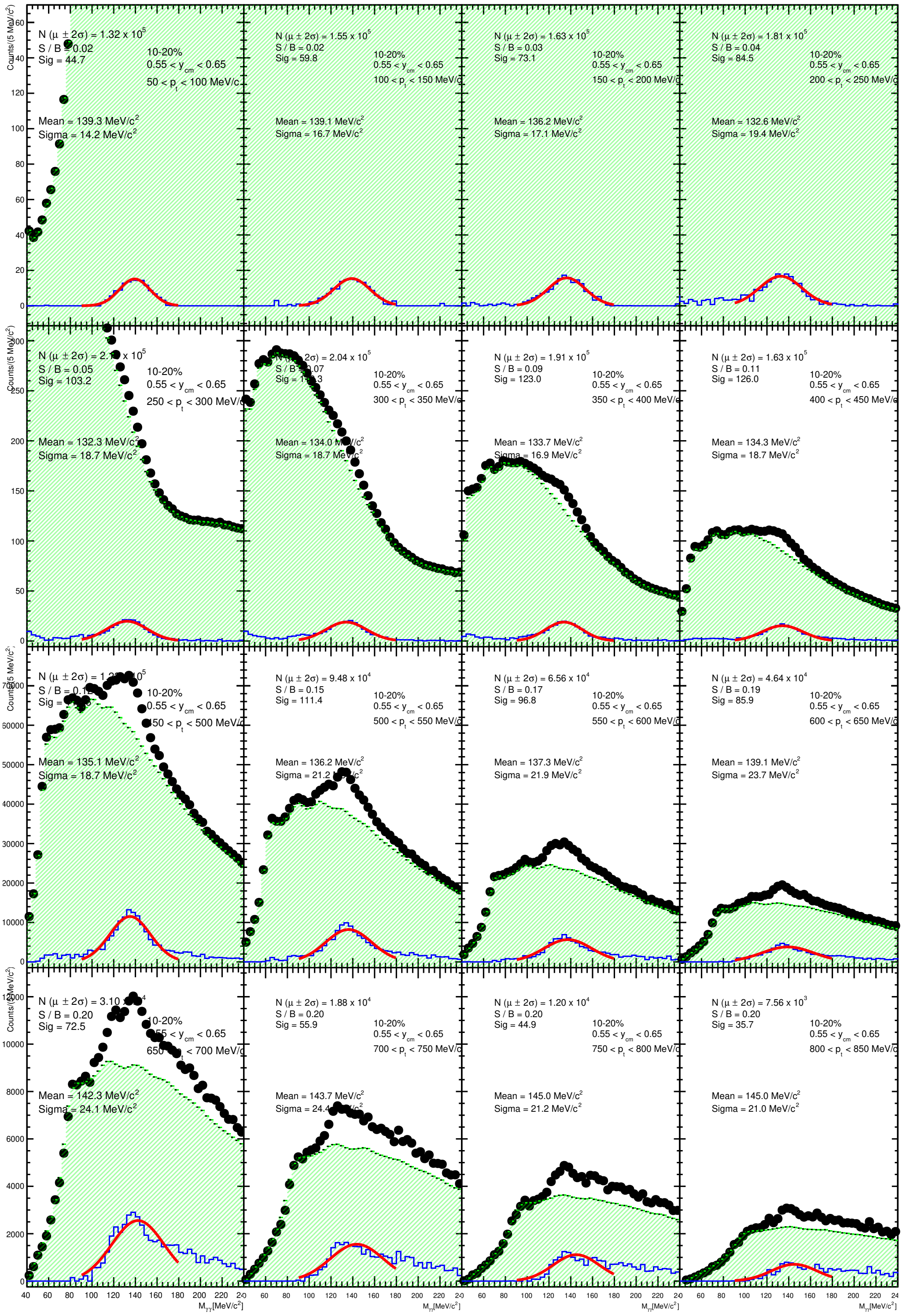

Figure C.10: Phase space dependent diphoton invariant mass spectrum with mixed event background (green)

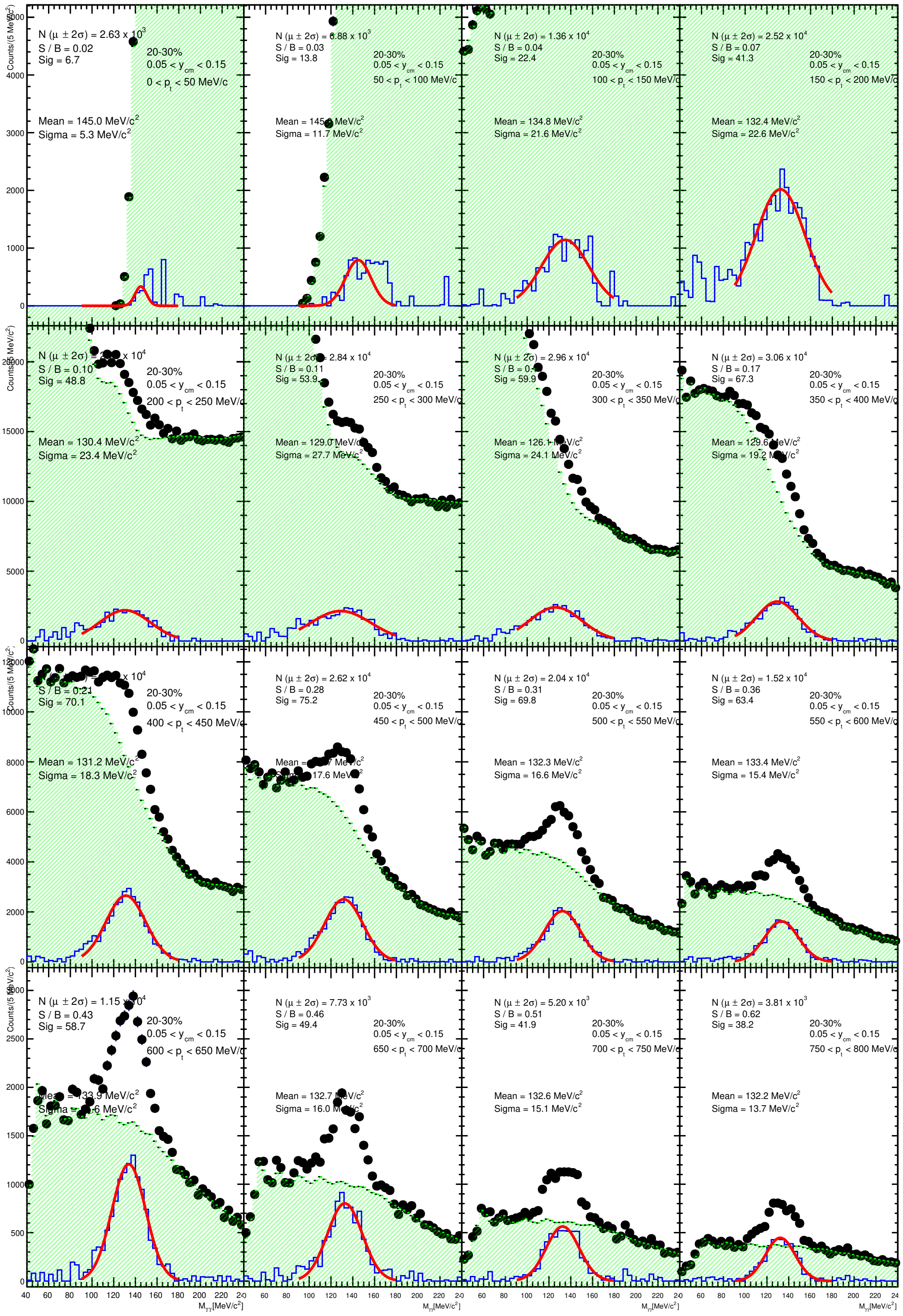

Figure C.11: Phase space dependent diphoton invariant mass spectrum with mixed event background (green)

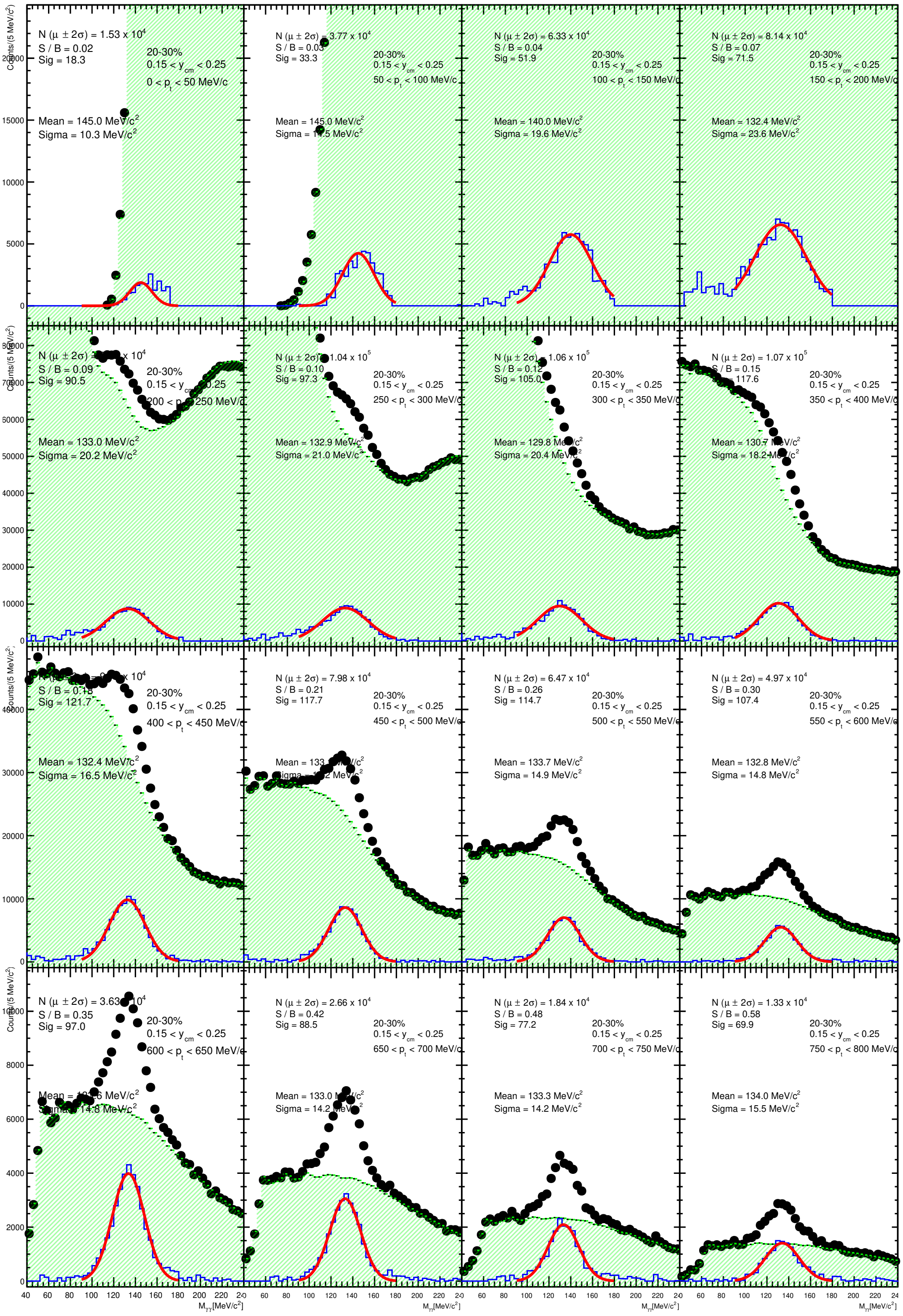

Figure C.12: Phase space dependent diphoton invariant mass spectrum with mixed event background (green)

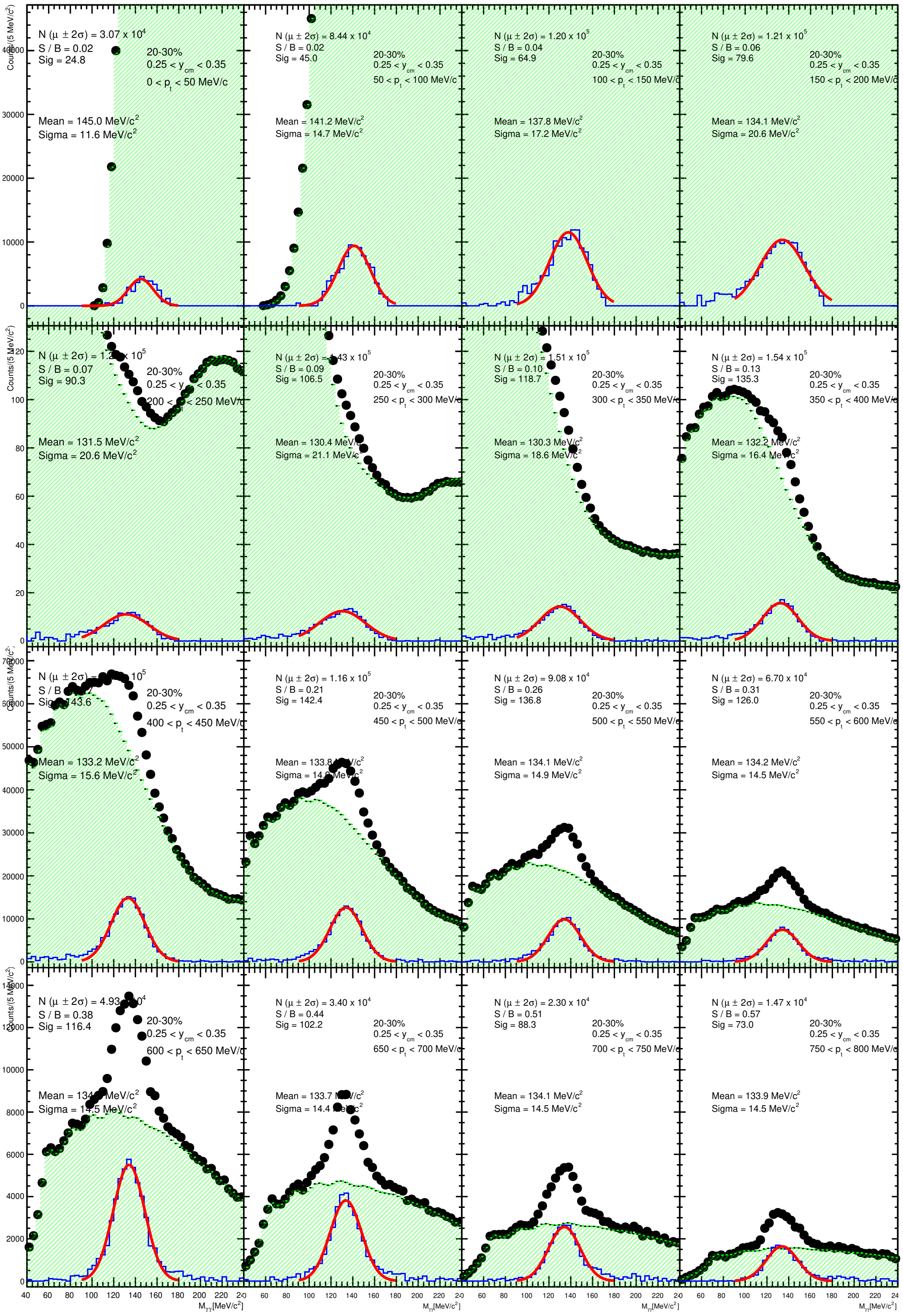

Figure C.13: Phase space dependent diphoton invariant mass spectrum with mixed event background (green)

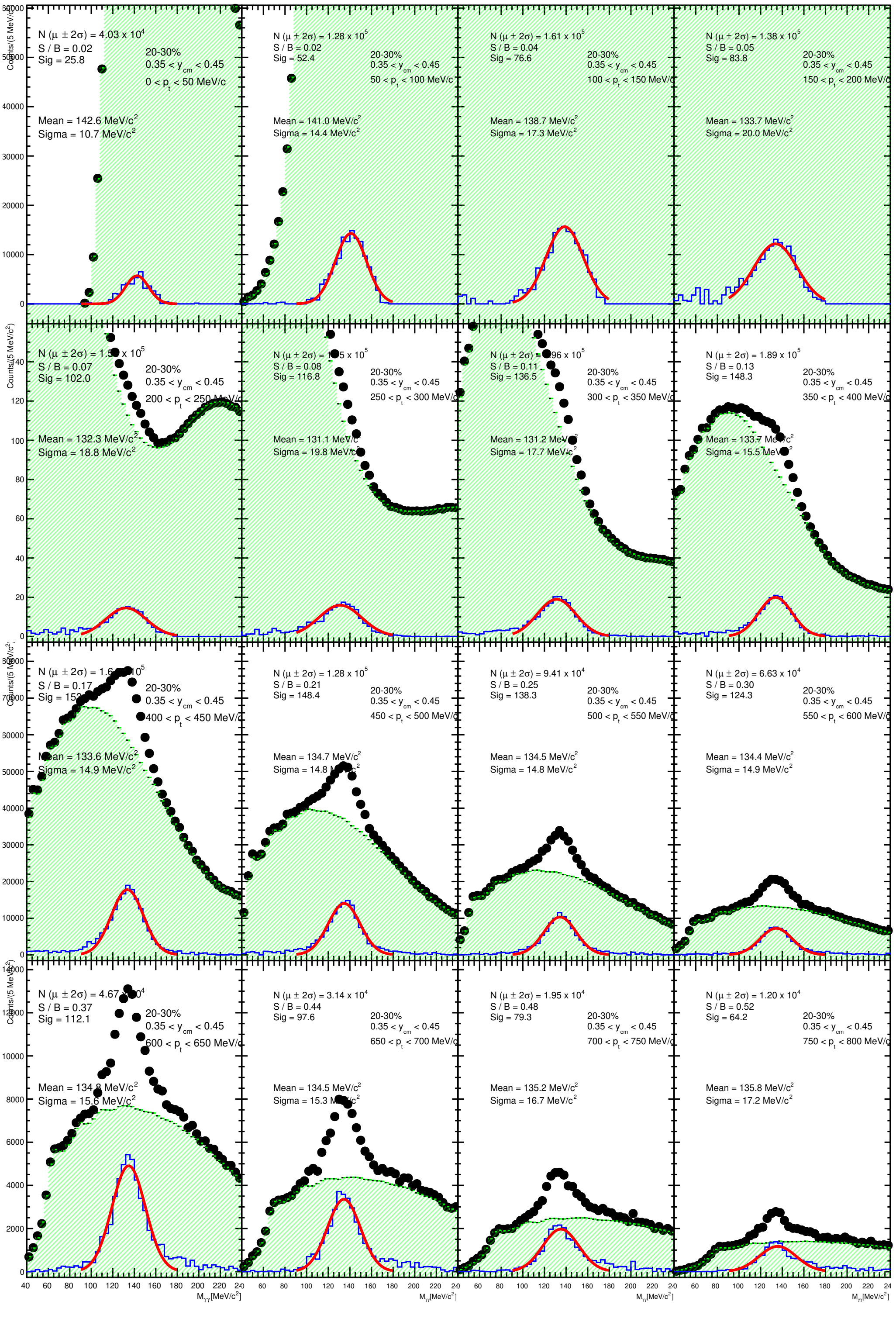

Figure C.14: Phase space dependent diphoton invariant mass spectrum with mixed event background (green)

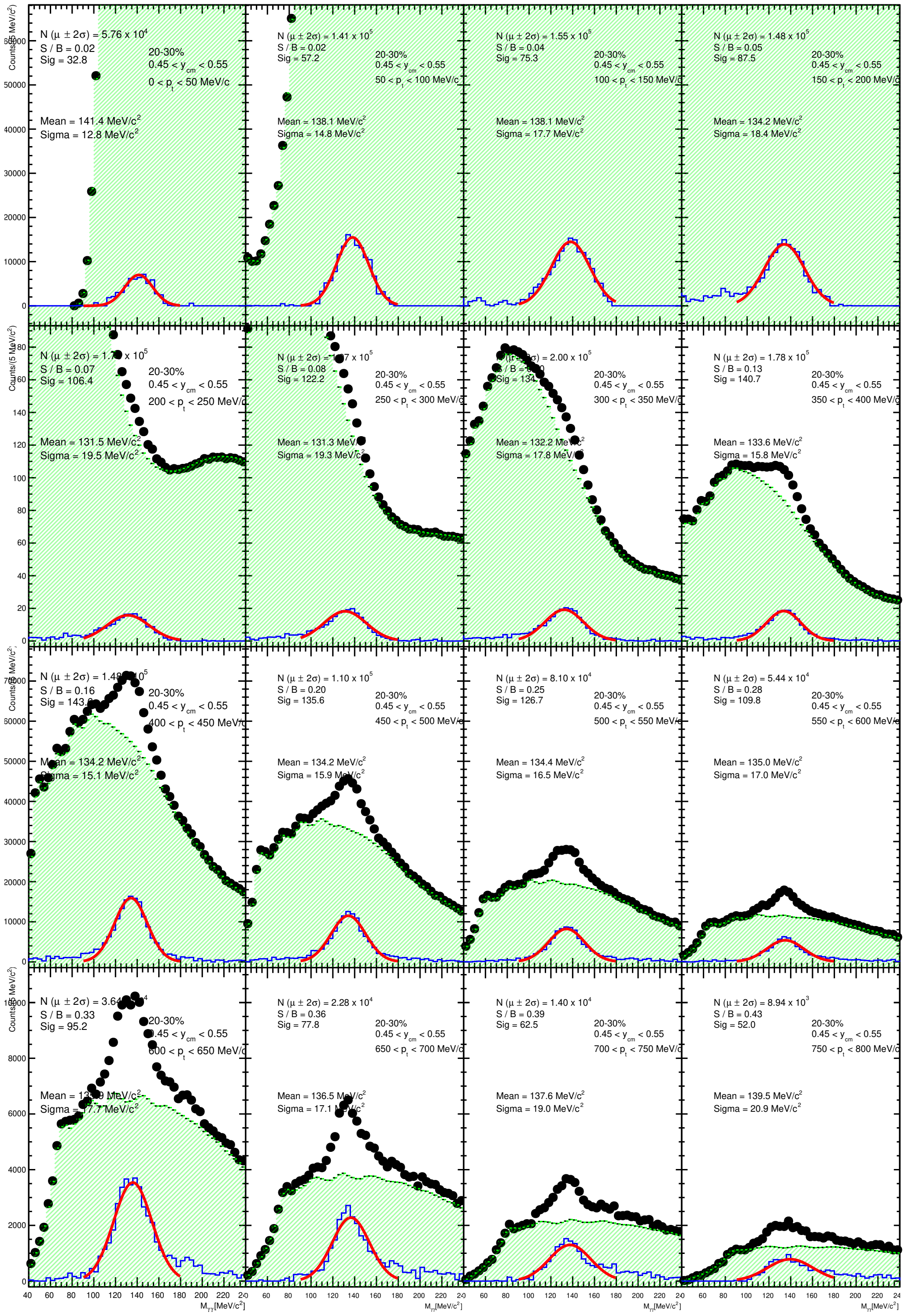

Figure C.15: Phase space dependent diphoton invariant mass spectrum with mixed event background (green)

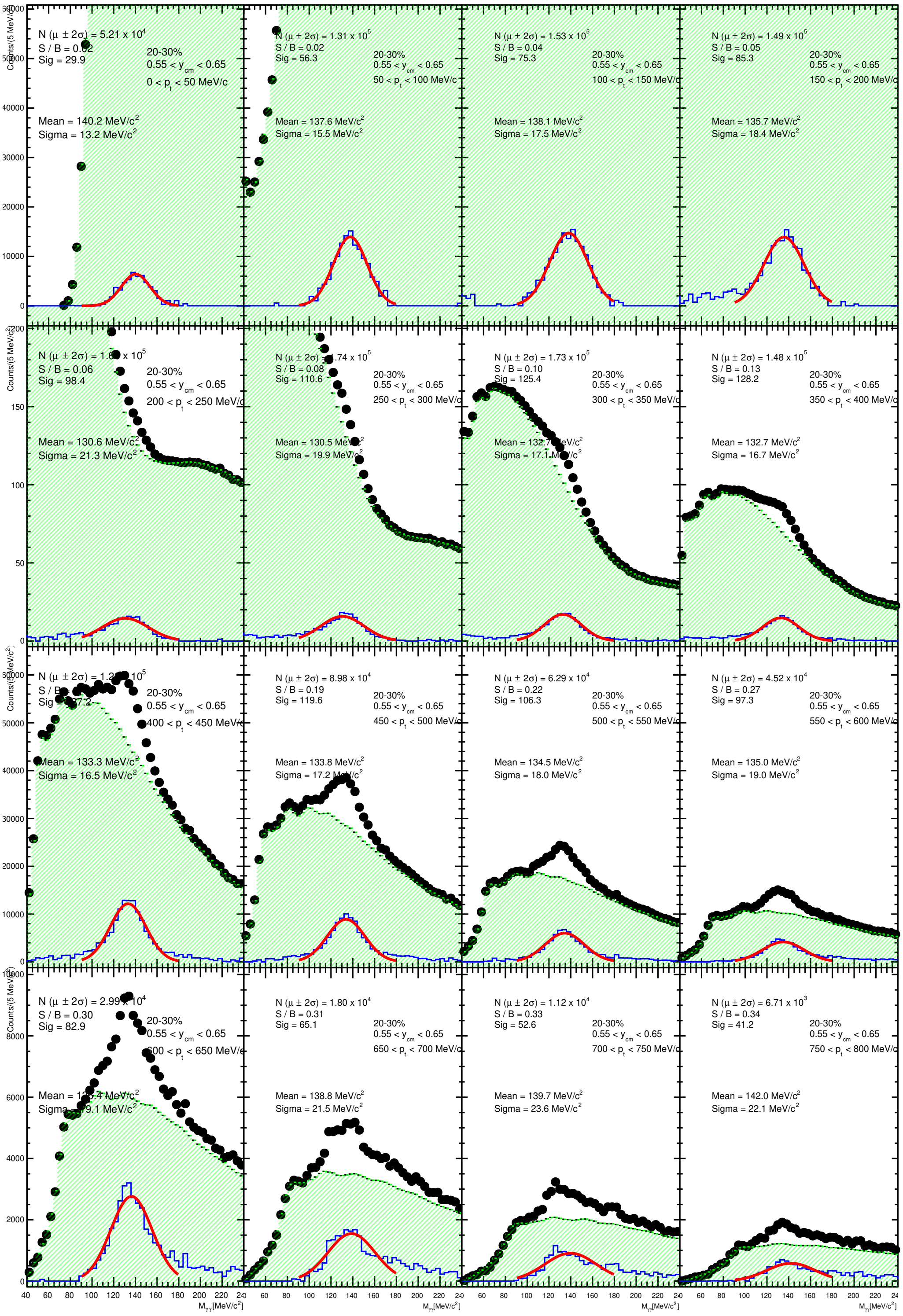

Figure C.16: Phase space dependent diphoton invariant mass spectrum with mixed event background (green)

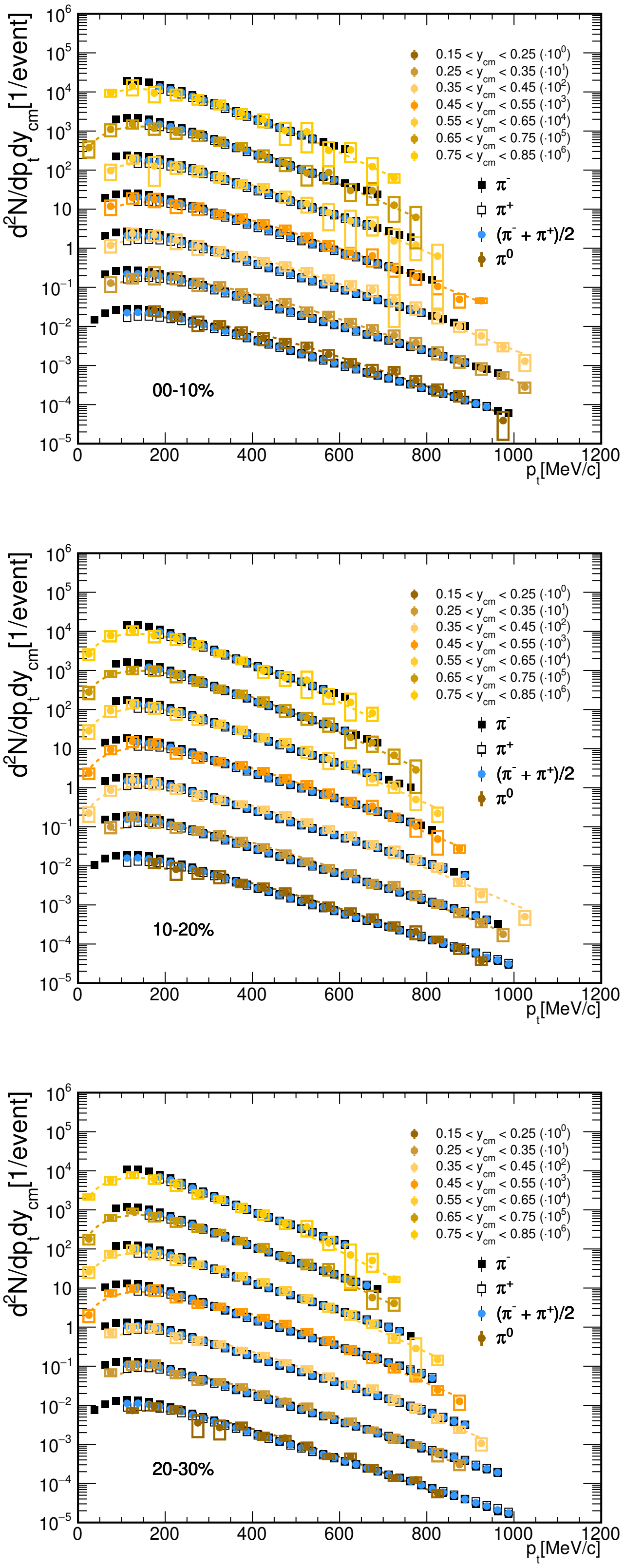

Figure C.17: Transverse momentum distributions of neutral and charged pions in the rapidity bin of width $dy = 0.1$ between 0.15 and 0.75.

D. Supplementary figures for π^0 flow results

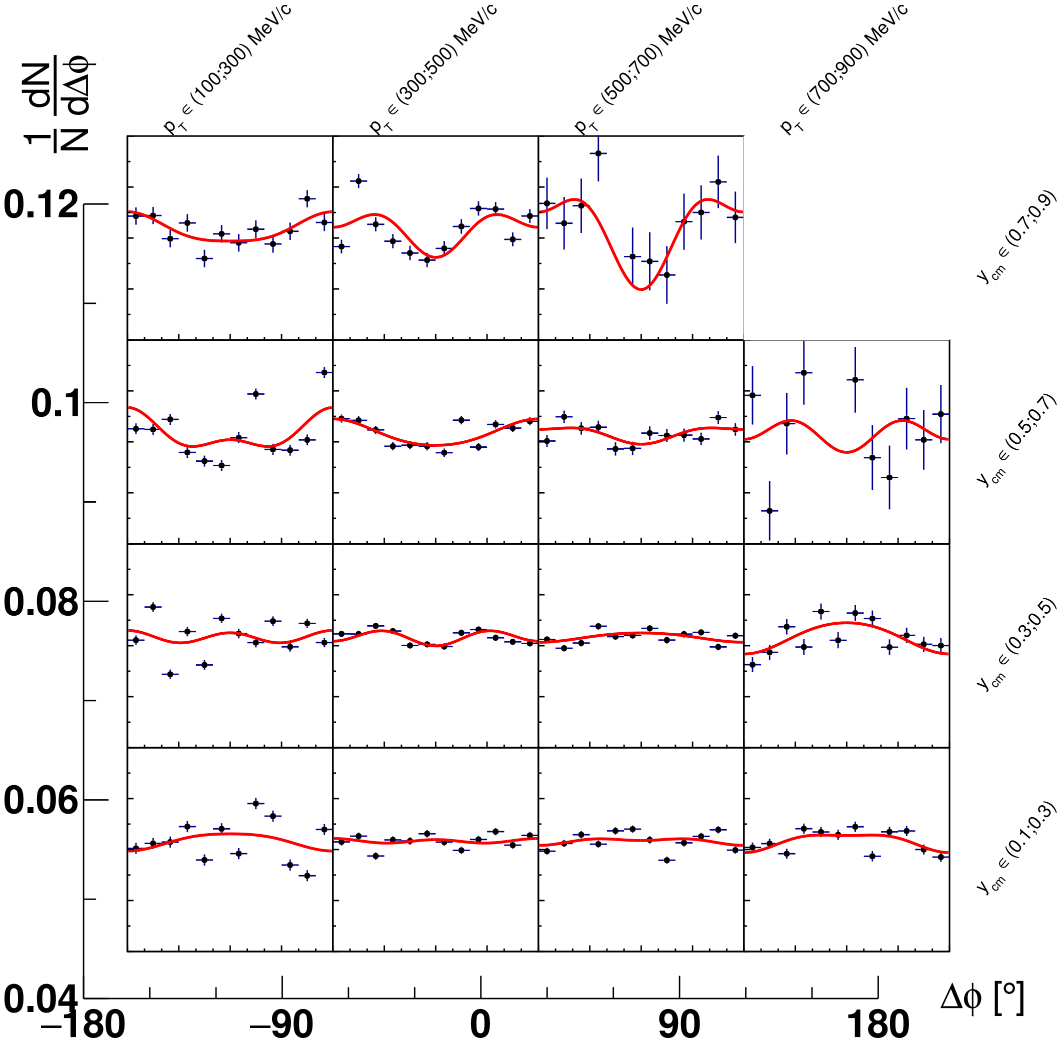

Figure D.1: π^0 normalized azimuthal angle distributions w.r.t. event plane for centrality class 0 - 10 %, fit is done with a function 4.16.

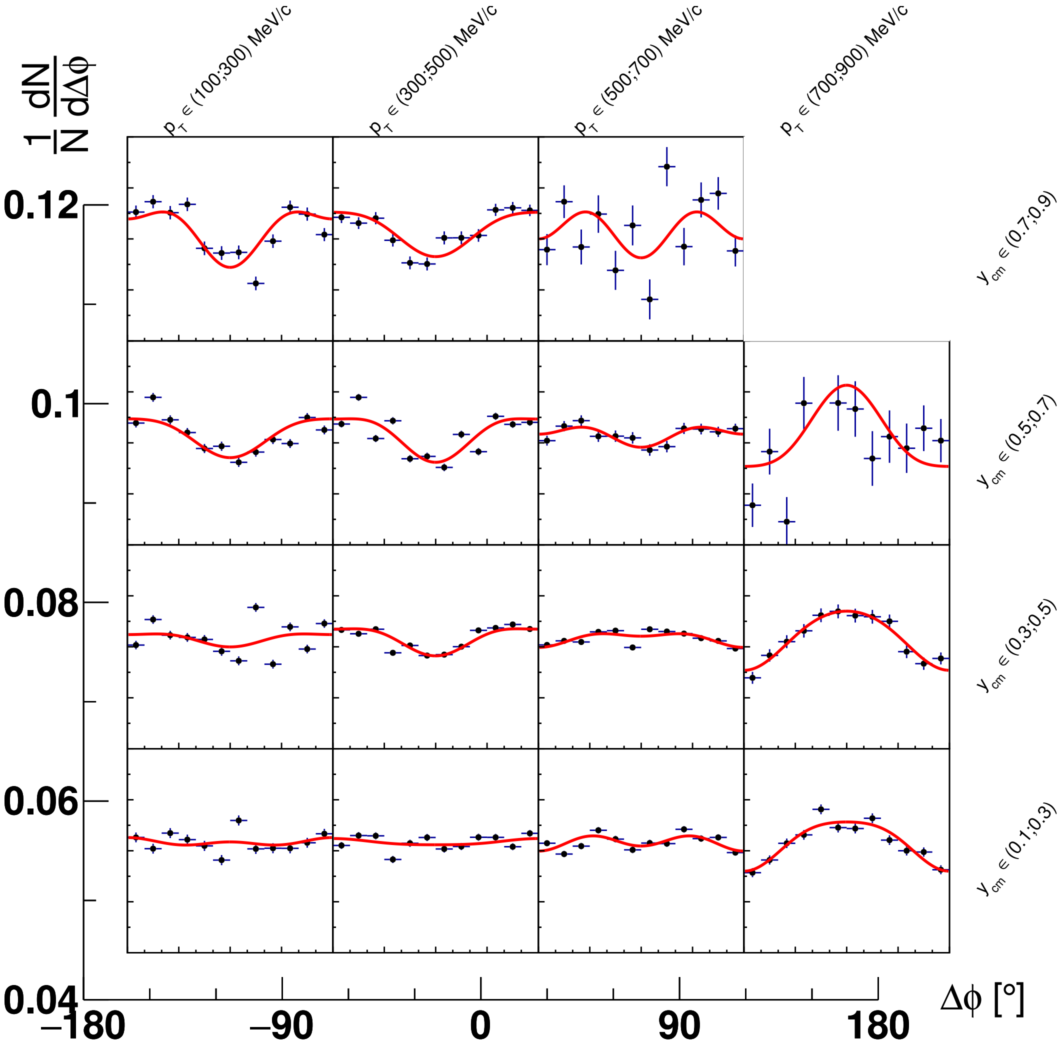

Figure D.2: π^0 normalized azimuthal angle distributions w.r.t. event plane for centrality class 10 - 20 %, fit is done with a function 4.16.

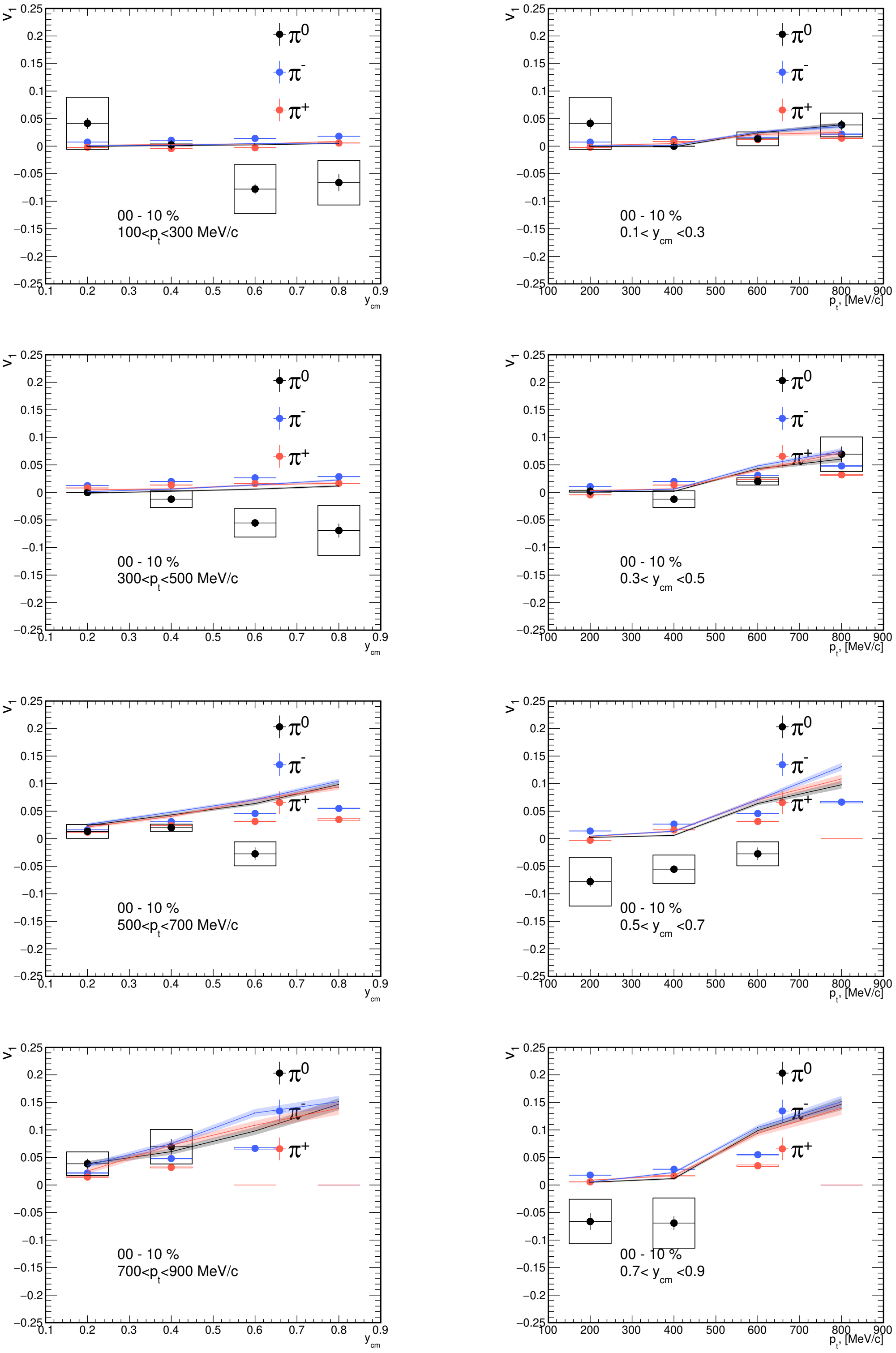

Figure D.3: Directed flow for 0-10 % centrality. Transparent colors represent model UrQMD EOS. **Left** plots show projections versus rapidity, **right** plots show projections versus transverse momentum.

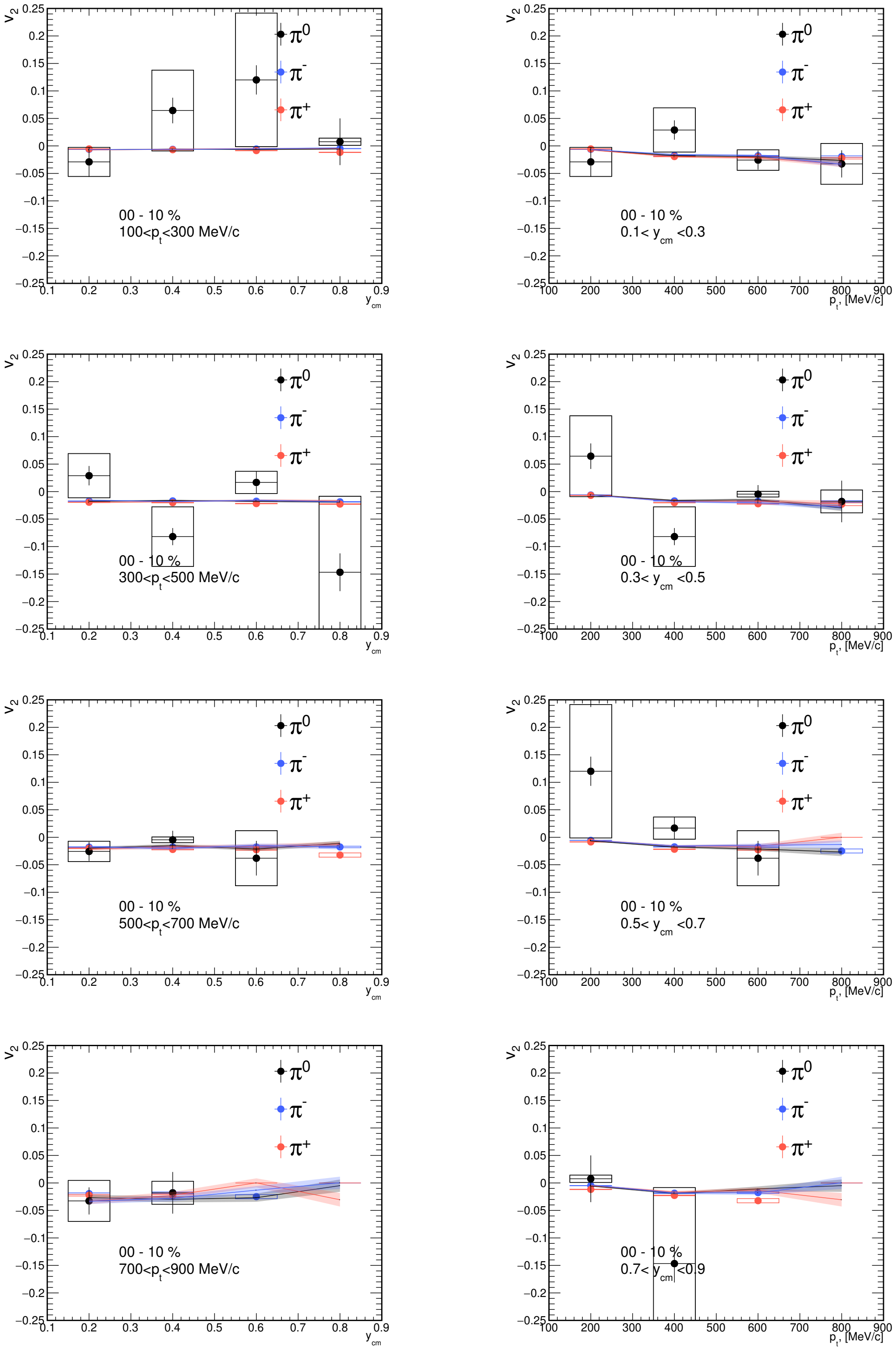

Figure D.4: Elliptic flow for 0-10 % centrality. Transparent colors represent model UrQMD EOS. **Left** plots show projections versus rapidity, **right** plots show projections versus transverse momentum.

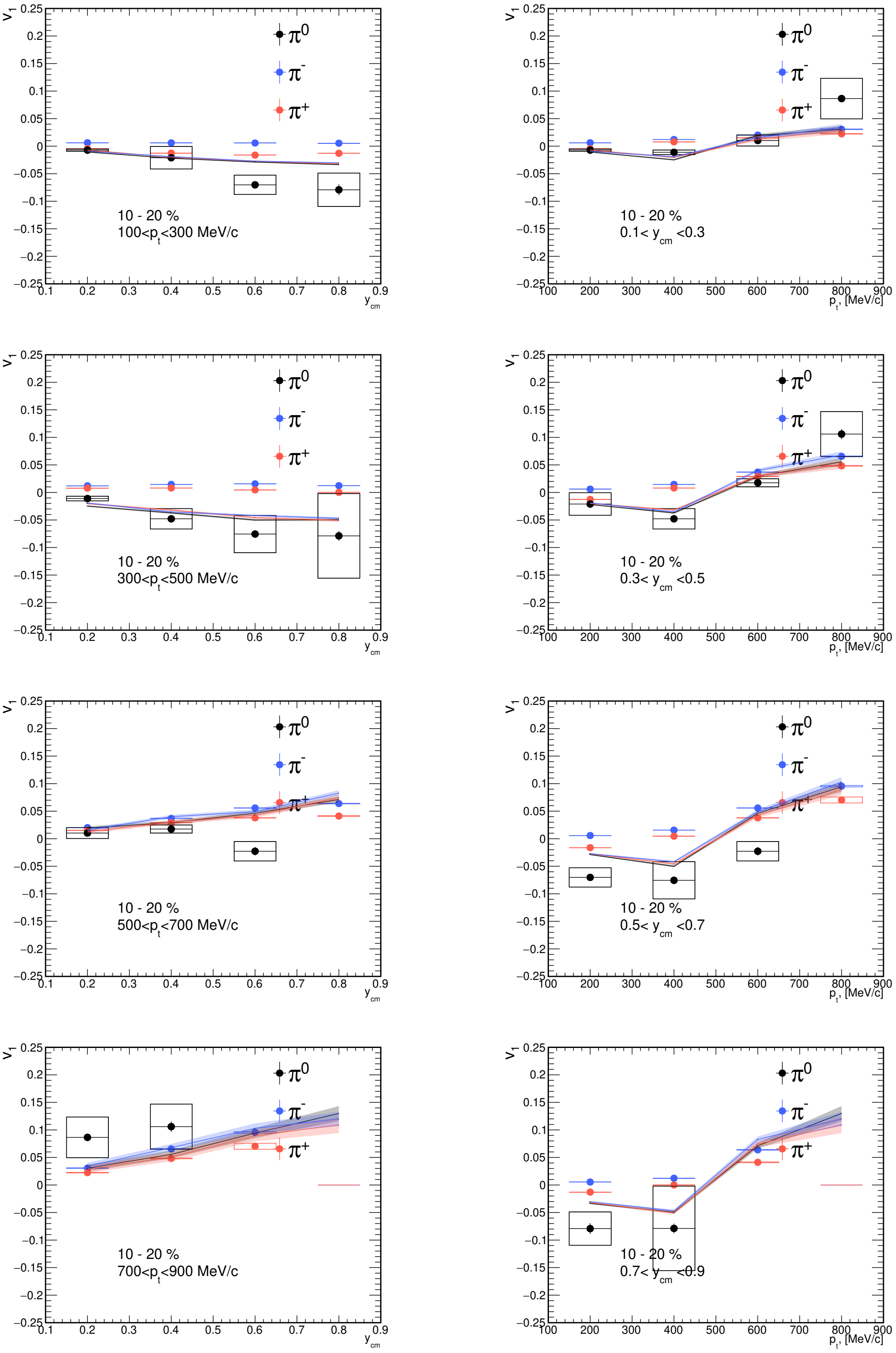

Figure D.5: Directed flow for 10-20 % centrality. Transparent colors represent model UrQMD EOS. **Left** plots show projections versus rapidity, **right** plots show projections versus transverse momentum.

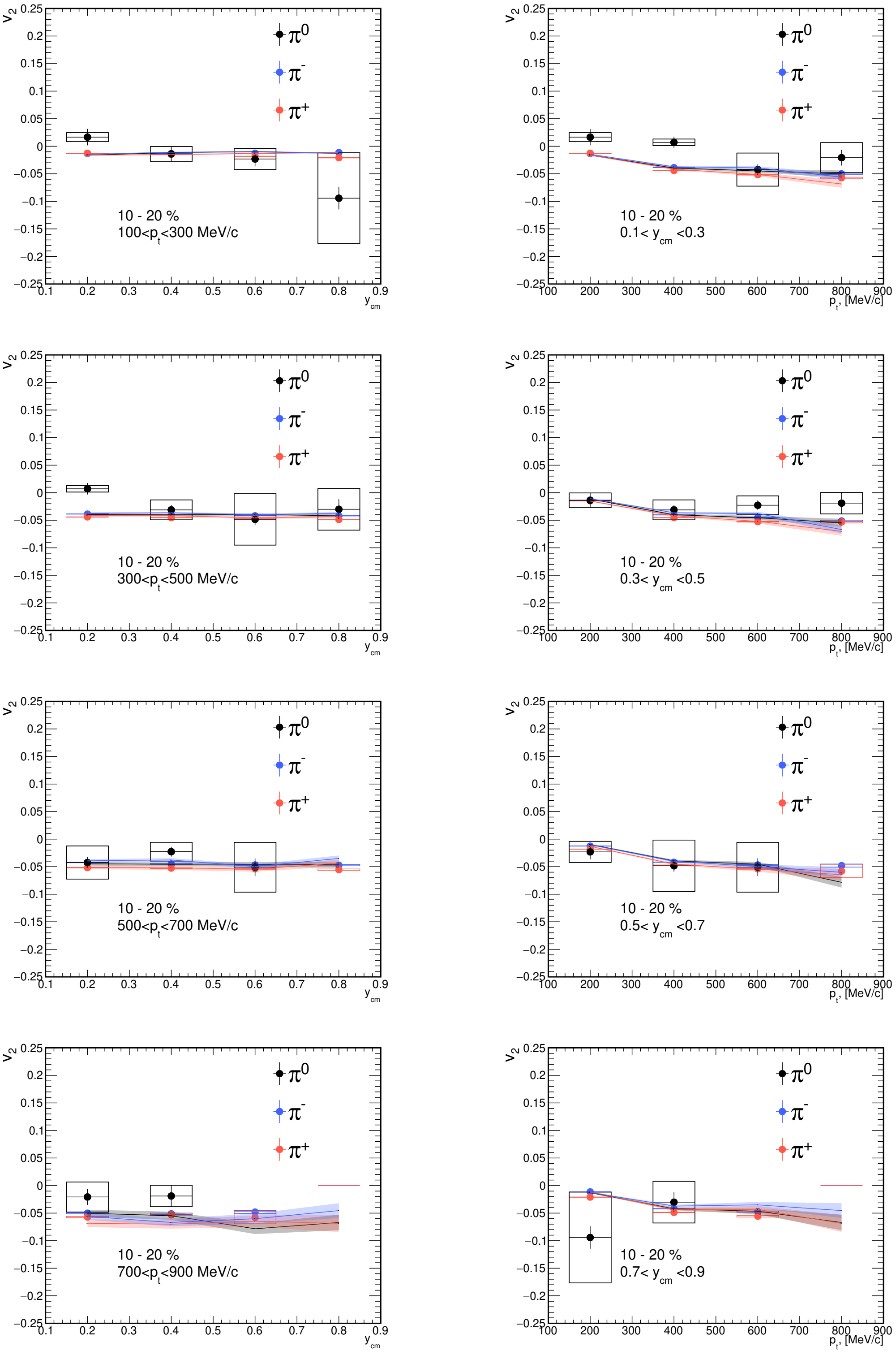

Figure D.6: Elliptic flow for 10-20 % centrality. Transparent colors represent model UrQMD EOS. **Left** plots show projections versus rapidity, **right** plots show projections versus transverse momentum.

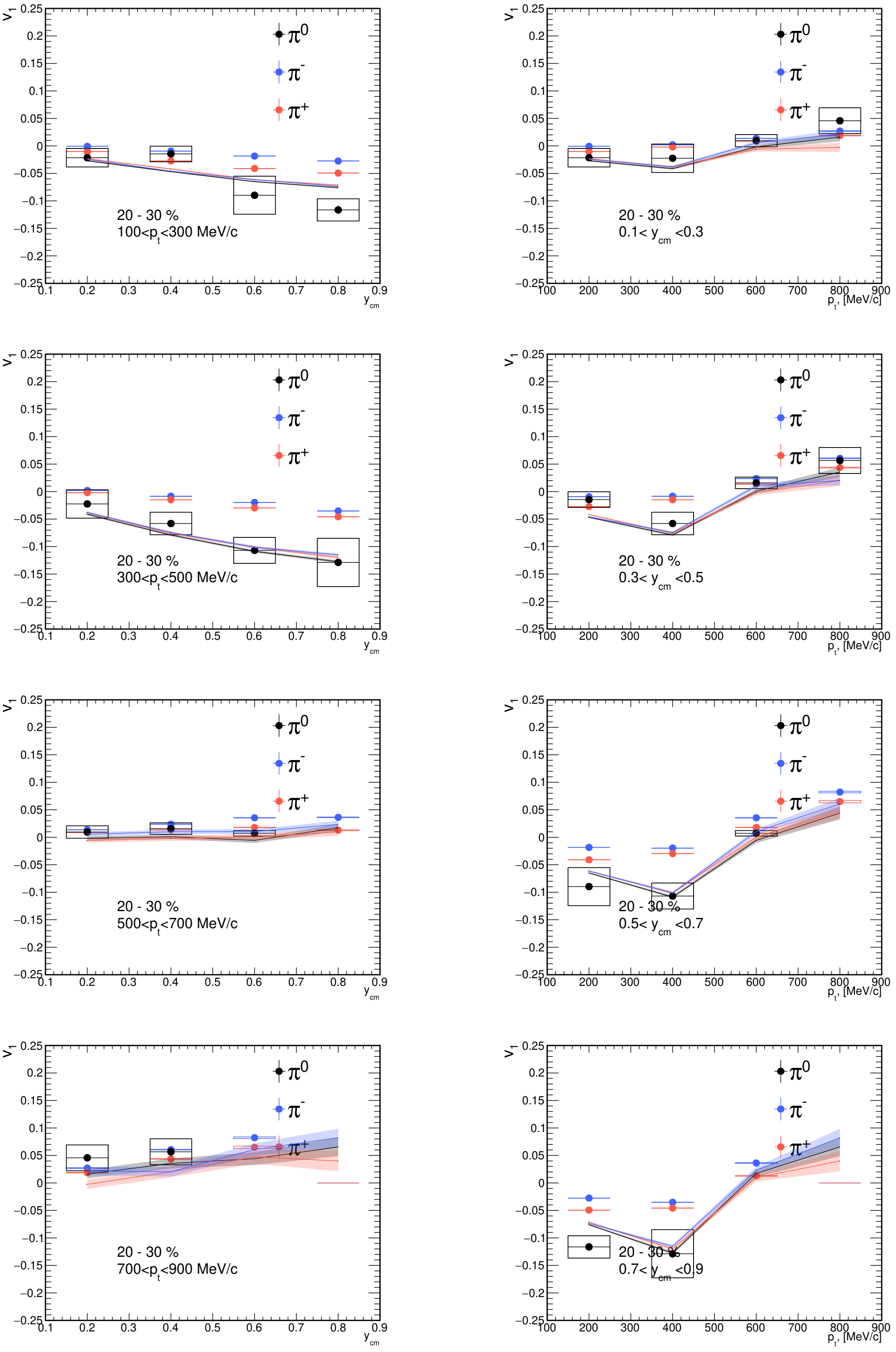

Figure D.7: Directed flow for 20-30 % centrality. Transparent colors represent model UrQMD EOS. **Left** plots show projections versus rapidity, **right** plots show projections versus transverse momentum.

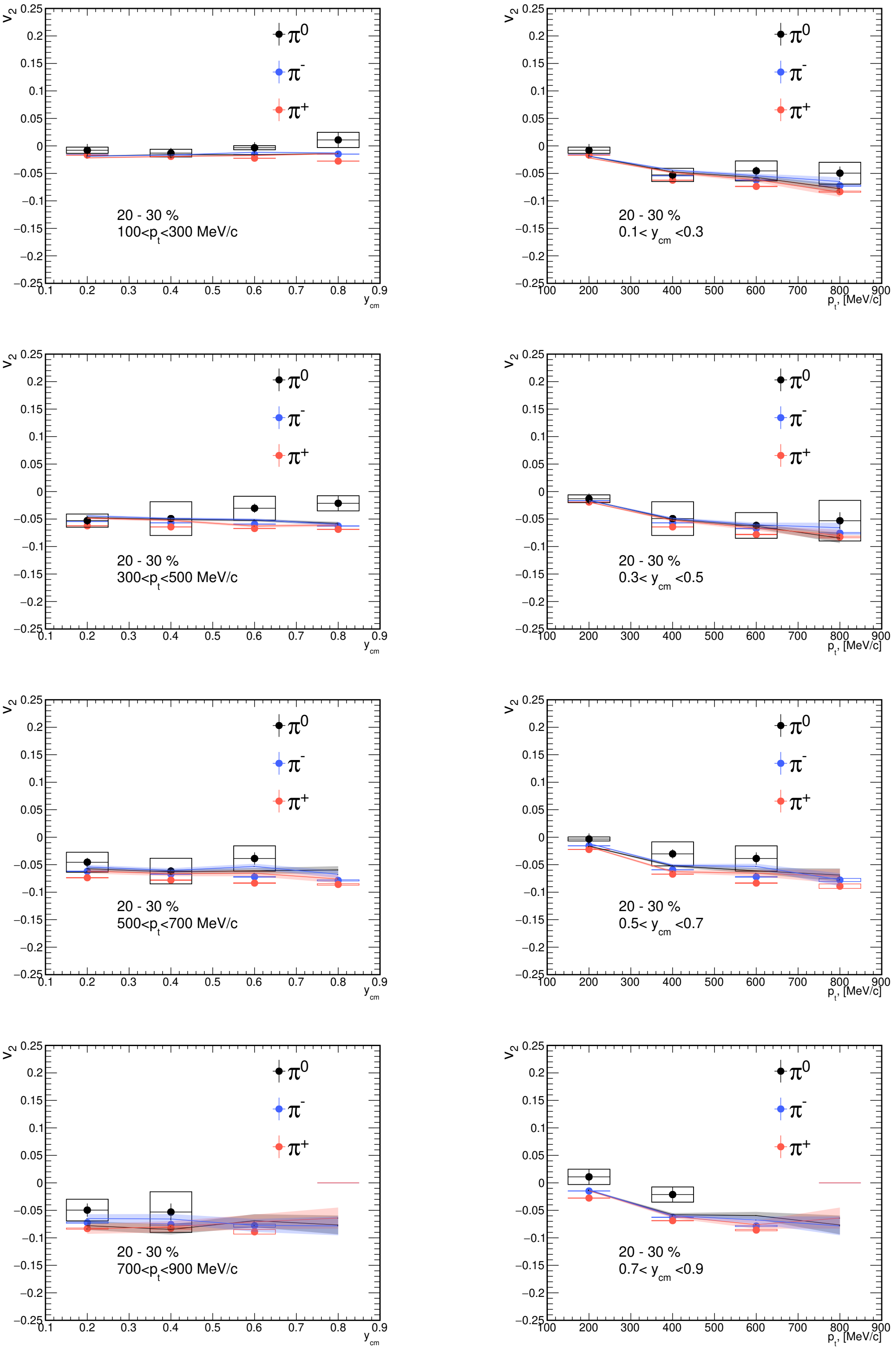

Figure D.8: Elliptic flow for 20-30 % centrality. Transparent colors represent model UrQMD EOS. **Left** plots show projections versus rapidity, **right** plots show projections versus transverse momentum.

E. π^0 , π^+ , π^- flow comparison within models

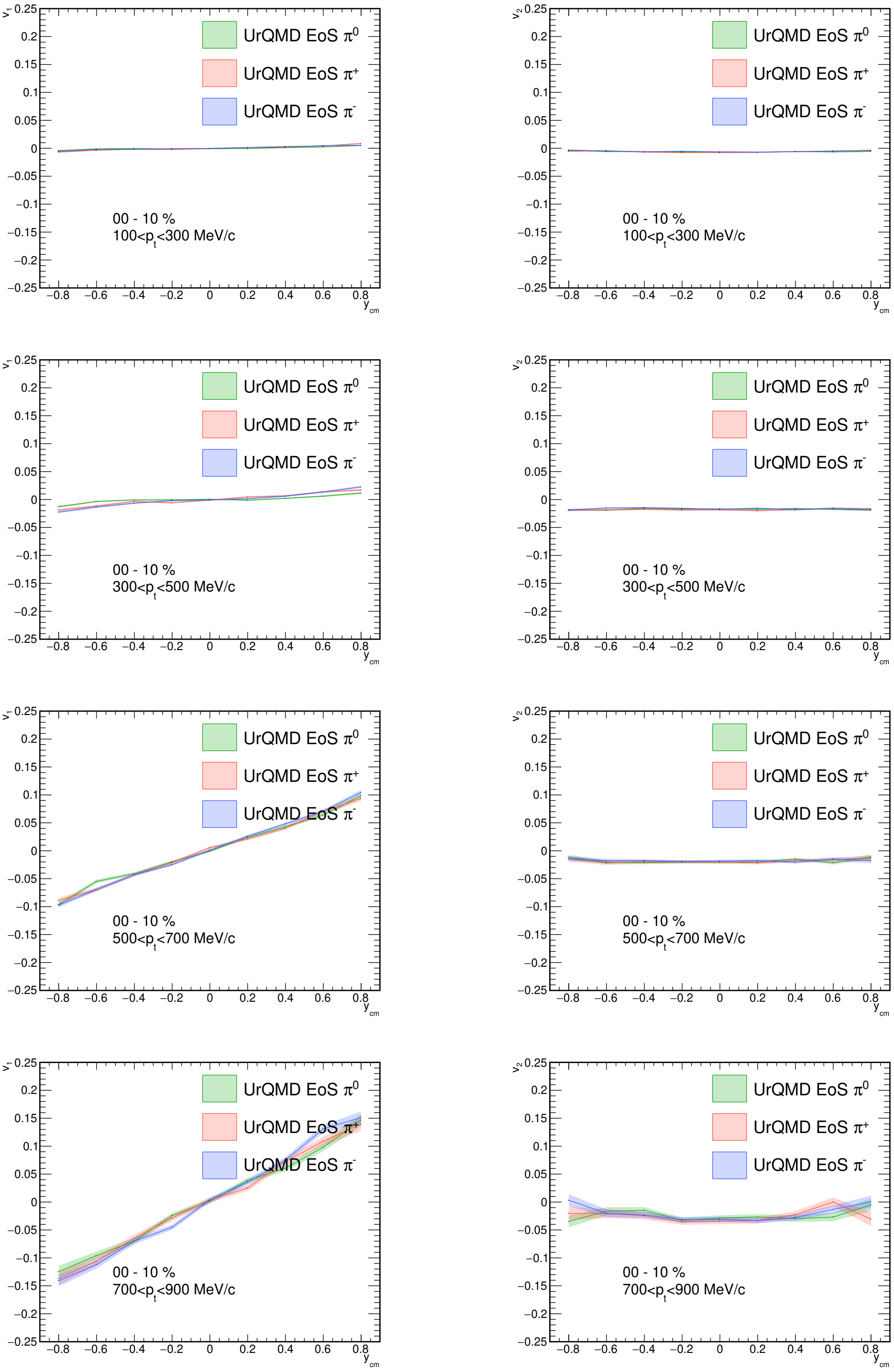

Figure E.1: Simulated flow for pions in $0 - 10\%$ most central $Ag + Ag$ collisions for **UrQMD with EoS**. **Left** plots show directed flow, **right** plots show elliptic flow.

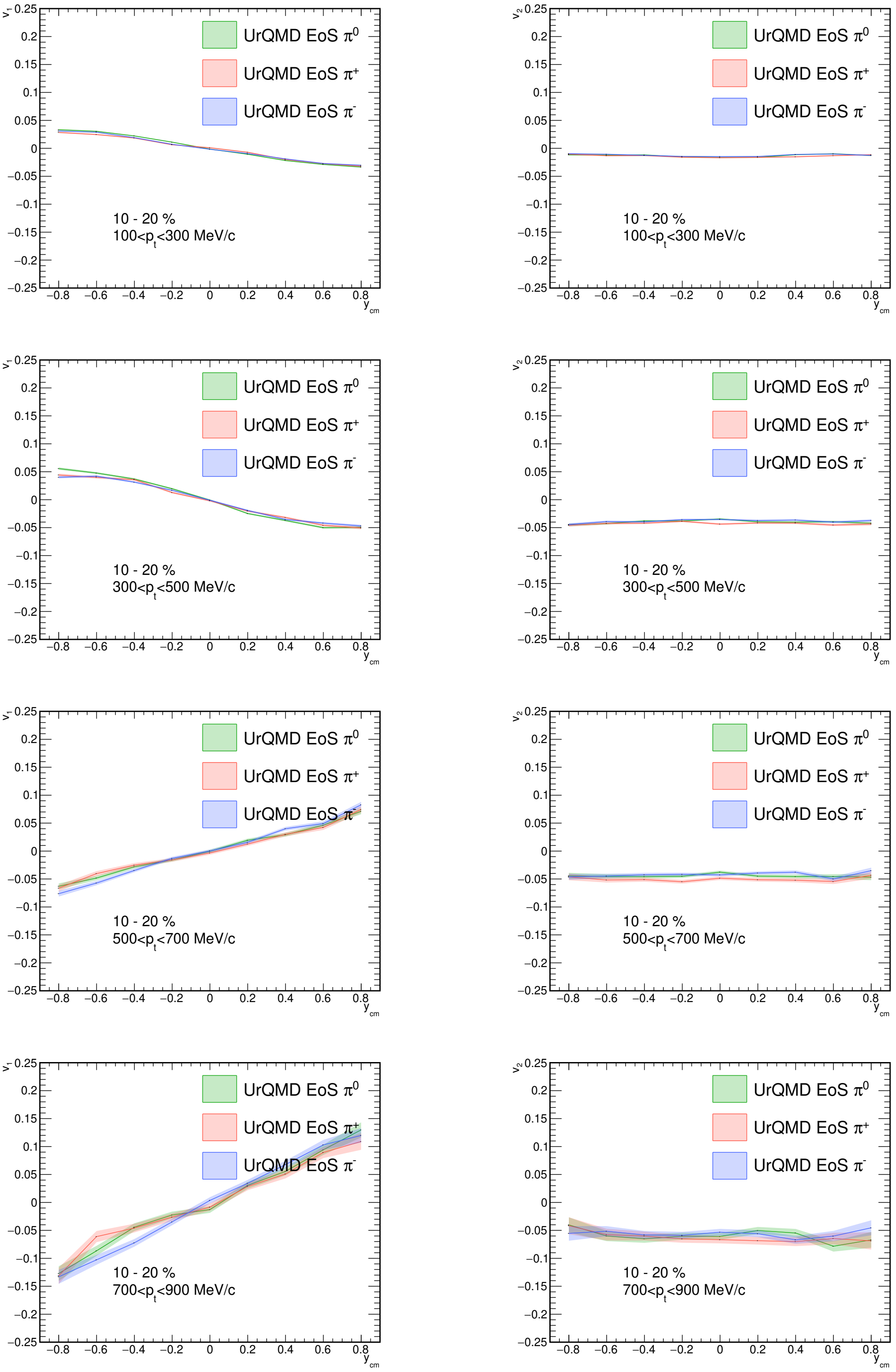

Figure E.2: Simulated flow for pions in $10-20\%$ most central $Ag+Ag$ collisions for **UrQMD with EoS**. **Left** plots show directed flow, **right** plots show elliptic flow.

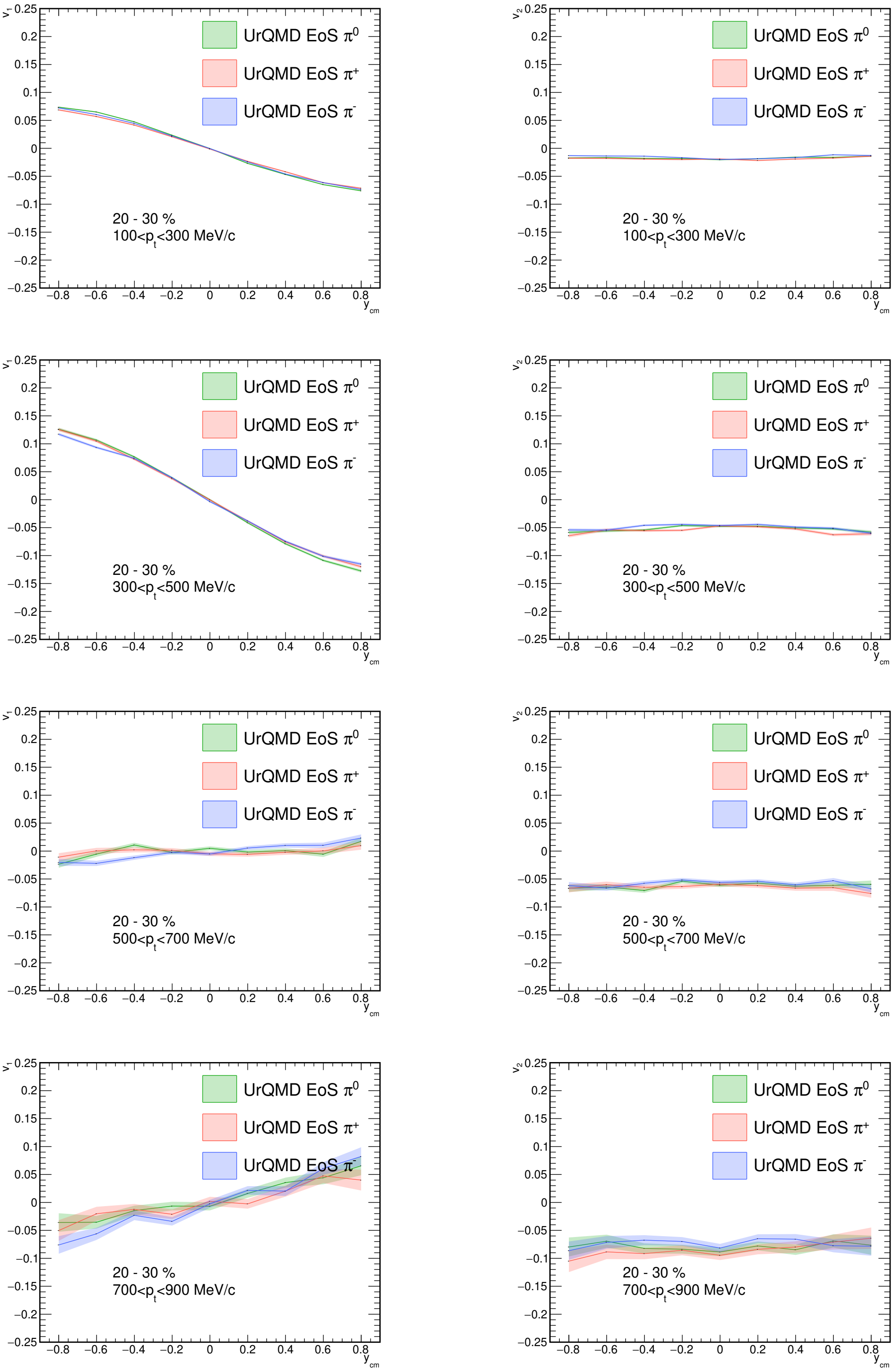

Figure E.3: Simulated flow for pions in $20 - 30\%$ most central $Ag + Ag$ collisions for **UrQMD with EoS**. **Left** plots show directed flow, **right** plots show elliptic flow.

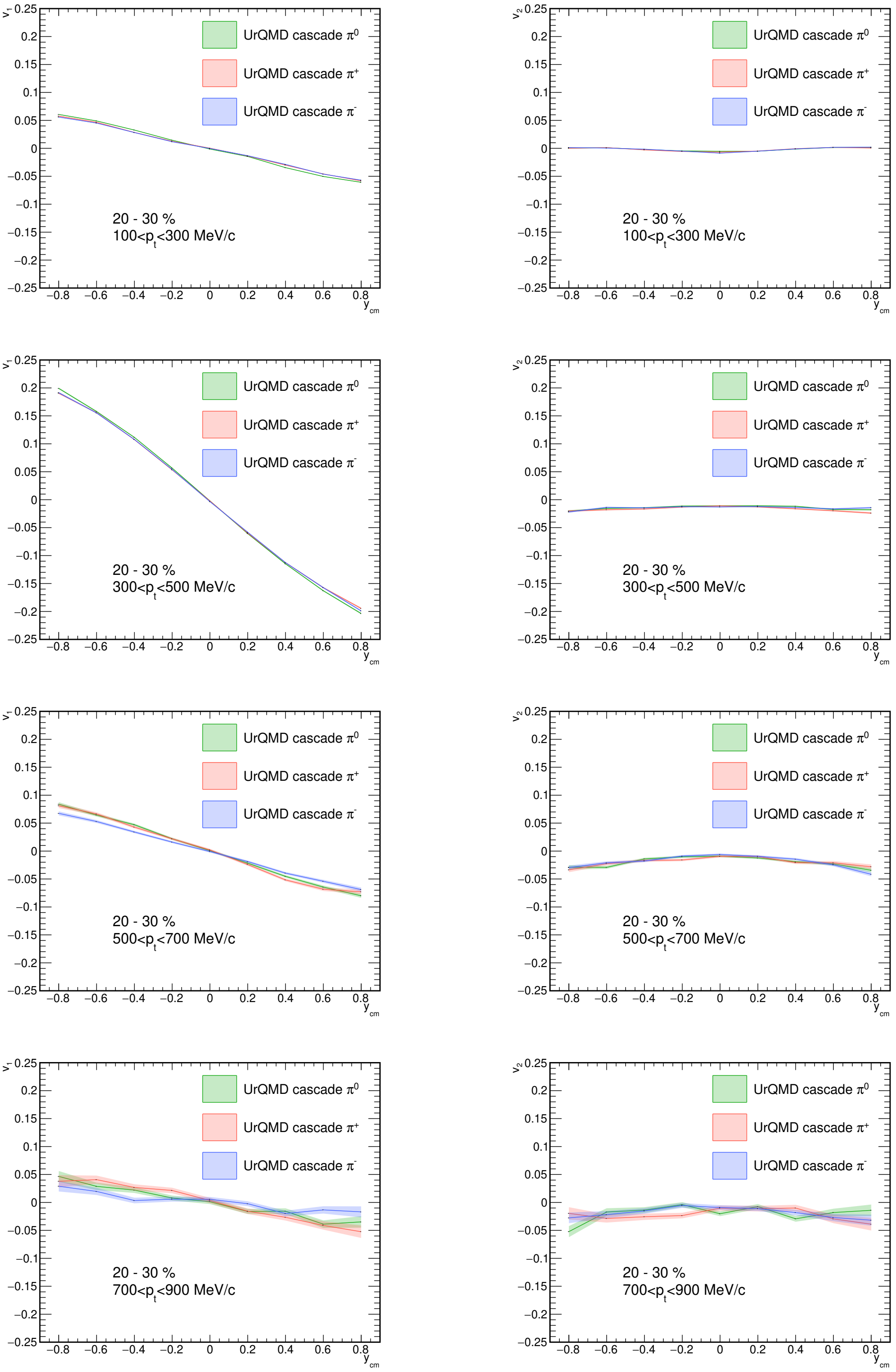

Figure E.4: Simulated flow for pions in $20-30\%$ most central $Ag+Ag$ collisions for **UrQMD cascade**. **Left** plots show directed flow, **right** plots show elliptic flow.

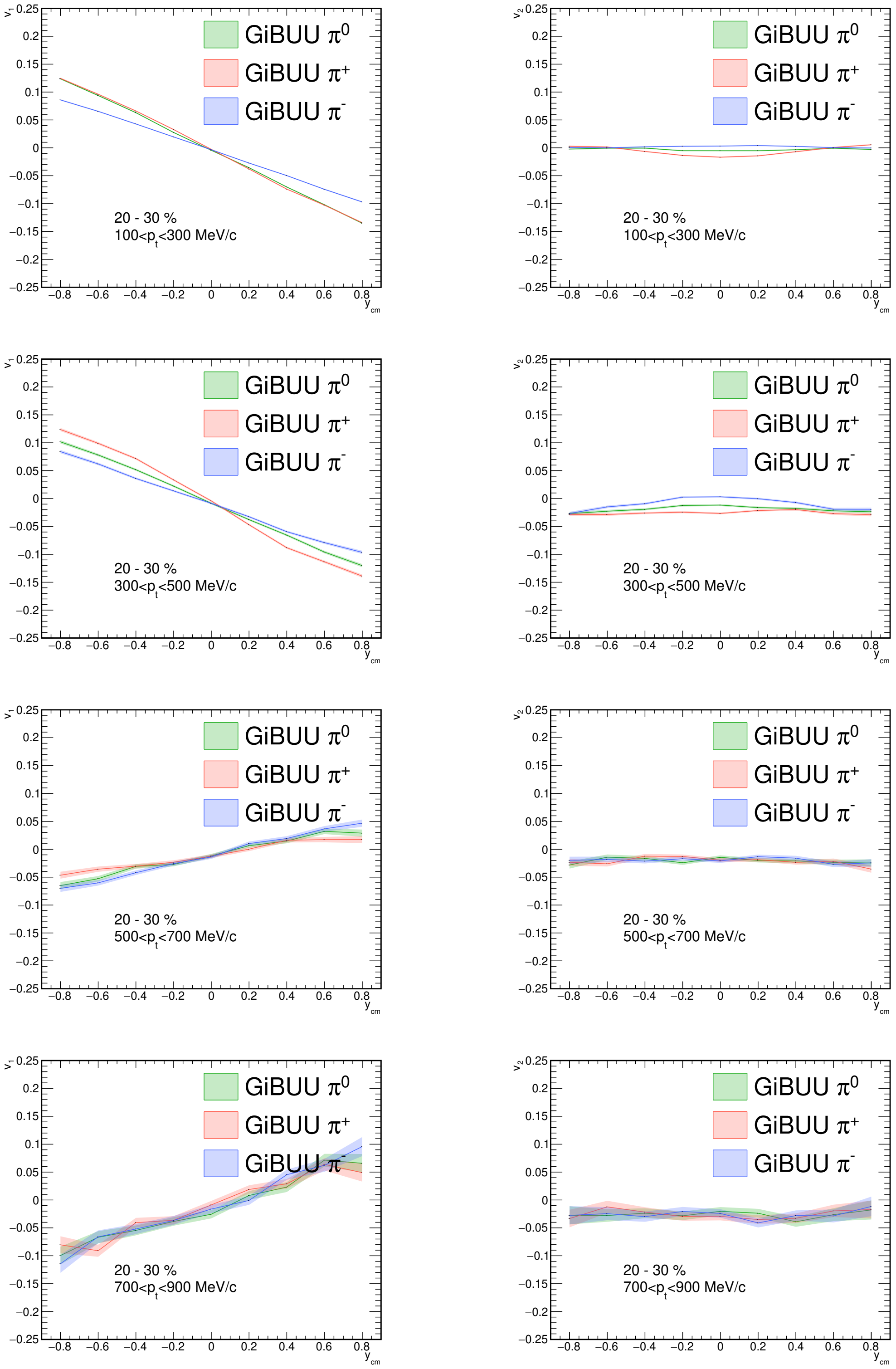

Figure E.5: Simulated flow for pions in $20 - 30\%$ most central $Ag + Ag$ collisions for **GiBUU**. **Left** plots show directed flow, **right** plots show elliptic flow.

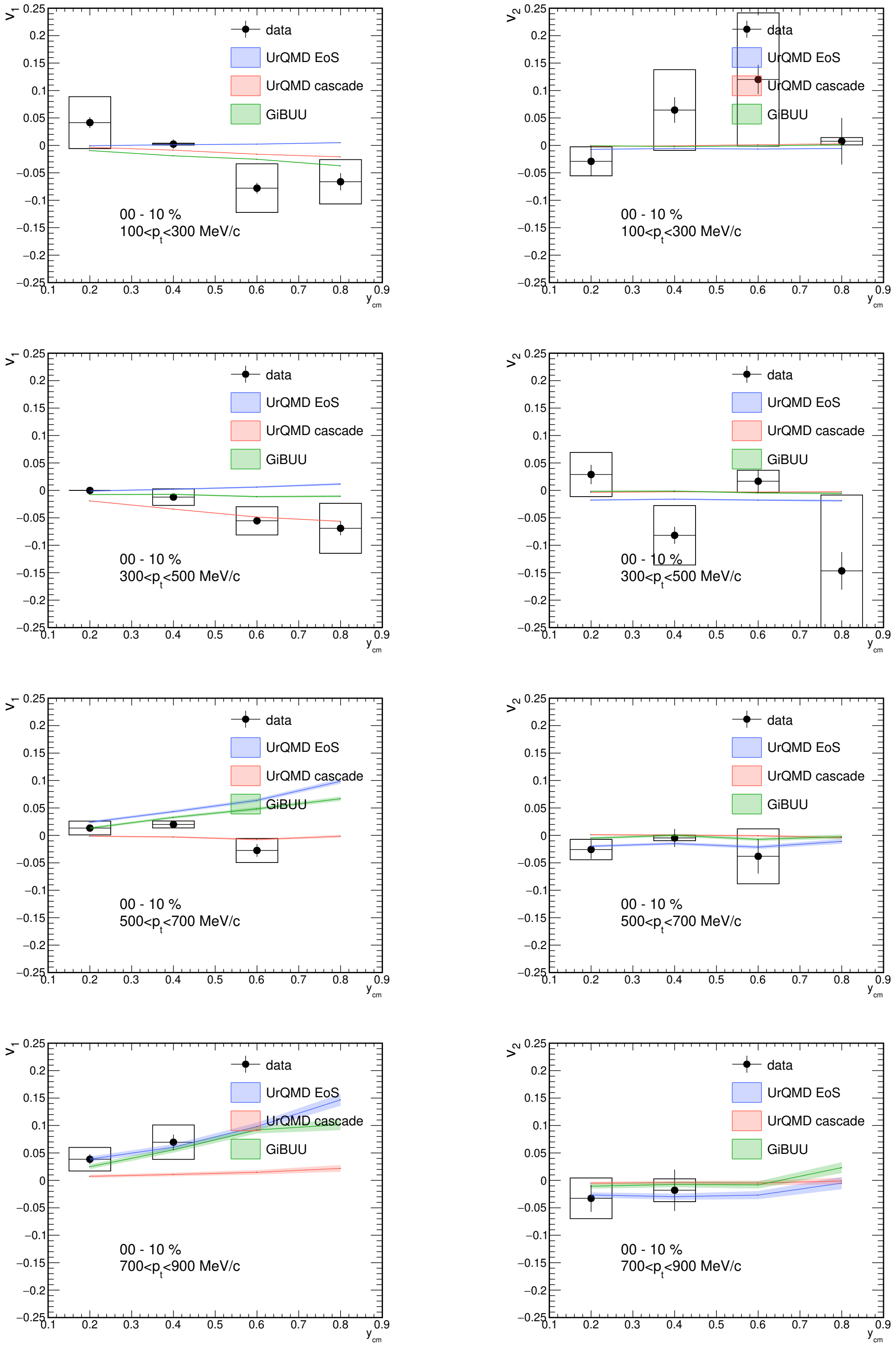

Figure E.6: Comparison of the data result and the predictions of the flow for three models - **UrQMD cascade**, **UrQMD with EoS**, and **GiBUU** for 0-10% centrality. The **Left** plots show directed flow, and the **right** plots show elliptic flow.

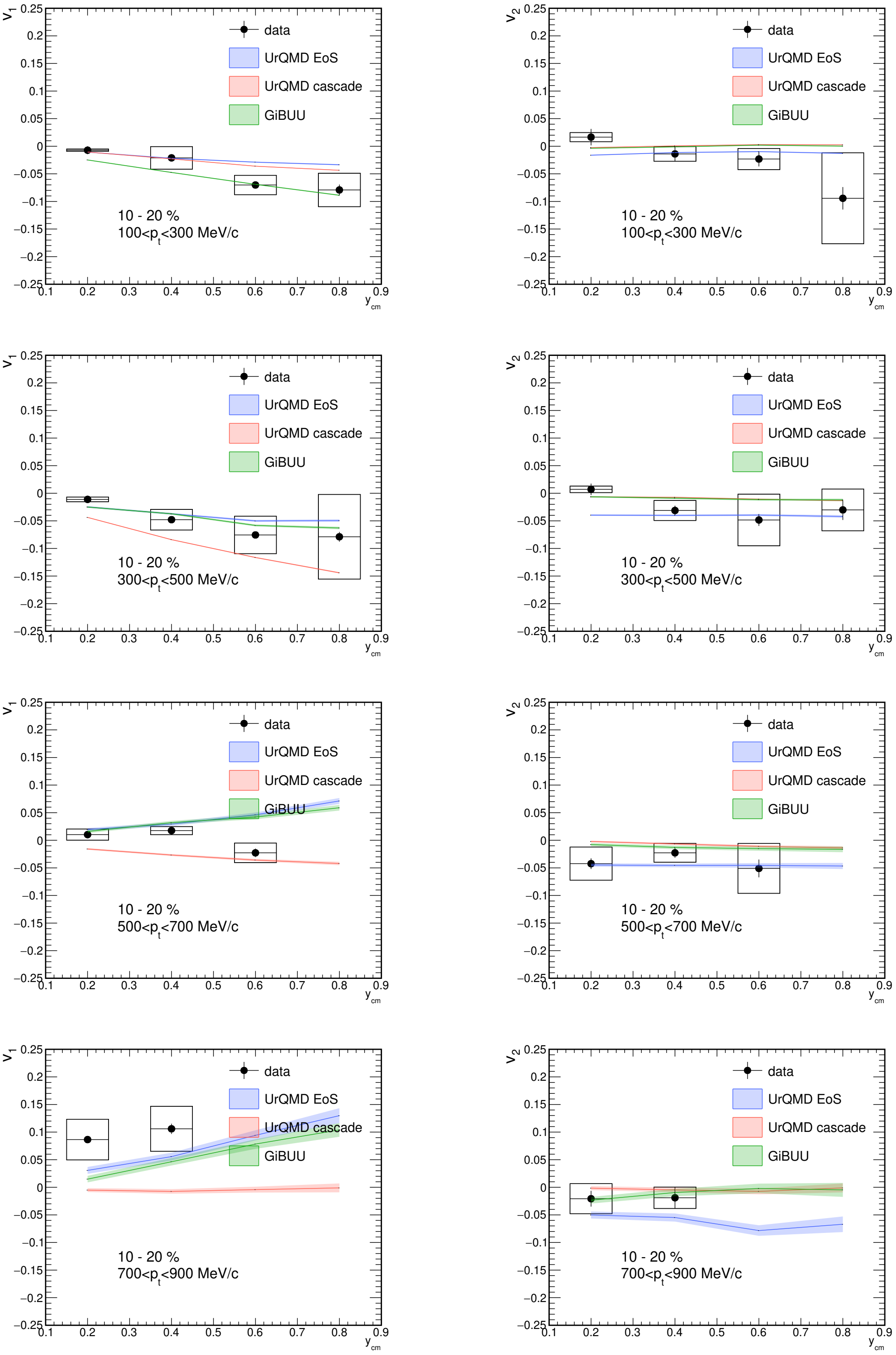

Figure E.7: Comparison of the data result and the predictions of the flow for three models - **UrQMD cascade**, **UrQMD with EoS**, and **GiBUU** for 10-20% centrality. The **Left** plots show directed flow, and the **right** plots show elliptic flow.

F. Other research activities

Shifts:

- 2019: three weeks as ECAL and TOF detector operator, daq operator, AgAg with $\sqrt{s_{NN}} = 2.42 GeV$
- 2022: two weeks as ECAL and TOF detector operator as a shift leader

HADES Collaboration meetings:

- XXXV 19 - 23 February GSI/FAIR Darmstadt, Germany
- XXXVI 11 - 15 March GSI/FAIR Darmstadt, Germany
- XXXVII 23 - 27 September, Krakow, Poland
- XXXVIII 02 - 06 March 2020, Helmholtz-Zentrum Dresden, Germany
- XXXIX 12 - 15 October 2020, virtual/ GSI/FAIR Darmstadt, Germany
- XL 08 - 12 March 2021, virtual/ GSI/FAIR Darmstadt, Germany
- XLI 04 - 08 October 2021, virtual/ GSI/FAIR Darmstadt, Germany
- XLII 21 - 25 March 2022, GSI/FAIR Darmstadt, Germany
- XLIII 19 - 23 September 2022, Coimbra, Portugal
- XLIV 13 - 17 March 2023, GSI/FAIR Darmstadt, Germany

HADES Analysis meetings:

- HADES Analysis meeting I 04 December - 06 December 2018, Prague, Czech Republic
- HADES Analysis meeting II 01 July - 03 July 2019, Seligenstadt
- HADES Analysis meeting III 22 June -24 June, 2020, virtual
- HADES Analysis Meeting IV 28 June - 30 June, 2021, virtual
- HADES Analysis meeting V. 11 July - 13 July 2022, Warsaw, Poland

Workshops:

- Workshop of the DAQ group in HADES in November 2017 at Frankfurt Goethe University, Frankfurt, Germany
- Workshop of DAQ group in HADES in January 2018 at Frankfurt Goethe University, Frankfurt, Germany
- Workshop on analysis tools for HADES in June 2018, GSI/FAIR Darmstadt, Germany

- Workshop on analysis techniques for centrality determination and flow measurements at FAIR and NICA, August 24-28, 2020, virtual
- Hades workshop, February 14-16, 2023, virtual

Service tasks:

- 2017 -2018: programming of FPGAs for DAQ, helping with ECAL installation
- Calibration of Electromagnetic Calorimeter for two big experiments, mainly AgAg with $\sqrt{s_{NN}} = 2.42$ GeV and pp with $\sqrt{s_{NN}} = 3.6$ GeV
- March 2018 at GSI/FAIR - Installation of cables for ECAL detector
- August 2018 at GSI/FAIR - Control check and repair of TOF detector
- 2019 - 2020 - Installation of ECAL sectors and shielding of PMTs, in total, two months stay.
- 2021 - 2022 - Last ECAL sector assembly, in total one month.

Erasmus+ program: 24.09.2020 - 01.01.2021 GSI/FAIR Darmstadt, Germany

Help in organization of ICHEP 2020, 40th International Conference on High-Energy Physics, Prague, Czech Republic / virtual.

F.1 Public presentations

This Appendix contains a list of publications and public presentations (talks and posters) given by the author from the beginning of the doctoral studies until finishing this thesis. The following are also presentations and publications published with my primary authorship.

- FAIRNESS 2019, talk, Arenzano, Italy, 19/05/2019 - 23/05/2019
- ZIMANYI SCHOOL 2018, talk, December 3-7, 2018, Budapest, Hungary
- MESON 2021 conference, 16th International Workshop on Meson Physics online via ZOOM, talk, Krakow 17th - 20th May 2021
- Quark Matter 2022, poster presentation, 04/04 - 04/10/2022, Krakow, Poland
- FAIRNESS 2022, talk, Paralia, Greece, 23/05 - 28/05/2022
- Bormio 2023, talk, Bormio, Italy, 23/01 - 29/01/2023